JOURNAL OF APPLIED PHYSICS

JOURNAL OF APPLIED PHYSICS

Vol. 25, No. 10 OCTOBER, 1954

In This Issue

Special Issue on High Polymer Physics **Page**

Effect of Crystallinity on the Dynamic Mechanical Properties of Polyethylenes Lawrence E. Nielsen 1209
Dynamic Bulk Viscosity of Polyisobutylene Robert S. Marvin, R. Aldrich, and H. S. Sack 1213
Studies of Rubberlike Polymers by Nuclear Magnetism V. R. Honnold, F. McCaffrey, and B. A. Mrowca 1219
Measurement of Orientation in Polystyrene Monofilaments by Means of Double Refraction R. D. Andrews 1223
Theory of Orientation and Double Refraction in Polymers Edward F. Gurnee 1232

Regular Contributed Original Research

Transformation of Scattering Cross Sections P. F. Zweifel and H. Hurwitz, Jr. 1241
Spurious Areas in Pole Figures A. H. Geisler 1245
Radiation from a Point Dipole Located at the Tip of a Prolate Spheroid E. C. Hatcher, Jr., and A. Leitner 1250
Effect of Uniform Displacement on the Stress Distribution of a Wood Plate Kenneth C. Walters and C. Bassel Smith 1254
Method of Averages and Its Comparison with the Method of Least Squares Morris Morduchow 1260
Effects of Cathode and Anode Resistance on the Retarding Potential Characteristics of Diodes G. C. Dalman 1263
Theory of Strong Electromagnetic Waves in Massive Iron William MacLean 1267
PPI Light Spot Brightness Probability Distributions George C. Sponsler and Fern L. Shader 1271
Direct Cellular Evaluation of the Density of States in Phase Space and the Accurate Calculation of Fermi Levels Louis Gold 1278
Focusing of a Long Cylindrical Electron Stream by Means of Periodic Electrostatic Fields Ping King Tien 1281
Transient Flow of Non-Ideal Gases in Porous Solids—One-Dimensional Case J. S. Aronofsky and O. D. Ferris 1289
Effect of a Transverse Electric Field on Carrier Diffusion in the Base Region of a Transistor J. S. S. Kerr, J. S. Schaffner, and J. J. Suran 1293
Analyses of Basic Dielectric Amplifier Circuits Shou-Hsien Chow 1297
Applications of the Dirac Delta Function to the Evaluation of Certain Integrals Murray R. Spiegel 1302
Compression Wave Velocity Experiments with Copper Jacob Savitt, R. H. Stresau, and L. E. Starr 1307
Stationary Temperature Distribution in an Electrically Heated Conductor Charles A. Domenicali 1310
Method for Determining the Viscoelastic Properties of Dilute Polymer Solutions at Audio-Frequencies Karl Sittel, Prince E. Rouse, Jr., and Emerson D. Bailey 1312
Torsion of a Shaft with a Toroidal Cavity G. Weiss and L. E. Payne 1321
Thickness-Shear and Flexural Vibrations of a Circular Disk R. D. Mindlin and H. Deresiewicz 1329
Low-Energy Electron Diffraction Investigation of Chemisorbed Gases on the (100) Faces of Copper and Nickel Single Crystals R. E. Schlier and H. E. Farnsworth 1333
On the Flicker Noise Generated in an Interface Layer H. J. Hannam and A. van der Ziel 1336
Letters to the Editor:
Scalloped Beam Amplification T. G. Mihran 1341
Equation of State of Argon R. H. Christian and R. G. Shreffler 1341
Additional Comments on "Diffraction of Electromagnetic Waves by an Aperture in a Plane Screen" Ralph D. Kodis 1342
Electron Beam Effects on Thin Evaporated Bismuth Films P. J. Bryant, H. U. Rhoads, and A. H. Weber 1343
Re-examination of Low-Temperature Properties of Crystalline Quartz A. Pavlovic and R. Pepinsky 1344
Additional Observation on Thermal Effects in Point Contact Rectifiers H. L. Armstrong 1345
Erratum: Low Loss Ferrites L. G. Van Uitert, J. P. Schafer, and C. L. Hogan 1345
Erratum: A Note on "Effect of Filament Voltage on the Plate Current of a Diode" Henry S. C. Chen 1345
Cover Photograph 1346
Index to Advertisers xxii

ROBERT L. SPROULL
Editor

ELMER HUTCHISSON,
EARLE C. GREGG,
Retiring Editors

Board of Editors
MAURICE A. BIOT
RAY E. BOLZ
WALLACE J. ECKERT
ROBERT D. HEIDENREICH
LOUIS A. PIPES
ROMAN SMOLUCHOWSKI
W. R. SMYTHE
ARTHUR V. TOBOLSKY
ALVIN M. WEINBERG

Publication of the
American Institute of Physics

OFFICERS
FREDERICK SEITZ,
Chairman
GEORGE B. PEGRAM,
Treasurer

GOVERNING BOARD
ROBERT F. BACHER
J. W. BUCHTA
KARL K. DARROW
S. A. GOUDSMIT
DEANE B. JUDD
HUGH S. KNOWLES
C. C. LAURITSEN
W. H. MARKWOOD, JR.
WILLIAM F. MEGGERS
PHILIP M. MORSE
BRIAN O'BRIEN
HARRY F. OLSON
GEORGE B. PEGRAM
ERIC RODGERS
RALPH A. SAWYER
FREDERICK SEITZ
WILLIAM SHOCKLEY
RICHARD M. SUTTON
J. H. VAN VLECK
MARK W. ZEMANSKY

Consultant on Printing
MELVIN LOOS

ADMINISTRATIVE STAFF
HENRY A. BARTON,
Director
WALLACE WATERFALL,
Executive Secretary
THEODORE VORBURGER,
Advertising Manager
RUTH F. BRYANS,
Publication Manager
EDITH I. NEFTEL
Circulation Manager
KATHRYN SETZE
Assistant Treasurer

The JOURNAL OF APPLIED PHYSICS, published monthly at Prince and Lemon Sts., Lancaster, Pa., is devoted to physics in its role as the science basic to other natural sciences and to the arts and industries. Previous to 1937 this publication was known as PHYSICS. The JOURNAL OF APPLIED PHYSICS publishes editorials and reviews, as well as technical papers of applied physics. Articles appearing in it are indexed regularly, according to their field, by Physics Abstracts, Chemical Abstracts, Engineering Index, Inc., Industrial Arts Index, etc.

Manuscripts should be submitted to Robert L. Sproull, Editor, Rockefeller Hall, Cornell University, Ithaca, New York. Unless otherwise stated, submission of a manuscript is a representation that it has been neither copyrighted, published, nor submitted for publication elsewhere. The authors' institutions are requested to pay a **publication charge** of $8 per page which, if honored, entitles them to 100 reprints without further charge. Instructions will be sent with galley proofs.

Subscriptions, renewals, and orders for back numbers should be addressed to the American Institute of Physics, 57 East 55 Street, New York 22, New York.

Subscription Price	U.S. and Canada	Elsewhere
To members of the American Institute of Physics and Affiliated Societies	$10.00	$11.00
To all others	12.00	13.00

Back Number Prices

Yearly back number rate when complete year is available: $14.00.
Single copies: $1.25 each.

Changes of address should be sent to the American Institute of Physics; **corrected proofs** should be sent to the Publication Manager, American Institute of Physics. **Advertising rates** supplied on request. Orders, advertising copy, and cuts should be sent to the American Institute of Physics.

Entered as second class matter January 22, 1937, at the Post Office at Lancaster, Pennsylvania, under the Act of March 3, 1879. Accepted for mailing at the special rate of postage provided for in paragraph (d-2), section 34.40, P. L. & R. of 1948, authorized May 2, 1932.

Journal
of
Applied Physics

Volume 25, Number 10 October, 1954

Special Issue on High Polymer Physics

The following five papers were presented at the meeting of the Division of High Polymer Physics of the American Physical Society in Detroit, Michigan, March 18–20, 1954.

Effect of Crystallinity on the Dynamic Mechanical Properties of Polyethylenes

LAWRENCE E. NIELSEN
Plastics Division, Monsanto Chemical Company, Springfield, Massachusetts
(Received March 12, 1954)

Six polyethylenes which differed widely in the degree of crystallinity were studied. The crystallinity was determined from density measurements. Both the density and the dynamic mechanical measurements were made over the temperature range from 25°C to above the melting point of the material.

The dynamic shear modulus drops rapidly as the melting point is approached. The mechanical damping goes through a maximum near 60°C and then through a minimum just below the melting point. It is possible to predict the density of any of the polyethylenes at any temperature below the melting point from the value of the shear modulus at the same temperature. The more crystalline materials have the higher shear moduli and the higher melting points.

INTRODUCTION

THE rigidity of polyethylene is due to its crystallinity. Polyethylene without crystallinity would be a viscous liquid or a rubbery material. This investigation was undertaken to see in a quantitative manner how mechanical properties depend upon the degree of crystallinity. The density increases with the degree of crystallinity, and since such measurements are relatively simple and accurate, density measurements were used rather than x-ray measurements to determine the percent of crystallites in polyethylene. The dynamic shear modulus and mechanical damping were chosen as two of the most important mechanical properties. Such dynamic tests give more information about the structure and behavior of a material than most other mechanical tests.

EXPERIMENTAL DETAILS

Six polyethylenes, which differed widely in their properties, were studied; three of these were commercial materials and three were experimental polymers. Infrared spectra were used to check the purity of the materials and to determine the degree of chain branching as measured by the CH_3-to-CH_2 ratio.[1,2]

The test specimens were made by molding sheets of the materials between press-polish plates at 160°C under pressure. The sheets were cooled slowly (at least ½ hour) between the melting points and 60°C. They were conditioned at least one day at room temperature before being used.

For the density determinations, sheets 0.080 in. in thickness and weighing 10 to 15 grams were used. From 18°C to 70°C the density was determined by Archimedes' principle using water as the immersion liquid and an analytical balance for the weighings. Measurements up to 160°C were made by a pycnometer method using Dow-Corning silicone oil 200 as the immersion liquid. The density measurements are expected to be accurate to a few parts in ten thousand. The temperature control at the higher temperatures was accurate to only about ±½°C.

The dynamic mechanical properties were measured by a recording torsion pendulum, which has been de-

[1] Cross, Richards, and Willis, Disc. Faraday Soc. 9, 235 (1950).
[2] J. D. Cotman, Jr., Ann. N. Y. Acad. Sci. 57, 417 (1953).

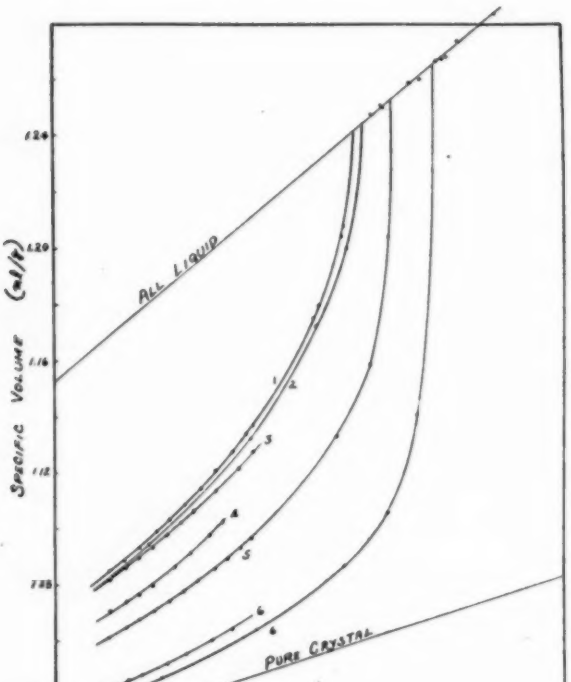

FIG. 1. Specific volume of six polyethylenes as a function of temperature.

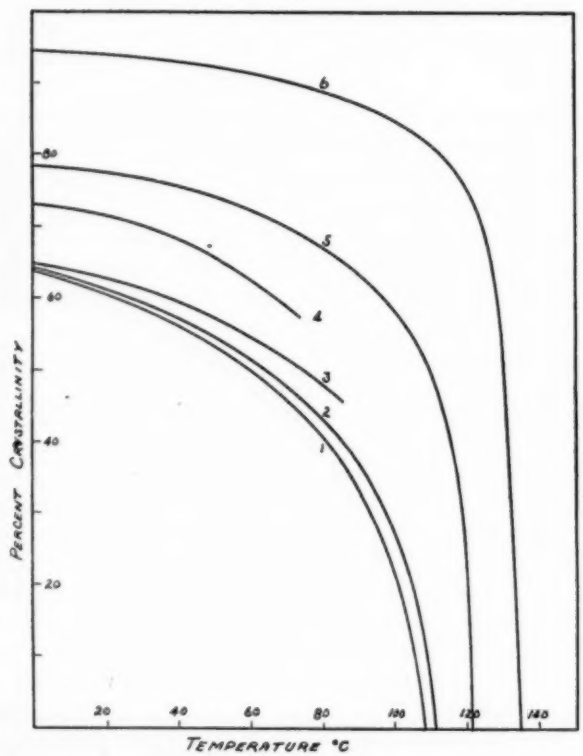

FIG. 2. Crystallinity of polyethylenes as a function of temperature.

scribed previously.[3] The shear modulus was calculated from the specimen dimensions, the moment of inertia of the oscillating system, and the frequency of the oscillation. The mechanical damping (logarithmic decrement) was calculated from the rate of dying down of the free vibrations. Most of the specimens were 4 in. $\times\frac{3}{8}$ in. $\times$0.035 in. The frequency in general varied from 0.2 to 1.0 cycle per second. Measurements were made from 25°C to the melting point or above.

RESULTS

Figure 1 shows the specific volume (reciprocal of the density) plotted against temperature for the six polyethylenes. The curves show the characteristic behavior of some melting over a wide temperature range with most of the melting, however, occurring within a few

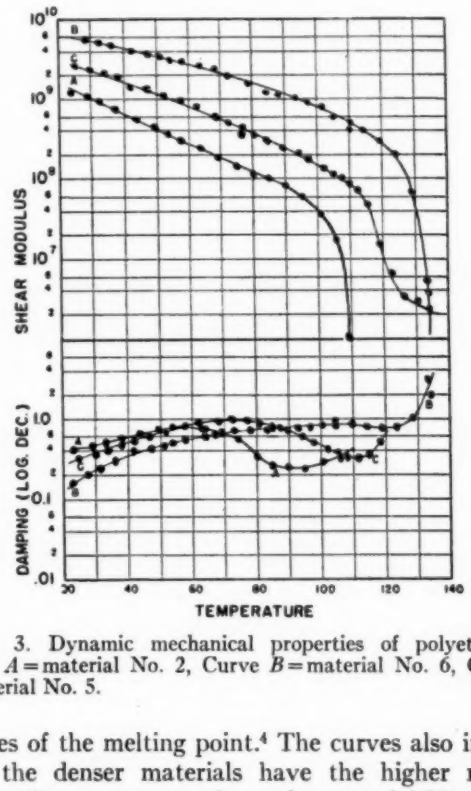

FIG. 3. Dynamic mechanical properties of polyethylenes. Curve A = material No. 2, Curve B = material No. 6, Curve C = material No. 5.

degrees of the melting point.[4] The curves also indicate that the denser materials have the higher melting points. Two curves are shown for material No. 6. The curve with the higher specific volume was obtained on a specimen prepared as described above. The other curve was obtained on the same specimen after it had been annealed at 60°C to 70°C for several hours. These curves illustrate how the crystallinity can be changed by heat treatment.

The degree of crystallinity can be calculated by the equation

$$X=\frac{V_a-V}{V_a-V_c}$$

[3] L. E. Nielsen, Rev. Sci. Instr. **22**, 690 (1951).
[4] E. Hunter and W. G. Oakes, Trans. Faraday Soc. **41**, 49 (1945).

where V_a is the specific volume of the liquid or amorphous portion at a given temperature, V_c is the specific volume of the pure crystal at the same temperature, and V is the observed specific volume. X is the fraction of the material in the crystalline form.[5] The following values were used:

$$V_c = 1.025 \text{ at } 0°\text{C}$$
$$V_a = 1.152 \text{ at } 0°\text{C}.$$

The coefficient of expansion of the crystals, $dV_c/V_c dT$, was taken as 3×10^{-4} and for the liquid or amorphous material as 6.75×10^{-4}. The value for the liquid was extrapolated from the data as shown in Fig. 1. The value for the crystalline part was obtained from Price[5] and from the value for polyethylene No. 6, which is nearly all in the crystalline phase. The value of V_c is a somewhat arbitrary value between the value used by Price[5] and the value obtained by Bunn.[6] The calculated percent crystallinity for the polyethylenes is given in Fig. 2. The more highly crystalline materials not only have higher melting points, but they also have the sharper melting points.

The dynamic mechanical properties are plotted in Figs. 3 and 4 as a function of temperature. Even at room temperature the shear modulus has a greater temperature dependence than most high polymers such as polystyrene.[7] The modulus drops off very rapidly near the melting point. Polyethylenes No. 3 and No. 5 still have measurable moduli even above the melting point; presumably these materials have higher molecular weights than the others.

The mechanical damping goes through a maximum in all cases between about 50°C and 70°C. The structural factors giving rise to this maximum are not clearly understood. Just below the melting point the damping goes through a minimum. At this stage the material is quite rubbery as many of the crystals have melted, but enough remain to crosslink the molecules and minimize the effects of viscous flow. At the melting point, viscous flow becomes important, and the damping increases rapidly.

The most interesting result of this investigation is the approximate linear dependence of the logarithm of the shear modulus on the specific volume. This is illustrated in Fig. 5. This functional dependence holds for all six of the materials studied over the temperature range from room temperature to the melting point. Thus, the following relationship holds for the specific volume and shear modulus G over the range of moduli from 10^7 to 10^{10} dynes/cm^2.

$$\log_{10}G = A - BV$$

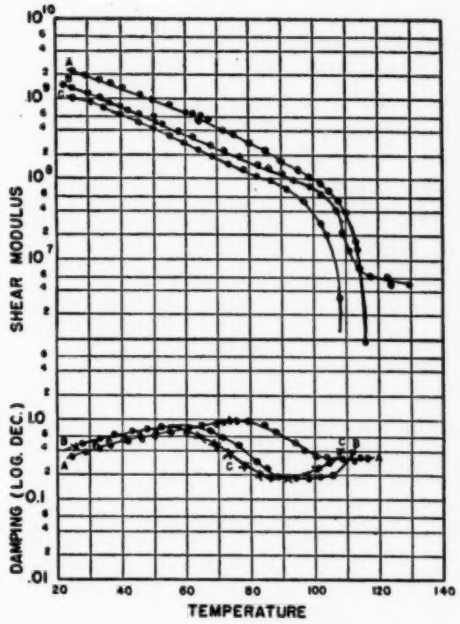

FIG. 4. Dynamic mechanical properties of polyethylenes. Curve A = material No. 4, Curve B = material No. 3, Curve C = material No. 1.

where $A = 26.671$ and $B = 16.21$. No similar relationship exists between the modulus and the degree of crystallinity. For any given material the modulus can be expressed as a function of the degree of crystallinity as

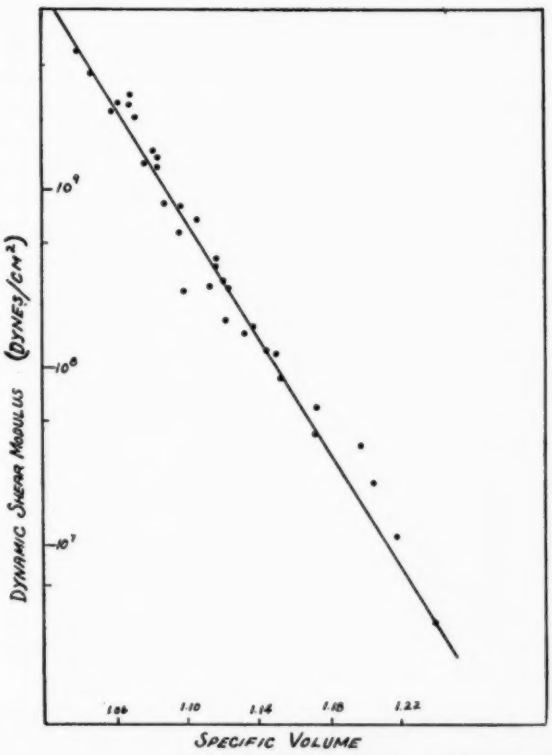

FIG. 5. Relation between dynamic shear modulus and specific volume of polyethylenes.

[5] F. P. Price, J. Chem. Phys. **19**, 973 (1951).
[6] C. W. Bunn and T. C. Alcock, Trans. Faraday Soc. **41**, 317 (1945).
[7] L. E. Nielsen and R. Buchdahl, Soc. Plastics Engrs. J. **9**, No. 5 (1953).

the temperature is changed, but a different relationship holds for each material. A given value of the modulus can be obtained by heating a highly crystalline polyethylene to a higher temperature than a material with a low degree of crystallinity so that the density has the same value in the two cases. It seems that increases in volume due to either thermal expansion or to decreasing crystallinity are nearly equivalent as far as changing the modulus is concerned.

Sperati *et al.*[8] have recently announced a similar relation between the stiffness of polyethylenes at 23°C and their density at the same temperature. The present relationship covers a much greater modulus range, and is not limited to a single temperature.

A typical commercial polymer such as material No. 2 has a calculated crystallinity as shown in Fig. 2 which is comparable to the values published previously.[4,5] The values given in Fig. 2 can be shifted somewhat by using different densities for the pure polyethylene crystal. The value 1.025 used here for the specific volume at 0°C may be somewhat too large, so that the calculated crystallinity may also be too large.

TABLE I. Molecular branching from infrared data.

Material	Optical density at 1378 cm^{-1} [a] / Optical density at 1350 cm^{-1} 40°C	140°C
1	1.68	0.85
2	1.47	0.79
3	1.12	0.64
4	1.34	0.62
5	0.83	0.63
6	0.62	0.48

[a] Background absorption has been subtracted from optical densities.

[8] Sperati, Franta, and Storkweather, J. Am. Chem. Soc. **75**, 6127 (1953).

It is known that the crystallinity of polyethylene is closely related to the extent of chain branching in the molecules.[1,9] This chain branching can be determined from measurements of the infrared absorption bands due to CH_2 and CH_3 vibrations. As expected, the materials with the greater branching (more intense CH_3 band absorption) were the less crystalline. Table I lists the approximate ratio of the optical densities at 1378 cm^{-1} to 1350 cm^{-1} at temperatures of 40°C and 140°C using the method described by Cotman.[2] This ratio is proportional to the ratio of CH_3 to CH_2 and therefore is a measure of the branching in the molecules. It was found the optical densities varied considerably with temperature but the order found in Table I agrees quite well with the expected order found with the more accurate density and the dynamic data.

ACKNOWLEDGMENT

The infrared data were obtained by G. Claver. The author is thankful for the many helpful discussions with Rolf Buchdahl on this subject.

[9] W. M. D. Bryant, J. Polymer Sci. **2**, 547(1947). W. M. D. Bryant and R. C. Voter, J. Am. Chem. Soc. **75**, 6113 (1953).

JOURNAL OF APPLIED PHYSICS VOLUME 25, NUMBER 10 OCTOBER, 1954

The Dynamic Bulk Viscosity of Polyisobutylene

ROBERT S. MARVIN, *National Bureau of Standards, Washington, D. C.*

AND

R. ALDRICH* AND H. S. SACK, *Cornell University, Ithaca, New York*†

(Received May 10, 1954)

The dynamic bulk modulus of a high molecular weight polyisobutylene is calculated from measured longitudinal-wave and shear moduli. A viscous or energy-dissipating process associated with pure volume deformation is found, which appears to be a relaxation process. The peak in absorption of the shear and bulk moduli and the apparent activation energies associated with the two types of deformation are at least approximately the same, suggesting that the fundamental molecular mechanism involved in the two types of deformation may be the same.

I. INTRODUCTION

THE fact that there is a viscous, i.e., energy-dissipating, mechanism associated with pure volume deformation for many liquids has in recent years become quite firmly established.[1]

In the case of polymeric materials the information on this subject is scanty and rather contradictory. Mason *et al.*,[2] found an appreciable volume viscosity for certain polyisobutylenes, whereas Nolle and Sieck[3] found, within a fairly wide range of uncertainty, no volume viscosity for a Buna-N vulcanizate in the range of frequency and temperature investigated.

There is a basic experimental problem involved in obtaining these values, in that almost all the information available comes from a comparison of the velocity and attenuation of shear waves (governed by the shear modulus, G) and longitudinal waves (governed by both the shear and bulk moduli, $K+4/3G$). A few attempts have been made to measure the bulk modulus K directly, using a transient technique[4] and also by a dynamic one in which the sample is placed at the antinode of a standing-wave system.[5]

The results presented here are based on the comparison of shear and longitudinal wave moduli, measured on samples from a single lot of polyisobutylene, of viscosity average molecular weight 1.35×10^6, distributed by the National Bureau of Standards. Longitudinal wave moduli were measured at Cornell University and are published here for the first time; shear moduli were measured by a number of investigators, and the results are summarized in a previous publication.[6] The reduced frequency range of interest to us here was covered by the measurements of J. D. Ferry, E. R. Fitzgerald, and L. Grandine at the University of Wisconsin; H. J. McSkimin at Bell Telephone Laboratories; and A. W. Nolle at Massachusetts Institute of Technology. Combination of these results permits a more complete evaluation of the variation of the bulk modulus with frequency and temperature than has been possible from previous work on polymeric materials.

II. PHENOMENOLOGICAL RELATIONSHIPS

The modulus of primary interest here, the bulk modulus, is associated with a pure volume deformation. The new measurements reported here were made on the propagation of plane irrotational (longitudinal) waves, in which the particle motion is in the same direction as the wave propagation. For a purely elastic material, the modulus governing propagation of such waves, the longitudinal-wave modulus M, is equal to $K+4/3G$, where K is the bulk modulus and G the shear modulus. As shown in the Appendix, for the propagation of longitudinal waves in a viscoelastic medium, if steady-state sinusoidal time dependence of stress and strain is achieved, the same combined modulus is applicable, except that both K and G become complex, frequency-dependent functions rather than constants. They will be written as $K^*(\omega)=K'(\omega)+iK''(\omega)$, and $G^*(\omega)=G'(\omega)+iG(\omega)$. If the longitudinal wave is expressed as $u=u_0\exp[i\omega t-(\alpha+i\omega/c)x]$, where u represents the strain, ω the radian frequency, α the attenuation per centimeter, c the phase velocity, x the distance from the source, and t the time, and if the modulus governing the propagation is written as $M^*=M'+iM''=K^*+4/3G^*$, the relations between the experimentally measured quantities, α and c and the moduli M' and M''

* Present address, General Electric Company, Syracuse, New York.

† The work at Cornell University was supported by the U. S. Office of Naval Research.

[1] S. M. Karim and L. Rosenhead, Revs. Modern Phys. 24, 108 (1952), review this subject, with an extensive bibliography; see also T. A. Litovitz and D. Sette, J. Chem. Phys. 21, 17 (1953).

[2] Mason, Baker, McSkimin, and Heiss, Phys. Rev. 75, 936 (1949).

[3] A. W. Nolle and P. W. Sieck, J. Appl. Phys. 23, 888 (1952).

[4] R. O. Davies and G. O. Jones, Proc. Roy. Soc. (London) A217, 26 (1953).

[5] W. Kuhl and E. Meyer, "Dynamical Properties of Rubber and Rubberlike Materials in a Large Frequency Range" in Report of the 1948 Summer Symposium of the Acoustics Group, *Noise and Sound Transmission* (The Physical Society, London, 1949), pp. 181–188; C. S. Sandler, J. Acoust. Soc. Am. 22, 685 (1950).

[6] R. S. Marvin, *Proceedings of the Second International Congress on Rheology* (Butterworths Scientific Publications, London, 1954), pp. 156–163.

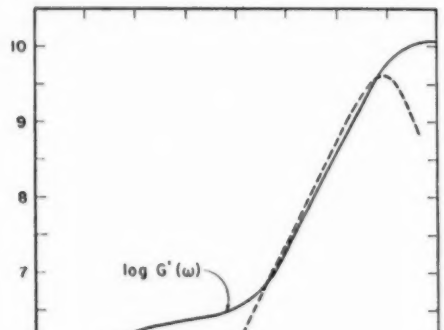

FIG. 1. Dynamic shear modulus of polyisobutylene. Real (——) and imaginary (– – –) parts averaged from experimental results of several investigators. From reference 6.

at a given frequency ω can easily be shown to be:

$$K'+4/3G'=M'=\frac{\rho c^2\left(1-\frac{\alpha^2c^2}{\omega^2}\right)}{\left(1+\frac{\alpha^2c^2}{\omega^2}\right)^2} \quad (1)$$

$$K''+4/3G''=M''=\frac{2\rho c^2(\alpha c/\omega)}{\left(1+\frac{\alpha^2c^2}{\omega^2}\right)^2}, \quad (2)$$

where ρ is the density.

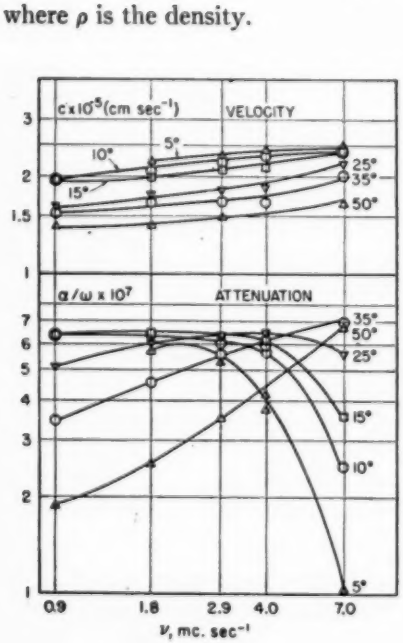

FIG. 2. Velocity and attenuation of longitudinal waves.

III. EXPERIMENTAL METHOD

For the measurement of longitudinal waves both pulse and steady-state (using frequency modulation) techniques were employed, which have been described briefly before.[7] The results reported in this paper were obtained from measurements in a frequency range from 0.9 to 7 megacycles per second and a temperature range from 5 to 50°C.‡ The samples were suspended in a liquid—water above 0°C and ethylene glycol below—which served to transmit a plane wave from a piezoelectric transducer to the sample, and from the sample to a similar receiver. The velocity was determined by measuring the phaseshift introduced in the received signal on inserting the sample into the bath. The absorption was measured by comparing the received intensity of the wave transmitted through samples of several different thicknesses, thus eliminating the influence of reflection losses. Care has to be taken that the surfaces are clean and that no air is adsorbed. The samples were allowed to stand in the bath for several hours before measurements were made in order to eliminate adsorbed air on the surface.

Many more measurements were obtained than are included here; we have selected a few cases which are representative of the whole set of data and for which values of both attenuation and velocity were measured at the same frequency and temperature. A more complete presentation of these results is contained in the thesis of Aldrich.[8]

IV. RESULTS

The real and imaginary parts of the dynamic shear modulus at a temperature of 25°C are shown in Fig. 1, reproduced from an earlier paper.[6] These curves, summarizing the work of several investigators, were obtained at temperatures ranging from −60° to +100°C and reduced to a temperature of 25°C using the well-known reduction scheme of Ferry[9] and the variation of the ordinary flow viscosity with temperature. The spread of the particular experimental points used to determine these average curves is approximately ±5 percent.

The longitudinal-wave data are shown in Fig. 2 for six temperatures and at five frequencies, these values having been selected as representative of all the data

[7] H. S. Sack and R. W. Aldrich, Phys. Rev. **75**, 1285 (1949).

‡ The equipment available (see reference 8) permitted measurements over considerably larger ranges. But in this special case the conditions were such that the measurements outside the ranges mentioned above were not precise enough or could not be used to supplement the characterization of the material. In particular, at frequencies higher than 7 mc, the losses are so high that films with a thickness of a fraction of a millimeter had to be used. These films were cast from solutions, and the possibility exists that they were not completely free of solvent. Since even a small amount of solvent markedly influences the mechanical properties, the results presented here are those obtained on samples pressed out without addition of solvent.

[8] R. Aldrich, Ph.D. thesis, Cornell University, 1951.

[9] J. D. Ferry, J. Am. Chem. Soc. **72**, 3746 (1950).

available. Using Eqs. (1) and (2), values of the real and imaginary parts of the longitudinal-wave modulus were calculated at each point shown; these are given in Fig. 3.

The curves of both Figs. 2 and 3 appear amenable to the application of a superposition treatment, but since we are dealing with phenomena which involve two separate mechanisms, shear and volume deformations, it seemed wise to separate the appropriate moduli before proceeding to reduce them to a common temperature.

This can be done by calculating, from the averaged shear curves, values of the real and imaginary parts of the shear modulus at each temperature and frequency involved, using the standard reduction formulas. These values were calculated, and $4/3G'$ or $4/3G''$ substracted from the longitudinal-wave moduli to give values of K' and K'' at each experimental point. The results are plotted in Fig. 4.

We see here evidence of considerably more scatter than in the previous curves, which is to be expected

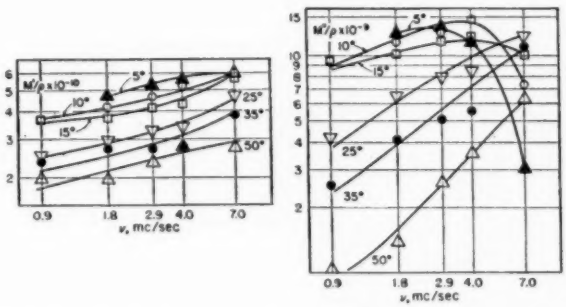

FIG. 3. Longitudinal-wave modulus of polyisobutylene, $M^*=K^*$ $+4/3G^*$. Calculated from values of Fig. 2.

since we have now taken differences between two experimental quantities. The relative values of these quantities will be discussed below.

Despite the lack of precision in these derived values, it seems reasonable to reduce them to a common temperature. The K'' curve at 15° appears to peak at a lower value than the others, but this is almost certainly an error attributable to taking differences between nearly equal quantities. All the other curves seem to be capable of superposition.

Because of the scatter involved, it is impossible to find the best shifting factors with any certainty. Several shifts were tried on the functions K', K'', K'/ω, and K''/ω, and all yielded shifting factors which spread around the values previously found for the shear moduli by no more than ±20 percent. Since the shear factors appeared at least as satisfactory as any others they were used in reducing the curves to a common temperature of 25°C.

The reduced curves are shown in Fig. 5. The scatter

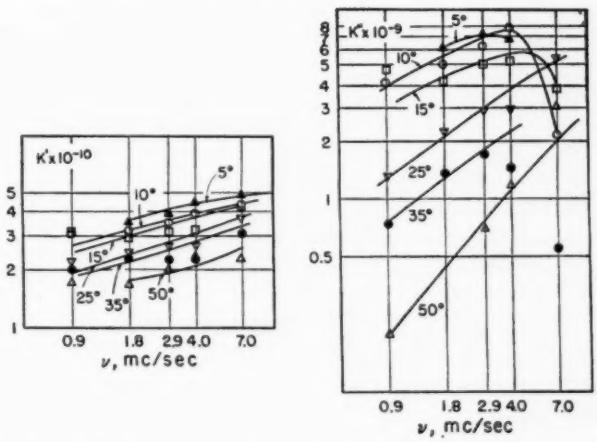

FIG. 4. Bulk modulus of polyisobutylene, $K^*=M^*-4/3G^*$. Calculated from values of Figs. 3 and 1.

appears quite reasonable in view of the precision of the data, and the points for each temperature scatter in an apparently random fashion about the average curves shown.

Since we have decided to use the same reduction factors for bulk moduli as were employed for shear, it is permissible to go back to the original longitudinal-wave moduli and reduce them to a common temperature. This permits a clearer visualization of the relation between the three moduli, and should give more reliable values of the imaginary part of the bulk modulus, since the averaging can be done before taking differences.

These values are shown in Figs. 6 and 7, with the moduli plotted to a linear rather than a logarithmic scale. The scatter of the points for M_0'' around the maximum is evidence of the difficulties encountered in making accurate measurements in this region of maximum loss.

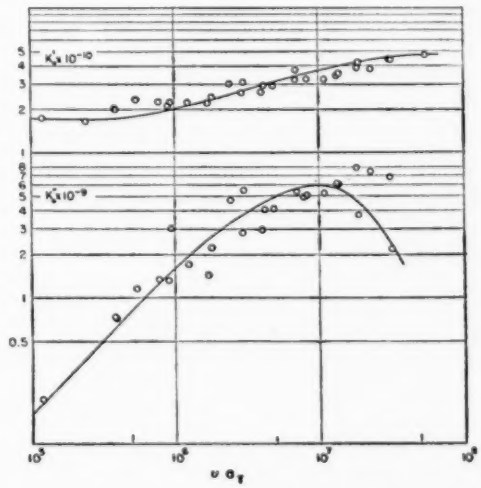

FIG. 5. Bulk modulus of polyisobutylene, reduced to 25°C. Shifting factors were the same as used for reducing the shear modulus (reference 6).

V. DISCUSSION

The precision available in this work is not great enough to permit very precise conclusions as to the relations between the shear and volume mechanisms involved, but it does permit some statements about orders of magnitude. It might be noted that the precision shown here compares favorably with that obtained by others using similar methods; the difficulties are inherent in the measurement of attenuation in materials with high losses.

Looking first at the real part of the moduli, Fig. 6, it seems evident that throughout the whole of the range in which this material shows rubberlike behavior, the bulk modulus will be the dominating factor for longitudinal waves. The low-frequency limit indicated from the experimental points, about 1.75×10^{10} dynes per cm^2, is in very good agreement with a value of 1.95×10^{10} obtained by Cramer at Naval Ordnance Laboratory[10] for this same material, using a standing wave technique at 1534 cycles per second. The curves have been drawn a trifle higher than the experimental points in this region to take this value into account. In this region the shear modulus is, by comparison, negligible, and it drops off very rapidly at frequencies lower than shown here. This confirms the evidence available from comparison of measured shear and Young's moduli at frequencies up to several kilocycles, where it is found that the Young's modulus is just three times the shear modulus. For this relation to hold the shear modulus must be negligible compared to the bulk modulus. This limiting bulk modulus should remain constant with frequency down to static measurements, and may be compared with a value of 3.17×10^{10} dynes per cm^2 obtained by Weir of the National Bureau of Standards, from measurements of the volume-pressure relationships for a sample of this same material at 25°C, using apparatus and technique which have been described previously.[11]

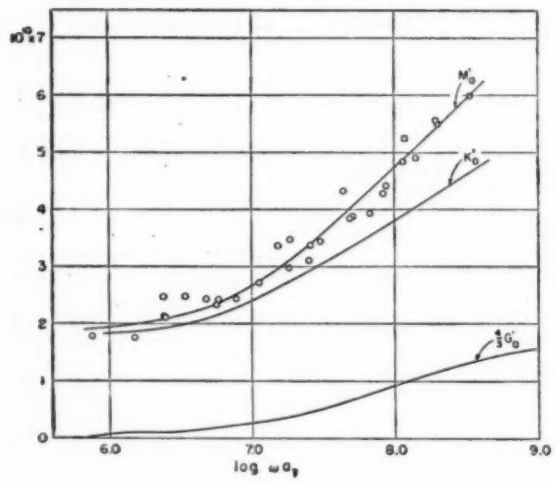

FIG. 6. Real parts of the reduced longitudinal-wave, shear, and bulk moduli. Reduced to 25°C. Note: moduli plotted linearly.

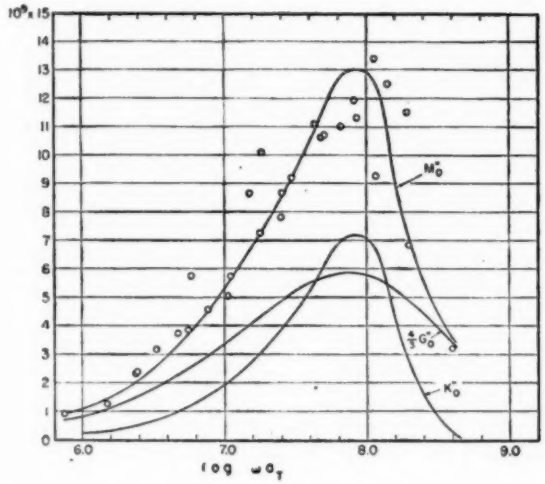

FIG. 7. Imaginary parts of the reduced longitudinal-wave, shear, and bulk moduli. Reduced to 25°C. Note: moduli plotted linearly.

This static value was obtained by extrapolating the $\Delta V/V_0$ *vs* P curve measured from 1223 to 8000 atmospheres to one atmosphere, and calculating its slope there. The curve appears approximately quadratic in form, so an extrapolation of this magnitude is certainly open to question, and even an agreement with the limiting dynamic value to within a factor of two might be considered reasonably good. However, it seems quite generally true that compressibilities calculated in this manner are somewhat lower than those measured directly at one atmosphere, and the most logical explanation for this fact is that it is impossible to remove all the air from a sample. This would have a large effect at one atmosphere, but practically none at higher pressures where the air would be compressed to a negligible fraction of its initial volume, and probably forced into solution in the polymer. Since about 20 parts per million of air in the polymer would account for the above difference in compressibilities, it seems entirely reasonable to adopt this explanation.

It has been suggested[3] that small inclusions of air, such as hypothesized here, might give rise to greater losses than would be expected from a continuum, owing to shear motions at the surfaces of the resulting small discontinuities. Such a suggestion could be checked directly only by making the shear measurements in the presence of a superposed static pressure, or some equivalent method of ensuring that no undissolved air remained in the sample. It should be noted, however, that included in the data from which the shear moduli were obtained in the reduced frequency range of interest

[10] W. S. Cramer, private communication, based on measurements using a method described in reference 5.

[11] C. E. Weir, J. Research Natl. Bur. Standards **45**, 468 (1950).

here are those of Ferry, Fitzgerald, and Grandine who measured simple shear at frequencies in the low kilocycle range at temperatures down to −44.6°C, and those of McSkimin who measured shear waves at 14.5 megacycles near room temperature. The good agreement of these two sets of measurements when reduced to a common temperature argues against the above suggestion, since the very small air bubbles considered here would hardly be expected to have any effect on shear measurements in the kilocycle region where the wavelength is at least several centimeters.

The high-frequency values of M_0' do not indicate approach to a limiting value in the range covered here, but it must be expected that they are close to their limit both from the value of the modulus indicated and the time-scale involved. The shear modulus has essentially reached a limit, so the course of M_0' and K_0' at higher frequencies should be parallel.

The scatter of the M_0'' values, in Fig. 7, is such that there is some uncertainty as to the exact location of the maximum. This is unfortunate, since the peak of the loss function indicates the location of the primary loss mechanism on the frequency or time scale. Despite the uncertainty, however, there can be no doubt that the peak is somewhere in the range of $\log\omega=7.6$ to 8.3. Since the peak in G_0'' occurs at about 7.8, it is safe to conclude that the dominating relaxation mechanisms in both shear and volume deformation have about the same relaxation times.

The fact that the shifting factors used for the bulk modulus reduction must be about the same as those used for the shear modulus reduction, means that the activation energies for volume deformations must be about the same as those for shear deformations.[12]

The final conclusions to be drawn from these measurements, then, are that there is a viscous or energy-dissipating process associated with volume deformation of this polymer, and that this is a relaxation process. Furthermore, the close relation of the peak in absorption of the shear and bulk moduli and of the activation energies suggests that the molecular mechanisms may be the same. More definite conclusions will probably have to await a more precise method for determining the loss component of the bulk modulus than is available to us at this time.

APPENDIX

The equations governing the propagation of waves in a viscoelastic medium are usually obtained by assuming that the real and imaginary parts of the complex modulus involved are constants. Since they are actually functions of frequency, this procedure is open to question.

Following the treatment of Alfrey and Newman,[13] the derivation of frequency-dependent moduli can be obtained in a satisfactory manner. In terms of displacements u_i, the components of the strain tensor are defined as

$$\epsilon_{ij}=1/2(\partial u_i/\partial x_j+\partial u_j/\partial x_i). \quad \text{(i)}$$

The mean normal stress and strain, σ and ϵ, are defined by

$$\sigma=1/3\sum_{j=1}^{3}\sigma_{jj} \quad \text{(ii)}$$

and

$$\epsilon=1/3\sum_{j=1}^{3}\epsilon_{jj}, \quad \text{(iii)}$$

and the deviatoric stress and strain tensors, s_{ij} and e_{ij}, by

$$s_{ij}=\sigma_{ij}-\delta_{ij}\sigma \quad \text{(iv)}$$

$$e_{ij}=\epsilon_{ij}-\delta_{ij}\epsilon, \quad \text{(v)}$$

where δ_{ij} is the Kronecker delta.

The usual relation between the stress components and the displacements, for small displacements, derived from Newton's second law,

$$\rho\partial^2u_i/\partial t^2=\sum_{j=1}^{3}\partial\sigma_{ij}/\partial x_j \quad \text{(vi)}$$

may be written in terms of the normal and deviatoric stresses as

$$\rho\partial^2u_i/\partial t^2=\sum_{j=1}^{3}\partial s_{ij}/\partial x_j+\partial\sigma/\partial x_i. \quad \text{(vii)}$$

For an ordinary elastic material the constants relating stress and strain can be defined in terms of the bulk (K) and shear (G) moduli by

$$\sigma=3K\epsilon \quad \text{(viii)}$$

$$s_{ij}=2Ge_{ij}, \quad \text{(ix)}$$

and substituting these relationships into (vii) leads directly to the differential equation governing the propagation of waves in such materials:

$$\rho\partial^2u_i/\partial t^2=(K-2/3G)\sum_{j=1}^{3}\partial^2u_j/\partial x_i\partial x_j$$

$$+G\sum_{j=1}^{3}(\partial^2u_i/\partial x_j{}^2+\partial^2u_j/\partial x_i\partial x_j). \quad \text{(x)}$$

For an irrotational wave propagated along the x_1 axis this reduces to the familiar form

$$\rho\partial^2u_1/\partial t^2=(K+4/3G)\partial^2u_1/\partial x_1{}^2. \quad \text{(xi)}$$

For an isotropic, linear viscoelastic material the relations between stress and strain are more complicated.

[12] J. D. Ferry and E. R. Fitzgerald, *Proceedings of the Second International Congress on Rheology* (Butterworths Scientific Publications, London, 1954), pp. 140–149.

[13] T. Alfrey, Jr. and T. J. Newman, paper presented at the 1950 meeting of the Society of Rheology; T. J. Newman, M.S. thesis, Polytechnic Institute of Brooklyn, 1951.

One method of expressing them is through the Operator Equations:[14]

$$P'(D)\sigma = 3Q'(D)\epsilon \qquad \text{(xii)}$$

$$P(D)s_{ij} = 2Q(D)e_{ij}, \qquad \text{(xiii)}$$

where P, P', Q, and Q' are operators of the form $\sum_n \alpha_n D^n$, and $D^n = \partial^n/\partial t^n$.

If the time dependence is expressed in the customary complex notation for steady-state sinusoidal stress and strain, these operators become power series in $i\omega$, and the usual complex bulk and shear moduli can be defined by

$$K^* = K' + iK'' = \sigma/3\epsilon = Q'(i\omega)/P'(i\omega) \qquad \text{(xiv)}$$

and

$$G^* = G' + iG'' = s_{ij}/2e_{ij} = Q(i\omega)/P(i\omega). \qquad \text{(xv)}$$

As thus defined the real and imaginary parts of each modulus will be functions of frequency.

The use of Eqs. (xii) and (xiii) in (vii) assuming the order of differentiation is immaterial, leads to

$$PP'\rho\partial^2 u_i/\partial t^2 = (PQ' - 2/3P'Q)\sum_{j=1}^{3} \partial^2 u_j/\partial x_i \partial x_j + P'Q\sum_{j=1}^{3}(\partial^2 u_i/\partial x_j^2 + \partial^2 u_j/\partial x_i \partial x_j) \qquad \text{(xvi)}$$

as the differential equation governing wave propagation in a viscoelastic medium, or to

$$PP'\rho\partial^2 u_1/\partial t^2 = (PQ' + 4/3P'Q)\partial^2 u_1/\partial x_1^2 \qquad \text{(xvii)}$$

for irrotational waves propagated along the x_1 axis in such material.

Equation (xvii) is too complicated to permit a simple solution for a general case, but if the displacement u can be expressed as $u_0 \exp[i\omega t - (\alpha + i\omega/c)x]$, the operators which involve only differentiation with respect to time again become power series in $(i\omega)$, and Eq. (xvii) becomes

$$-\omega^2\rho = [Q'(i\omega)/P'(i\omega) + 4/3Q(i\omega)/P(i\omega)] \times (\alpha + i\omega/c)^2 \qquad \text{(xviii)}$$

or, remembering the definitions of K^* and G^* above, and defining $M^* = M' + iM'' = K^* + 4/3G^*$:

$$-\omega^2\rho = M^*(\alpha + i\omega/c)^2. \qquad \text{(xix)}$$

This is now an ordinary equation relating the frequency-dependent moduli M', M'', and the experimental quantities α and c, all of which are constants at any given frequency. By separating (xix) into real and imaginary parts a pair of equations results, from which we can solve for M' and M'' in terms of α and c, obtaining Eqs. (1) and (2) of the text.

[14] T. Alfrey, Jr., *Mechanical Behavior of High Polymers* (Interscience Publishers, Inc., New York, 1948), p. 540.

JOURNAL OF APPLIED PHYSICS VOLUME 25, NUMBER 10 OCTOBER, 1954

Studies of Rubberlike Polymers by Nuclear Magnetism*

V. R. HONNOLD,†‡ F. MCCAFFREY,†‡ AND B. A. MROWCA
Department of Physics, University of Notre Dame, Notre Dame, Indiana
(Received May 10, 1954)

The actual width of the proton resonance line in uncured natural rubber has been determined at room temperature to be 0.06 gauss. Curing of polymers increases the line width at a given temperature. The small increase in natural rubber is possibly compatible with a physical bonding rather than the usually assumed cross linking. For a butadiene-styrene copolymer the increase in line width due to cure is somewhat larger. Carbon black loading increases the line width to a lesser degree than cure. This is compatible with the concept of physical bonding between the blacks and the polymer chain molecules. Variations in line width caused by changes in chemical composition and copolymerization were also investigated. Polypropylene and polypropylene oxide of roughly the same average molecular weight are compared. The polypropylene oxide exhibits a greater degree of "rotation" about its C—O bonds than polypropylene does about its C—C bonds. Two butadiene-acrylonitrile copolymers also have been studied as a function of temperature. Finally, spin-lattice relaxation time *vs* temperature studies are reported for a butadiene-acrylonitrile copolymer and for raw butyl, over the temperature range from −50°C to 70°C. Estimates of the magnitude of the barriers hindering "rotation" are made.

INTRODUCTION

RUBBERLIKE polymers exhibit characteristic physical properties which set them apart from other solids. An explanation of these characteristic properties is based on the assumption of "quasi-free rotation" within the long chain molecules which form the rubberlike polymers. The existence and the nature of these internal motions in simpler solids has been investigated by nuclear magnetic resonance absorption and nuclear induction.[1] These methods have been extended to the study of polymers.[2–4] By these methods the degree of "rotation" and segmental motion, and their changes with varying temperature, cure, loading, and the like can be directly observed in stressed or unstressed polymers.

The spin-spin relaxation time, the magnitude of which is a measure of the "freeness" of internal rotations in molecules, and the spin-lattice relaxation time were studied for the most part as a function of the temperature and other parameters. Butyl rubber, butadiene-styrene, and butadience-acrylonitrile copolymers were investigated in greater detail. Other polymers, such as natural rubber, GR-*S*, polypropylene, polypropylene oxide, and the silicones were investigated more briefly.

At higher temperatures, there is considerable "quasi-free rotation" leading to narrow line widths. On lowering the temperature, a broadening of the line width results, showing directly the decrease in thermal energies available for rotation.

The effect of cure seems to depend on the particular rubber considered. Natural uncured rubber and one cured with 8 percent sulfur do not exhibit a marked difference in line width, although the cured sample has a somewhat greater line width for any given temperature. A 50–50 butadiene-styrene copolymer, on the other hand, shows a somewhat higher line width in the cured state.

The effect of carbon loading on the line width seems to be relatively slight, which indicated that loading does not lead to a marked decrease of the degree of "rotation," at least in the temperature range from room temperature down to −50°C.

It is possible to draw more quantitative conclusions from line width *vs* temperature data, and from spin-lattice relaxation time *vs* temperature curves about the potential barriers hindering "rotation." In addition, one can also investigate the line shape as a function of the temperature. Recently Wilson and Pake[5] have done this for polyethylene and Teflon. From the analysis of the line shapes obtained at various temperatures they were able to draw some conclusions about the degree of crystallization in these materials.

EXPERIMENTAL PROCEDURE

The equipment, and the experimental procedure used in the measurement of the absorption line widths, was for the most part the same as described in our earlier work.[4] The absorption lines were measured in a static field of 6800 gauss. These were detected in the conventional manner by a Twin-T bridge, and recorded from the output of a narrow band lock-in type amplifier on an Esterline Angus milliammeter. Temperatures were maintained to within 1°C, and were measured by a thermocouple imbedded in the sample. Spin-lattice *vs* temperature data was obtained by the progressive saturation method[6] which is suitable in the case of broad absorption lines.

* Supported in part by the U. S. Office of Naval Research.
† Portion of a thesis presented in partial fulfillment of the requirements for the Ph.D. degree.
‡ Now at U. S. Naval Ordnance Test Station, Inyokern, California.
[1] G. E. Pake, Am. J. Phys. **18**, 438 (1950) reviews work done up to 1950.
[2] N. L. Alpert, Phys. Rev. **75**, 398 (1949).
[3] R. Newman, J. Chem. Phys. **18**, 1303 (1950).
[4] Holroyd, Codrington, Mrowca, and Guth, J. Appl. Phys. **22**, 696 (1951).
[5] C. W. Wilson, III and G. E. Pake, J. Polymer Sci. **10**, 503 (1953).
[6] Bloembergen, Purcell, and Pound, Phys. Rev. **73**, 679 (1948).

RESULTS AND DISCUSSION

Line Widths for Natural, Silicone, and Butyl Rubbers

In our previous work[4] it was shown that both natural rubber and GR-*S* have line widths at room temperature of less than 0.08 gauss. This value represented the lower limit that could be measured with our magnet and was attributed to magnetic field inhomogeneity. In the meantime, the actual line width for natural rubber (smoked sheet) was determined to be 0.06 gauss. Such extremely narrow line widths show directly the high degree of "quasi-free rotation" of proton groups and of chain segments, proving the basic assumption in the statistical network theory of rubber elasticity.

Narrow lines limited by our field inhomogeneity were found to persist in the case of a silicone oil and two samples of elastomers down to temperatures below −50°C. It is known that silicone rubbers retain their characteristic elasticity and flexibility down to temperatures of the order of −100°C. It seems reasonable to attribute this behavior of the silicones to a greater ease of rotation about Si−O bonds. A further contribution to the line narrowing in the case of the silicones undoubtedly stems from the rotation of the methyl side groups about their C_3 symmetry axis. Powles[7] has shown, in the case of simple compounds containing methyl groups, that "quasi-free rotation" takes place at a sufficiently high frequency at temperatures as low as −148°C to contribute to the narrowing of the proton resonance absorption line. Furthermore, in the case of the silicones the relatively wide separation of the methyl groups, due to the presence of oxygen atoms along the chain skeleton, tends to reduce the steric hinderance to this rotation.

Synthetic rubbers with the exception of GR-*S* were found to have line widths exceeding 0.1 gauss at room temperature. However, all of the rubbers investigated show a line width behavior at elevated temperatures which is similar to that shown for butyl in Fig. 1. The line width decreases with increasing temperature until it is limited by the resolution of the magnetic field. The line width transition for butyl is very broad.

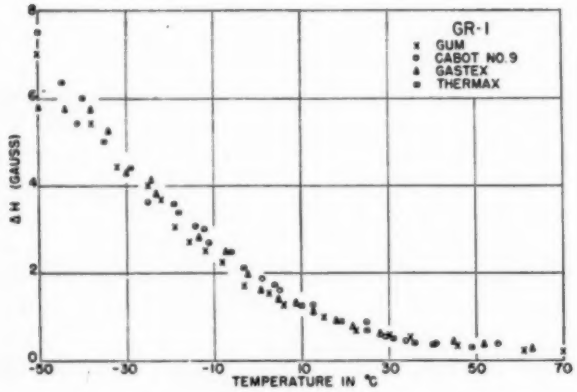

FIG. 1. Line width *vs* temperature for Butyl gum (GR-*I*) loaded with three different carbon blacks.

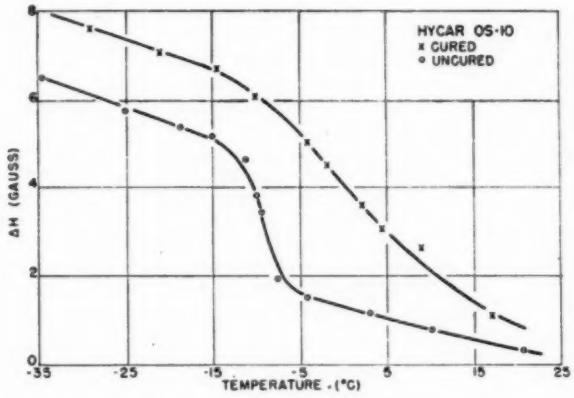

FIG. 2. Line width *vs* temperature for an uncured and a cured butadiene-acrylonitrile copolymer (Hycar OS-10).

Effect of Cure on Line Width

Cure increases the line width of both natural rubber and GR-*S*. Even at room temperatures the line width is above 0.1 gauss. For natural rubber the increase is small for samples cured with as much as 8 percent sulfur. For a 50–50 butadiene-styrene copolymer (Hycar OS-10), the increase in line width with cure is somewhat larger. This is shown in Fig. 2. In principle, it should be possible to investigate the mechanism of cure by this method. For instance, a small change in the line width *vs* temperature curves could indicate that the curing process involves a "physical" cross-linking, leading to an increased interaction between adjacent chains. On the other hand, a larger change would indicate a chemical cross-linking, which is the process usually assumed. Gutowsky and Meyer[8] have recently investigated the line width *vs* temperature curve for cured natural rubber. This investigation shows that the degree of cure affects to a greater extent the onset of rotation of CH_3 groups than that of segmental motion. From this is drawn the conclusion that cure does not take place by actual chemical cross-linking between chains.

Effect of Carbon Loading on Line Width

The addition of carbon black to a rubber matrix results in an increase of elastic rigidity. This reinforcement by the addition of carbon black has been attributed to strong adsorptive forces between the rubber and the filler. More recently arguments have been presented in favor of a chemical bond between the rubber and the strongly reinforcing carbon blacks. It

[7] J. G. Powles and H. S. Gutowsky, J. Chem. Phys. **21**, 1704 (1953).

[8] H. S. Gutowsky and L. H. Meyer, J. Chem. Phys. **21**, 2122 (1953).

TABLE I. Line width ΔH of loaded stocks.

Parts	Carbon blacks	Hycar OS-10	GR-S	Natural rubber	Butyl
21	Thermax		0.29		
	Wyex		0.27		
40	R-40	0.63	0.27	0.32	0.58
	Shawinigan	0.63	0.27	0.25	
	Philblack	0.63	0.27	0.31	0.63
	Micronex	0.56	0.27	0.27	0.8
	Statex	0.61	0.27	0.29	0.61
	E.P.C.	0.65	0.27	0.31	0.61
50	Thermax		0.27		
	Wyex		0.27		

is rather difficult to distinguish between physical and chemical forces. In either case, one would expect these forces to immobilize chain segments of the rubber matrix. This additional cross-linkage provided by the carbon-rubber "bonds" should affect to some extent the "rotation" and thus the line width. A number of stocks loaded with different blacks as well as different percentages of the same black were studied at room temperature. The results are shown in Table I.

As is evident from these results, no appreciable increase in the width of the absorption line was obtained for the polymers and blacks investigated. The slight decrease observed in line intensity with loading would be compatible with the formation of a few strong bonds between the carbon particles and the rubber matrix, or a large number of physical bonds which are comparatively weak. The latter assumption would seem to be more plausible. In any case the bonds formed produce an effect that is small compared to that produced by vulcanization, which would further make the assumption of chemical bonding not very plausible.

To compare in greater detail the effect of carbon loading with vulcanization a study was made of the line width transition for butyl rubber loaded with 36 parts by weight of Gastex, Thermax, and Cabot No. 9. Butyl rubber was chosen for this study since it is imperative to use systems having the same concentration of cross links. Butyl is a polymer of limited unsaturation, which reduces considerably the probability of intra-molecular linkages. If in compounding, an excess of sulfur and accelerator is used, a saturated concentration of cross links results. Therefore, with an excess of curing agents, differences in the adsorptive capacities of the added pigments do not alter the concentration of cross links.

Gastex, Thermax, and Cabot 9 were chosen as pigment fillers representing roughly particle sizes of 30, 80 and 200 millimicrons, respectively. Gastex and Thermax are channel blacks, whereas the Cabot 9 is a furnace black. This choice of blacks, incorporated in the Butyl matrix gave three widely-different systems. The temperature range studied included $-50°C$ to $70°C$. There is very little indication of any shift or change in character of the line width transition with change of carbon black filler. A sample of Paracril-35 loaded with 50 parts of neospectra, a very fine carbon black, exhibited a similar behavior. This behavior is in sharp contrast with the effect produced by vulcanization, which broadens the line width transition and shifts the center of the transition to higher temperatures as shown for Hycar OS-10 in Fig. 2.

Polypropylene and Polypropylene Oxide

Line width *vs* temperature data was taken for the relatively new polymer polypropylene and its oxide, and is shown in Fig. 3. The polypropylene had a number average molecular weight of 5000 as compared to 4100 for the oxide. The line width for the polypropylene decreased with increasing temperature above room temperature until it was limited by the resolution of the magnet. Below room temperature the line broadens gradually with the line width transition centered at about 10°C. In contrast, the line width for the oxide remains narrow down to a temperature of $-40°C$, and the line width transition occurs at approximately $-50°C$. Part of the shift in the line width transition could be attributed to the discrepancy in molecular weights, since the effect of increasing the molecular weight tends to shift in general the line transition to higher temperatures, as was found in studied of fractionated polymers.[4] The drastic change in the behavior of the line width with temperature could be readily explained by the assumption of a greater ease of rotation about C—O bonds in the oxide as compared with that about the C—C bonds in the unoxidized polymer. Also, as in the case of the silicones, the oxygen tends to decrease the steric hindrance to the rotation of side groups.

Paracril-35 and-26

Two samples of butadiene acrylonitrile copolymers were investigated over a temperature range above the glassy transition region. Paracril-35 contains 65 parts

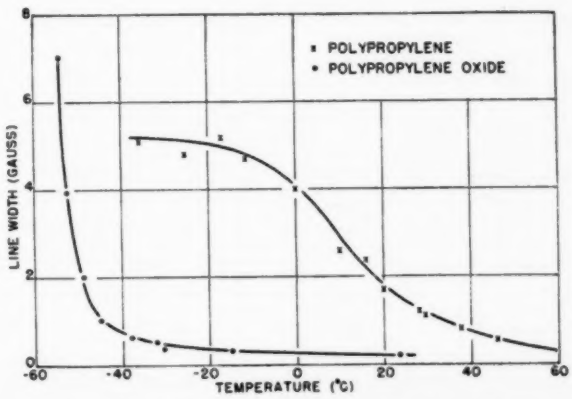

FIG. 3. Line width *vs* temperature for polypropylene and polypropylene oxide.

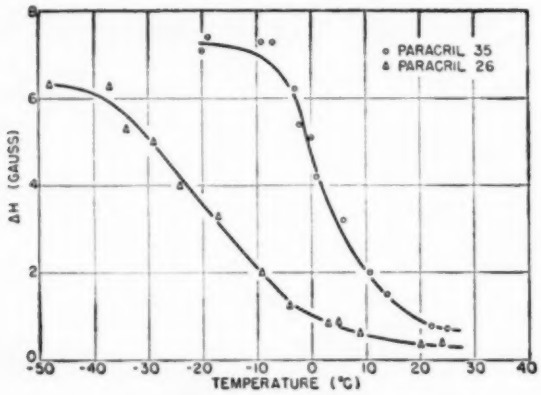

FIG. 4. Line width *vs* temperature for two butadiene-acrylonitrile copolymers (Paracril-35 and-26).

by weight of butadiene and 35 parts of acrylonitrile, whereas the Paracril-26 contains 26 parts of acrylonitrile. The line width transition of the Paracril-35 is centered at about 0°C compared to that of −7°C for the butadiene-styrene copolymer shown in Fig. 4. The Paracril-26 curve shows a transition centered at about −15°C. It is considetably broader than that of the 35 polymer. The greater steepness of the line transition may be due in part to the greater homogeneity realized in the polymer containing the higher concentration of nitrile groups, since it was found in the case of fractionated polystyrene[4] that an increased homogeneity produced a similar effect. The increased dipole moment in Paracril-35 compared to that in the 26 polymer would tend to increase the barriers against molecular motion and thus raise the temperature at which the line width transition would occur.

Spin-Lattice Relaxation Times

The method of progressive saturation[6] was used to determine T_1 for samples of raw and cured natural rubber at room temperature. Little, if any, effect on T_1 was observed at room temperature, due to vulcanization. An average value of 0.22 second was obtained for the two samples.

Spin-lattice relaxation times as a function of temperature were obtained for Butyl and Paracril-35 over a temperature range of −50°C to 70°C. A T_1 *vs* temperature curve for the Paracril-35 is shown in Fig. 5. The general shape of the T_1 *vs* temperature curves for the two polymers is similar. The minimum for the Paracril-35 occurs at 20°C, and that for the raw Butyl was about 10°C lower.

In the low temperature region to the left of the minimum in the T_1 *vs* temperature curves the correlation time, or average time during which a given molecular configuration persists, is proportional to T_1. If the variation of the correlation time with temperature is assumed to follow the usual equation for thermally

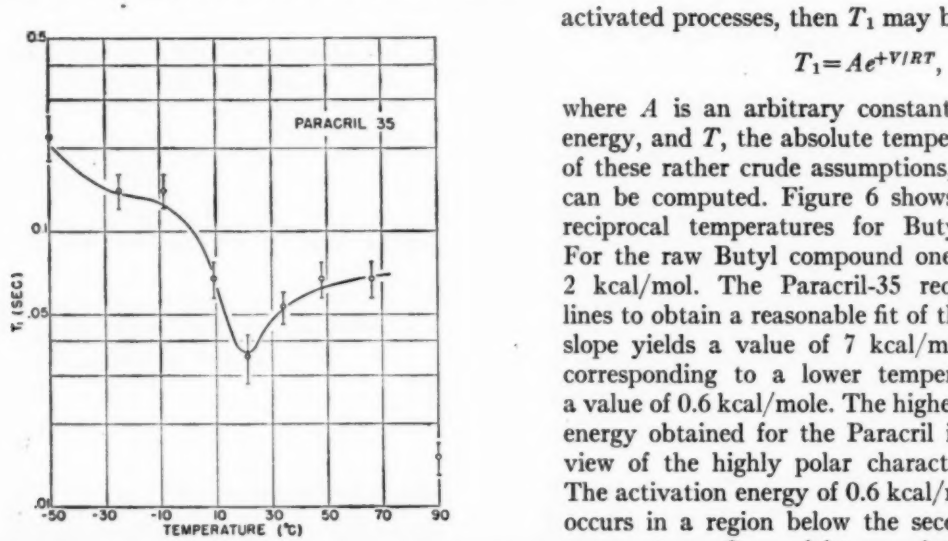

FIG. 6. Log T_1 plotted against $1/T$ for a butadiene-acrylonitrile copolymer (Paracril-35) and raw Butyl (GR-*I*).

activated processes, then T_1 may be expressed as

$$T_1 = Ae^{+V/RT},$$

where A is an arbitrary constant, V, the activation energy, and T, the absolute temperature. On the basis of these rather crude assumptions, activation energies can be computed. Figure 6 shows plots of log T_1 *vs* reciprocal temperatures for Butyl and Paracril-35. For the raw Butyl compound one obtains a value of 2 kcal/mol. The Paracril-35 required two straight lines to obtain a reasonable fit of the data. The steeper slope yields a value of 7 kcal/mol, while the other, corresponding to a lower temperature region, gives a value of 0.6 kcal/mole. The higher value of activation energy obtained for the Paracril is to be expected in view of the highly polar character of this polymer. The activation energy of 0.6 kcal/mole for the Paracril occurs in a region below the second order transition temperature. One might associate the higher value occurring in the rubbery state with a larger scale

FIG. 5. Spin-lattice relaxation time as a function of temperature for a butadiene-acrylonitrile copolymer (Paracril-35).

segmental motion, whereas the lower value would be more in keeping with the "rotation" of smaller groups.

Activation energies were also computed from T_2 data based on an approximate equation relating the line width and the correlation time introduced by Gutowsky and Pake.[9] Values obtained from T_2 data were considerably higher than those obtained from T_1 measurements. More accurate measurements of the line width are being made at lower temperatures, in the vicinity of the "rigid lattice" line width, in an attempt to obtain more reliable values.

The authors wish to thank Dr. E. Guth for his many suggestions and discussions during the progress of this research.

[9] H. S. Gutowsky and G. E. Pake, J. Chem. Phys. **18**, 162 (1950).

JOURNAL OF APPLIED PHYSICS VOLUME 25, NUMBER 10 OCTOBER, 1954

Measurement of Orientation in Polystyrene Monofilaments by Means of Double Refraction

R. D. ANDREWS
Physical Research Laboratory, The Dow Chemical Company, Midland, Michigan
(Received June 3, 1954)

The molecular orientation in polystyrene monofilaments can be determined by measuring the optical double refraction, or birefringence, which the orientation produces. When the oriented filaments are observed with monochromatic light under a polarizing microscope, a pattern of interference fringes is seen which can be analyzed. The general theory of this interference pattern is discussed, including consideration of the molecular basis of optical birefringence in polystyrene. Reversals of fringe order in the interference pattern can occur, but this complication can be handled by suitable methods. A number of experimental techniques useful in these studies are described. It is found that the birefringence is greater near the outside surface of the filaments than in the center, and this can be understood in terms of the rate of cooling during the orientation process.

INTRODUCTION

It is known that molecular orientation has an important effect on the mechanical properties of polymeric materials. In the case of polystyrene monofilaments, a one-dimensional orientation obtained by stretching the filament at a temperature above the second-order transition temperature and then quickly cooling, is found to improve greatly the mechanical properties of the filament, e.g., the elongation at break, tensile strength, and flex life. This is important in the practical applications of such filaments, as in brush and broom bristles, and is also of considerable theoretical interest.

Oriented polystyrene monofilaments can be prepared by a continuous process, as has been described by Bailey,[1] and more recently by Cleereman, Karam, and Williams.[2] The latter authors give a diagrammatic sketch of their orientation unit, which is reproduced in Fig. 1. Molten polystyrene is extruded from a die with a circular orifice. The temperature is then lowered by passing the strand through a bath B_1 which is held at a suitable stretching temperature. The filament is stretched between rolls R_1 and R_2 by rotating the second pair of rolls more rapidly than the first (baths B_1 and B_2 are generally kept at the same temperature). After orienting, the filament then passes through bath B_3 which cools it below the transition temperature, and it is finally wound on a collecting drum. By varying the temperature of the liquid baths and the rate of stretching, a variety of filaments of different orientation can be prepared. These filaments range in size from 0.5- to 1.4-mm diameter. The filaments described in the present paper were all prepared with this unit, and were kindly furnished to the author by H. J. Karam of the Dow Styron Laboratory.

Because of its important effect on the mechanical properties, it is desirable to be able to determine the orientation in these filaments with accuracy. Since molecular orientation produces an optical double refraction (or birefringence) in the polymer,[3] the use of this phenomenon to measure the orientation immediately suggests itself.

In addition to their practical interest, oriented polystyrene monofilaments provide a valuable system for fundamental study of the relationship between molecular orientation and birefringence. These filaments have two notable advantages for such a study: first, polystyrene is a completely amorphous polymer,[4] so that the birefringence observed arises entirely from molecular orientation, with no complications due to crystallization; and, second, the orientation is of a simple one-dimensional type, in a sample of simple geometrical

[1] J. Bailey, India Rubber World **118**, 225 (1948).
[2] Cleereman, Karam, and Williams, Modern Plastics **30**, 125 (May, 1953).
[3] F. H. Müller, Kolloid-Z. **95**, 138, 306 (1941).
[4] S. Krimm and A. V. Tobolsky, Textile Research J. **21**, 805 (1951).

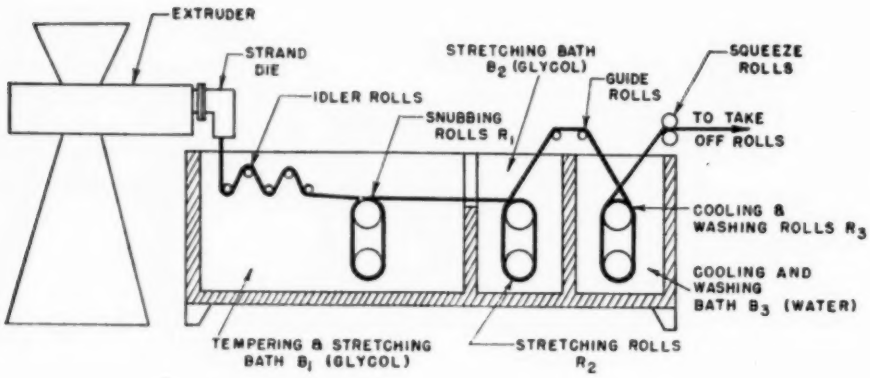

FIG. 1. Orientation unit for polystyrene monofilament.

form. The fact that the orientation is quite uniform along the length of the filament, allowing duplicate samples to be studied, is also an important advantage.

INTERFERENCE PATTERNS

When these oriented filaments are examined through a polarizing microscope, a series of interference fringes is seen which run parallel to the axis of the filament, and are more closely spaced at the edges of the filament than at the center.[2,5,6] By suitable interpretation of this interference pattern considerable information may be obtained on the state of orientation of the sample. Methods for doing this, including some newly developed experimental techniques, will be described. It may be of interest to consider first, however, the way in which this interference pattern arises.

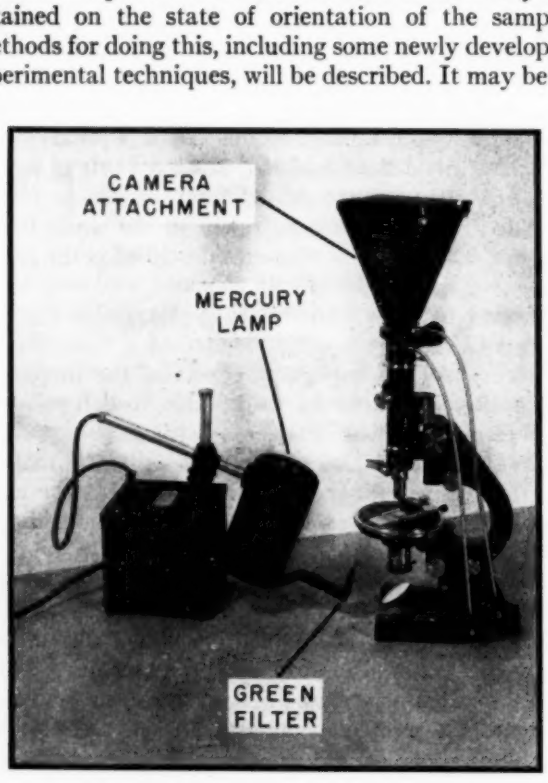

FIG. 2. Polarizing microscope with camera attachment and mercury lamp.

In unoriented polystyrene the optical properties are isotropic, even though the local polarizability of the polystyrene chain varies with direction, because of the random configuration of the chains; the local chain segments in this case are oriented with equal probability in all directions. However, when the chains are oriented preferentially in some direction, such as by stretching[7] (in the solid state) or by setting up flow gradients in a solution,[8a,b] the orientation of local chain segments is no longer random and the optical properties are no longer isotropic. In particular, the index of refraction will have different values in the direction of orientation and in the perpendicular direction. This difference is known as the birefringence or double refraction, and is usually symbolized by Δ, where

$$\Delta = n_1 - n_2. \qquad (1)$$

Here n_1 and n_2 are the indices of refraction in the orientation direction and the perpendicular direction, respectively. The birefringence may obviously be either positive or negative depending on the chemical structure of the molecular chains. In the case of polystyrene the major part of the polarizability of the chain comes from the benzene rings, which are attached as side groups, rather than from the hydrocarbon backbone. When the chains are extended the benzene rings tend to orient in a direction perpendicular to the direction of extension, and the polarizability and therefore the index of refraction increases in the perpendicular direction. The sign of the birefringence produced by molecular orientation in polystyrene is therefore negative.[3] It has been reported,[1,9] however, that for small strains, at temperatures appreciably below the transition temperature, the sign of the birefringence in polystyrene is positive. This indicates that the molecular mechanism of strain is different in the glassy state from the molecular orientation mechanism in the rubbery state above

[5] Williams, Cleereman, Karam, and Rinn, J. Polymer Sci. 8, 345 (1952).
[6] L. A. Matheson and J. L. Saunderson, *Styrene*, R. H. Boundy and R. F. Boyer, Editors (Reinhold Publishing Corporation, New York, 1952), Chap. 11, p. 530.
[7] R. S. Stein and A. V. Tobolsky, Textile Research J. 18, 201, 302 (1948).
[8] (a) W. Kuhn and H. Kuhn, Helv. Chim. Acta 26, 1324 (1943). (b) R. Cerf and H. A. Scheraga, Chem. Revs. 51, 185 (1952).
[9] See reference 3, footnote 102.

the transition temperature. This same difference in sign of the birefringence above and below the transition temperature has also been observed[10] for polyethyl acrylate (Lactoprene rubber). The sign of the birefringence in the oriented polystyrene monofilaments studied here is negative in all cases since we are observing the effects of molecular orientation produced above the transition temperature and then "frozen in" by quick cooling to a temperature below the transition temperature. The absolute magnitude of the positive birefringence is much smaller than that of the negative birefringence, and it is believed that positive birefringence is either completely absent or present to a negligible degree in these filaments.

To convert birefringence into an observable optical interference pattern, the sample is placed between two polarizers; and since these filaments are small, in this work this was done by use of a polarizing (or petrographic) microscope. Monochromatic light was obtained by use of a mercury vapor lamp with a filter which transmitted only the mercury green line (5461A). The experimental setup, with camera attachment on the microscope to allow photographs to be made of the interference patterns, is shown in Fig. 2. In order to see the interference patterns satisfactorily it was necessary to immerse the filaments in a liquid of refractive index corresponding to that of polystyrene ($n=1.59$), in order to eliminate the lens effects resulting from the cylindrical shape of the filament (a solution of $HgI_2 \cdot KI$ in glycerine was the liquid used).

When a filament is examined between crossed polarizers, with the filament axis at an angle of 45° with respect to the optic axes of the polarizers, dark bands are seen where the retardation Γ, which is the path difference produced between the two components of the polarized light beam, equals integral numbers of wavelengths; the background of the field is dark since this corresponds to zero retardation. A typical interference pattern of this sort is shown in Fig. 3. When the polarizers are parallel, dark bands are seen on the filament where the retardation is halfway between integral numbers of wavelengths; the background is light in this case. The reason for this difference in the interference patterns observed between crossed and parallel polarizers is illustrated schematically in Fig. 4; essentially, crossed polarizers cause the components emerging from the sample to oppose each other, while parallel polarizers cause the emerging components to reinforce each other; thus there is a phase difference of 180° in the interference behavior in the two cases.

In the case of crossed polarizers, if the sample is rotated between the polarizers the entire field goes dark at the four positions 90° apart where the optic axes of the sample (direction of orientation and the perpendicular direction) coincide with the axes of polarization of the polarizers. The light bands on the sample reach a maximum intensity at the intermediate 45° positions. This dependence of transmitted light intensity on retardation and orientation of the optic axes of the sample

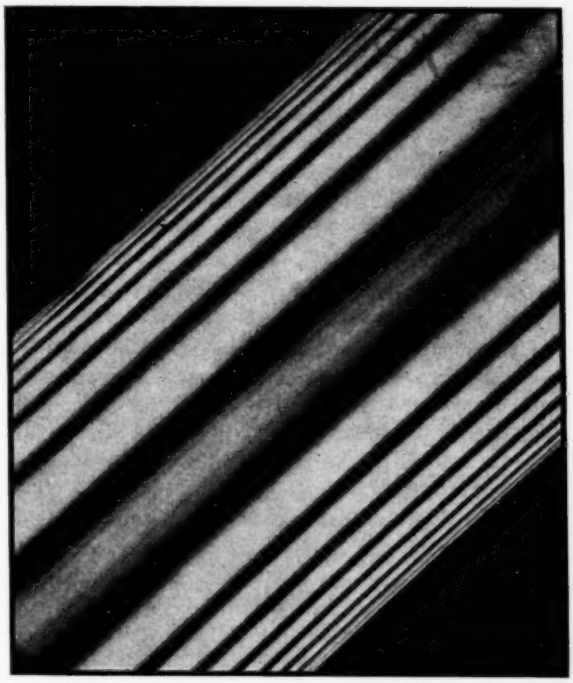

FIG. 3. Typical oriented polystyrene monofilament as seen through crossed polarizers.

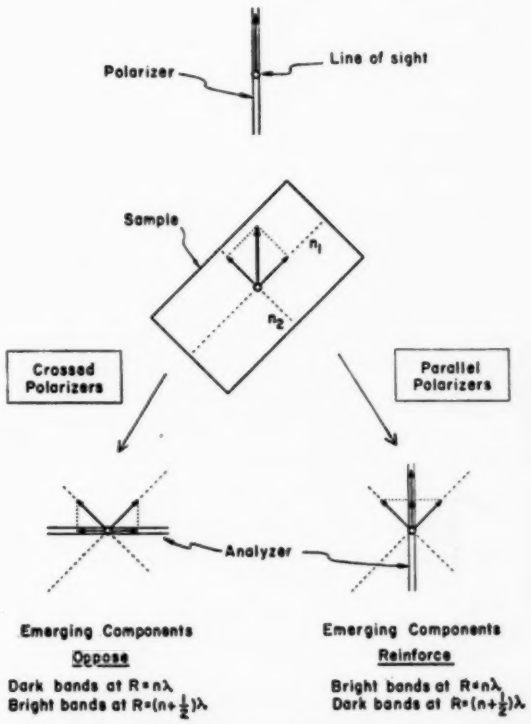

FIG. 4. Cause of difference in fringe pattern for crossed and parallel polarizers (sample oriented at 45° with respect to polarizers). Retardation is denoted by R.

[10] Stein, Krimm, and Tobolsky, Textile Research J. **19**, 8 (1949).

can be expressed by the equation

$$I_t(N,\theta)=I_0\cdot A(N)\cdot B(\theta), \tag{2}$$

where I_t is the transmitted intensity, I_0 is the incident light intensity, θ is the angular orientation of the optic axes of the sample with respect to the optic axes of the polarizers, and N is the retardation expressed as number of wavelengths (i.e., $N=\Gamma/\lambda$). The two functions $A(N)$ and $B(\theta)$ have the form

$$A(N)=\sin^2(\pi N) \tag{3a}$$

$$B(\theta)=4\sin^2\theta\cos^2\theta. \tag{3b}$$

These two symmetrical functions are shown graphically in Fig. 5. The abscissa scale for retardation N actually represents the interval between any two successive integral numbers of wavelengths, and not merely the interval between 0 and 1 wavelength.

In the case of parallel polarizers, the entire field is light when the optic axes of the sample coincide with those of the polarizers. As the sample is rotated through any quadrant, dark bands appear and become darker as the sample approaches the 45° position where a maximum is reached, then fade out again as the sample is rotated through the other half of the quadrant. The intensity of light transmitted as a function of retardation and sample orientation can be represented by the equation

$$I_t(N,\theta)=I_0[F_1(\theta)+F_2(\theta)\cdot G(N)], \tag{4}$$

where I_t and I_0 have the same significance as before, and the functions $F_1(\theta)$, $F_2(\theta)$, and $G(N)$ have the form

$$F_1(\theta)=\sin^4\theta+\cos^4\theta \tag{5a}$$

$$F_2(\theta)=2\sin^2\theta\cos^2\theta \tag{5b}$$

$$G(N)=\cos(2\pi N). \tag{5c}$$

However, Eq. (4) can be further transformed, and expressed in terms of the functions $A(N)$ and $B(\theta)$ by use of the relations

$$F_2(\theta)=B(\theta)/2 \tag{6a}$$

$$G(N)=1-2A(N) \tag{6b}$$

$$F_1(\theta)+F_2(\theta)=1. \tag{6c}$$

This gives the result

$$I_t(N,\theta)=I_0[1-A(N)\cdot B(\theta)]. \tag{7}$$

It is seen, therefore, by comparison of Eqs. (2) and (7), that the transmitted light intensities for crossed and parallel polarizers at any point of an interference pattern, whatever the values of N and θ, satisfy the relation

$$I_t(\text{parallel})=I_0-I_t(\text{crossed}). \tag{8}$$

We might denote this fact by saying that the interference patterns for crossed and parallel polarizers are "inverse." Typical interference patterns for an oriented monofilament between crossed and parallel polarizers, with the optic axes of the filament oriented at 45° to the axes of the polarizers, are shown in Fig. 6.

All of the results discussed above can readily be derived from an analysis in terms of components. Such an analysis is carried out in terms of the amplitude of the electric vector of the components, and this must then be converted to light intensity by squaring the resultant amplitude. In examining vector diagrams for crossed and parallel polarizers in the complex plane, it is noted that the distinction illustrated in Fig. 4—that emerging components are opposed in the case of crossed polarizers and reinforce in the case of parallel polarizers—can be amplified by the additional fact that the emerging components are always of equal amplitude in the case of crossed polarizers, independent of the value of θ, whereas in the case of parallel polarizers the emerging components are in general not equal, and in fact are equal only when $\theta=45°$. As a consequence, complete extinction (I_t equals zero) can be obtained with parallel polarizers only when $\theta=45°$.

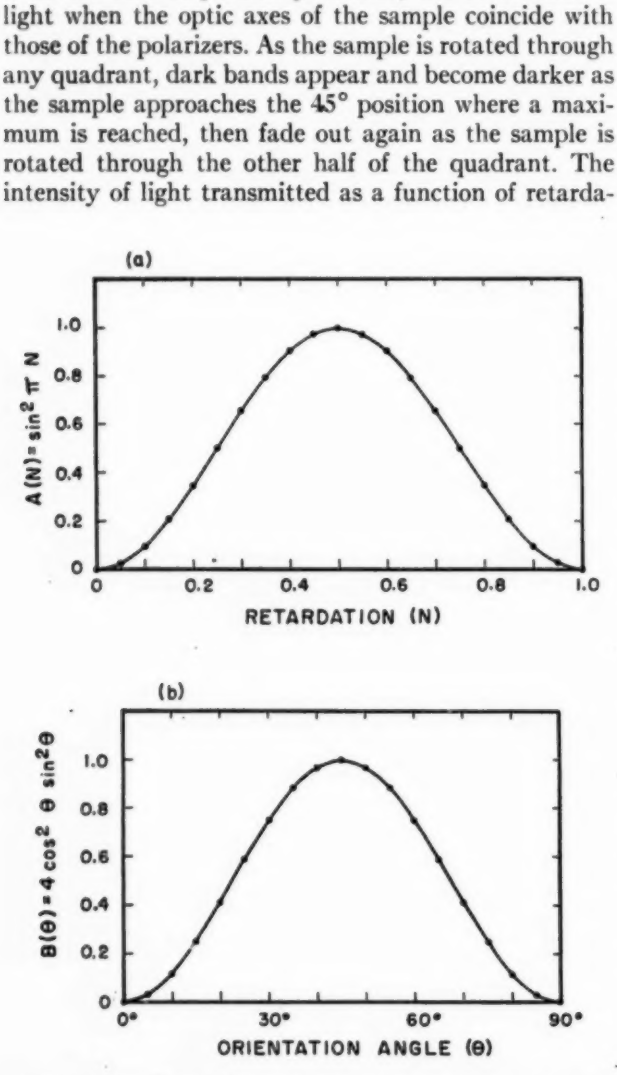

FIG. 5. Functions $A(N)$ and $B(\theta)$ representing dependence of transmitted light intensity on retardation and sample orientation.

ANALYSIS OF INTERFERENCE PATTERNS

The analysis of photoelastic patterns (for example, of engineering structures) usually involves determining both the magnitude of the retardation and the direction

of the optic axes from point to point in the pattern. Analyzing complicated patterns sometimes requires the use of auxiliary techniques such as slicing the model and examining the optical pattern of the individual sections, in order to obtain more details than are afforded by the pattern for the model as a whole, which is essentially a two-dimensional projection. The analysis of the interference patterns of oriented monofilaments has the simplifying feature that the direction of the optic axes is constant throughout (since the orientation is all in the axial direction), and only the magnitude of the retardation across a diameter of the filament needs to be determined to completely specify the pattern. The fact that the filaments are almost perfectly cylindrical in shape is also a simplifying feature, since the thickness of the sample at each point, as well as the retardation, must be known to compute the birefringence. Ideally, the radial distribution of birefringence in the filament would be computed from the interference pattern, since this would be the most fundamental way of expressing data of this sort.

One would hope to obtain from such an analysis knowledge of whether the orientation was constant throughout the filament, or if not, the manner in which it varied, and also the degree of orientation throughout. Actually, one can determine directly from the interference pattern only the way in which the *birefringence* varies in the filament. For the purposes of the present discussion we may assume that orientation and birefringence are synonymous, since as the degree of orientation increases, the birefringence increases also. Relating birefringence to molecular orientation is a problem in itself, which involves setting up a suitable definition of molecular orientation; this particular problem is discussed in an accompanying paper by Gurnee.[11]

Kolb and Sturkey[12] have proposed a method for analyzing the interference patterns of oriented filaments which does not require a knowledge of the order (number of wavelengths retardation) of the fringes. This method has also been used by Cleereman, Karam, and Williams.[2] In this method, the thickness of the sample is calculated at the points where two adjacent fringes are located. Then assuming that the retardation differs by one wavelength and the difference in thickness is known, an average birefringence for the part of the sample between the two fringes can be calculated from the equation

$$\Delta=\lambda/(t_i-t_{i-1}), \tag{9}$$

where λ is the wavelength of the light used and t_i-t_{i-1} is the difference in thickness. Birefringence can obviously be regarded as the length of path difference (retardation) produced per unit optical path length. However a mathematical analysis of the above method shows that Eq. (9) holds exactly only for the case where the birefringence is constant throughout the filament. It is not generally valid even when fringe order increases regularly from zero to some maximum value going from the edge of the filament to the center; and in cases where reversal of fringe order occurs, this method is meaningless.

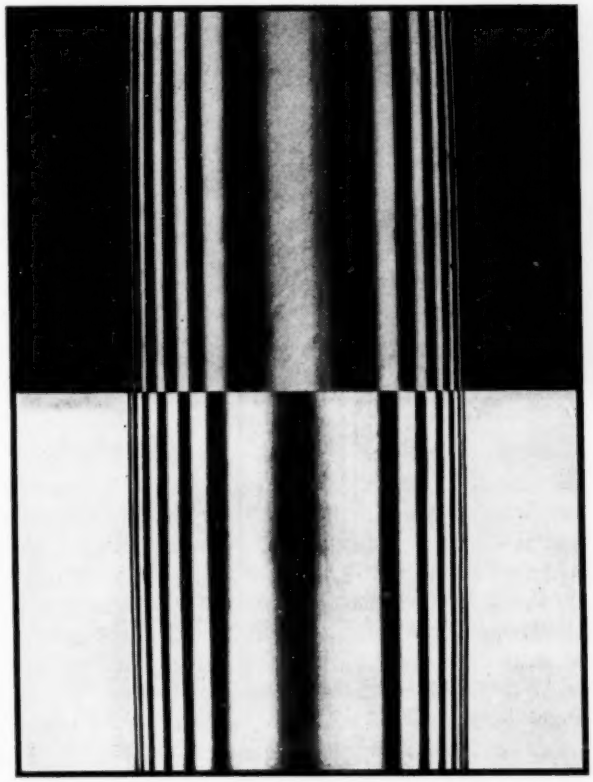

FIG. 6. Comparison of interference patterns given by an oriented filament between crossed polarizers (upper half) and parallel polarizers (lower half).

In connection with this method, and as a mental point of reference, it is useful to consider the case of a filament with uniform birefringence. The interference pattern and a cross-section view of such a filament is shown in Fig. 7. For such a filament the interference pattern arises entirely from the variation of thickness. The positions at which fringes are located correspond to equal increments of thickness. Fringes of order N from 0 to 5 are shown in the figure.

In cases where the birefringence is not uniform it may be assumed from the method of fabrication that the distribution of birefringence in the filament is cylindrically symmetrical; i.e., the birefringence will be a function of the radial distance from the central axis r alone. In this case if the cross diameter of the filament in the direction perpendicular to a vertical line of sight is taken to define a y axis, with origin at the center of the filament, the retardation $\Gamma(y)$ along a line of sight displaced a distance y from the center of the filament,

[11] E. F. Gurnee, J. Appl. Phys. **25**, 1232 (1954).
[12] A. F. Kolb and L. Sturkey, Dow Chemical Company (unpublished work).

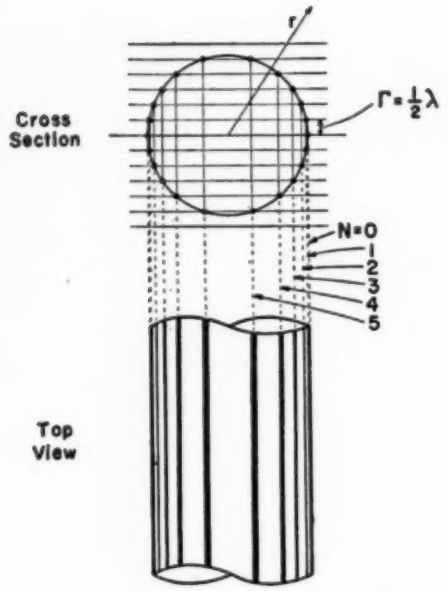

FIG. 7. Interference pattern for filament with uniform birefringence between crossed polarizers.

will be given by the equation

$$\Gamma(y)=2\int_{r=y}^{R}\frac{\Delta(r)r}{(r^2-y^2)^{\frac{1}{2}}}dr, \tag{10}$$

where $\Delta(r)$ is the radial distribution of birefringence, R is the radius of the filament, and the radial distance r is used as the variable of integration along a vertical path (the line of sight). This is illustrated schematically in Fig. 8.

If the retardation is divided by the optical path length p one obtains an average birefringence Δ_{Av} for that particular optical path, which will be related to $\Delta(r)$ through the equation

$$\Delta_{Av}=\frac{\Gamma(y)}{p(y)}=\frac{\int_{r=y}^{R}\frac{\Delta(r)r}{(r^2-y^2)^{\frac{1}{2}}}dr}{(R^2-y^2)^{\frac{1}{2}}}. \tag{11}$$

This average might be called a "linear average." This is the type of average that one would obtain by dividing the total retardation at the center of a filament by its diameter, as proposed by Cleereman, Karam, and Williams[2] as a simple method of characterizing the birefringence of a filament (they call this the "birefringence number" of the filament).

This "linear" average is also the type of average birefringence which is obtained most directly from an interference pattern. A typical curve of Δ_{Av} *vs* the diameter of the filament is given in Fig. 9, calculated from the filament pattern which was shown in Fig. 3. This pattern shows fringes of order N from 0 to 10 going from the edges to the center. The curve for Δ_{Av} (solid curve) is fairly flat in the center, shows a sharp rise approaching the edges of the filament followed by a sharp drop right at the edges. Determination of the radial distribution of birefringence $\Delta(r)$ for other filaments by a different method[11] indicates, however, that this drop-off at the edges is probably fictitious; it seems to be an experimental artifact, caused perhaps by a slight difference in refractive index between the filament and immersion liquid. It will also be noted that the curve is not perfectly symmetrical on the two sides of the center, as it should ideally be; this may be the result of slight deviations of the filament from perfect cylindrical shape. This general form of curve—with higher birefringence at the edges than in the center—is typical of these filaments. This result can be explained in terms of cooling rates during the fabrication process. It will be remembered that after the filament is oriented above the transition temperature, it runs into a "quenching" bath which chills it quickly to a temperature below the transition temperature, in order to "freeze in" the orientation. However the surface of the filament is cooled immediately while the interior is cooled more slowly, as a result of the finite thermal conduction rate. Decay of orientation takes place fairly rapidly above the transition temperature, and therefore more of the orientation in the center has time to decay out before the local temperature drops below the transition temperature.

A. Measurement of Fringe Order

In almost all these calculations an essential step is the determination of the order of the fringes observed in the interference patterns, and it may be useful to discuss some of the ways in which this can be done. We will consider here only filaments where the fringe order increases regularly from the edge to the center of the filament; the case of filaments where a reversal of fringe order occurs will be discussed later.

For interference patterns in which only a few fringes are observed, the order of the fringes can easily be determined by visual counting. Fringes up to ten orders,

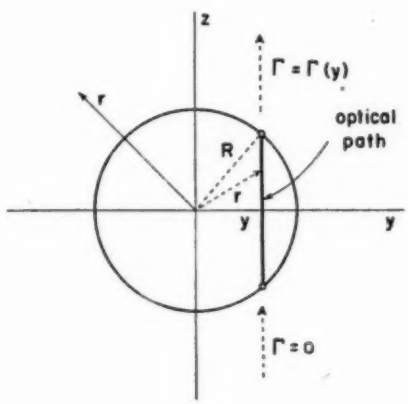

FIG. 8. Cross section of filament with nonuniform distribution of birefringence.

as in Fig. 3, represent about the practical limit for this method; for patterns where the fringes go to higher orders, they become too crowded at the edges of the filament to be clearly distinguished. In cases where the number of fringes is small, it is often desirable to obtain interference patterns using both crossed and parallel polarizers; this will give twice the number of points for use in calculations.

The use of compensators is another possible method of determining fringe order. Various compensators are available, such as the quartz wedge,[13] Babinet,[14] Soleil,[14] and Berek[13] types. By use of white light as illumination, compensation to zero retardation can be identified by the fact that the zero order fringe is black while all higher order fringes are colored. The residual fraction of a fringe at the center of the filament can be determined most accurately and conveniently with monochromatic light. The principal limitation on the use of compensators is that they usually have a range of only a few wavelengths, while some of the polystyrene monofilaments have fringes in the range of 20th to 30th order. The last fraction of a wavelength retardation (not total retardation) can be measured by the Tardy or Sénarmont method,[15] involving the use of quarter-wave plates and rotating polarizers. These methods give greater accuracy than the compensators, and can be used to measure total retardation if some auxiliary method is available for measuring the number of whole wavelengths.

A method which is very useful in counting high fringe orders involves the use of a heated microscope stage.

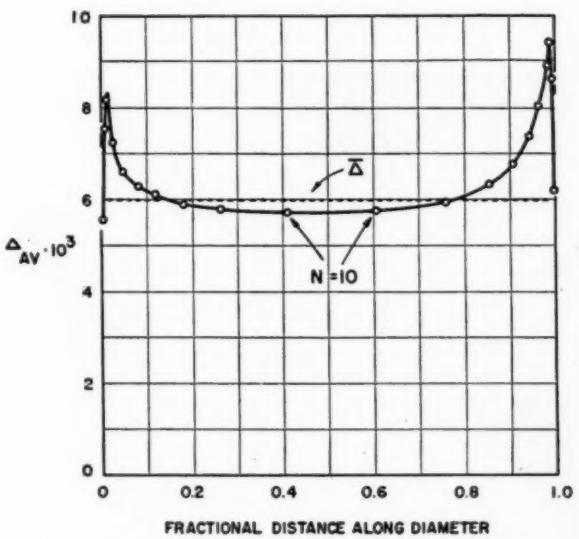

FIG. 9. Linear average birefringence *vs* diameter and weighted average birefringence calculated from Fig. 3.

[13] E. E. Wahlstrom, *Optical Crystallography* (John Wiley and Sons, Inc., New York, 1951), second edition.

[14] F. A. Jenkins and H. E. White, *Fundamentals of Optics* (McGraw-Hill Book Company, Inc., New York, 1950), second edition.

[15] H. T. Jessop, Brit. J. Appl. Phys. 4, 138 (1953).

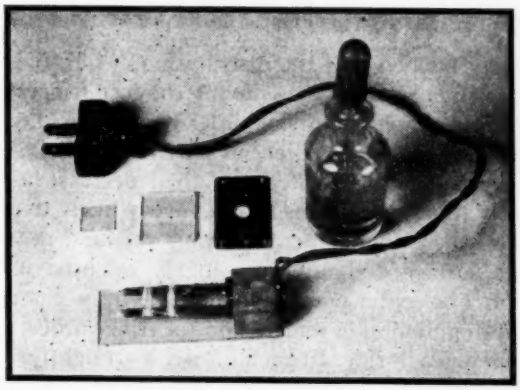

FIG. 10. Heated microscope stage.

The filament is heated in this way above its transition temperature where it rapidly contracts. As it contracts, corresponding fringes (i.e., fringes of equal order) come in to the center from the two sides, fuse and disappear, until finally the entire field goes dark as the zero fringe spreads over the filament. By controlling the rate of heating, the rate of contraction can be controlled so that the fringes going by can be counted at a convenient rate. The experimental setup used in the present work is shown in Fig. 10. A pair of small heating coils are wound on a pair of supports attached through a plastic block to a microscope slide. A thin metal plate with a hole in the center rests on top of the coils to distribute the heat, and on top of this is a special glass plate with a groove cut in it to hold the filament with a cover glass on top. The usual immersion fluid is used, and the heating coil is plugged into a Variac variable transformer to regulate the degree of heating.

Another potential method of measuring retardation or fringe order would be the spectroscopic analysis of interference colors. In this method, the sample would be illuminated with white light, having a continuous spectrum. To determine the retardation at any point of the colored interference pattern which would result, the light from that point of the pattern would be passed through a spectroscope and analyzed. Certain wavelengths would be missing from the spectrum, at values where the retardation equaled an integral number of those wavelengths (with the sample between crossed polarizers) and therefore destructive interference occurred. Two adjacent wavelengths that were missing would differ by one in the number of wavelengths retardation they represented, and assuming that the retardation was independent of wavelength, one could easily calculate the amount of retardation. There would undoubtedly be practical problems in using this method (e.g., in obtaining suitable light intensity), but it would have the advantage that retardation could be determined with equal ease at any retardation value, and not simply at integral and half-integral numbers of wavelengths.

B. Reversal of Fringe Order

It may happen that the distribution of birefringence in the filament is such that the interference fringes may not show a simple increasing order going from the edge of the filament to the center but may reach a maximum before reaching the center and then decrease as the center is approached. This is particularly likely to occur in cases where the filament is highly oriented near the outside surface and not very highly oriented in the interior. The center point may then have the character of a local minimum of retardation (or fringe order) with maxima on each side. In such a case, a straightforward counting of fringes will not give the correct order. It is therefore important to be able to recognize when such a reversal of order is present.

One method of doing this which requires no auxiliary equipment is to cross two pieces of the filament and examine the interference pattern in the square area of overlap of the two filaments. There will be a black zero fringe in the shape of a cross between diagonal corners of the square. The four quadrants between the arms of this cross will have identical interference patterns, and each pattern will be symmetrical around the bisector of the quadrant. Where no reversal occurs, the interference fringes observed in each quadrant will be of a generally hyperbolic shape, pointed toward the center of the intersection square and cut off by the side of the square. An example of this is shown in Fig. 11. Where a reversal of order takes place, a nested set of "islands" or closed paths are observed in each quadrant which do not touch the boundaries of the quadrant; this type of fringe pattern is illustrated in Fig. 12. When a reversal is present, the position of the maxima can be easily seen by this method if they occur toward the center of the filament, since they will be located at the centers of the nested sets of islands. A detailed analysis of the interference pattern in the square intersection area is usually not possible because of the difficulty in getting a pattern which is completely in focus; the limited depth of field of the microscope causes difficulties here.

When a filament with reversal of order is contracted on a heated stage, the presence of the reversal can be seen from the fact that as the contraction begins, the fringes at the center of the filament move outward rather than inward, and the fringes converge, fuse, and disappear at the two positions on each side of the center where the maxima are located. Although the presence of a reversal can be seen from a contraction experiment of this sort, it is difficult to count fringe order by this method when a reversal is present, because of the complicated motion of the fringes.

Probably the most convenient method of checking a filament for reversal is by use of a compensator. When the compensation is increased, the fringes move apart from the center and in from the edges and converge at the two points where the actual maxima are located, similarly to the contraction experiment. The advantage in the use of the compensator is that this observation can be repeated as many times as desired on the same filament sample, if there is any doubt about the first observation. This method also allows a slower and more detailed examination of the sample.

It should be emphasized that a reversal of fringe order does not mean that a change in sign of the birefringence has taken place; the reversal is simply a consequence of the form of the radial distribution of birefringence $\Delta(r)$ together with the cylindrical shape of the filament.

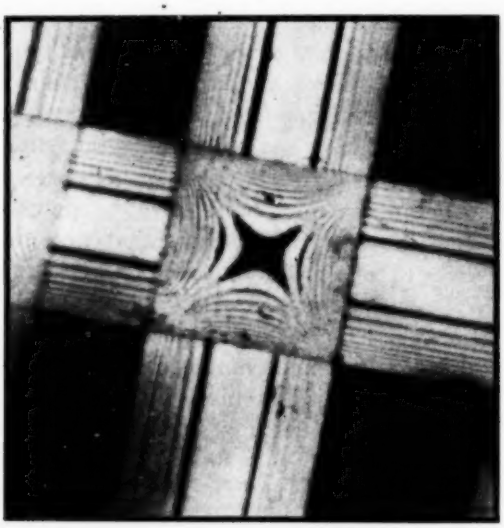

FIG. 11. Crossed filament with no reversal of fringe order.

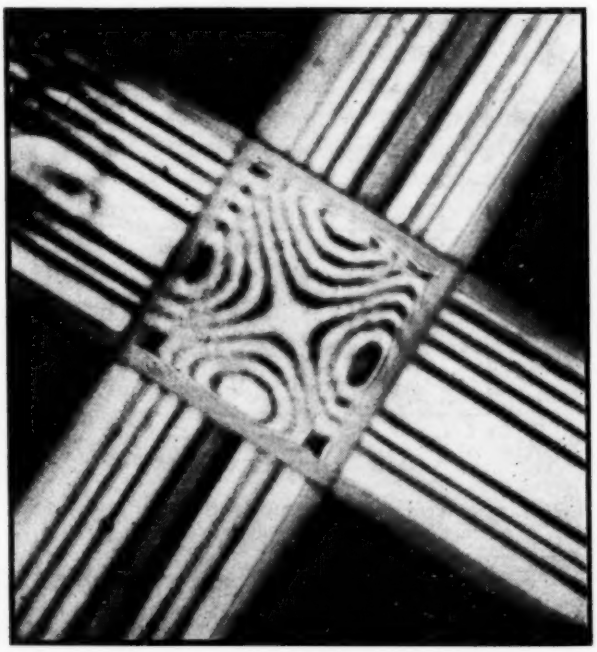

FIG. 12. Crossed filament with reversal of fringe order.

CONCLUSION

When the order of all the fringes is known, a curve of the "linear average" birefringence $\langle\Delta\rangle_{Av}$ can easily be computed, as illustrated in Fig. 9. In order to obtain an average birefringence for the filament as a whole, the value of $\langle\Delta\rangle_{Av}$ at the center of the filament could be taken, as mentioned earlier. However, a somewhat better method is to compute a weighted average $\langle\Delta\rangle_{Av}$ from the curve of $\langle\Delta\rangle_{Av}$. This can be done by dividing a cross section of the filament into a set of vertical strips each one containing one fringe. The over-all average birefringence can then be computed by weighting the value of $\langle\Delta\rangle_{Av}$ at the position of each fringe by the area of the strip associated with it. The resulting value of $\langle\Delta\rangle_{Av}$ is shown in Fig. 9 as a dashed line. The strongly favored weighting of the central values is apparent from this graph.

However, we must remind ourselves again that the fundamental quantity we would like to know is the radial distribution of birefringence $\Delta(r)$. Computing this from $\langle\Delta\rangle_{Av}$ involves essentially the inversion of an integral, or the solution of an integral equation given as Eq. (11). This could undoubtedly be done numerically on an electronic computing machine, by replacing the integral with a series of finite increments of suitable size. However, the radial distribution function $\Delta(r)$ can also be directly measured experimentally, by cutting a wedge (or cone) on the end of the filament, and analyzing the interference pattern which results, as discussed in the accompanying paper[11] by Gurnee, and this is probably the more satisfactory method.

No attempt has been made in the present paper to carry out comparative measurements of birefringence on filaments which vary in a systematic way (e.g., as a function of fabricating variables). We have considered here only the basic nature of the problem of measuring the molecular orientation by study of the associated birefringence, together with background theory and experimental methods useful for this purpose. The application of these techniques is reserved for future publications.

Theory of Orientation and Double Refraction in Polymers

EDWARD F. GURNEE
Physical Research Laboratory, Dow Chemical Company, Midland, Michigan
(Received June 14, 1954)

Orientation and birefringence in linearly oriented amorphous polymers are discussed with particular emphasis on polystyrene type chains. A system of completely uncoiled parallel zigzag chains is defined as 100 percent orientation. The variation of birefringence with orientation is assumed to follow the same expression as that for the variation of polarization anisotropy with extension for a single random coil chain. With these assumptions and reasonable models for the completely uncoiled polystyrene chain it is possible to express any given birefringence as a percentage orientation.

Methods are developed for the experimental determination of the birefringence at a particular point in an oriented monofilament instead of the usual determination of an average birefringence through the monofilament. The application of these methods to actual examples leads to reasonable values of the orientation.

INTRODUCTION

IT is well known that orientation of polymers produces marked changes in their physical properties. One of the most powerful methods for studying orientation in polymers is by means of birefringence measurements. The partial alignment of polymer chains during linear orientation produces a difference between the electronic polarizability in the direction of stretch and that in the direction perpendicular to the stretch. This polarization anisotropy gives rise to a difference between the refractive indexes in these directions, which is by definition the birefringence.

The first part of this paper will be concerned with a discussion of the relationships between chain structure and birefringence in linearly oriented amorphous polymers in an attempt to put orientation on a quantitative, although somewhat arbitrary, basis. In the second section, experimental methods are developed for the determination of the birefringence in the particular case of oriented monofilaments.

PART I. A RELATIONSHIP BETWEEN BIREFRINGENCE AND ORIENTATION

Chain Structure and Polarization Anisotropy

The optical anisotropy of a randomly linked chain has been worked out by Kuhn and Grün.[1] They arrived at the equation

$$(\alpha_z-\alpha_x)=n(\alpha_1-\alpha_2)\left[1-\frac{3(r/nl)}{\mathfrak{L}^{-1}(r/nl)}\right], \qquad (1)$$

where α_1 and α_2 are the electronic polarizabilities, parallel and perpendicular, respectively, to the individual links; α_z and α_x are the total electronic polarizabilities parallel and perpendicular, respectively, to the vector r (Fig. 1); n is the number of links in the chain; r is the straight line distance between the ends of the chain; l is the length of each link; and $\mathfrak{L}^{-1}$ is the inverse Langevin function.

For a zigzag chain of n links, a portion of which is also shown in Fig. 1, it can be shown from standard optical theory that

$$(\alpha_z-\alpha_x)=n(\alpha_1-\alpha_2)[1-\tfrac{3}{2}\sin^2\theta]. \qquad (2)$$

In the derivation of this equation, the zigzag chain is assumed to have free rotation about the r vector. This introduction of three-dimensional character is necessary in order to make a comparison between Eqs. (1) and (2). It is also assumed that in any extension of this zigzag chain the bond angles all change in the same manner, i.e., the chain moves like an accordion. Equation (2) may also be written as

$$(\alpha_z-\alpha_x)=n(\alpha_1-\alpha_2)[\tfrac{3}{2}(r/nl)^2-\tfrac{1}{2}]. \qquad (3)$$

In Fig. 2 the relative polarization anisotropy referred to the completely extended chain, $(\alpha_z-\alpha_x)/n(\alpha_1-\alpha_2)$, is plotted against the extension (r/nl) for the random coil[2] and the zigzag chain. The extensions for this latter chain corresponding to a tetrahedral bond angle and a ninety-degree bond angle are shown as dotted lines as a matter of reference. Because of the fact that the graphs for both types of chain structures nearly coincide at very high extensions, it is reasonable to define orientation of the random coil in terms of the structure of the zigzag chain.

We will assume that a chain that is completely uncoiled and stretched in one direction to its maximum

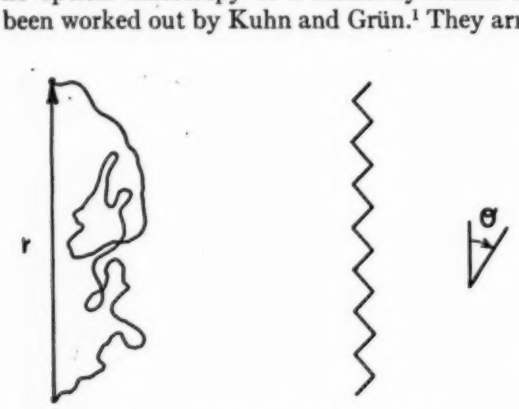

FIG. 1. The random coil and zigzag chains.

[1] W. Kuhn and F. Grün, Kolloid-Z. **101**, 248 (1942).

[2] L. R. G. Treloar, Trans. Faraday Soc. **43**, 277 (1947).

length without deformation of the bond angles, i.e., the zigzag chain with tetrahedral bond angle, represents 100 percent orientation, and that the orientation is directly proportional to the extension (r/nl); this calibrates the abscissa of Fig. 2 in terms of orientation. Then, by determining the quantity $(\alpha_z-\alpha_x)$ for this zigzag chain for the polymer being considered and by means of the Lorentz-Lorenz equation, it is possible to calibrate the ordinate of Fig. 2 in terms of birefringence. We then make the rather arbitrary assumption that a system of linear chains has the same relationship between orientation and birefringence as shown in Fig. 2 for a single random coil. Even though this relation is somewhat arbitrary, it should prove especially useful in comparing orientations in similar chemical type monomers, such as polystyrene, vinyltoluene, α-methylstyrene, etc.

It should be pointed out that there is a certain ambiguity in the location of the polarization anisotropy corresponding to 100 percent orientation due to the

FIG. 2. The relative polarization anisotropy plotted against chain extension for the random coil and zigzag chains.

fact that the two curves do not exactly correspond at this value of the extension. In addition the zero birefringence in a system of random linear chains is due to the random distribution of the random chains. Any one random coil with an end separation given by the mean square length, $\bar{r}^2=nl^2$, has a polarization anisotropy given by[1]

$$(\alpha_z-\alpha_x)=\tfrac{3}{5}(\alpha_1-\alpha_2). \tag{4}$$

When this is substituted into Eq. (1), we find the relative polarization anisotropy of such a chain to be $3/5n$. For large values of n, however, it is essentially zero.

We shall now calculate the quantity $(\alpha_z-\alpha_x)$ for the zigzag polystyrene chain with tetrahedral bond angles.

Polarization Anisotropy of Completely Oriented Polystyrene Chains

We shall assume the general model shown in Fig. 3. In this figure the dotted bonds are perpendicular to the z axis and extend toward the rear; the extra dark bonds are perpendicular to the z axis and extend toward the

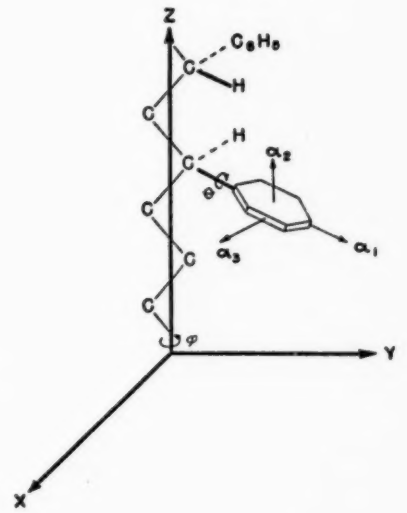

FIG. 3. The polystyrene model.

front. The zigzag chain is completely oriented in the z direction and lies in a plane which can be randomly distributed about the z axis (variable φ). The axis of symmetry of each phenyl group is perpendicular to the z axis, and the rotation of the phenyl group about its symmetry axis is described by the variable θ. Let us make the assumption, which will be justified later, that the entire polarizability of the chain arises from three component polarizabilities of the phenyl groups. These components are: α_1 along the axis of symmetry; α_2 perpendicular to the plane of the phenyl group; α_3 perpendicular to α_1 and α_2. Several cases will now be considered with different restrictions on the variable θ.

Case A. Free Rotation of the Phenyl Groups

The phenyl groups are first assumed to have free rotation about their axes of symmetry. This assumption can certainly be objected to on physical grounds; however, it leads to equations that are readily specialized to other cases that will be investigated.

The probability that the phenyl group is positioned in the neighborhood of the coordinates φ and θ is given by

$$P_{\varphi,\theta}d\varphi d\theta=(d\varphi/2\pi)(d\theta/\pi). \tag{5}$$

The coordinate φ varies from 0 to 2π and θ varies from 0 to π. Actually these limits are somewhat arbitrary, and it is only necessary that they cover all possible configurations and that Eq. (5) is normalized. The effective polarizabilities in the x, y, and z directions are calculated for each phenyl group as functions of φ and θ with the aid of Fig. 4. They are designated $\alpha_{\varphi,\theta}^{\,z}$, $\alpha_{\varphi,\theta}^{\,y}$ and $\alpha_{\varphi,\theta}^{\,x}$, and turn out to be

$$\alpha_{\varphi,\theta}^{\,z}=\alpha_1\cos^2\varphi+\alpha_2\sin^2\varphi\sin^2\theta+\alpha_3\sin^2\varphi\cos^2\theta, \tag{6}$$

$$\alpha_{\varphi,\theta}^{\,y}=\alpha_1\sin^2\varphi+\alpha_2\cos^2\varphi\sin^2\theta+\alpha_3\cos^2\varphi\cos^2\theta, \tag{7}$$

$$\alpha_{\varphi,\theta}^{\,x}=\alpha_2\cos^2\theta+\alpha_3\sin^2\theta. \tag{8}$$

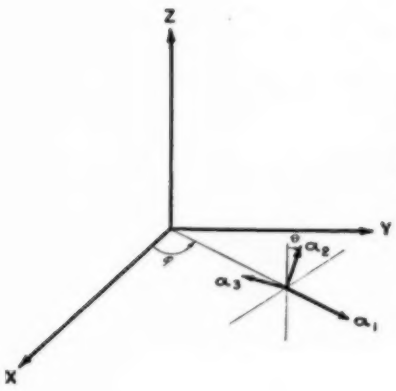

FIG. 4. The position of the polarizabilities of the phenyl groups as a function of the variables φ and θ.

The total polarizability components α_x, α_y, and α_z for each phenyl group are found by averaging these effective polarizabilities with the above probability function. This leads to

$$\alpha_x=\int_{\theta=0}^{\pi}\int_{\varphi=0}^{2\pi}\alpha_{\varphi,\theta}{}^{x}(d\varphi/2\pi)(d\theta/\pi), \tag{9}$$

and similarly for α_y and α_z.

The combination of Eqs. (6), (8), and (9) leads to a polarization anisotropy of

$$(\alpha_z-\alpha_x)=-(\alpha_1/2-\alpha_2/4-\alpha_3/4). \tag{10}$$

This anisotropy can also be calculated by taking the average of two special configurations: one with θ fixed at 0, the other with θ fixed at $\pi/2$. For these fixed structures it follows directly from Eqs. (6) and (8), after averaging over φ, that

$$(\alpha_z-\alpha_x)=-(\alpha_1/2-\alpha_2+\alpha_3/2) \quad \text{at} \quad \theta=0, \tag{11}$$

$$(\alpha_z-\alpha_x)=-(\alpha_1/2+\alpha_2/2-\alpha_3) \quad \text{at} \quad \theta=\pi/2. \tag{12}$$

The arithmetic average of the last two equations gives the same anisotropy as that for the model with free rotation, i.e., Eq. (10).

It might be argued that Eqs. (11) and (12) should not be weighted equally since the configuration represented by $\theta=\pi/2$ might have a lower probability due to the steric hindrance of the bulky phenyl groups.[3] However, Eq. (10) is correct as long as each phenyl group can assume all values of θ with equal average probability during a time interval that is long compared to the time for one rotation of the phenyl groups, even though at any one particular instant, i.e., a time that is small compared to the rotation of the phenyl groups, the values of θ available may be considerably restricted by the influence of the neighboring phenyl groups.

It is interesting to illustrate this statement with a specialized model that allows each phenyl group to take on all values of θ, but specifically excludes, among others, the configuration in which all of the phenyl groups are perpendicular to the xy plane. We will let adjacent phenyl groups be alternately parallel and perpendicular to the xy plane; they are all considered to rotate with the same angular velocity. The polarizability per monomer unit in the x and z directions is given by

$$\alpha_{\varphi,\theta}{}^{x}=\alpha_1\cos^2\varphi+\tfrac{1}{2}(\alpha_2+\alpha_3)\sin^2\theta, \tag{13}$$

and

$$\alpha_{\varphi,\theta}{}^{z}=\tfrac{1}{2}(\alpha_2+\alpha_3). \tag{14}$$

After averaging these equations with the probability function given by Eq. (5), essentially averaging over φ, we arrive at Eq. (10), the anisotropy formula for free rotation.

Case B. Restricted Rotation of the Phenyl Groups

Let us consider a model similar to Fig. 3 except that we now have restricted rotation of the phenyl groups. Assume that each phenyl group rotates in an average potential field given by $V(\theta)$. The probability that a phenyl group has the coordinates (φ,θ) is given by

$$P_{\varphi,\theta}d\varphi d\theta=\exp[-V(\theta)/kT]d\varphi d\theta, \tag{15}$$

where k=Boltzmann constant and T=absolute temperature. Since we do not know the exact analytical form of $V(\theta)$ it is more convenient not to normalize Eq. (15). The average polarizability in a given direction, say x, for each phenyl group is

$$\alpha_x=\frac{\displaystyle\int_{\theta=0}^{\pi/2}\int_{\varphi=0}^{2\pi}\alpha_{\varphi,\theta}{}^{x}\exp[-V(\theta)/kT]d\varphi d\theta}{\displaystyle 2\pi\int_{\theta=0}^{\pi/2}\exp[-V(\theta)/kT]d\theta}. \tag{16}$$

Similar equations apply to the y and z directions. Let us assume, as shown in Fig. 5, that $V(\theta)=V_0$, for $0\leq\theta\leq\theta_v$ and $V(\theta)=\infty$, for $\theta>\theta_v$. The physical picture implied by this potential is a model in which the phenyl groups may be found with equal probability at an angle less than θ_v, while the configuration represented by $\theta>\theta_v$ is forbidden. The explicit evaluation of Eq. (16) with the aid of Eqs. (6) and (8) yields

$$(\alpha_z-\alpha_x)=-\{\alpha_1/2-\alpha_2/4-\alpha_3/4+\tfrac{3}{8}(\alpha_3-\alpha_2)\sin 2\theta_v/\theta_v\}. \tag{17}$$

As $\theta_v\to 0$, this equation reduces to Eq. (11); as $\theta_v\to\pi/2$, it reduces to Eq. (10).

Other functions may be assumed for $V(\theta)$ rather than the "square-well potential." For example, we may take (see Fig. 5)

$$V(\theta)=V_0\sec^2\theta. \tag{18}$$

However, we are then faced with integrals of the type

$$\int_0^{\pi/2}\cos^2\theta\exp[-V_0\sec^2\theta/kT]d\theta. \tag{19}$$

[3] J. H. deBoer, Trans. Faraday Soc. 32, 10 (1936).

These integrals appear simple, but involve fairly complicated functions. Thus, it seems more profitable, in view of the uncertainty of this function in the first place, to use the simpler "square-well potential."

Relationship between Polarization Anisotropy and Birefringence

Electronic polarizability and refractive index are related by means of the Lorentz-Lorenz equation

$$\left[\frac{n^2-1}{n^2+2}\right]\frac{M}{\rho}=\frac{4\pi}{3}N\alpha, \tag{20}$$

where n=refractive index, M=molecular weight, α=electronic polarizability, N=Avogadro's number, and ρ=density. This equation is also applicable to the component polarizabilities and refractive indices. Thus,

$$\left[\frac{n_z^2-1}{n_z^2+2}-\frac{n_x^2-1}{n_x^2+2}\right]\frac{M}{\rho}=\frac{4\pi}{3}N(\alpha_z-\alpha_x). \tag{21}$$

It should be noted that the molecular weight and the polarizabilities are for the monomer unit. If the entire chain is considered, both sides of Eq. (21) would have to be multiplied by q, the number of units in the chain; this would certainly not change the equation. This remark applies only when the electronic interactions between the phenyl groups are negligible. If such were not the case, one side of Eq. (21) would have to be multiplied by some interaction function $f(q)$. We will assume negligible electronic interactions between the phenyl groups; hence $f(q)=1$, and the birefringence of the chain as given by Eq. (23) below is independent of the number of links.

TABLE I. Summary of calculations.

Model		$(\alpha_z-\alpha_x)$	(n_z-n_x)
Free rotation		-2.54×10^{-24}	−0.141
Fixed phenyl groups	$\theta=0$	-7.17×10^{-24}	−0.399
	$\theta=\pi/2$	$+2.10\times10^{-24}$	+0.118
Restricted rotation	$\theta_v=0°$	-7.17×10^{-24}	−0.399
	$\theta_v=15°$	-6.97×10^{-24}	−0.388
	$\theta_v=30°$	-6.37×10^{-24}	−0.355
	$\theta_v=45°$	-5.49×10^{-24}	−0.306
	$\theta_v=60°$	-4.46×10^{-24}	−0.248
	$\theta_v=75°$	-3.43×10^{-24}	−0.191
	$\theta_v=90°$	-2.54×10^{-24}	−0.141
Müller[a]		-0.30×10^{-24}	...
Kuhn and Grün[b]		-18.0×10^{-24}	...
Observed[a]		-5.0×10^{-24}	...

[a] See reference 5.
[b] See reference 1.
[c] See reference 5.

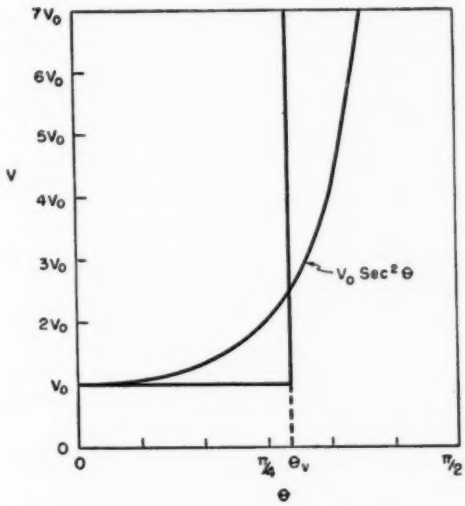

FIG. 5. The comparison between the "square-well" potential and a potential function which varies as $\sec^2\theta$.

For small values of the birefringence (n_z-n_x) we make use of the approximation[1]

$$\left[\frac{n_z^2-1}{n_z^2+2}-\frac{n_x^2-1}{n_x^2+2}\right]\approx\frac{6\bar{n}}{(\bar{n}^2+2)^2}(n_z-n_x), \tag{22}$$

where $\bar{n}$ is the arithmetic average of n_z and n_x. This approximation is good to within one part per thousand, even for birefringence values as large as 0.3. By combining Eqs. (21) and (22) we arrive at

$$(n_z-n_x)=\frac{2\pi}{9}\frac{N\rho}{M}\frac{(\bar{n}^2+2)^2}{\bar{n}}(\alpha_z-\alpha_x). \tag{23}$$

This is the desired relation between birefringence and polarization anisotropy.

Numerical Evaluation of the Formulas

For polystyrene, Eq. (23) can be written as

$$(n_z-n_x)=5.57\times10^{22}(\alpha_z-\alpha_x), \tag{24}$$

where we have used the values $\bar{n}=1.6$, $M=104$ and $\rho=1.06$ g/cm³.

The polarizabilities α_1, α_2, and α_3 are assumed to be the same as those for toluene. This seems reasonable in view of the similarity between the monomer chain segment and toluene, and the fact that the polarizabilities of the zigzag carbon chain have been neglected. Stuart[4] lists these values of the polarizabilities as $\alpha_1=15.64\times10^{-24}$ cm³/molecule, $\alpha_2=7.48\times10^{-24}$ cm³/molecule, and $\alpha_3=13.66\times10^{-24}$ cm³/molecule. The calculated values of the polarization anisotropy for the different models, as well as the corresponding birefringence as given by Eq. (24), are summarized in Table I.

[4] H. A. Stuart and H. Volkmann, Z. Physik. **80**, 107 (1933).

There are several experimental determinations of the polarization anisotropy of the polystyrene statistical chain segment, which is presumably comparable to the maximum possible anisotropy as calculated above. From measurements of birefringence as a function of stress, Müller[5] has arrived at the value of $(\alpha_z-\alpha_x)$ listed in Table I. Kuhn and Grün,[1] using the same experimental data, have determined the somewhat different value, which is also listed in this Table. From measurements of flow birefringence Kuhn and Kuhn[6] have obtained the value of -3.0×10^{-24} for the polarization anisotropy of the polystyrene chain link. Because of the complications of the so-called "form birefringence," this value is probably consistent with the somewhat larger negative values of Table I.

The observed value is reported by Müller[5] as determined from the Kerr effect.

In general, the calculated values for the various models are all of reasonable magnitude with the exception of the improbable structure with θ fixed at $\pi/2$. It is interesting to note that this is the only result with a positive sign, and consequently any deformation that would tend to tip the phenyl groups in this direction would yield a positive birefringence. It should be strongly emphasized, however, that the converse, i.e., that a positive birefringence necessarily implies a tipping of the phenyl groups, is not necessarily true.

In order to arrive at a final answer, we will take $\theta_v=45°$; the polarization anisotropy will then be -5.5×10^{-24} and the birefringence corresponding to 100 percent orientation will be -0.3. These values would not be changed appreciably by a different choice of θ_v, but it should be kept in mind that they are dependent on the value of the polarizabilities α_1, α_2, and α_3.

Effect of Other Atoms on Polarization Anisotropy

It has been assumed that the polarization anisotropy of the polystyrene chain can be calculated by considering only the polarizabilities of the phenyl groups. This has been somewhat justified by using the polarizabilities for toluene rather than those for benzene. If the polarization anisotropy due to the C−C and C−H bonds in the chains are calculated using Denbigh's[7] values for bond polarizabilities, it is found that the presence of these atoms contributes a polarization anisotropy of $+0.6\times10^{-24}$ cm³/molecule. In view of the uncertainty of the bond polarizabilities and the smallness of this value, it was deemed reasonable to use the polarizabilities for toluene and neglect the other bonds.

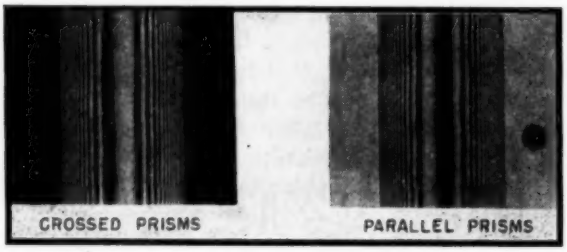

FIG. 6. Typical fringe patterns of oriented monofilaments observed with the polarizing microscope using crossed and parallel Nicol prisms.

[5] F. H. Müller, Kolloid-Z. **95**, 138 (1941).
[6] W. Kuhn and H. Kuhn, Helv. Chim. Acta **26**, 1394 (1943).

PART II. EXPERIMENTAL DETERMINATION OF BIREFRINGENCE

Birefringence of Oriented Monofilaments*

The most readily available linearly oriented polymers are the polystyrene monofilaments previously described by Cleereman.[8] In order to determine the orientation in these samples it is first necessary to have some accurate method for measuring their birefringence.

Typical fringe patterns observed between crossed and parallel Nicol prisms under a microscope using monochromatic light are shown in Fig. 6. The fringes obtained under crossed Nicol prisms represent relative retardations of integral multiples of the wavelength, while those obtained with parallel Nicols represent relative retardations of half-integral multiples of the wave length. From these photographs, however, it is impossible to determine the order of each fringe, i.e., it is impossible to exactly specify to which integral multiple each fringe corresponds. This is because it is not possible to resolve the fringes near the edge, and because the radial distribution of birefringence in the monofilament is not a constant. Thus some new method of examining these filaments is desirable that not only gives the location of the fringes, but will also unambiguously give the order of each fringe. It should then be possible to determine the radial distribution of birefringence for these monofilaments.

Figure 7 indicates the cross section of a monofilament of radius R. If the birefringence at any point r on the radius vector is given by the function $D(r)$, then the retardation through the element of vertical distance dz at the fixed point y is given by

$$d\Gamma_y=D(r)dz, \tag{25}$$

and the total retardation through the vertical path at the point y is thus

$$\Gamma_y=2\int_{z=0}^{z=(R^2-y^2)^{\frac{1}{2}}} D(r)dz. \tag{26}$$

If we eliminate z in favor of the variable r we arrive at

$$\Gamma_y=2\int_y^R (r^2-y^2)^{-\frac{1}{2}}D(r)rdr. \tag{27}$$

[7] K. G. Denbigh, Trans. Faraday Soc. **36**, 936 (1940).
[8] K. J. Cleereman, *et al.*, Modern Plastics **30**, 119 (1953).
* The manufacture of the monofilaments and the use of the microscope in these optical studies is discussed in the preceding paper by R. D. Andrews.

This is the basic expression for the retardation that would be observed looking down through a filament at a distance y from the center. From this equation it is possible to determine the fringe pattern from a given radial distribution of birefringence.

The reverse process, in which we are primarily interested, of finding $D(r)$ from a given fringe pattern cannot be carried out directly from Eq. (27). It would be possible to fit the fringe pattern by making various assumptions as to the form of $D(r)$; Bozza and Bonauguri[9] have discussed the case where the distribution function is assumed to be a power series. These indirect methods are somewhat laborious, and we will therefore discuss two new methods for determining the birefringence of these monofilaments.

Cone Method

Consider an oriented filament that has been cut cone shaped at one end as shown in Fig. 8. Let us first consider the birefringence to be uniform, i.e., $D(r)=K$,

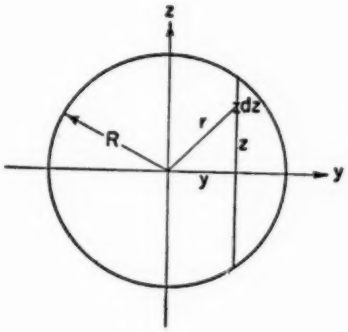

FIG. 7. Cross section of a monofilament showing the variables used in the mathematical development. The birefringence is a function of r only. The x axis is along the axis of the monofilament.

and determine the shape of the fringes in the xy plane. For any point (x,y) the thickness through the cone is equal to $2t$, where

$$t=(x^2\tan^2\theta-y^2)^{\frac{1}{2}},$$

and θ is one-half of the apex angle of the cone. For retardations corresponding to n-multiples of the wave length λ, the fringe pattern on the cone, can be expressed as

$$\frac{x^2}{(n\lambda/2K\tan\theta)^2}-\frac{y^2}{(n\lambda/2K)^2}=1. \tag{28}$$

Thus, the fringe pattern through a cone with uniform distribution of birefringence is a series of hyperbolas given by Eq. (28). These hyperbolas all have the same asymptote, namely, $y=\pm x\tan\theta$, which is the equation for the projection of the cone itself onto the xy plane.

If the birefringence through the original filament is not uniform but is given by the function $D(r)$, then the

[9] G. Bozza and E. Bonauguri, Kolloid-Z. **122**, 23 (1951).

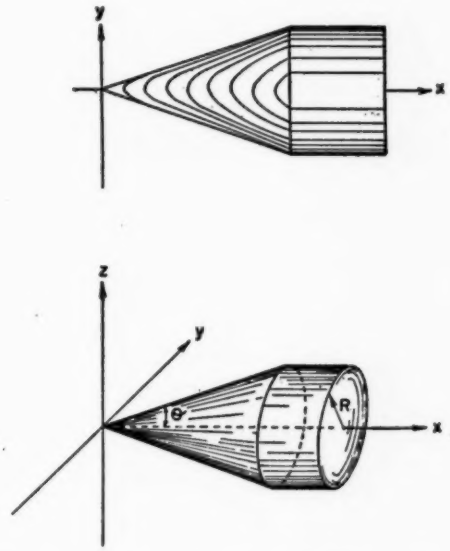

FIG. 8. Diagram of a cone on the end of a monofilament. The fringe pattern in the upper picture shows the hyperbolas formed in the case of uniform radial distribution of birefringence.

retardation at any point (x,y) on the cone is given by

$$\Gamma_{x,y}=2\int_y^{x\tan\theta}(r^2-y^2)^{-\frac{1}{2}}D(r)r\,dr. \tag{29}$$

Consider only those points for which $y=0$. Then

$$\Gamma_{x,0}=2\int_0^{x\tan\theta}D(r)\,dr, \tag{30}$$

and consequently

$$\frac{d\Gamma_{x,0}}{dx}=2\tan\theta\cdot D(x\tan\theta), \tag{31}$$

or

$$D(r)=\tfrac{1}{2}\cot\theta\frac{d\Gamma_{x,0}}{dx}. \tag{32}$$

The quantity $\Gamma_{x,0}$ is determined experimentally from the fringe pattern on the cone. From the derivative of this function with respect to x, i.e., the slope of the graph $\Gamma_{x,0}$ against x, the function D can be obtained by means of Eq. (32).

For the particular filaments on hand it was rather difficult to cut an accurate cone. Since the only points of interest are those along the central axis of the cone, Eq. (32) also applies to a "double wedge" with its apex at the center of the filament. This is also rather difficult to form but it immediately suggests simply cutting the monofilament at an angle and using a "single wedge."

Wedge Method

Consider a filament cut at an angle θ as shown in Fig. 9. For the case of uniform distribution of bire-

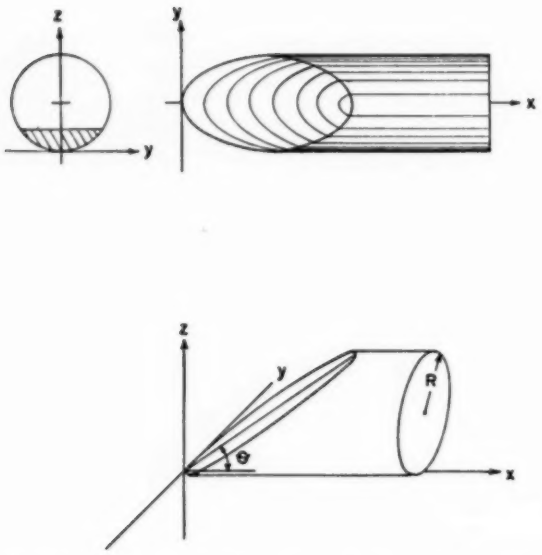

FIG. 9. Diagram of a wedge on the end of a monofilament. The fringe pattern in the upper picture shows the portions of the ellipses formed in the case of uniform radial distribution of birefringence.

fringence it is readily shown that the fringes have the shape of the projection of the surface of the wedge onto the xy plane and are equally spaced along the x axis. Since we only consider points within the wedge, the fringes obtained are only the portions of these equally spaced ellipses that are cut off by the wedge.

If the birefringence is not uniform, we have, in a manner similar to the derivation of Eq. (32),

$$D(z)=\cot\theta d\Gamma_{z,0}/dx. \tag{33}$$

Here we do not use the variable r since it becomes ambiguous; instead we use the variable z as shown in Fig. 9. Thus Eq. (33) maps out the birefringence across the diameter, while Eq. (32) gives the birefringence across a radius.

Experimental Examples

The wedge method described above will now be applied to two polystyrene monofilaments, designated Sample I and Sample II, with the diameters of 0.0504 and 0.1339 cm, respectively. In order to form an accurate wedge on the end of a filament, a hole the same size as the filament is drilled at some convenient angle through a brass block. The filament is held firmly in this hole while the end is scraped off with a razor blade until it is flush with the block. The wedge is then observed by mounting it in a small cell filled with KI-HgI_2-glycerine as an immersion liquid.

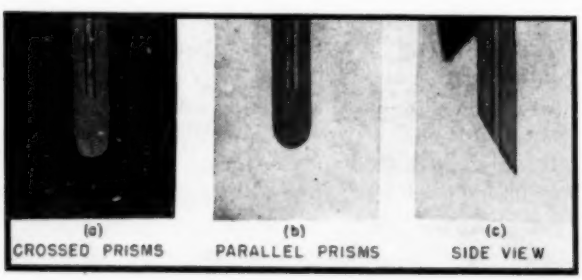

FIG. 10. Fringe pattern of a wedge on an oriented polystyrene monofilament (Sample I).

Figure 10 is a photograph of a wedge on Sample I taken through a polarizing microscope using monochromatic light (mercury green, 5461A). Figure 11 is a plot of the retardation against the distance x measured from the edge of the wedge and along the axis of the filament. The ordinate is expressed in multiples of the wavelength, and the abscissa is expressed in millimeters; the measurements were made on the negatives which represented a magnification of 31 times the actual filament dimensions. The slopes at various points of

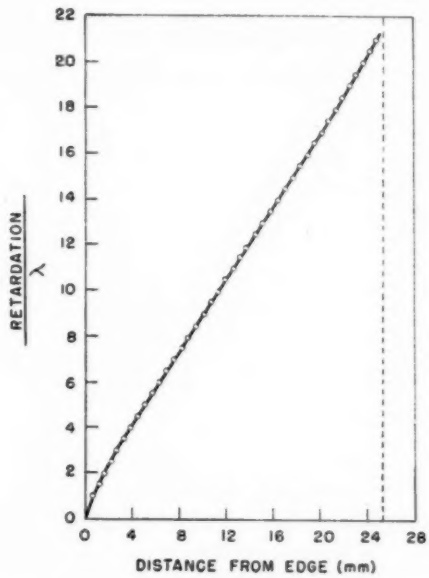

FIG. 11. Optical retardation through the filament as a function of the distance along the wedge (Sample I).

Fig. 11 are then measured, and by the application of Eq. (33) the distribution of birefringence across the diameter is calculated. These results are shown in Fig. 12 with the diameter of the filament referred to unity.

From Fig. 10 it can be seen that the wedge is flat over most of its length, but that there is some distortion near the ends. The birefringence near the edge is best determined by cutting a sharp nick in the filament with a razor blade and using this nick as a wedge. The three end points in Fig. 12 were actually obtained from such a nick rather than the wedge shown, and consequently the results shown are not in error due to the rounding at the edge of the wedge.

The foregoing procedure has been repeated with Sample II. The photographs of the wedge are shown in Fig. 13, Figure 13(d) is a composite picture made up of photographs taken through crossed and parallel prisms

at a higher magnification (98.57); this photograph gives better resolution of the fringes near the thin edge. The measured retardations, as determined from these photographs, are plotted in Fig. 14 and the calculated distribution of birefringence is shown in Fig. 15. As before the edge detail was determined from separate nicks cut in the side of the filament. Figure 16 shows two nicks for Sample II. It is interesting to note that the fringe pattern observed on the filament proper is quite different in these six views due to the fact that the filament is not perfectly round. In fact, the patterns are so complicated that it would be impossible to analyze them without using the wedge technique.

It is interesting to note that although the fringe patterns of these two samples are considerably different, the calculated distributions of birefringence have approximately the same qualitative shape.

Discussion

In determining the birefringence by the wedge or cone method it is not necessary to know the order of

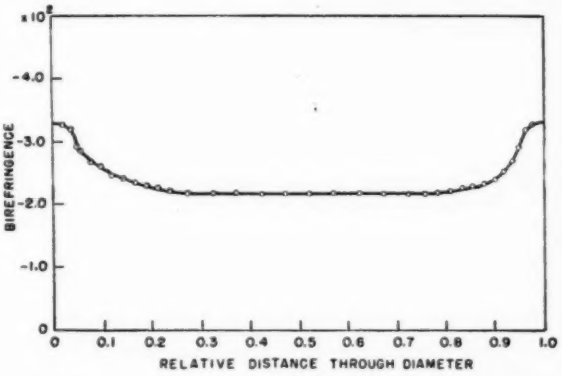

FIG. 12. The distribution of birefringence of Sample I.

the fringes; the only requirement is that the fringe order is continually increasing as the thickness through the wedge or cone increases. For a linearly oriented polymer this will always be true. It so happens that the absolute orders of the fringes are known, since it is always possible to cut the wedge at a sufficiently small angle to insure complete resolution of the fringes.

The sign of the birefringence, which is negative in the case of these linearly oriented polystyrene monofilaments, is readily determined by noting the direction of motion of the fringes on the wedge with the insertion of a suitably positioned quartz wedge, quarter-wave plate, or other compensator.[10] It should be noted that the determination of the sign of the birefringence by this method can lead to ambiguous results if applied to the filament proper rather than to the wedge. Thus, the central fringes on the two samples discussed in this report move in opposite directions under similar influ-

[10] E. Wahlstram, *Optical Crystallography* (John Wiley and Sons, Inc., New York, 1951).

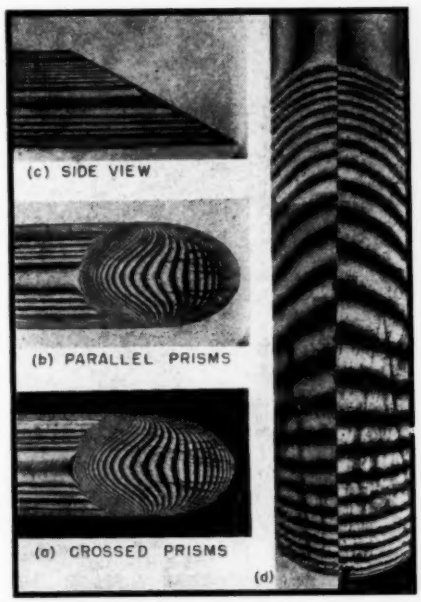

FIG. 13. Fringe pattern of a wedge on an oriented polystyrene monofilament (Sample II). Part (d) is a composite picture, taken at a higher magnification, of crossed and parallel views.

ences from a compensator. The fringes on the wedge, however, where the fringe order steadily increases, move in the same direction and thus clearly determine the sign.

Since the radial distribution function, $D(r)$ has been determined, it is possible to substitute this function into Eq. (27) and to calculate the fringe pattern that would

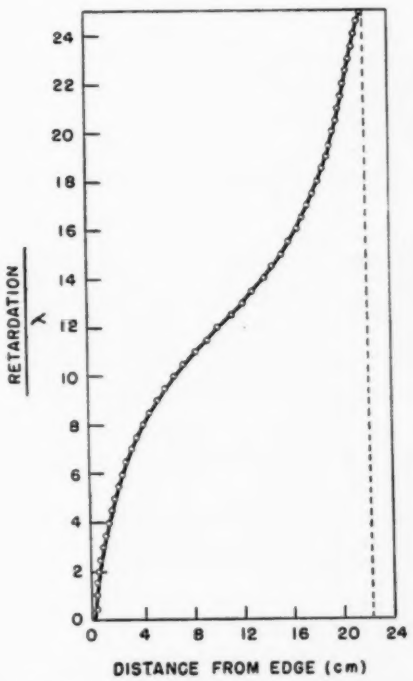

FIG. 14. Optical retardation through the filament as a function of the distance along the wedge (Sample II).

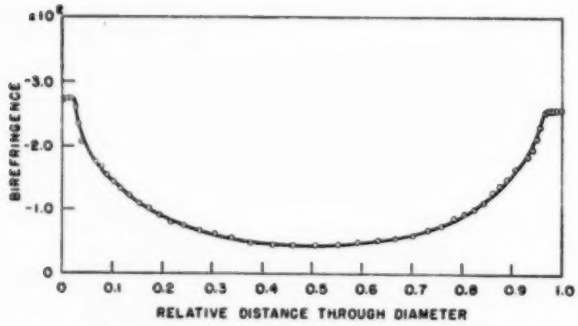

FIG. 15. The distribution of birefringence of Sample II.

be observed looking down through the filament.† This would be a rather tedious task except at the point $y=0$, i.e., the center of the filament. For this case, the radical in Eq. (27) disappears and the average value of the birefringence is readily obtained from the area under the distribution curve. This area was measured with a planimeter and the calculated value of the average birefringence was compared with the directly measured average value. The measured value is simply the retardation at the center, as determined from the fringe count on the wedge, divided by the diameter of the filament. The calculated and observed values of the average birefringence are listed in Table II for these two monofilaments and are found to be in good agreement.

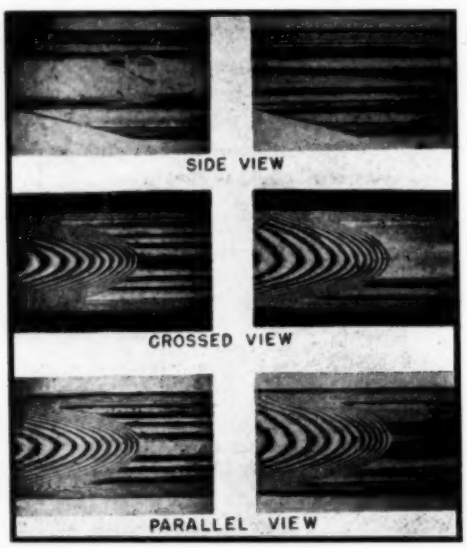

FIG. 16. Two nicks cut into the side of Sample II for analysis of edge detail. Note the widely varying fringe pattern on the filament proper.

† This calculation has now been carried out for the two monofilaments under consideration. The calculated fringe patterns are in good agreement with those observed.

CONCLUSION

In the first part of this paper we showed that 100 percent orientation in polystyrene corresponds to a birefringence of -0.3. The maximum value that was obtained with the two filaments studied was -0.03, which, from the random coil graph, corresponds to an orientation of about 36 percent. This seems to be a reasonable value in view of the amorphous nature of polystyrene. Treloar[11] obtained a maximum birefringence for rubber of about $\frac{1}{3}$ that of the theoretical maximum. It would be expected that crystalline polymers would approach their maximum birefringence values more readily than amorphous ones.

The wedge method could also be applied to small fibers. In this case, however, because of the small diameter, it would be necessary to use white light and interpret a series of polarization colors either by eye or with a compensator. In addition some difficulties might be encountered in cutting an accurate wedge on a small fiber.

TABLE II. Comparison between the observed and calculated values of the average birefringence.

	Sample I	Sample II
Calculated	-2.364×10^{-2}	-1.021×10^{-2}
Observed	-2.370×10^{-2}	-1.020×10^{-2}

Other techniques have been used to determine the birefringence of the "skin" and "core" of rayons. Preston and Narasimhan[12] have made use of the Becke immersion method and polarized light to determine the birefringence of the skin; they have determined the birefringence of the "core" with the aid of a fiber refractometer. Hermans[13] has used a "peeling-off" technique in which the change in refractive indices is measured as progressive layers are removed from the fiber chemically. It should be noted that rayon no longer has the cylindrical symmetry that simplifies the discussion of polystyrene monofilaments.

The wedge method has also proved useful in routine examination of monofilaments. A complete determination of the distribution of birefringence is not necessary, but the average birefringence is determined and a qualitative estimate of the uniformity is made by examining the curvature of the fringes on a wedge.

[11] L. R. G. Treloar, Trans. Faraday Soc. 43, 284 (1947).
[12] J. M. Preston and K. I. Narasimhan, J. Textile Inst. 40, T327 (1949).
[13] P. H. Hermans, Textile Research J. 20, 553 (1950).

Regular Contributed Original Research

Transformation of Scattering Cross Sections

P. F. Zweifel and H. Hurwitz, Jr.
Knolls Atomic Power Laboratory, Schenectady, New York*
(Received October 10, 1953)

A simple method is presented for the calculation of the transformation matrices between the Legendre polynomial expansion coefficients of the scattering cross section in the laboratory and center-of-mass systems. Approximate expressions for the matrices are given. Applications to transport problems involving the elastic scattering of neutrons are discussed.

I. THE GENERAL TRANSFORMATION

IN solving problems in transport theory, one often finds it desirable to expand the laboratory system scattering cross section in Legendre polynomials of the cosine of the scattering angle. For theoretical analysis of the cross section, however, it is usually more convenient to make the corresponding expansion in the center-of-mass system.[1] The calculation of the transformation matrix between the coefficients of the Legendre polynomials in the laboratory and center-of-mass systems is in principle straightforward. The following approach, however, enables one to obtain the matrix in a particularly simple manner.

Consider a particle of mass m_1 incident upon a particle of mass m_2, yielding reaction products of mass m_3 and m_4, with an energy release Q. Let E be the energy of the incident particle in the laboratory system. If $2\pi\sigma^c(\mu_c,E)d\mu_c$ is the cross section for the emission of m_3 into the solid angle $d\Omega_c=2\pi d\mu_c$ in the center-of-mass system, and if $2\pi\sigma^0(\mu_0,E)d\mu_0$ is the corresponding cross section in the laboratory system where μ_c and μ_0 are the cosines of the angle between the directions of m_1 and m_3 in the center-of-mass and laboratory systems, respectively, then

$$\sigma^0(\mu_0,E)=\sigma^c(\mu_c,E)\frac{d\mu_c}{d\mu_0}. \tag{1}$$

The quantities μ_0 and μ_c are related in the nonrelativistic limit by[2]

$$(1-\mu_c^2)^{\frac{1}{2}}/(\gamma+\mu_c)=(1-\mu_0^2)^{\frac{1}{2}}/\mu_0, \tag{2}$$

where

$$\gamma=\left(\frac{m_1m_3}{m_2m_4}\frac{E_c}{E_c+Q}\right)^{\frac{1}{2}}. \tag{3}$$

Here E_c is the initial kinetic energy in the center-of-mass system, and is related to E by

$$E_c=m_2E/(m_1+m_2). \tag{4}$$

In neutron transport problems involving elastic scattering (see Sec. II), $Q=0$, and no mass interchange occurs. Then γ is the ratio of the neutron mass to the mass of the scattering nucleus. (We shall consider the case $\gamma<1$, for which both μ_0 and μ_c go between -1 and 1. Most cases of physical interest correspond to $\gamma<1$.)

We expand $\sigma^c(\mu_c)$ and $\sigma^0(\mu_0)$ in the following form[3]

$$\sigma^c(\mu_c)=\sum_{L=0}^{\infty}\frac{2L+1}{4\pi}B_L{}^cP_L(\mu_c), \tag{5a}$$

$$\sigma^0(\mu_0)=\sum_{L=0}^{\infty}\frac{2L+1}{4\pi}B_L{}^0P_L(\mu_0), \tag{5b}$$

where the $B_L{}^c$ are, except for a factor $4\pi\lambda\!\!\!^{-2}$, equivalent to the B_L of reference 1. The $P_L(\mu)$ are the Legendre polynomials.

The total cross section σ is given by

$$\sigma=\int\sigma^c(\mu_c)d\Omega_c=\int\sigma^0(\mu_0)d\Omega_0=B_0{}^c=B_0{}^0. \tag{6}$$

Given the $B_L{}^c$, the $B_L{}^0$ may be obtained by making use of the orthogonality properties of the Legendre polynomials and Eq. (1):

$$B_L{}^0=2\pi\int d\mu_0P_L(\mu_0)\sigma^0(\mu_0)=2\pi\int d\mu_cP_L(\mu_0)\sigma^c(\mu_c)$$
$$=\sum_{L'=0}^{\infty}T_{LL'}B_{L'}{}^c, \tag{7}$$

with

$$T_{LL'}=\frac{2L'+1}{2}\int_{-1}^{1}P_L(\mu_0)P_{L'}(\mu_c)d\mu_c. \tag{8}$$

The inverse transformation is given by

$$B_L{}^c=\sum_{L'=0}^{\infty}T_{LL'}{}^{-1}B_{L'}{}^0, \tag{9}$$

* Operated for the U. S. Atomic Energy Commission by the General Electric Company under Contract No. W-31-109 Eng. 52.

[1] J. M. Blatt and L. C. Biedenharn, Revs. Modern Phys. 24, 258 (1952).

[2] L. Schiff, *Quantum Mechanics* (McGraw-Hill Book Company, Inc., New York, 1949).

[3] See reference 1. For convenience, the dependence on energy is not indicated explicitly here. Thus the B_L appearing in Eq. (5) are really functions of E.

with

$$T_{LL'}{}^{-1}=\frac{2L'+1}{2}\int_{-1}^{1}P_L(\mu_c)P_{L'}(\mu_0)d\mu_0. \quad (10)$$

The integrals appearing in the expressions for $T_{LL'}$ and $T_{LL'}{}^{-1}$ may be evaluated conveniently through the introduction of the variable U which represents the logarithm of the ratio of the energy which particle m_3 would have if it were ejected in the forward direction to the energy it has if it is ejected into the solid angle $d\Omega_c$. (The energies are measured in the laboratory system.) Then[4]

$$\mu_c(U)=1-\frac{(1+\gamma)^2}{2\gamma}(1-e^{-U}), \quad (11a)$$

$$\mu_0(U)=1/2\gamma[(1+\gamma)e^{-U/2}-(1-\gamma)e^{U/2}] \quad (11b)$$

$$0\leq U\leq\ln\left(\frac{1+\gamma}{1-\gamma}\right)^2.$$

Then

$$T_{LL'}=-\frac{2L'+1}{2}\int_0^{\ln[(1+\gamma/1-\gamma)]^2}P_L(\mu_0(U))\times P_{L'}(\mu_c(U))\frac{d\mu_c}{dU}dU, \quad (12a)$$

$$T_{LL'}{}^{-1}=-\frac{2L'+1}{2}\int_0^{\ln[(1+\gamma/1-\gamma)]^2}P_L(\mu_c(U))\times P_{L'}(\mu_0(U))\frac{d\mu_0}{dU}dU. \quad (12b)$$

The quantities $T_{LL'}$ and $T_{LL'}{}^{-1}$ thus reduce to the sum of integrals of exponential functions. One finds, for example,

$$T_{0L'}=\delta_{L'}{}^0 \quad T_{21}=\frac{9-6\gamma^2+9\gamma^4}{16\gamma^3}+\frac{9-9\gamma^2-9\gamma^4+9\gamma^6}{64\gamma^4}\times\ln\left(\frac{1-\gamma}{1+\gamma}\right)^2, \quad (13)$$

$$T_{10}=\tfrac{2}{3}\gamma \quad T_{20}=\frac{5\gamma^2-3}{8\gamma^2}-\frac{3-6\gamma^2+3\gamma^4}{32\gamma^3}\ln\left(\frac{1-\gamma}{1+\gamma}\right)^2,$$

$$T_{11}=\tfrac{1}{5}(5-3\gamma^2),$$

and

$$T_{0L'}{}^{-1}=\delta_{L'}{}^0,$$

$$T_{10}{}^{-1}=-\tfrac{2}{3}\gamma,$$

$$T_{11}{}^{-1}=\frac{3}{8\gamma^2}(1+\gamma^2)-\frac{3(1+\gamma)^2(1-\gamma)^2}{32\gamma^3}\ln\left(\frac{1+\gamma}{1-\gamma}\right)^2. \quad (14)$$

[4] Marshak, Brooks, and Hurwitz, Nucleonics **5**, No. 1, 53 (1948).

For small values of γ, $T_{LL'}$ and $T_{LL'}{}^{-1}$ may be represented by the following approximations, correct to terms of order γ:

$$T_{LL'}=\delta_{L'}{}^L-\gamma\left(\frac{L'(L'-1)}{2L'-1}\delta_{L'}{}^{L+1}-\frac{(L'+1)(L'+2)}{2L'+3}\delta_{L'}{}^{L-1}\right), \quad (15a)$$

$$T_{LL'}{}^{-1}=\delta_{L'}{}^L+\gamma\left(\frac{L'(L'-1)}{2L'-1}\delta_{L'}{}^{L+1}-\frac{(L'+1)(L'+2)}{2L'+3}\delta_{L'}{}^{L-1}\right). \quad (15b)$$

II. APPLICATION TO NEUTRON TRANSPORT PROBLEMS WITH ELASTIC SCATTERING

In neutron transport problems, it is often necessary to consider the change of neutron energy in a collision as well as the scattering angle. The Boltzmann equation for the energy-dependent, one-dimensional transport problem in an infinite medium has the form[5]

$$\mu\frac{dN(\mu,x,u)}{dx}+\sigma_T N(\mu,x,u)=\eta\int d\Omega_0'\int_{u-q}^{u}\sigma^0(\mu_0,u',U)N(\mu',x,u')du'+S(u,\mu). \quad (16)$$

Here $N(x,u,\mu)$ is the flux per unit logarithmic energy range and unit solid angle at the energy $E=E_0e^{-u}$, E_0 being some convenient reference energy; $S(u,\mu)$ is the source function, σ_T is the total cross section of the moderator, $q=\ln[(1+\gamma/1-\gamma)]^2$ is the maximum logarithmic energy loss in a collision while η represents the number of moderating atoms per unit volume. Because of the assumed plane symmetry, the flux depends only on the angle $\cos^{-1}\mu$ between the neutron direction vector and the x axis. The scattering angle, $\cos^{-1}\mu_0$, does, however, depend on the azimuthal angle between the neutron direction before and after scattering.

The quantity $\sigma(\mu_0,u',U)$ is the cross section for scattering of a neutron of energy $E_0e^{-u'}$ through the angle $\cos^{-1}\mu_0$ with a logarithmic energy reduction $U=u-u'$. Although μ_0 and U are uniquely related by the kinetics of the collision, it is convenient to consider the cross section to be a function of μ_0 and U as independent variables. This may be accomplished if one

[5] R. E. Marshak, Revs. Modern Phys. **19**, 185 (1947). Equation (16) is written for a single type of moderating nucleus. If more than one type is present, the integral in Eq. (16) must be summed over all types.

writes[4]

$$\sigma^0(\mu_0,u',U)d\Omega_0 du=\sigma^0(\mu_0,u')\delta(\mu_0(U)-\mu_0)\times\left(-\frac{d\mu_0(U)}{dU}\right)du d\Omega_0, \quad (17)$$

where $\mu_0(U)$ is given by Eq. (11b).

Then

$$\sigma^0(\mu_0,u')=\int_0^{\ln[(1+\gamma/1-\gamma)]^2}\sigma^0(u',\mu_0,U)dU. \quad (18)$$

Furthermore, the integral over solid angle in Eq. (16) may be conveniently carried out if both N and σ are expanded in a series of Legendre polynomials.[5] Letting

$$\sigma^0(\mu_0,u',U)=\sum_{L=0}^{\infty}\frac{2L+1}{4\pi}B_L{}^0(u',U)P_L(\mu_0), \quad (19)$$

and

$$N(\mu,x,u)=\sum_{L=0}^{\infty}\frac{2L+1}{4\pi}N_L(x,u)P_L(\mu), \quad (20)$$

one obtains by means of the spherical harmonics addition theorem[4]

$$\int d\Omega_0'\int_{u-q}^{u}\sigma^0(\mu_0,u',U)N(\mu',x,u')du'=\sum_{L=0}^{\infty}\frac{2L+1}{4\pi}J_L(x,u)P_L(\mu), \quad (21)$$

where

$$J_L(x,u)=\int_{u-q}^{u}N_L(x,u')B_L{}^0(u',U)du'. \quad (22)$$

From Eqs. (17) and (19)

$$B_L{}^0(u',U)=2\pi\int P_L(\mu_0)\sigma^0(\mu_0,u',U)d\mu_0=2\pi\sigma^0(\mu_0(U))P_L(\mu_0(U))\left(-\frac{d\mu_0(U)}{dU}\right), \quad (23)$$

or from Eq. (1) and Eq. (5a)

$$B_L{}^0(u',U)=\sum_{L'=0}^{\infty}T_{LL'}(U)B_{L'}{}^c(u'), \quad (24)$$

with

$$T_{LL'}(U)=\frac{2L'+1}{2}P_L(\mu_0(U))\times P_{L'}(\mu_c(U))\left(-\frac{d\mu_c(U)}{dU}\right). \quad (25)$$

[Here $\mu_0(U)$ and $\mu_c(U)$ are given by Eqs. (11a) and (11b).]

Note that the $T_{LL'}$ defined in Sec. I are related to the $T_{LL'}(U)$ by

$$T_{LL'}=\int_0^{\ln[(1+\gamma/1-\gamma)]^2}T_{LL'}(U)dU. \quad (26)$$

We thus have for the integral term[6]

$$J_L(u)=\sum_{L'}\int_{u-\ln[(1+\gamma/1-\gamma)]^2}^{u}N_L(x,u')\times T_{LL'}(U)B_{L'}{}^c(u')du', \quad (27)$$

$$u-u'=U.$$

For the special case in which the scattering is spherically symmetric in the center-of-mass system (S-wave scattering) we have $B_{L'}{}^c=0$ for $L'>0$, so that

$$B_L{}^0(u',U)=T_{L0}(U)B_0{}^c(u')=T_{L0}(U)\sigma_S(u'). \quad (28)$$

Thus, from Eqs. (25) and (11b),

$$B_L{}^0(u',U)=\frac{(1+\gamma)^2}{4\gamma}e^{-U}P_L\left(\frac{1}{2\gamma}[(1+\gamma)e^{-U/2}-(1-\gamma)e^{+U/2}]\right)\sigma_S(u')=f_L(u-u')\sigma_S(u'), \quad (29)$$

which are the well-known expansion coefficients of the slowing-down kernel which appear in problems of neutron transport involving isotropic center of mass scattering.[4] This makes it clear that the use of Eq. (24) rather than the more usual (28) to describe $B_L{}^0(u',U)$ takes into account the anisotropic center-of-mass scattering.

In solving the Boltzmann equation, a frequently used procedure for approximating the integral term is to expand the product $\sigma_S(u')N_L(u')$ in a Taylor's series about the point $u'=u$. Proceeding in this manner we expand the product $N_L(u')B_L{}^c(u')$, obtaining

$$J_L(u)=\eta\sum_{L'=0}^{\infty}\sum_{n=0}^{\infty}\frac{(-)^n}{n!}\frac{\partial^n}{\partial u^n}(N_L(u)B_{L'}{}^c(u'))\times\int_0^{\ln[(1+\gamma/1-\gamma)]^2}U^nT_{LL'}(U)dU \quad (30)$$

$$=\eta\sum_{L',n=0}^{\infty}T_{LL'}{}^n\frac{\partial^n}{\partial u^n}(N_L(u)B_{L'}{}^c(u)), \quad (31)$$

where

$$T_{LL'}{}^n=\frac{(-)^n}{n!}\int_0^{\ln[(1+\gamma/1-\gamma)]^2}U^nT_{LL'}(U)dU. \quad (32)$$

[6] Note that although $B_{L'}{}^c(u')$ refers to the expansion of the scattering in the center-of-mass system, u' is defined in terms of the incident neutron energy in the laboratory system.

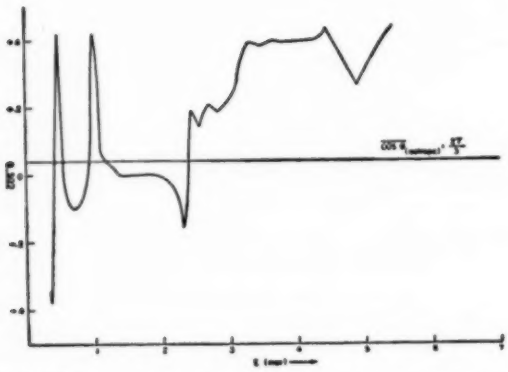

FIG. 1. The average value of the laboratory system scattering angle of neutrons on oxygen as a function of incident neutron energy.

In many problems it is sufficient to retain only the $n=0$ and 1 terms in (31). Note that the $T_{LL'}{}^0$ are identical with the $T_{LL'}$ discussed in Sec. I, while the $T_{LL'}{}^1$ are related to the average logarithmic energy change $\bar{U}$ suffered by the neutron in making a collision.

To clarify this, we note that for isotropic scattering in the center-of-mass system, one has[5]

$$\eta^{-1}J_0=N_0(u)\sigma_S(u)-\xi\frac{\partial}{\partial u}(N_0(u)\sigma_S(u))+\cdots, \quad (33)$$

$$\eta^{-1}J_1=N_1(u)\sigma_S(u)\langle\cos\theta\rangle_{Av}+\cdots, \quad (34)$$

while for nonisotropic scattering

$$\eta^{-1}J_0=N_0(u)\Sigma_{L'}B_{L'}{}^cT_{0L'}{}^0+\frac{\partial}{\partial u}(N_0(u)\Sigma_{L'}B_{L'}{}^cT_{0L'}{}^1)+\cdots, \quad (35)$$

$$\eta^{-1}J_1=N_1(u)\Sigma_{L'}B_{L'}{}^cT_{1L'}{}^0+\cdots. \quad (36)$$

Thus,

$$\sigma_S=\Sigma_{L'}B_{L'}{}^cT_{0L'}{}^0=B_0{}^c, \quad (37)$$

$$\xi\sigma_S=-\Sigma_{L'}B_{L'}{}^cT_{0L'}{}^1, \quad (38)$$

$$\langle\cos\theta\rangle_{Av}\sigma_S=\Sigma_{L'}B_{L'}{}^cT_{1L'}{}^0. \quad (39)$$

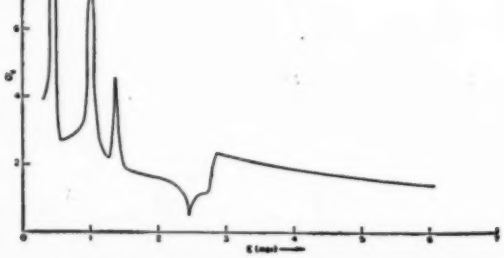

FIG. 2. Scattering cross section of oxygen as a function of energy. The value of the cross section was taken from reference 7.

Explicit expressions for the $T_{0L'}{}^1$ are

$$T_{00}{}^1=-\xi=-\left(1-\frac{(1+\gamma)^2}{2\gamma}\ln\frac{1+\gamma}{1-\gamma}\right)\to-2\gamma \quad \text{for } \gamma \text{ small}, \quad (40)$$

$$T_{01}{}^1=\frac{3+3\gamma^2}{4\gamma}-\frac{3-6\gamma^2+3\gamma^4}{16\gamma^2}\ln\frac{1+\gamma}{1-\gamma}\to2\gamma \quad \text{for } \gamma \text{ small}, \quad (41)$$

where $T_{0L}{}^1$ for $L>1$ vanishes to order γ.

Since from Eq. (11b)

$$U=2\gamma\left[1-\mu_0+\frac{\gamma^2}{2}(1-\mu_0)^2+\cdots\right],$$

we have

$$\xi\cong\bar{U}=2\gamma\left[1-\langle\cos\theta\rangle_{Av}+\frac{\gamma^2}{2}\langle(1-\cos\theta)^2\rangle_{Av}+\cdots\right]. \quad (42)$$

Thus to one order in γ

$$-T_{0L}{}^1=2\gamma(T_{0L}{}^0-T_{1L}{}^0)=2\gamma(T_{0L}-T_{1L}).$$

In Fig. 1 $\langle\cos\theta\rangle_{Av}$ for oxygen as obtained from Eq. (39) divided by Eq. (37) is plotted as a function of energy. The total scattering cross section σ is plotted in Fig. 2. Values of $B_{L'}{}^c$ were furnished by Goldstein[7] who extrapolated the results of Baldinger *et al.*[8] The value $2\gamma/3$ which would correspond to isotropic scattering in the center of mass system is also indicated. The average logarithmic energy change ξ, as obtained by dividing Eq. (38) by (37) is for practical purposes equal to $2\gamma(1-\langle\cos\theta\rangle_{Av})$. Numerical calculations on the spatial distribution of neutrons slowing down in water are in progress for the purpose of evaluating the effect of anisotropic oxygen scattering. The method being used for solving the Boltzmann equation and the numerical results will be discussed in a subsequent paper.

An alternative approach to the evaluation of the J_L must be used if the $B_L{}^0$ are known rather than the $B_L{}^c$. Then, from Eqs. (22) and (23)

$$J_L(u)=\eta\int_{u-\ln[(1+\gamma/1-\gamma)]^2}^{u}N_L(u')2\pi\sigma^0(\mu_0(U))\times P_L(\mu_0(U))\left(-\frac{d\mu_0(U)}{dU}\right)du' \quad (43)$$

$$=-\eta\sum_{L'=0}^{\infty}\frac{2L'+1}{2}\int N_L(u')B_{L'}{}^0P_{L'}(\mu_0(U))\times P_L(\mu_0(U))\frac{d\mu_0(U)}{dU}du' \quad (44)$$

$$=\eta\sum_{n,L'=0}^{\infty}\frac{\partial^n}{\partial u^n}(N_L(u)B_{L'}{}^0)S_{LL'}{}^n, \quad (45)$$

[7] H. Goldstein, Nuclear Development Associates, Inc., Memo 15C-15.

[8] Baldinger, Huber, and Proctor, Helv. Phys. Acta **25**, 142 (1952).

where

$$S_{LL'}{}^{n}=\frac{(-)^n}{n!}\frac{2L'+1}{2}\int_0^{\ln[(1+\gamma/1-\gamma)]^2} U^n P_{L'}(\mu_0(U)) \times P_L(\mu_0(U))\frac{d\mu_0(U)}{dU}dU. \quad (46)$$

Therefore,

$$S_{LL'}{}^{0}=\delta_{L'}{}^{L}, \quad (47)$$

and, for small γ

$$S_{LL'}{}^{1}=-2\gamma\left[\delta_{L'}{}^{L}-\frac{L'+1}{2L'+1}\delta_{L'}{}^{L-1}-\frac{L'}{2L'+1}\delta_{L'}{}^{L+1}.\right] \quad (48)$$

JOURNAL OF APPLIED PHYSICS VOLUME 25, NUMBER 10 OCTOBER, 1954

Spurious Areas in Pole Figures

A. H. GEISLER
General Electric Research Laboratory, Schenectady, New York
(Received October 3, 1953)

Spurious maxima are frequently observed in pole figures determined by x-ray diffraction techniques employing the Geiger-counter spectrogoniometer. Their origin must be fully understood in order to avoid misleading interpretations of the pole-figure data. By making film patterns and by the balanced filter technique—in each case with the specimen oriented for the appearance of one of the spurious peaks—these spurious maxima can be identified as diffraction of a component from the white radiation by a strongly diffracting (hkl) plane, and at a 2θ angle corresponding to K_α diffraction from the (hkl) plane under investigation. Spurious (110) and (112) peaks of this type may be observed in the (200) pole figure of iron and its alloys; spurious (111) and (220) peaks may appear in the (200) pole figure of face-centered-cubic metals such as nickel. These cannot be completely suppressed by filtering the Mo radiation used or by modifying the operating conditions such as tube voltage, spectrometer resolution, or counter type. Spurious $(10\bar{1}1)$ peaks may appear in the (0002) pole figure of titanium and zirconium as the result of CuK_α diffraction, and they can be avoided by increasing the resolution of the slit system.

THE advantages of the x-ray diffraction spectrogoniometer technique over the older film techniques for determining the preferred orientations of polycrystalline materials have become well recognized during the last five years. The individual limitations of several variations of the spectrogoniometer technique have been summarized in a recent review.[1] On the other hand there appears to be an important characteristic that must be considered in any application of the spectrogoniometer for pole figure determination, but it has not been described in detail in previous literature. The characteristic manifests itself as unexpected maxima in pole figures. Their origin must be fully understood in order to avoid misleading interpretations of the pole figure data. Consequently, all users of the Geiger counter spectrogoniometer technique must be made aware of the phenomenon, and furthering this awareness is the main purpose of this paper.

Spurious maxima were first recognized in pole figures for samples of a cold-rolled iron alloy. The well-known texture can be described as [110] in the rolling direction with rotation about the rolling direction from (100) to (111) parallel to the rolling plane. Such a texture accounts for the maxima that extend at an angle of 45° to the rolling direction in each quadrant of the pole figure for the (200) planes as in Fig. 1a. In addition, the spectrogoniometer method revealed an unexpected maximum in the rolling direction for the (200) pole figure shown as the intermediately located peak in Fig. 1a and 1b. If this peak were truly a (200) reflection it would suggest a new component for the cold-rolling texture which would be identified as [100] in the rolling direction. Since no such component had been reported in previous determinations of the texture by means of film techniques, the validity of the peak was suspected. It is noteworthy that an intense maximum also occurs in the rolling direction for the (110) pole figure as in Fig. 2.

The source of the spurious peak was identified by making a pinhole pattern on film which is reproduced in Fig. 3. It was found that the spurious maximum represented not a (200) reflection but a (110) reflection for a component of the white radiation which is diffracted at $2\theta=28.75°$, the Bragg angle for MoK_α diffraction from (200) planes. The white radiation tail for the (110) reflection apparent in Fig. 3 extends out to the angle for the (200) MoK_α reflection so that the spectrogoniometer detector picks up the (110) reflection of the wavelength $(2)^{\frac{1}{2}}\lambda_{MoK_\alpha}$ or 1.00A at the same 2θ setting as the (200) reflection of λ_{MoK_α}. The high inherent intensity for the (110) reflection apparently compensates for the low intensity of the white radiation at the $\lambda=1.00$A wavelength to produce a diffraction peak comparable to that for the MoK_α reflection from the less strongly diffracting (200) planes as evident in

[1] A. H. Geisler, "Crystal Orientation and Pole Figure Determination," *Modern Research Techniques in Physical Metallurgy* (American Society for Metals, Cleveland, 1953), pp. 131–153.

FIG. 1a. Pole figure for reflections at $2\theta = 28.75°$ corresponding to (200) MoK_α for a cold rolled Fe-35 percent Co alloy.

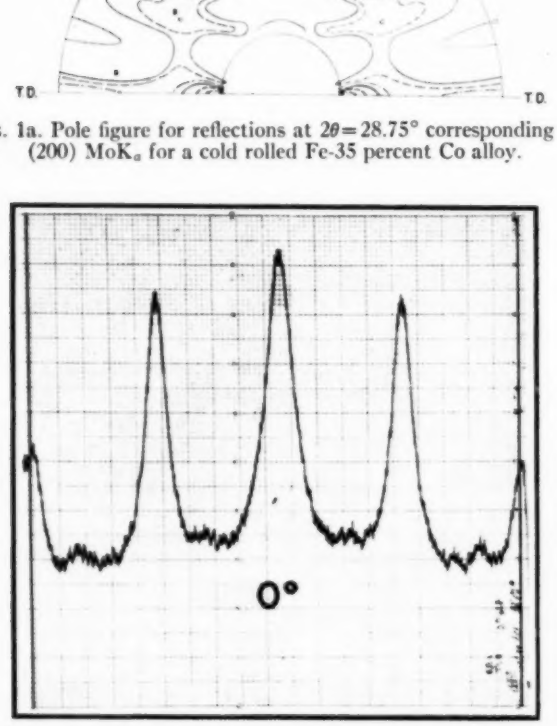

FIG. 1b. Intensity (vertical) trace for $2\theta = 28.75°$ with varying β angle (horizontal) about axis normal to rolled surface and with tilt angle $a = 0°$.

Fig. 1b. The distribution of intensity *versus* wavelength in Fig. 4 made by scanning through 2θ with the specimen oriented for the (110) planes that are normal to the rolling direction, shows that with a zirconium filter an intensity of 200 counts per second appears at $\lambda = 1.00$A. This intensity is about the same as the intensity for the (200) MoK_α reflection at $2\theta = 28.75°$. An intensity of 200 counts per second corresponds to about 4 times that for the (200) reflection from a sample with randomly oriented crystallites.

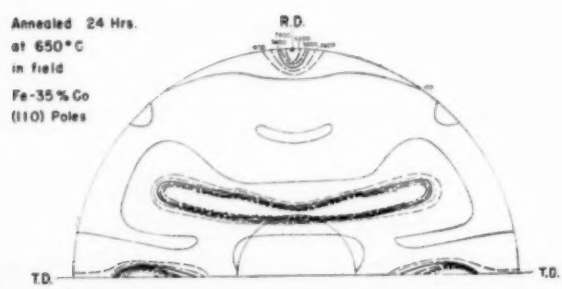

FIG. 2. Pole figure for (110) reflections at $2\theta = 19.75°$ for the cold rolled Fe-35 percent Co alloy. Intense areas agree in location with spurious areas marked "B" in Fig. 1.

Several other examples of spurious areas in pole figures determined by spectrogoniometer techniques have been encountered. Examination of Fig. 5 shows that inconsistent areas for the (200) pole figure of a cube texture could be attributed to spurious (111) and (220) reflections of the appropriate components of the white radiation. The pinhole pattern in Fig. 6 lends support to this interpretation. Results for both cold rolled and annealed samples of titanium have also been observed containing inconsistent areas which could be attributed to spurious $(10\bar{1}1)$ poles in the (0002) pole figure. In these cases, the source of the spurious areas was somewhat different from those in Figs. 1a and 5, and will be discussed later.

A detailed study has been made for texture analyses of cold rolled iron-base alloys. Attempts have been made to remove the spurious (110) reflection at $\lambda = 1.00$A by filtering with materials that are characterized by a large slope in the absorption *versus* wavelength curve in the region 0.7 to 1.0A. Since a large

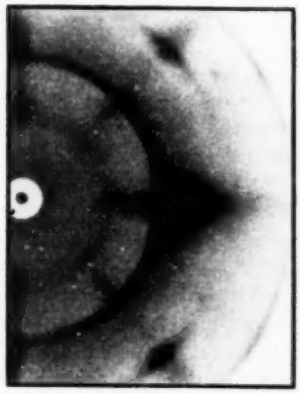

FIG. 3. Pinhole pattern produced by Mo radiation and the cold rolled Fe-35 percent Co alloy with the rolling surface tilted $14\frac{1}{2}°$ to the beam. White radiation streak on equator from (110) planes extends into region for (200) MoK_α reflection shown 45° above and below equator.

slope generally is found at wavelengths slightly below the absorption edge, materials such as copper, zinc, and germanium which have absorption edges at wavelengths somewhat higher than 1.00A were examined. Also included were zirconium, palladium and aluminum which exhibit a pronounced increase in absorption coefficient in the range of 1.00A between the wavelength of MoK_α (0.71A) and CuK_α (1.54A). Evaluations were made in two ways: 1) by determining the relative height of the spurious peak on a β trace such as Fig. 1b, and 2) by determining the relative spread of wavelength distribution for the (110) peak such as in Fig. 4. The data were obtained using a cold rolled iron-base alloy with aluminum. For the first type of evaluation the spectrogoniometer was set at $2\theta = 28.75$ (Bragg angle for the MoK_α reflection from {200}) and a 180° β trace was made for $a = 0°$.

Data for various filters are listed in Table I where the second column refers to the ratio of the absorption coefficients at 1.00A and 0.71A for the various metals which were used for filtering. The maximum intensities

for the (200) and spurious (110) peaks taken from the chart trace are listed in the third and fourth columns, while the fifth column entitled "Background" is the intensity at the lowest position on the trace. The effectiveness of the filters in removing the spurious (110) peak is indicated by the ratio of intensities I_{110}/I_{200} in the sixth column, whereas the ability of the filters to suppress the background of secondary and non-Bragg radiation is indicated by the intensity ratio in the last column. The zirconium filter alone or in combination is most effective in keeping the background down to 20 percent; palladium permits a background to 25 to 30 percent; aluminum about 35 percent; and materials which fluoresce such as copper, zinc and germanium give a high background of 60 percent of the (200) peak intensity. It was not possible to reduce the spurious peak to below 40 percent of the (200) peak. The best filter appeared to be that of palladium which reduced the spurious peak from 129 percent of the (200) peak for the usual zirconium filter to 74 percent without excessively raising the background and with some slight gain in (200) peak intensity. This behavior confirms that predicted from the ratio of the absorption coefficients in the second column where zirconium possesses the lowest ratio and palladium the highest.

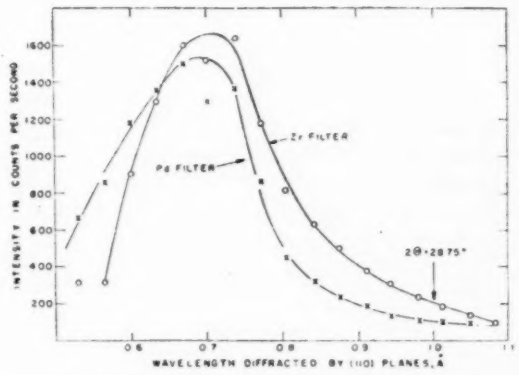

FIG. 4. Variation of intensity with wavelength diffracted from (110) planes normal to the rolling direction of a cold rolled Fe-Al alloy recorded by scanning 2θ with a tilt angle $a=0°$.

For the second type of evaluation the sample was oriented for a strong (110) peak and the intensity distribution was determined by scanning through the reflection angle, 2θ. The intensities at the K_a wavelength and at 1A, where the spurious (110) peak originates, were measured. With a zirconium filter the intensity of the (110) reflection diffracted at the same angle as the (200) MoK_a reflection (29°) was 14 percent of the (110) MoK_a peak, whereas with the palladium filter, it was 7 percent. The twofold difference is apparent in Fig. 4 where the full distribution curves have been plotted. Some of the other types of filters appear to be promising on the basis of the data, but have the disadvantages of producing high background or low (200) peak intensity mentioned in regard to Table I.

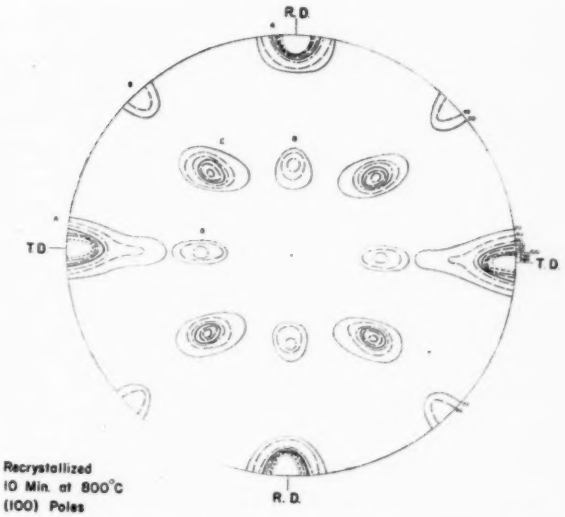

FIG. 5. Pole figures for reflections at $2\theta=24°$ corresponding to (200) MoK_a for an annealed sample of a Ni-Fe alloy. "A" represents (200) poles whereas "B" and "C" are spurious (220) and (111) poles, respectively.

Spurious peaks that originate from white radiation may also be identified and modified by manipulating other factors in addition to selective filtering of the responsible white component. For example, increasing the potential applied to the x-ray tube will increase the intensity of the shorter wavelengths in the well-known fashion. Results in the first two rows of Table II show that the spurious (110) area has a peak intensity about $2\frac{1}{2}$ times that of the real (200) areas when the molybdenum tube was operated at 40 kv, while the ratio is $1\frac{1}{2}$ at 50 kv. Spurious white radiation peaks could be identified by their presence in traces made using a filter that removes the characteristic component of the radiation. For example, when a SrO_2 filter was used with Mo radiation, the real (200) peak was suppressed to near background level with the result that the intensity ratio increased to about $3\frac{1}{2}$ according to the third row of Table II. Likewise, the use of the SrO_2 filter removed the (200) peaks for the nickel-iron alloy and left the spurious one (B and C in Fig. 5) relatively un-

FIG. 6. Pinhole pattern produced by Cu radiation and the annealed sample of a Ni-Fe alloy. Sample tilted 47° about an axis 45° to rolling direction. No (200) MoK_a reflections are observed, whereas the equatorial white radiation streak for (111) planes causes the spurious areas of the "C" type in Fig. 5, and the (220) streaks at 45° to the equator cause the central areas of the "B" type.

TABLE I. Effect of filtering on appearance of (110) component in (200) $a=0°$ trace at $2\theta=28.75°$.[a]

Filters	$\frac{\mu_{1A}}{\mu_{0.7A}}$	Intensity in counts/second At $\beta=45°$ (200)	At $\beta=90°$ (110)	Bkg	I_{110}/I_{200}	I_{Bkg}/I_{200}
0.002″ Zr	1.80	182	235	38	1.29	0.21
Zr+0.0035″ Al		162	167	34	1.03	0.21
Zr+0.007″ Al		142	135	28	0.95	0.20
Zr+0.0105″ Al		124	97	26	0.78	0.21
Zr+0.015″ Al		107	76	20	0.71	0.19
0.015″ Al	2.46	199	248	67	1.24	0.34
0.040″ Al		84	72	30	0.86	0.36
0.0015″ Pd	2.63	198	146	50	0.74	0.25
Pd+0.015″ Al		76	62	25	0.81	0.33
Ge powder	2.13	55	59	33	1.06	0.60
0.0015″ Cu	2.21	345	330	216	0.96	0.63
Cu+Zr		78	34	16	0.43	0.21
Cu+Pd		50	36	16	0.72	0.32
0.0015″ Zn	2.22	462	445	272	0.97	0.59

[a] Set for (200) MoK_a reflection using 3° source slit and no detector slit.

changed. A quantitative separation of the real and spurious white radiation peaks could be obtained using the balanced filter technique. When a set of traces is made using a zirconium filter and second set is made using a well-balanced SrO_2 filter, subtraction of the two will give the intensity distribution for diffraction of the wavelengths between the two absorption edges (between 0.69 and 0.77A). Areas of the pole figure plotted for the difference would be devoid of any spurious peaks caused by white radiation.

Another factor which will influence the apparent intensity of spurious areas caused by white radiation is the sensitivity of the Geiger counter as a function of wavelength. Most of the work reported here was conducted using the standard aluminum multiple-chamber tube which is argon filled. It is well known that the efficiency of the argon tube decreases rapidly at wavelengths below 1A. The decreasing sensitivity with decreasing wavelength is apparent from the fourth row of data in Table II. For silver radiation ($\lambda=0.56$A), the spurious (110) peak is about $4\frac{1}{2}$ times as intense as the (200) K_a peak which represents a loss in sensitivity for detection of the real peak by a factor of about three when compared with the results for Mo radiation. Since Mo is the most appropriate choice of radiation for analyzing iron-base alloys in contrast to other, longer wavelength radiations such as copper or cobalt, improvement in detection sensitivity must be sought by means of other types of counters. Krypton-filled counters are generally recommended for use with Mo radiation, for they are expected to be about twice as efficient in detecting MoK_a radiation as the argon-filled counter. Results in the last row of Table II verify this performance, for comparison with the data in the second row shows that about twice the intensity was observed for the (200) K_a peak while the ratio to spurious (110) intensity was halved when the krypton-filled counter was used.

Since the XRD-3 spectrogoniometer is being used under conditions of poor resolution with a 3° source slit and no detector slit, attempts were made to eliminate the spurious (110) peak by improving the resolution with the results given in Table III. The spectrogoniometer was set at 28.75° for the (200) MoK_a peak (except for the second test), and 180° β traces were made for $a=0°$. For the second test, 2θ was increased to an angle greater than 28.75° to lower the (110) intensity along the tail of the curve shown on the right-hand side of Fig. 4. The ratio of the intensity of the (110) to (200) reflection decreased in the expected manner but some of the (200) peak intensity was sacrificed. The spurious (110) peak intensity could be lowered from 129 percent of the (200) intensity to 40 percent by using a 1° source slit and 0.2° detector slit with a reduction of the back ground to 10 percent, but with a 9-fold sacrifice in the (200) peak intensity. Intermediate reductions might be practical when working with a material that has a very pronounced texture. It should be noted that when the filter is omitted the background increases to 60 percent or more of the (200) peak intensity.

The second source of spurious areas in pole figures could be avoided more easily than the previously-described ones that depended on white radiation. On the basis of inconsistent relationships between pole figures for $(10\bar{1}0)$ and (0002) planes for rolled sheet of the metals titanium and zirconium, spurious areas were identified in the analyses of samples employing filtered copper radiation. For example, spurious $(10\bar{1}1)$ peaks extended to an intensity of 32 times that for randomly oriented crystallites in the (0002) pole figure of a cold rolled titanium sample. Since the peaks were removed when a cobalt filter was used to remove the CuK_a wavelength, they must have been caused by radiation at or near the K_a wavelength in contrast to a more remote component of the white radiation for the iron and nickel alloys previously discussed. Verification was obtained by improving the resolution used in the spectrometer. The spurious $(10\bar{1}1)$ peaks observed using a 3° source slit were removed to leave only the true (0002) peaks by substituting a 1° source slit. The 2θ angles for (0002) and $(10\bar{1}1)$ differ by only 2°, and apparently both reflections are detected when the 3° source slit and nonfocusing geometry of the transmission-type specimens are used. Of the three reflections, $(10\bar{1}0)$, (0002), and $(10\bar{1}1)$, the $(10\bar{1}0)$ reflections

TABLE II. Effect of other variables on appearance of (110). Component in $a=0°$ trace for 2θ set for (200).

Radiation	Filter	Applied potential	Counter type	I_{200}	Intensity ratios I_{110}/I_{200}	I_{Bkg}/I_{200}
Mo	Zr	40 kv	Std. A	65	2.41	0.41
Mo	Zr	50 kv	Std. A	113	1.51	0.30
Mo	Sr	50 kv	Std. A	40	3.43	0.77
Ag	Pd	50 kv	Std. A	155	4.67	0.42
Mo	Zr	50 kv	Kr	240	0.81	0.24

would be expected to be the most reliable for analyses of the textures of zirconium and titanium, since they are 3° to 4° removed from the nearest neighboring reflection, (0002). The $(10\bar{1}1)$ and (0002) reflections are only $1\frac{1}{2}°$ to 2° apart in 2θ and have been observed to interfere with each other during analysis of samples in various conditions. On the other hand, unaccountable features of the $(10\bar{1}0)$ pole figures also must be regarded with suspicion, for recent work has revealed that areas in the transverse direction of published pole figures for zirconium[2] are spurious (0002) K_α reflections.

From the previously described results, it is evident that, while the intensity of the (110) spurious peak in (200) pole figures of iron alloys can be modified by filtering and by changing operating conditions such as tube voltage, slit size, and counter type, it has not been successfully removed. The surest way to avoid spurious peaks of this type would be to use monochromatic radiation, but a large sacrifice in intensity would have to be accepted. In lieu of a monochromated beam, the balanced filter technique could be used. Neither of these methods would suffice when the spurious areas were due to nearby K_α reflections, as in titanium and zirconium. In this case, the use of better resolution or a reflection more remote from its neighbors would help avoid spurious areas. In the case of iron alloys, appreciable improvement would be provided by using the very strong (110) reflection to determine the pole figures for the spurious (200) and (112) peaks which have been observed for single crystals represent less than $\frac{1}{2}$ percent of the intensity of the (110) peak.[3]

[2] Keeler, Hibbard, and Decker, Trans. Am. Inst. Met. Mining Engrs. **197**, 932–936 (1953).

[3] C. G. Dunn, General Electric Company, Pittsfield, Massachussetts (private communication).

TABLE III. Effect of beam definition on appearance of (110) component at $\beta=90°$ in (200) $\alpha=0°$ trace at $2\theta=28.75°$.[a]

Filter	2θ	Source slit	Detector slit	Intensity in counts/second (200)	(110)	Bkg	I_{110}/I_{200}	I_{Bkg}/I_{200}
Zr	28.75°	3°	none	182	235	38	1.29	0.21
Zr	30°	3°	none	152	152	41	1.00	0.27
Zr	28.75°	3°	0.2°	41	35	6	0.85	0.15
Zr	28.75°	1°	none	75	50	8	0.67	0.11
Zr	28.75°	1°	0.2°	20	8	2	0.40	0.10
Zr	28.75°	0.4°	none	8	2	2	0.25	0.25
none	28.75°	1°	none	560	560	418	1.00	0.75
none	28.75°	1°	0.2°	123	115	84	0.94	0.68
none	28.75°	0.4°	none	56	47	35	0.84	0.63

[a] Set for (200) MoK_α reflection.

Because of the convenience of the (200) pole figure in interpreting the texture, for most purposes its determination may be justified if the spurious areas can be identified and ignored. A check of the consistency between pole figures for two different (hkl) planes may be adequate, but making a pinhole pattern like Fig. 3 or a 2θ trace like Fig. 4 for a properly oriented specimen is easier, quicker, and more reliable. White radiation peaks can be identified by using a K_α absorption filter, while spurious K_α peaks can be distinguished from real K_α peaks by noting the relative change in intensity on refining the spectrometer slit system.

ACKNOWLEDGMENT

The author wishes to express his appreciation to Mrs. A. Cooper and Mrs. J. K. Mallery who collected the data reported here. He is also grateful to C. G. Dunn, J. H. Keeler, and J. L. Walter for their contributions to the paper.

Radiation from a Point Dipole Located at the Tip of a Prolate Spheroid*

E. C. Hatcher, Jr.,† and A. Leitner
Department of Physics, Michigan State College, East Lansing, Michigan
(Received October 7, 1953)

The radiation patterns of prolate spheroidal conductors, excited by an electric dipole in its tip, are calculated, for a number of spheroids of varying thickness, the wavelengths being equal to roughly π, $\pi/2$, and $\pi/3$ times their major axes.

INTRODUCTION

THE spheroidal coordinates are among a number of axially symmetric systems in which Maxwell's equations are reducible to separable scalar form, provided the manner of excitation possesses the same symmetry. Among the problems that have been solved because of this advantage is the work of Chu and Stratton,[1] who study the properties of the center fed prolate spheroidal transmitting antenna. Contributions to this problem have also been made by Page and Adams,[2] and Ryder.[3] In this paper we consider the case of a prolate spheroidal conductor excited by a point dipole located at the tip (see Fig. 1). It should be of some interest in antenna theory and to those who are concerned with the modes of radiation by shells or guided missiles.

Several general properties of such radiators can be stated at the start: axially symmetric conductors, excited with like symmetry, will not radiate along the axis, i.e., due ahead or due back of the radiator. Furthermore, when a magnetic dipole is brought close to the surface of a good conductor, with its moment so oriented as to be perpendicular to the surface, the net result will be cancellation of the dipole field in the limit of zero distance. Thus we need consider electric dipoles only in our problem.

In order to simplify the boundary conditions we make the assumption that the spheroid is perfectly conducting.

SOLUTION

The z axis is taken as the axis of symmetry of the spheroidal coordinates η, ξ, φ, *viz.*,

$$x=a(\xi^2-1)^{\frac{1}{2}}(1-\eta^2)^{\frac{1}{2}}\cos\varphi, \tag{1}$$

$$y=a(\xi^2-1)^{\frac{1}{2}}(1-\eta^2)^{\frac{1}{2}}\sin\varphi, \tag{2}$$

$$z=a\xi\eta, \tag{3}$$

where $-1\leqslant\eta\leqslant 1$, $1\leqslant\xi\leqslant\infty$, $0\leqslant\varphi\leqslant 2\pi$, $2a$ being the interfocal distance.

If the electromagnetic field is assumed axially symmetric about z, then it is independent of the coordinate φ and Maxwell's equations, expanded in these coordinates, separate into two independent groups: transverse electric and magnetic, corresponding to excitation of the magnetic and electric dipole type, respectively. Of these, only the latter case is of interest here, e.g.,

$$-i\epsilon\omega a(\xi^2-\eta^2)^{\frac{1}{2}}E_\eta=(\partial/\partial\xi)(\xi^2-1)^{\frac{1}{2}}H_\varphi, \tag{4}$$

$$i\epsilon\omega a(\xi^2-\eta^2)^{\frac{1}{2}}E_\xi=(\partial/\partial\eta)(1-\eta^2)^{\frac{1}{2}}H_\varphi, \tag{5}$$

$$i\mu\omega a(\xi^2-\eta^2)H_\varphi=(1-\eta^2)^{\frac{1}{2}}(\partial/\partial\eta)(\xi^2-\eta^2)^{\frac{1}{2}}E_\xi - (\xi^2-1)^{\frac{1}{2}}(\partial/\partial\xi)(\xi^2-\eta^2)^{\frac{1}{2}}E_\eta, \tag{6}$$

where E_η, E_ξ, H_φ are functions of ξ and η; where we have assumed harmonic time variation in the form $e^{-i\omega t}$ and where ϵ, μ are the constants of the medium surrounding the spheroid. These equations may be reduced to H_φ alone, e.g.,

$$LH_\varphi=\left[\frac{\partial}{\partial\xi}(\xi^2-1)\frac{\partial}{\partial\xi}+\frac{\partial}{\partial\eta}(1-\eta^2)\frac{\partial}{\partial\eta} -\left(\frac{1}{1-\eta^2}+\frac{1}{\xi^2-1}\right)+k^2a^2(\xi^2-\eta^2)\right]H_\varphi=0. \tag{7}$$

This differential equation is satisfied by the infinite set of prolate spheroidal wave functions of order one

$$R_{1l}(ka,\xi)S_{1l}(ka,\eta), \quad l=0, 1, 2, \cdots \tag{8}$$

as described by Stratton *et al.*[4] H_φ may therefore be represented by an expansion in terms of these functions.

The spheroidal functions depend on the value of $ka(k=\omega(\epsilon\mu)^{\frac{1}{2}}=2\pi/\lambda)$, which is a measure of the length of the prolate spheroid relative to the free-space wavelength λ. It is one of the variable parameters of our problem.

The S_{1l} are called angular functions; they form an orthogonal set in the range $-1\leqslant\eta\leqslant 1$, with norm N_{1l} whose value depends on ka.

A variety of radial functions has to be defined. The fundamental set $R_{1l}^{(1)}$, $R_{1l}^{(2)}$ is called functions of the first and second kind, respectively. All other radial functions must be linear combinations of these. Among

* Submitted by E. C. H. to the Faculty of Michigan State College in partial fulfilment of the requirements for the Degree of Master of Science.

† Now at Douglas Aircraft Company, Santa Monica, Calif.

[1] L. J. Chu and J. A. Stratton, J. Appl. Phys. **12**, 241 (1941).

[2] L. Page and N. J. Adams, Jr., Phys. Rev. **53**, 819 (1938); L. Page, Phys. Rev. **65**, 98, 111 (1944).

[3] R. M. Ryder, J. Appl. Phys. **13**, 327 (1942).

[4] Stratton, Morse, Chu, and Hutner, *Elliptic Cylinder and Spheroidal Wave Functions* (John Wiley and Sons, Inc., New York, 1941), p. 61. We are here using the same notation and definitions for these functions.

them $R_{1l}^{(3)}=R_{1l}^{(1)}+iR_{1l}^{(2)}$, the function of the third kind, has outgoing wave behavior at a large distance from the origin, a property called for by the radiation condition.

Let the coordinate of the radiating prolate spheroid be known as ξ_0. This quantity will be the second of two variable parameters of this problem, the other being ka, already mentioned above. Since we assume the spheroid to be perfectly conducting, the appropriate boundary conditions are

$$(\partial/\partial\xi)(\xi^2-1)^{\frac{1}{2}}H_\varphi=0, \quad \text{when} \quad \xi=\xi_0, \tag{9}$$

and the radiation condition at infinity.

In deriving the expansion for H_φ in terms of the prolate spheroidal wave functions, it is convenient to obtain the appropriate Green's function. If all sources are so situated and oriented that their fields possess the same axial symmetry as the prolate spheroid ξ_0, then this function does not depend on the azimuthal variable and must be a solution of

$$LG(\xi,\eta;\xi',\eta')=-\delta(\xi-\xi')\delta(\eta-\eta')/2\pi(\xi^2-\eta^2), \tag{10}$$

symmetric in $(\xi,\eta;\xi',\eta')$.[5] So it follows that G can also be represented in terms of the set given in (8).

Once Green's function is known, H_φ is given by its boundary values through

$$H_\varphi(\xi,\eta)=\int_{\sigma'}\left[H_\varphi(\xi',\eta')\frac{\partial G}{\partial n'}-G\frac{\partial}{\partial n'}H_\varphi(\xi',\eta')\right]d\sigma', \tag{11}$$

where σ can be reduced to a surface enclosing the sources alone provided G satisfies exactly the same boundary conditions as those required of H_φ.

Thus we find

$$G=-(k/2\pi)\sum_{l=0}^{\infty}[S_{1l}(ka,\eta)S_{1l}(ka,\eta')/N_{1l}w_{1l}^{(3)\prime}(\xi_0)]\times\begin{cases}R_{1l}{}^{I}(ka,\xi)R_{1l}^{(3)}(ka,\xi'), & \xi\leqslant\xi',\\ R_{1l}^{(3)}(ka,\xi)R_{1l}{}^{I}(ka,\xi'), & \xi\geqslant\xi',\end{cases} \tag{12}$$

where $R_{1l}{}^{I}$ is a radial function satisfying the boundary condition (9) on the spheroid ξ_0, *viz.*,

$$R_{1l}{}^{I}=w_{1l}^{(2)\prime}(\xi_0)R_{1l}^{(1)}(ka,\xi)-w_{1l}^{(1)\prime}(\xi_0)R_{1l}^{(2)}(ka,\xi). \tag{13}$$

A prime denotes differentiation. The symbol w_{1l} is an abbreviation for $(\xi^2-1)^{\frac{1}{2}}R_{1l}(ka,\xi)$.

Expression (12) represents Green's function for any arbitrary axially symmetric set of transverse magnetic sources in the presence of a perfectly conducting spheroid ξ_0.

The field in the immediate neighborhood of an electric point dipole of unit strength is given by

$$H_\varphi=-(i\omega/4\pi)\sin\Theta(e^{ikR}/R^2), \tag{14}$$

[5] See for example P. M. Morse and H. Feshbach, *Methods of Theoretical Physics* (McGraw-Hill Book Company, Inc., New York, 1953), Vol. I, Chap. 7, or A. Leitner and R. D. Spence, J. Appl. Phys. **21**, 1001 (1950).

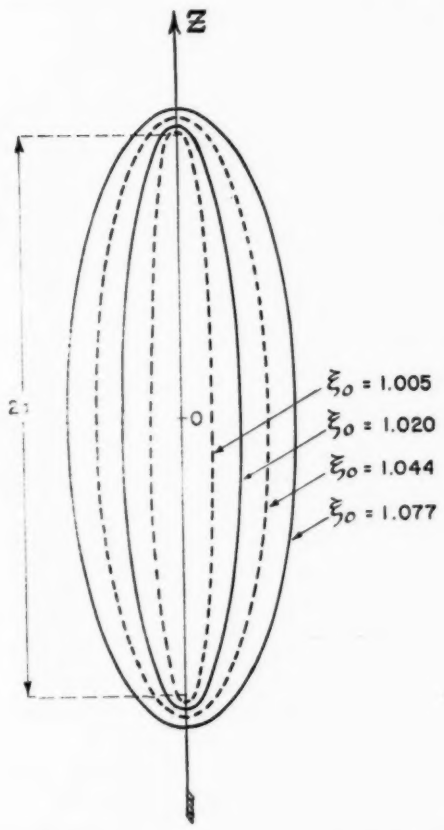

FIG. 1. Proportions of the spheroidal radiators selected for computation. The dipole is situated at the upper tip, along $+z$.

where R is the distance from the dipole and Θ is the polar angle measured from its axis.

This function is substituted into (11) and the integral evaluated over a surface arbitrarily close to the dipole, which is imagined to lie somewhere on the z axis outside the spheroid ξ_0, oriented parallel to the z axis. When in addition the dipole is then approached arbitrarily close to the surface of this spheroid one obtains the final result

$$H_\varphi=\{ik/a^2\pi(\epsilon\mu)^{\frac{1}{2}}\}\sum_{l=0}^{\infty}B_lS_{1l}(ka,\eta)R_{1l}^{(3)}(ka,\xi), \tag{15}$$

which, in conjunction with Eqs. (4) and (5), completely specifies the values of the entire electromagnetic field at any point $\xi(\geqslant\xi_0)$, η. In this expression

$$B_l=c_0{}^{1l}/N_{1l}(\xi_0{}^2-1)w_{1l}^{(3)\prime}(\xi_0), \tag{16}$$

where

$$c_0{}^{1l}=[S_{1l}(ka,\eta)/(1-\eta^2)^{\frac{1}{2}}]_{\eta=1}.$$

The functions $w_{1l}^{(3)\prime}$ are singular in the manner $\log(\xi_0-1)$ as ξ_0 approaches the value 1, corresponding to a wire of zero thickness and length $2a$. Consequently the B_l go infinite in that limit and our problem breaks down.

At large distance r from the origin, where

$$R_{1l}^{(3)}(ka,\xi)\doteq(-i)^{l+1}e^{ikr}/kr, \tag{17}$$

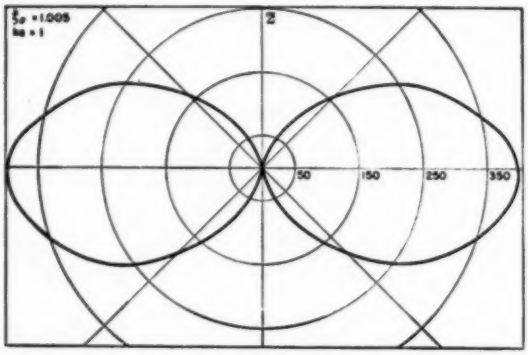

FIG. 2.

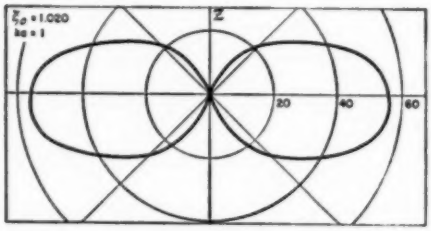

FIG. 3.

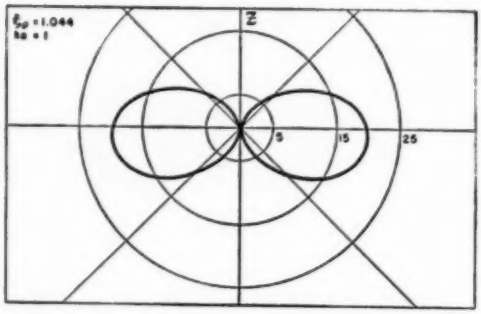

FIG. 4.

FIG. 5.

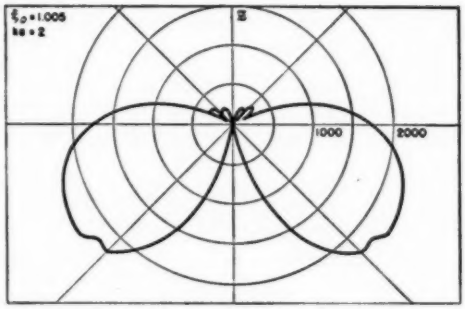

FIG. 6.

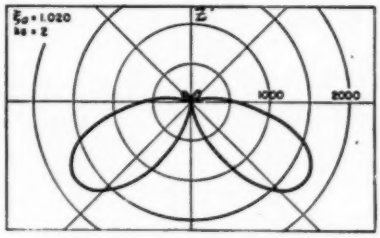

FIG. 7.

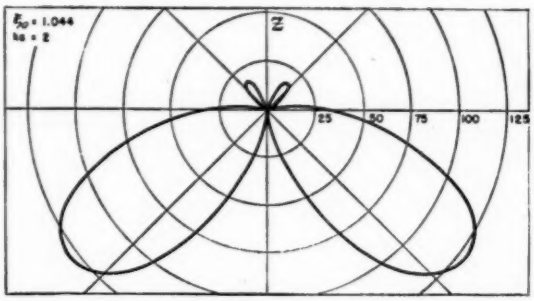

FIG. 8.

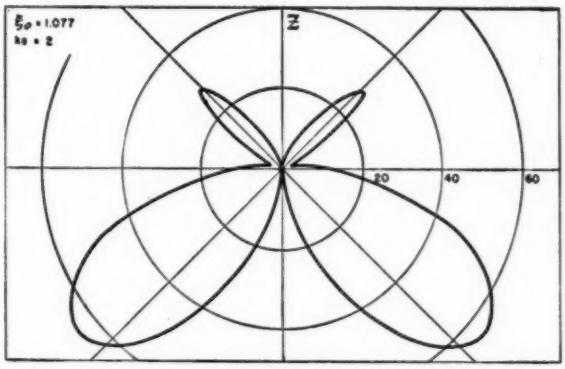

FIG. 9.

we obtain the expression

$$S = f(\eta; ka, \xi_0)/2\pi^2 a^4 \epsilon(\epsilon\mu)^{\frac{1}{2}} r^2 \tag{18}$$

for the Poynting flux. The function

$$f(\eta; ka, \xi_0) = |\sum_{l=0}^{\infty} (-i)^l B_l S_{1l}(ka, \eta)|^2 \tag{19}$$

gives us the radiation pattern of the system. At points far from the origin $\eta = \cos\theta$, where θ is the polar angle.

DISCUSSION

We selected a set of four spheroids ξ_0 of varying proportions, illustrated in Fig. 1. This is the same group as was used by Spence and Granger[6] in their calculations on the scattering of sound by spheroids. Spence[7] has

[6] R. D. Spence and S. Granger, J. Acoust. Soc. Am. **23**, 701 (1951).

[7] R. D. Spence, Final Report, U. S. Office of Naval Research Contract NONR-o2400 (1951).

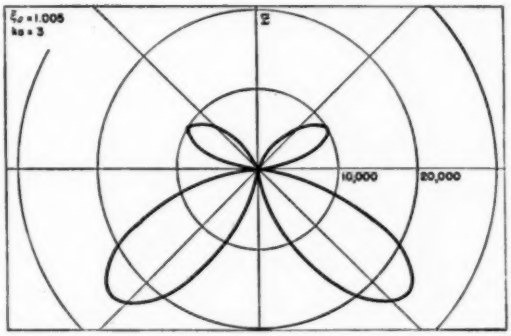

FIG. 10.

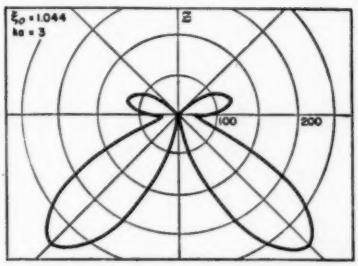

FIG. 12.

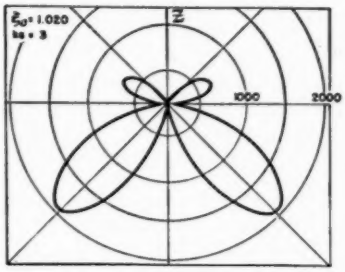

FIG. 11.

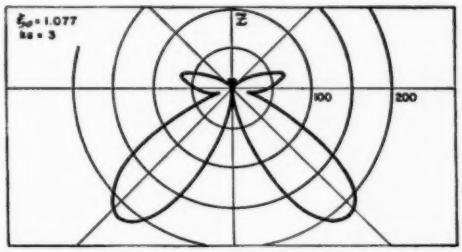

FIG. 13.

FIGS. 2 to 13. Radiation patterns.

already tabulated many of the spheroidal functions and constants required here.

The parameter ka was assigned the values 1, 2, 3, corresponding in the order given to wavelengths equal to roughly 3, $\frac{3}{2}$, and 1 times the length of the speroids.

The convergence of the series representing the radiation patterns generally deteriorates with increasing ka and ξ_0. The above cases are those where computation was possible with good accuracy while using no more than five terms in the series mentioned, i.e., $l=0$ to 4. This in itself required extension of the tabulations of Stratton *et al.*[4] and Spence.[7]

The radiation patterns are illustrated in Figs. 2 to 13. They are characterized by an asymmetry about the equatorial plane $\theta=90°$. Radiation is thrown into the range between 90° and 180°, i.e., backwards, and the effect is markedly increased with increasing ka (shorter wavelength). The effect is also increased by thicker spheroids, but not so strongly.

This result reflects a fact already empirically known, namely that a thick antenna serves as a good matching transformer between the transmission line and free space, i.e., that there will be little reflection at the free end. An analogy may therefore be drawn to the linear wave antenna. From the theory of this model we obtain the result that the maximum of the principal radiation lobe occurs at the angle θ_0, where

$$\cos\theta_0=(\pi/kL)-1. \tag{20}$$

Here L is the length of the wire. θ_0 monotonically increases with kL toward 180° as $kL\to\infty$. When a comparison is made between (20) and our results we find that θ_0 is greater than predicted by (20), if for L we use either the major axis or even half the circumference of the ellipse ξ_0. In this latter case (20) predicts angles about 15° less than actually occur. The effective length thus considerably exceeds the axial dimension of the spheroid on the basis of this comparison.

We wish to thank Dr. Spence for the loan of unpublished portions of his tables in the field of spheroidal functions and for a number of enlightening discussions.

Effect of Uniform Displacement on the Stress Distribution of a Wood Plate*

KENNETH C. WALTERS AND C. BASSEL SMITH
University of Florida, Gainesville, Florida

(Received November 2, 1953)

The principle of virtual work was employed to determine the stress distribution in a wood plate subjected to a load distribution such as to effect a uniform displacement in the y direction.

The displacement u along $x=\pm a$ developed an unexpected contour. The average value of u appears to occur near the ends. This cautions against the common practice of placing the instruments for measuring Poisson's ratio near the middle. In the case of isotropic material the unexpected contours still prevail but are barely perceptible.

The work was carried out for a fourth approximation (not presented) with sufficient accuracy to assure that the same contour was developing. These unexpected results were first observed in the laboratory of the U. S. Forest Products Laboratory, Madison, Wisconsin—an experience which prompted this theoretical confirmation.

1. INTRODUCTION

IN a chapter devoted to strain-energy methods Timoshenko and Goodier[1] have explained the *principle of virtual work*. They define virtual displacement in the case of an elastic body as any small displacement compatible with the condition of continuity of the material and with the conditions for the displacements at the surface of the body, if such conditions are prescribed.

Let us consider the case of plane stress distribution in a plate. If from an orthotropic material a flat plate is cut parallel to a plane of elastic symmetry, it will have two perpendicular axes of symmetry in the plane of the plate. Such a plate is said to be orthotropic.

If we denote by u and v the components of actual displacements due to the load and by δu and δv the components of a virtual displacement from the loaded position of equilibrium, these latter components are arbitrary small quantities satisfying the conditions of continuity, and the work done against the mutual actions between the particles is equal to the strain energy corresponding to the displacements.

The principle of virtual work states that the total work done during the virtual displacement of any system in equilibrium must vanish. Hence we have[2]

$$\delta\left\{\int\int V_0 dxdy-\int\int(Xu+Yv)dxdy-\int(\bar{X}u+\bar{Y}v)ds\right\}=0 \quad (1)$$

where δ means variation, X and Y are component body forces per unit volume of the plate, $\bar{X}$ and $\bar{Y}$ are components of body forces per unit area of the plate, and u and v are displacements in the x and y directions, and where the first term in the bracket is the potential energy of deformation and the second and third terms together represent the potential energy of forces acting on the body if the potential energy of such forces for the unstressed condition is taken as zero. The complete expression in the brackets of Eq. (1) represents the total potential energy of the system. We can then say that the total potential energy of the system at the position of equilibrium is a maximum or a minimum; and since, for stable equilibrium, it is always necessary to insist upon a positive work for any virtual displacement, the total potential energy of the system at this position is always a *minimum*.

For our problem we shall assume no body forces, so that Eq. (1) becomes

$$\delta\left\{\int\int V_0 dxdy-\int(\bar{X}u+\bar{Y}v)ds\right\}=0. \quad (2)$$

For a plate of unit thickness the strain energy per unit volume V_0 can be written as

$$V_0=\tfrac{1}{2}(X_x l_{xx}+Y_y l_{yy}+X_y l_{xy}). \quad (3)$$

In general the components of boundary forces per unit area of the plate can be expressed as

$$\begin{aligned}\bar{X}&=lX_x+mX_y,\\ \bar{Y}&=mY_y+lX_y,\end{aligned} \quad (4)$$

where l and m are the cosines of the angles between the normal and the axes x and y respectively.

For the problem which we wish to consider, the boundary forces are to be exerted compressively normal to the boundaries $y=\pm b$ only and no shearing forces are applied.

Then

$$\bar{X}=0 \quad \text{and} \quad \bar{Y}=Yy. \quad (5)$$

For orthotropic material the components of stress and strain are connected by the following relations[3]:

$$\begin{aligned}l_{xx}&=a_{11}X_x+a_{12}Y_y,\\ l_{yy}&=a_{21}X_x+a_{22}Y_y,\\ l_{xy}&=a_{33}X_y,\end{aligned} \quad (6)$$

*Submitted by Kenneth C. Walters in partial fulfilment of the requirements for the degree of Doctor of Philosophy, June, 1952.

[1] S. Timoshenko and J. N. Goodier, *Theory of Elasticity* (McGraw-Hill Book Company, Inc., New York, 1951), second edition, chapter on strain-energy methods.

[2] See reference 1, p. 2.

[3] U. S. Forest Products Laboratory Report No. 1503.

where

$$a_{11}=(1/E_x),\quad a_{12}=-(\sigma_{yx}/E_y),\quad a_{21}=-(\sigma_{xy}/E_x),$$
$$a_{22}=(1/E_y),\quad a_{33}=(1/u_{xy}), \tag{7}$$

and for which E_x and E_y are Young's moduli in the x and y directions, respectively. Poisson's ratio σ_{xy} is the ratio of the contraction parallel to the y axis to the extension parallel to the x axis associated with a tension parallel to the x axis and similarly for σ_{yx}. The quantity u_{xy} is the modulus of rigidity associated with the directions of x and y.

For an orthotropic plate like the one we shall use, the relation $\sigma_{xy}E_y=\sigma_{yx}E_x$ holds so that $a_{12}=a_{21}$ for our problem.[4]

Since the equations of equilibrium are obtained independently of the law connecting stresses and strains, they will be satisfied by a stress function ϕ such that

$$X_x=(\partial^2\phi/\partial y^2),\quad Y_y=(\partial^2\varphi/\partial x^2),$$
$$X_y=-(\partial^2\phi/\partial x\partial y). \tag{8}$$

With the knowledge of Eqs. (3), (5), (6), (7), and (8) we can write Eq. (2) for our problem in the form

$$\delta\left\{2\int_0^b\int_0^a\left[a_{22}\frac{\partial^2\varphi}{\partial x^2}+a_{11}\frac{\partial^2\varphi}{\partial y^2}+2a_{12}\frac{\partial^2\varphi}{\partial x^2}\frac{\partial^2\varphi}{\partial y^2}+a_{33}\frac{\partial^2\varphi}{\partial x\partial y}\right]dxdy-4\int_0^a(Y_y v)_{y=b}dx\right\}=0. \tag{9}$$

If we denote the expression in brackets by V, we can write

$$\delta V=0. \tag{10}$$

Then a stress function taken in the form

$$\phi=\phi_{11}c_{11}+\phi_{21}c_{21}+\phi_{12}c_{12}+\phi_{22}c_{22}+\cdots+\phi_{mn}c_{mn}+\cdots, \tag{11}$$

where c_{mn} for $m=1, 2, 3, \cdots$ and $n=1, 2, 3, \cdots$ can be determined from the minimum conditions

$$\partial V/\partial c_{11}=0,\quad \partial V/\partial c_{21}=0,\quad \partial V/\partial c_{12}=0,\quad \cdots,$$
$$\partial V/\partial c_{mn}=0,\quad \cdots. \tag{12}$$

We shall apply this theory to the following problem.

2. THE STRESS DISTRIBUTION OF A WOOD PLATE WITH UNIFORM DISPLACEMENT

Suppose we take a rectangular plate of Sitka spruce of unit thickness, length $2b$, and width $2a$. Referring to Fig. 1, let us prevent the corners A, B, C, D from any horizontal displacement, and place such a compressive load distribution (to be determined later) along sides AB and CD, only, as to cause the vertical displacements of all points along AB to be $-k$ and along CD to be $+k$, where k is a positive constant.

Stated formally, the boundary conditions which the stress function ϕ must satisfy are

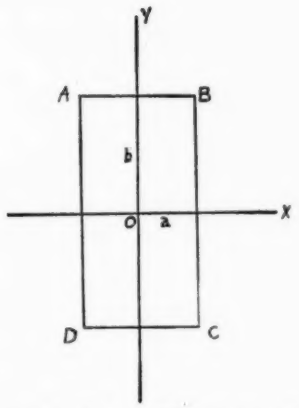

FIG. 1. A rectangular plate of Sitka spruce of unit thickness.

$$\begin{aligned}&\text{for}\quad x=\pm a,\quad X_x=0,\quad X_y=0;\\ &\text{for}\quad y=+b,\quad v=-k,\quad X_y=0;\\ &\text{for}\quad y=-b,\quad v=+k,\quad X_y=0,\end{aligned} \tag{13}$$

at the corners (a,b), $(a,-b)$, $(-a,b)$, $(-a,-b)$, $u=0$.

A suitable choice of the stress function ϕ for the problem under consideration is

$$\phi=A_k\left\{\left(1+\cos\frac{\pi x}{a}\right)\cos\frac{\pi y}{b}-\frac{a_{11}\pi^2}{2a_{12}b^2}x^2+\sum_{m=1}^{\infty}\sum_{n=1}^{\infty}(1-\delta m_1\delta n_1)c_{mn}\left[\left(\cos\frac{m\pi x}{a}-\cos m\pi\right)\times\cos\frac{n\pi y}{b}-\frac{a_{11}n^2\pi^2}{2a_{12}b^2}x^2\cos m\pi\cos n\pi\right]\right\}, \tag{14}$$

where A_k (the k subscript on A_k indicates the number of constants C_{mn} that are included in each approximation) is an arbitrary constant to be adjusted to any desired total load on the sides $y=\pm b$ of the rectangle, and δ_{mn} is the Kronecker delta.

Using Eq. (8) the stresses can readily be determined as follows:

$$X_y=-\frac{\partial^2\varphi}{\partial x\partial y}=-\frac{A_k\pi^2}{ab}\left[\sin\frac{\pi x}{a}\sin\frac{\pi y}{b}+\sum_{m=1}^{\infty}\sum_{n=1}^{\infty}(1-\delta_{m1}\delta_{n1})c_{mn}\sin\frac{m\pi x}{a}\sin\frac{n\pi y}{b}\right]. \tag{15}$$

We observe that $X_y=0$ along $x=\pm a$ in accord with the boundary conditions as given by Eqs. (13).

$$X_x=\frac{\partial^2\phi}{\partial y^2}=-\frac{A_k\pi^2}{b^2}\left[\left(1+\cos\frac{\pi x}{a}\right)\cos\frac{\pi y}{b}+\sum_{m=1}^{\infty}\sum_{n=1}^{\infty}(1-\delta_{m1}\delta_{n1})n^2c_{mn}\times\left(\cos\frac{m\pi x}{a}-\cos m\pi\right)\cos\frac{n\pi y}{b}\right]. \tag{16}$$

[4] See U. S. Forest Products Laboratory Report No. 1503, p. 7.

We also see that $X_x=0$ along $x=\pm a$ as should be true for the boundary conditions as given by Eqs. (13).

$$Y_y=\frac{\partial^2\phi}{\partial x^2}=-A_k\left[\frac{\pi^2}{a^2}\cos\frac{\pi x}{a}\cos\frac{\pi y}{b}+\frac{a_{11}\pi^2}{a_{12}b^2}\right.$$
$$+\sum_{m=1}^{\infty}\sum_{n=1}^{\infty}(1-\delta_{m1}\delta_{n1})c_{mn}\left(\frac{m^2\pi^2}{a^2}\cos\frac{m\pi x}{a}\cos\frac{n\pi y}{b}\right.$$
$$\left.\left.+\frac{a_{11}n^2\pi^2\cos m\pi\cos n\pi}{a_{12}b^2}\right)\right]. \quad (17)$$

Since $l_{xx}=\partial u/\partial x$, the first of Eqs. (6) allows us to write

$$\frac{\partial u}{\partial x}=-\frac{A_k a_{11}\pi^2}{b^2}\left[\left(1+\cos\frac{\pi x}{a}\right)\cos\frac{\pi y}{b}\right.$$
$$+\sum_{m=1}^{\infty}\sum_{n=1}^{\infty}(1-\delta_{m1}\delta_{n1})n^2c_{mn}$$
$$\times\left(\cos\frac{m\pi x}{a}-\cos m\pi\right)\cos\frac{n\pi y}{b}\Big]$$
$$-a_{12}\pi^2\left[\frac{1}{a^2}\cos\frac{\pi x}{a}\cos\frac{\pi y}{b}+\frac{a_1}{a_{12}b^2}\right.$$
$$+\sum_{m=1}^{\infty}\sum_{n=1}^{\infty}(1-\delta_{m1}\delta_{n1})c_{mn}\left(\frac{m^2}{a^2}\cos\frac{m\pi x}{a}\cos\frac{n\pi y}{b}\right.$$
$$\left.\left.-\frac{a_{11}n^2\cos m\pi\cos n\pi}{a_{12}b^2}\right)\right], \quad (18)$$

and integrating with respect to X,

$$u=-\frac{A_k a_{11}\pi^2}{b^2}\left[x\cos\frac{\pi y}{b}+\frac{a}{\pi}\sin\frac{\pi x}{a}\cos\frac{\pi y}{b}\right.$$
$$+\sum_{m=1}^{\infty}\sum_{n=1}^{\infty}(1-\delta_{m1}\delta_{n1})n^2c_{mn}$$
$$\times\left(\frac{a}{m\pi}\sin\frac{m\pi x}{a}\cos\frac{n\pi y}{b}-x\cos m\pi\cos\frac{n\pi y}{b}\right)\Big]$$
$$-A_k a_{12}\pi^2\left[\frac{1}{a\pi}\sin\frac{\pi x}{a}\cos\frac{\pi y}{b}+\frac{a_1 x}{a_{12}b^2}\right.$$
$$+\sum_{m=1}^{\infty}\sum_{n=1}^{\infty}(1-\delta_{m1}\delta_{n1})c_{mn}\left(\frac{m}{a\pi}\sin\frac{m\pi x}{a}\cos\frac{n\pi y}{b}\right.$$
$$\left.\left.+\frac{a_{11}n^2x\cos m\pi\cos n\pi}{a_{12}b^2}\right)\right]. \quad (19)$$

To check our boundary conditions again we see that $u=0$ at the corners (a,b), $(-a,b)$, $(a,-b)$, $(-a,-b)$.

Also, since $l_{yy}=\partial V/\partial y$, the second of Eqs. (6) allows us to write

$$\frac{\partial V}{\partial y}=-\frac{A_k a_{12}\pi^2}{b^2}\left[\left(1+\cos\frac{\pi x}{a}\right)\cos\frac{\pi y}{b}\right.$$
$$+\sum_{m=1}^{\infty}\sum_{n=1}^{\infty}(1-\delta_{m1}\delta_{n1})n^2c_{mn}$$
$$\times\left(\cos\frac{m\pi x}{a}-\cos m\pi\right)\cos\frac{n\pi y}{b}\Big]$$
$$-A_k a_{22}\pi^2\left[\frac{1}{a^2}\cos\frac{\pi x}{a}\cos\frac{\pi y}{b}+\frac{a_{11}}{a_{12}b^2}\right.$$
$$+\sum_{m=1}^{\infty}\sum_{n=1}^{\infty}(1-\delta_{m1}\delta_{n1})c_{mn}\left(\frac{m^2}{a^2}\cos\frac{m\pi x}{a}\cos\frac{n\pi y}{b}\right.$$
$$\left.\left.+\frac{a_{11}n^2\cos m\pi\cos n\pi}{a_{12}b^2}\right)\right], \quad (20)$$

and integrating with respect to y, we have

$$V=-\frac{A_k a_{12}\pi^2}{b^2}\left[\frac{b}{\pi}\left(1+\cos\frac{\pi x}{a}\right)\sin\frac{\pi y}{b}+\frac{b}{\pi}\right.$$
$$\times\sum_{m=1}^{\infty}\sum_{n=1}^{\infty}(1-\delta_{m1}\delta_{n1})nc_{mn}$$
$$\times\left(\cos\frac{m\pi x}{a}-\cos m\pi\right)\sin\frac{n\pi y}{b}\Big]$$
$$-A_k a_{22}\pi^2\left[\frac{b}{a^2\pi}\cos\frac{\pi x}{a}\sin\frac{\pi y}{b}+\frac{a_{11}y}{a_{12}b^2}\right.$$
$$+\sum_{m=1}^{\infty}\sum_{n=1}^{\infty}(1-\delta_{m1}\delta_{n1})c_{mn}\left(\frac{m^2b}{n\pi a}\cos\frac{m\pi x}{a}\sin\frac{n\pi y}{b}\right.$$
$$\left.\left.+\frac{a_{11}n^2y\cos m\pi\cos n\pi}{a_{12}b^2}\right)\right], \quad (21)$$

for which

$$V_{y=\pm b}=\mp\frac{A_k a_{11}a_{22}\pi^2}{a_{12}b}$$
$$\times\left[1+\sum_{m=1}^{\infty}\sum_{n=1}^{\infty}(1-\delta_{m1}\delta_{n1})n^2c_{mn}\cos m\pi\cos n\pi\right]$$
$$=\text{a constant.} \quad (22)$$

Substituting from Eqs. (15), (16), (17), (22) into Eq. (10) gives

$$\delta V=2(A_k)^2\int_0^b\int_0^a\Big\{a_{22}\Big[\frac{\pi^2}{a^2}\cos\frac{\pi x}{a}\cos\frac{\pi y}{b}+\frac{a_{11}\pi^2}{a_{12}b^2}$$
$$+\sum_{m=1}^{\infty}\sum_{n=1}^{\infty}(1-\delta_{m1}\delta_{n1})c_{mn}\Big(\frac{m^2\pi^2}{a^2}\cos\frac{m\pi x}{a}$$
$$\times\cos\frac{n\pi y}{b}+\frac{a_{11}n^2\pi^2\cos m\pi\cos n\pi}{a_{12}b^2}\Big)\Big]^2$$
$$+\frac{a_{11}\pi^4}{b^4}\Big[\Big(1+\cos\frac{\pi x}{a}\Big)\cos\frac{\pi y}{b}$$
$$+\sum_{m=1}^{\infty}\sum_{n=1}^{\infty}(1-\delta_{m1}\delta_{n1})n^2c_{mn}\Big(\cos\frac{m\pi x}{a}-\cos m\pi\Big)$$
$$\times\cos\frac{n\pi y}{b}\Big]^2+\frac{2a_{12}\pi^2}{b^2}\Big[\frac{\pi^2}{a^2}\cos\frac{\pi x}{a}\cos\frac{\pi y}{b}+\frac{a_{11}\pi^2}{a_{12}b^2}$$
$$+\sum_{m=1}^{\infty}\sum_{n=1}^{\infty}(1-\delta_{m1}\delta_{n1})c_{mn}\Big(\frac{m^2\pi^2}{a^2}\cos\frac{m\pi x}{a}\cos\frac{n\pi y}{b}$$
$$+\frac{a_{11}n^2\pi^2\cos m\pi\cos n\pi}{a_{12}b^2}\Big)\Big]\cdot\Big[\Big(1+\cos\frac{\pi x}{a}\Big)\cos\frac{\pi y}{b}$$
$$+\sum_{m=1}^{\infty}\sum_{n=1}^{\infty}(1-\delta_{m1}\delta_{n1})n^2c_{mn}\Big(\cos\frac{m\pi x}{a}$$
$$-\cos m\pi\Big)\cos\frac{n\pi y}{b}\Big]+\frac{a_{33}\pi^2}{a^2b^2}\Big[\sin\frac{\pi x}{a}\sin\frac{\pi y}{b}$$
$$+\sum_{m=1}^{\infty}\sum_{n=1}^{\infty}(1-\delta_{m1}\delta_{n1})c_{mn}\sin\frac{m\pi x}{a}\sin\frac{n\pi y}{b}\Big]\Big\}dxdy$$
$$-\frac{4(A_k)^2aa_{11}^2a_{22}\pi^4}{a_{12}^2b^3}\Big[1+\sum_{m=1}^{\infty}\sum_{n=1}^{\infty}(1-\delta_{m1}\delta_{n1})$$
$$\times n^2c_{mn}\cos m\pi\cos n\pi\Big]^2=0. \quad (23)$$

We know that the more terms that are used for the stress function ϕ the greater the accuracy of our results. However, experience with past problems based upon the principle of virtual displacement has usually shown that the use of about three constants yields results of a sufficiently high degree of accuracy. We shall limit our applied problem to the use of three constants in our discussions.

If, as a *first* approximation, we take

$$\phi=A_1\Big\{\Big(1+\cos\frac{\pi x}{a}\Big)\cos\frac{\pi y}{b}-\frac{a_{11}\pi^2}{2a_{12}b^2}x^2$$
$$+c_{21}\Big[\Big(\cos\frac{2\pi x}{a}-1\Big)\cos\frac{\pi y}{b}+\frac{a_{11}\pi^2x^2}{2a_{12}b^2}\Big]\Big\}, \quad (24)$$

substitute into Eq. (23), find $\partial V/\partial c_{21}$, and set $\partial V/\partial c_{21}=0$, we have

$$(16a_{22}r^4a_{12}^2-4a_{11}^2a_{22}+3a_{11}a_{12}^2+8a_{12}^3r^2$$
$$+4a_{33}r^2a_{12}^2)c_{21}=2a_{11}(a_{12}^2-2a_{11}a_{22}), \quad (25)$$

where $r=b/a$.

Taking as a *second* approximation

$$\phi=A_2\Big\{\Big(1+\cos\frac{\pi x}{a}\Big)\cos\frac{\pi y}{b}-\frac{a_{11}\pi^2}{2a_{12}b^2}x^2$$
$$+c_{21}\Big[\Big(\cos\frac{2\pi x}{a}-1\Big)\cos\frac{\pi y}{b}+\frac{a_{11}\pi^2x^2}{2a_{12}b^2}\Big]$$
$$+c_{12}\Big[\Big(\cos\frac{\pi x}{a}+1\Big)\cos\frac{2\pi y}{b}+\frac{2a_{11}\pi^2x^2}{a_{12}b^2}\Big]\Big\} \quad (26)$$
$$\partial V/\partial c_{21}=0,\quad \partial V/\partial c_{12}=0,$$

we get

$$c_{21}(16r^4a_{22}a_{12}^2-4a_{11}^2a_{22}+3a_{11}a_{12}^2+8r^2a_{12}^3$$
$$+4r^2a_{33}a_{12}^2)+c_{12}(-16a_{11}^2a_{22})$$
$$=2a_{11}(a_{12}^2-2a_{11}a_{22}); \quad (27)$$
$$c_{21}(-16a_{11}^2a_{22})+c_{12}(a_{22}r^4a_{12}^2-64a_{11}^2a_{22}$$
$$+48a_{11}a_{12}^2+8a_{12}^3r^2+4a_{33}r^2a_{12}^2)=-16a_{11}^2a_{22}.$$

Similarly, as a *third* approximation, using the three terms involving the coefficients c_{12}, c_{21}, c_{22} in Eq. (13), we have

$$c_{21}(16a_{22}r^4a_{12}^2-4a_{11}^2a_{22}+3a_{11}a_{12}^2+8a_{12}^3r^2$$
$$+4a_{33}r^2a_{12}^2)+c_{12}(-16a_{11}^2a_{22})+c_{22}(16a_{11}^2a_{22})$$
$$=-4a_{11}^2a_{22}+2a_{11}a_{12}^2;$$
$$c_{21}(-16a_{11}^2a_{22})+c_{12}(a_{12}^2a_{22}r^4-64a_{11}^2a_{22}$$
$$+48a_{11}a_{12}^2+8r^2a_{12}^3+4a_{33}r^2a_{12}^2)+c_{22}(64a_{11}^2a_{22}-32a_{11}a_{12}^2)=-16a_{11}^2a_{22}; \quad (28)$$
$$c_{21}(16a_{11}^2a_{22})+c_{12}(64a_{11}^2a_{22}-32a_{11}a_{12}^2)$$
$$+c_{22}(16r^4a_{12}^2a_{22}-64a_{11}^2a_{22}+48a_{11}a_{12}^2$$
$$+32r^2a_{12}^3+16r^2a_{12}^2a_{33})=16a_{11}^2a_{22}.$$

TABLE I. Elastic moduli of Sitka spruce.[a]

σ_{yz}	0.464
E_x	0.076×10^6 lb per sq in.
E_y	1.679×10^6 lb per sq in.
μ_{xy}	0.112×10^6 lb per sq in.

[a] The elastic moduli of Sitka spruce are average values obtained from a large number of tests made at the U. S. Forest Products Laboratory.

TABLE II. Elastic coefficients for Sitka spruce.

a_{11}	13.157×10^{-6} lb per sq in.$^{-1}$
a_{22}	0.59559×10^{-6} lb per sq in.$^{-1}$
a_{12}	-0.27635×10^{-6} lb per sq in.$^{-1}$
a_{21}	-0.27635×10^{-6} lb per sq in.$^{-1}$
a_{33}	8.9286×10^{-6} lb per sq in.$^{-1}$

To illustrate the problem for a particular case, suppose we take a plain-sawn plate of Sitka spruce with the grain of the wood parallel to the y axis for which the elastic moduli are taken to be those given by Table I.

Due to Eqs. (7) the values given in Table I lead to the values given in Table II for a_{11}, $a_{12}=a_{21}$, a_{22}, a_{33}.

Using the values of a_{mn} given by Table II and $r=4$ in Eqs. (25), (27), and (28), we arrive at the values of c_{mn} given in Table III.

Suppose we have a compression whose total load is P, where P is any positive constant. Considering the case for the third approximation, we obtain the total load required by the formula

$$2\int_0^a (Y_y)_{y=\pm b}dx=\frac{2aa_{11}\pi^2}{a_{12}b^2},$$

$$\times(4c_{12}+c_{21}-4c_{22}-1)A_3=-P. \quad (29)$$

For our applied problem we must therefore take

$$A_3=+1.227P. \quad (30)$$

The displacement u along $x=a$ for Sitka spruce in a rectangular plate.

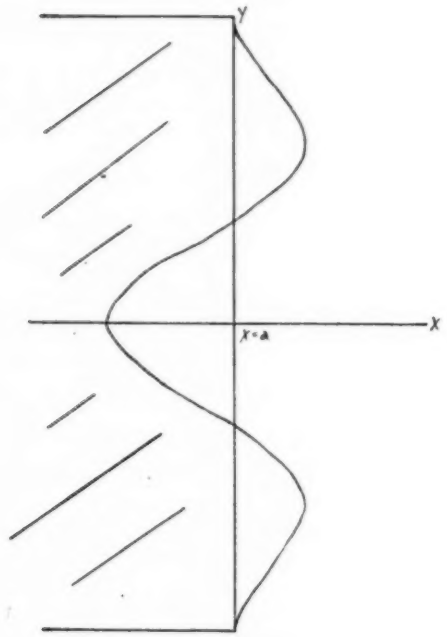

FIG. 2.
Unit in y direction—1 space$=1/16\ b$.
Unit in x direction—1 space$=2\times10^{-6}\ P$ in. measured from $x=a$.
Solid line—displacement u for Sitka spruce.

TABLE III. Values of c_{mn} for successive approximations for Sitka spruce.

	c_{21}	c_{12}	c_{22}
First approximation	+2.25400		
Second approximation	+0.03646	+0.24470	
Third approximation	+0.03359	+0.20620	−0.03887

We are very much interested in the displacements u and v along $x=\pm a$ and $y=\pm b$, respectively. Letting $x=\pm a=\pm1$ in Eq. (19) for the case where $k=3$ and substituting from Eq. (30) into Eq. (19), we have

$$u_{x=\pm a}=\pm\left(-9.627\cos\frac{\pi y}{b}\right.$$

$$\left.-9.765\cos\frac{2\pi y}{b}+0.1382\right)\times10^{-6}P. \quad (31)$$

The results for displacement u are shown in Table IV and by Fig. 2 for the third approximation.

For displacement v along $y=\pm b$ in the case where $k=3$, substitution of the constants into Eq. (23) gives

$$v_{y=\pm b}=\mp1.191\times10^{-6}P. \quad (32)$$

Now let us get the average value of u, call it $\bar{u}$, by

$$\bar{u}=\frac{2\int_0^b (u)_{x=a}dy}{2\int_0^b dy}. \quad (33)$$

For the third approximation we find that

$$\bar{u}=0.1382\times10^{-6}P. \quad (34)$$

Let us see if

$$\frac{\bar{u}/a}{P/2aE_y}=\sigma_{yx}, \quad (35)$$

We get

$$0.464=0.464. \quad (36)$$

TABLE IV. Displacement u along $x=\pm a$ (in multiples of $10^{-6}\ P$ units).[a]

For third approximation	
y	$u_{x=\pm a}$
b	± 0.000
$7/8\ b$	± 2.128
$3/4\ b$	± 6.945
$5/8\ b$	±10.590
$1/2\ b$	± 9.903
$3/8\ b$	± 3.359
$1/4\ b$	∓ 6.669
$1/8\ b$	∓15.660
0	∓19.250

[a] For rectangular plate of Sitka spruce.

Notice that u has the value $\bar{u}$ at two points along the boundary $x=a$, where $y=0.99$ lb and where $y=-0.99$ lb.

Using three constants c_{21}, c_{12}, c_{22} from Table III, we have

$$(Y_y)_{y=\pm b}=\pm\pi^2(1.227P)\left[(1-c_{12})\cos\frac{\pi x}{a}+4(c_{21}-c_{22})\cos\frac{2\pi x}{a}+\frac{a_{11}}{a_{12}b^2}(4c_{12}+c_{21}-4c_{22}-1)\right], \quad (37)$$

$$(Y_y)_{y=\pm b}=\pm\left(9.613\cos\frac{\pi x}{a}+3.509\cos\frac{2\pi x}{a}-0.4999\right)P. \quad (38)$$

The values of Y_y along $y=\pm b$ as given by Eq. (38) are shown in Table V and in Fig. 3.

In the dissertation the work was completely carried out for a square plate ($a=b$) and was then repeated for the isotropic material (structural steel, using $\sigma=0.3$), where

$$E_x=E_y=E, \quad \sigma_{yx}=\sigma, \quad \mu_{xy}=\frac{E}{2(1+\sigma)}, \quad (39)$$

TABLE V. Y_y along $y=\pm b$ for Eq. (38) (in multiples of P).[a]

For third approximation	
x	Y_y along $y=\pm b$
a	$\mp$ 6.604
7/8 a	$\mp$ 6.900
3/4 a	$\mp$ 7.297
5/8 a	$\mp$ 6.660
1/2 a	$\mp$ 4.009
3/8 a	$\pm$ 0.698
1/4 a	$\pm$ 6.297
1/8 a	$\pm$10.860
0	$\pm$12.620

[a] For rectangular plate of Sitka spruce.

Load distribution for Sitka spruce in a rectangular plate.

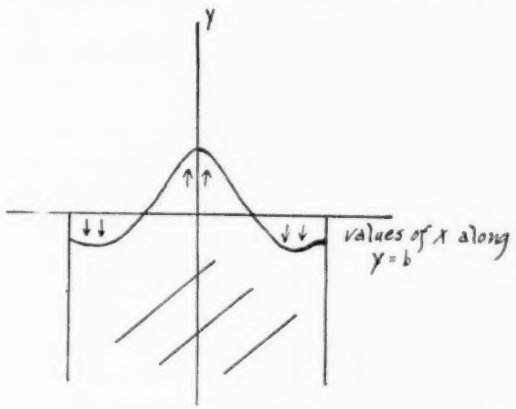

FIG. 3.
Unit along y axis—1 space$=5P$.
Unit parallel to x axis—1 space$=1/8\ a$.
Solid line—load distribution for Sitka spruce.

so that

$$a_{11}=\frac{1}{E}, \quad a_{12}=a_{21}=-\frac{\sigma}{E}, \quad a_{22}=\frac{1}{E}, \quad a_{33}=\frac{2(1+\sigma)}{E}.$$

The general results were the same in all cases. Of course the displacements were much smaller for isotropic material.

3. SUMMARY

As has been true of so many problems in the past, one might have expected the displacement u along $x=\pm a$ to cause a simple bulging contour. Instead, however, we get the unusual contour shown in Fig. 2.

It is very interesting to note that the average value of u, called $\bar{u}$, does not necessarily occur at large distances from the ends (as one might expect). In fact, in some cases, it appears that it occurs near the ends. This cautions against the common practice of placing the instruments for measuring Poisson's ratio near the middle.

In the case of isotropic material the unexpected contours still prevail but are barely perceptible, as shown in the original dissertation.

JOURNAL OF APPLIED PHYSICS VOLUME 25, NUMBER 10 OCTOBER, 1954

Method of Averages and Its Comparison with the Method of Least Squares

MORRIS MORDUCHOW
Department of Mathematics, Polytechnic Institute of Brooklyn, Brooklyn, New York
(Received November 23, 1953)

It is shown, under fairly general conditions, that the standard deviation of the residuals of the straight line fitting a set of points with uniformly spaced abscissas by the method of averages is at most $2/\sqrt{3}$ times as great as the standard deviation of the least-squares line. Theorems of significance in the practical use of the method of averages are proven in the course of the analysis.

INTRODUCTION

THE method of least squares is well known in curve fitting. The method of averages, which is also quite useful in curve fitting, appears not to be quite as well known, although it is described in the literature.[1] Briefly, the method of least squares is based on selecting the coefficients in an assumed functional form (e.g., a straight line) so that the sum of the squares of the residuals is minimized, while the method of averages is based on requiring that the average of the residuals be zero over the whole set of points, as well as over certain mutually exclusive subsets of these points. The number of such subsets depends on the number of coefficients to be determined. The method of averages, although somewhat less accurate than that of least squares, has the advantage that it usually involves considerably simpler computations.

The aim of this paper is to compare quantitatively, and with some generality, the accuracy of the method of averages with that of the method of least squares. For this purpose, the relatively simple problem of fitting a straight line to n points will be treated, and the standard deviations of the given points from the straight lines based on an application of each of the two methods will be derived and compared. The results derived from such a comparison can be of value not only in curve fitting but also in other types of problems, such as the approximate solution of differential equations with given boundary conditions, where the method of averages might be applied more easily than that of least squares.[2] A secondary result of the present analysis is the derivation or proof of certain theorems which have significance with respect to the practical use of the method of averages.

It will be assumed in this analysis that the given points are all of equal weight, that the abscissas are uniformly spaced, and that only the ordinates are subject to error. Instead of the given ordinates, the deviations of these ordinates from the straight line obtained by the method of averages will be treated as the parameters. This, it will be seen, leads to a particularly simple analysis.

BASIC EQUATIONS

Consider a set of $n(n\geqslant 2)$ points (ξ_i, y_i) with uniformly spaced abscissas. Then

$$\xi_i=\xi_0+ih(i=0,1,2,\cdots,n-1), \tag{1}$$

where ξ_0 and h are independent of i. Transforming to the variable x_i, defined by

$$x_i=(\xi_i-\xi_0)/h, \tag{2}$$

the abscissas become

$$x_i=i. \tag{3}$$

Let a straight line of the form

$$y=Ax+B \tag{4}$$

be fitted to these points by a method of averages, and let ϵ_i denote the deviations (residuals) of the given ordinates from this line. Then these ordinates will be

$$y_i=Ax_i+B+\epsilon_i. \tag{5}$$

From the condition that the average residual over the entire set of points be zero, it follows that[3]

$$\sum\epsilon_i=0. \tag{6}$$

In addition to Eq. (6), the condition that the average residual be zero for a subset (consisting of, say, ν points) of the given points must be applied. The most general form of such a condition will be

$$\sum_{i=\alpha_1,\cdots,\alpha_\nu}\epsilon_i=0 \quad (\nu<n), \tag{7}$$

where the summation in (7) is taken over any (different) ν of the ϵ_i's.

Let

$$y=\alpha x+\beta \tag{8}$$

denote the straight line fitting the given set of points according to the method of least squares. Then α and β must be such that

$$\sum(\alpha x_i+\beta-y_i)^2$$

[1] A clear account of these methods is given, for example, in J. B. Scarborough, *Numerical Mathematical Analysis* (Johns Hopkins Press, Baltimore, 1950), second edition, pp. 446–463.

[2] In this connection, the solution for the region $x=a, b$ can be assumed in a form satisfying the boundary conditions and containing undetermined coefficients. If the differential equation is in the form $F=0$, then according to the method of least squares, the coefficients would be determined by requiring that $\int_a^b F^2dx$ be a minimum.

[3] The symbol Σ without any indices will be used here to denote a summation from $i=0$ to $(n-1)$.

is minimized. Using Eq. (5) for y_i, and noting in addition to Eq. (6) the relations

$$\sum x_i=\sum i=\frac{n}{2}(n-1)$$

$$\sum x_i^2=\sum i^2=\frac{n}{6}(n-1)(2n-1),$$

the following values are obtained for α and β:

$$\alpha=A+\frac{12}{n(n^2-1)}M, \quad \beta=B-\frac{6}{n(n+1)}M, \tag{9}$$

where

$$M\equiv\sum i\epsilon_i. \tag{10}$$

Equations (9) indicate, in general terms, the deviation of the straight line to be obtained by the method of averages from the least-squares, or "regression," line.[4] This deviation is seen to depend not only on n but also on the quantity M, which is essentially the first moment of the residuals ϵ_i from the method-of-averages line. The latter line will coincide with the least-squares line only when $M=0$. Equations (9) can be used, incidentally, to determine rapidly the regression line from a set of data once a straight line has been fitted to the data by the method of averages and the resulting residuals have been calculated.

A simple means of determining the accuracy of the method of averages is to compare the standard deviation, or "root-mean-square" (σ_a) of the residuals with respect to the straight line thereby obtained with the standard deviation (σ_s) of the residuals obtained by the method of least squares. Such a comparison is particularly satisfactory in view of the fact that the least-squares standard deviation is necessarily the least possible for any straight line fitting the given data and since the least-squares line is usually regarded as the "best-fitting" line, in accordance with probability theory.[5]

By definition,

$$n\sigma_s^2=\sum[y_i-(\alpha x_i+\beta)]^2.$$

Substituting for y_i, α and β in accordance with Eqs. (5) and (9), it is found that

$$\sigma_s^2=\frac{\sum\epsilon_i^2}{n}-\frac{12}{n^2(n^2-1)}M^2. \tag{11}$$

Since

$$n\sigma_a^2=\sum\epsilon_i^2, \tag{12}$$

Eq. (11) can also be written in the form

$$\frac{\sigma_s}{\sigma_a}=\left[1-\frac{12}{n^2(n^2-1)}\frac{M^2}{\sigma_a^2}\right]^{\frac{1}{2}}, \tag{13}$$

where M and σ_a are defined by Eqs. (10) and (12) in terms of the residuals (ϵ_i) obtained by the method of averages. Equation (13) explicitly gives the improvement of the method of least squares relative to that of averages or, from another point of view, the loss of accuracy due to using a method of averages instead of that of least squares. The ratio (σ_s/σ_a) is seen to depend only on the number of points (n) and on the ratio (M^2/σ_a^2). Since (σ_s/σ_a) is thus dependent only on the distribution and not on the magnitude of the ϵ_i's, it follows that the magnitude of the residuals resulting from the method of least squares will be proportional to the magnitude of the residuals resulting from the method of averages. The method of averages may be considered to yield results of maximum accuracy when (σ_s/σ_a) is as close to unity as possible, and hence when $(M^2/n^2(n^2-1)\sigma_a^2)$ is a minimum. If (M^2/σ_a^2) is either kept fixed, or more generally, does not increase as rapidly with n as n^4, then $(\sigma_s/\sigma_a)\to 1$ as $n\to\infty$; i.e., as the number of points increases indefinitely, then under and *only* under, the above conditions on (M^2/σ_a^2), the straight line obtained by the method of averages tends to fit the data as "closely" as the least-squares line.

MINIMUM VALUE OF (σ_s/σ_a)

It is of interest to determine the minimum value of (σ_s/σ_a) for a given number (n) of points, since this will indicate the maximum possible improvement of the method of least squares over that of averages, and thus the maximum relative inaccuracy of the method of averages. For this purpose, the values of the ϵ_i (as ratios of ϵ_0) for a given n must, according to Eq. (13), first be determined such that (M^2/σ_a^2) will be a maximum, subject to the auxiliary conditions (6) and (7). Introducing Lagrange multipliers κ and λ, and setting

$$\frac{\partial}{\partial\epsilon_i}\left[\frac{M^2}{\sigma_a^2}+\kappa\sum_{j=\alpha_1,\cdots,\alpha_\nu}\epsilon_j+\lambda\sum_{j=\beta_1,\cdots,\beta_{n-\nu}}\epsilon_j\right]=0$$

$$(i=0, 1, 2, \cdots, n-1),$$

(where the second summation is taken over the remaining $(n-\nu)\epsilon_j$'s not included in the first summation), one finds:[6]

$$\left.\begin{aligned}\epsilon_i&=ci+\epsilon_0 \qquad (i=\alpha_1,\cdots,\alpha_\nu)\\ \epsilon_i&=ci+(\lambda/\kappa)\epsilon_0 \quad (i=\beta_1,\cdots,\beta_{n-\nu})\end{aligned}\right\}, \tag{14}$$

where $c=(n\sigma_a^2/M)$. Both c and (λ/κ) are independent of i. Substitution of Eqs. (14) into the conditions (6)

[4] It may be noted that by virtue of Eqs. (6) and (9) it can be easily shown that the straight lines obtained by both the method of averages and that of least squares pass through the centroid $[(\Sigma x_i)/n, (\Sigma y_i)/n]$ of the given set of points (x_i, y_i). Hence it is really necessary to compare only the slopes A and α.

[5] See, for example, J. B. Scarborough, reference 1, Chapters XIV, XV. Also, Whittaker and Robinson, *Calculus of Observations* (Blackie and Son Ltd., London), Chapter IX.

[6] It may be assumed, without loss of generality, that $j=0$ is included in the first summation.

and (7) yields the following values for c and (λ/κ):

$$c=-(\nu/s_1)\epsilon_0, \quad \lambda/\kappa=(\nu/n-\nu)(s_2/s_1), \tag{15}$$

where

$$s_1\equiv \sum_{i=a_1,\cdots,a_\nu} i, \quad s_2\equiv \sum_{i=\beta_1,\cdots,\beta_{n-\nu}} i. \tag{16}$$

Since, by definition, $s_1+s_2=\sum i$, it is evident that

$$s_1+s_2=(n/2)(n-1). \tag{17}$$

Equations (14) indicate the particular distribution of the residuals which would be least favorable for the method of averages in comparison with the method of least squares. By substituting for ϵ_i according to Eqs. (14) and (15) into Eqs. (10) and (12) to evaluate (M^2/σ_a^2), it is found from Eq. (13) that

$$\left(\frac{\sigma_s}{\sigma_a}\right)^2_{\min}=1-\frac{12}{n(n^2-1)} \times\left[\frac{n}{6}(n-1)(2n-1)-\left(\frac{s_1^2}{\nu}+\frac{s_2^2}{n-\nu}\right)\right]. \tag{18}$$

For a given number (n) of points and a given ν, Eq. (18) yields a simple expression for the minimum possible value of (σ_s/σ_a). This expression is evidently a function only of s_1 in addition to n and ν. The values of ν and s_1 remain open to choice and depend on which subset of points is chosen in the second averaging condition (7). It is customary to choose half, or very nearly half, of the total number of given points in this subset; i.e., it is customary to choose

$$\left.\begin{aligned}&\nu=n/2 \quad (n \text{ even})\\&\nu=(n+1)/2 \quad \text{or} \quad (n-1)/2 \quad (n \text{ odd})\end{aligned}\right\}. \tag{19}$$

It is also customary, moreover, to choose points with consecutive abscissas for this subset, so that the subset would consist of the points with the first ν abscissas. In that case,

$$s_1=\sum_{i=0}^{\nu-1} i=\nu(\nu-1)/2. \tag{20}$$

Equation (18) can be used to afford readily a mathematical justification for Eqs. (19) and (20). For, by substituting for s_2 in terms of s_1 [Eq. (17)], it is found that for a fixed ν, $(\sigma_s^2/\sigma_a^2)_{\min}$ as given by Eq. (18) will be a maximum when s_1 is as small as possible (consistent with the fixed ν), and hence when s_1 is given by Eq. (20). With this value for s_1 it is then found that $(\sigma_s^2/\sigma_a^2)_{\min}$ will be a maximum when $\nu=n/2$. This proves that the values of ν and s_1 as given by Eqs. (19) and (20) minimize the *maximum* possible improvement of the method of least squares over that of averages; i.e., by applying the method of averages for all cases in the simple manner indicated by Eqs. (19) and (20), one is sure to minimize the ratio σ_a/σ_s at least when the given points may be distributed in the manner [Eqs. (14)] least favorable to the method of averages.[7]

In view of these results, it may now be assumed that ν and s_1 will, in general, be chosen so as to have the values given by Eqs. (19) and (20). Substitution into Eq. (18) then leads to the following simple results:

$$\left.\begin{aligned}&(\sigma_s/\sigma_a)_{\min}=(\sqrt{3}/2)[n/(n^2-1)^{\frac{1}{2}}] \quad (n \text{ even}).\\&(\sigma_s/\sigma_a)_{\min}=\sqrt{3}/2 \quad (n \text{ odd})\end{aligned}\right\} \tag{21}$$

For n odd, $(\sigma_s/\sigma_a)_{\min}$ is seen to be independent of n, while for n even, $(\sigma_s/\sigma_a)_{\min}$ diminishes asymptotically, as $n\to\infty$, to the same value (*viz.*, $\sqrt{3}/2$) as for odd n. For n even and $n\geq 6$, $(\sigma_s/\sigma_a)_{\min}\approx\sqrt{3}/2$, while for $n=4$, $(\sigma_s/\sigma_a)_{\min}$ is approximately 7 percent greater than $\sqrt{3}/2$. Equations (21) thus imply that if the method of averages is applied in the usual simple manner [i.e., in accordance with Eqs. (19) and (20)] to fit a straight line to a set of n points with uniformly spaced abscissas, then, regardless of n, the standard deviation of the residuals thus obtained can in general be *at most* $2/\sqrt{3}$ times as great as, or approximately 15 percent greater than, the standard deviation from the regression line, i.e., from the straight line yielding the smallest possible standard deviation. Thus, at least for uniformly spaced abscissas of the given points, there is a definite limit to the degree of improvement, as measured by the standard deviation of the residuals, which the method of least squares can, in fitting a straight line, possibly yield over the method of averages when the latter is applied in the manner shown here. Since, in actual cases, the residuals obtained by the method of averages will rarely follow the particular distribution given by Eqs. (14), σ_s/σ_a will ordinarily be considerably closer to unity than the minimum values given by Eqs. (21). These results tend to lend mathematical justification for the use of the method of averages as an alternative to the method of least squares in cases where it is desired to simplify the computations at the possible expense of some accuracy.[8] A problem for further in-

[7] It cannot, of course, be inferred from the foregoing analysis that Eqs. (19) and (20) will necessarily minimize σ_a/σ_s for *any* given distribution of the ϵ_i's.

A particularly simple and striking illustration of the possible importance of choosing the averaging conditions in accordance with Eqs. (19) and (20) is the special case of three points (with uniformly spaced abscissas) which lie exactly on a straight line. If, contrary to Eqs. (19) and (20), it were required, in a method of averages, that a straight line be chosen so that the average of the residuals for the first and last points, as well as for all three points, be zero, then *any* line passing through the middle point could be obtained, including a line perpendicular to the actual line.

[8] There are, of course, important special cases, particularly those involving orthogonal functions, when the method of least squares is actually much easier to apply than that of averages. A classical example in this regard is the determination of the (Fourier) coefficients of a trigonometric series.

vestigation would be the extension of this analysis to the general case of nonuniformly spaced abscissas of the given points.[9]

[9] As an incidental application of the analysis presented here, it may be mentioned that, if desired, at least two types of inequalities, including a diophantine inequality, can be readily derived from the equations developed here, by writing $\sigma_s^2 \geqslant 0$ and using Eq. (11), and by writing $(\sigma_s/\sigma_a)^2_{\min} \geqslant 0$ and using Eq. (18).

The author hereby expresses his thanks to Professor R. M. Foster and Professor M. S. Klamkin for their valuable discussions.

JOURNAL OF APPLIED PHYSICS VOLUME 25, NUMBER 10 OCTOBER, 1954

Effects of Cathode and Anode Resistance on the Retarding Potential Characteristics of Diodes

G. C. DALMAN*
Sperry Gyroscope Company, Great Neck, New York
(Received January 11, 1954)

As a result of the processes of manufacture of tubes having oxide cathodes, high resistance layers often exist in the cathode and tube elements. This can produce anomalous retarding potential characteristics such as, for example, an apparently high electron temperature in diodes. By accounting for the effect of these resistances the apparent anomalies can be explained. Also given are the conditions required to minimize these errors and a method for evaluating the sum of these resistances.

I. INTRODUCTION

A DETAILED understanding of the retarding potential characteristics of diodes is of considerable interest since methods, which are based upon an analysis of these characteristics, have been proposed for evaluating the cathode temperature,[1–3] the anode-cathode contact difference of potential,[4] and the thermionic constants of the cathode.[5,6]

For pure metallic emitters excellent agreement has been found among the quantities evaluated using these methods and the standard methods. On the other hand, the results obtained where oxide coated emitters have been used are not in consistent agreement with the expected values. For example, while good agreement in cathode temperature determinations has been reported by Heinze and Haas,[1] Fan,[7] Hung,[8] and others, numerous reports dating as early as 1925 and 1926 by Koller,[9] and Rothe,[10] have shown that temperatures as high as six times the corrected optically determined values have been obtained.

To explain the observed errors in temperature measurements, it has been hypothesized[11,12] that a deficiency of slow speed electrons exists in the energy distribution of the emitted electrons, due to the presence of a potential barrier in the surface of the cathode. It is necessary, however, to investigate the existence of additional causes since the experimental errors observed in temperature measurements are considerably greater than can be explained by this theory alone.

Earlier studies[13,14] of this anomalous behavior of tubes having oxide cathodes have shown that large deviations from the theoretical retarding potential characteristics will occur when the cathodes used have high values of resistance or have poor cathode "activity." High resistance anode films will produce similar deviations. It is suggested, therefore, that this anomalous behavior of diodes under retarding potential conditions can be explained by including the effect of the nonohmic resistances of the cathode and anode in the analysis of the retarding potential characteristics. The condition for minimizing the errors introduced by these resistances is obtained as a result of this analysis, and a method for evaluating the sum of these resistances is also given.

Experimental data on the retarding potential characteristics of diodes were actually obtained on several hundreds of tubes. For the sake of brevity, however, only typical results illustrating some of the effects of the cathode and anode resistances on the retarding potential characteristics of diodes are included here.

* The material for this paper has been extracted from a doctoral thesis submitted to the Department of Electrical Engineering, Polytechnic Institute of Brooklyn (1949).

[1] W. Heinze and W. Haas, Z. Physik **6**, 166 (1938).
[2] D. K. C. MacDonald and R. Fürth, Proc. Phys. Soc. (London) **59**, 375 (1947).
[3] R. Champeix, Le Vide **5**, 763 (1950).
[4] J. Millman and S. Seely, *Electronics* (McGraw-Hill Book Company, Inc., New York, 1951), p. 108.
[5] H. Rothe and W. Kleen, *Grundlagen und Kennlinien der Elektronenröhren* (Akademische Verlagsgesellschaft, Becker und Erler kom.-ges. Leipzig, 1943), Chapters II and III.
[6] S. Sano, Electrotechn. J. (Japan) **5**, 78 (1941).
[7] H. Y. Fan, J. Appl. Phys. **14**, 552 (1943).
[8] C. S. Hung, J. Appl. Phys. **21**, 37 (1950).
[9] L. R. Koller, Phys. Rev. **25**, 671 (1925).
[10] H. Rothe, Z. Physik **37**, 414 (1926).
[11] W. B. Nottingham, Phys. Rev. **41**, 793 (1932).
[12] H. Dormont, J. phys. radium **12**, 710 (1951).
[13] W. R. Ferris, R. C. A. Rev. **10**, 134 (1949).
[14] G. C. Dalman, M.E.E. thesis, Polytechnic Institute of Brooklyn (1947).

II. THE EFFECT OF ANODE AND CATHODE RESISTANCES ON THE RETARDING POTENTIAL CHARACTERISTICS

For a diode having parallel plane electrode geometry, the fundamental equation for the current flow under retarding potential conditions is given by the Maxwell-Boltzmann relation,

$$i = I_s \epsilon^{-(V_r/V_T)}, \tag{1}$$

where

i = retarding potential current (amp/cm²);
I_s = total emitted current (amp/cm²);
V_r = retarding voltage (volts);
V_T = voltage equivalent of the temperature T, $T°K/11\,600$ (volts).

For the ideal case, which has usually been assumed, V_r is equal in magnitude to $V_{cp}-V_a$, where V_{cp} is the contact difference in potential between the anode and cathode and V_a is the voltage applied externally between the anode and cathode. If, however, as a result of the existence of ohmic or non-ohmic resistances in the cathode and anode, a voltage V_{k+a} exists when the current i is flowing, the retarding voltage is actually

$$V_r = -V_a + V_{cp} + V_{k+a}. \tag{2}$$

Equation (1) can be rewritten, therefore, as

$$i = \epsilon^{-(V_{k+a}/V_T)} I_s \epsilon^{-(V_{cp}-V_a)/V_T}. \tag{3}$$

For small values of the ratio V_{k+a}/V_T, the first two terms of a series expansion can be used for the first exponential term, and Eq. (3) simplifies into

$$i = (1 - V_{k+a}/V_T) I_s \epsilon^{-(V_{cp}-V_a)/V_T}. \tag{4}$$

For this case, it is evident that the percent error in current introduced by assuming that the anode and cathode resistances are negligible, is simply $V_{k+a}/V_T \times 100$.

Since considerable information on the resistance of commercial type oxide cathodes is available, the error contributed by this resistance alone is evaluated readily. Figure 1 shows graphically the errors existing for typical cathodes with and without interface resistance and for both the partially and completely activated states.[14–16] The assumed value of 0.0025-in. cathode coating thickness is a nominal value typical of most receiving tubes. The 25 $\mu a/cm^2$ retarding field current is also a nominal value, typically used when tubes normally rated at about 20 ma or less plate current are measured using 0–10 μa microammeters. These curves serve to illustrate the order of magnitude of the errors which can exist in the measurement. It is seen from the figure that at low temperatures, depending on the condition of the cathode, the error term can be considerable. At the higher cathode temperatures, however, the error becomes quite small.

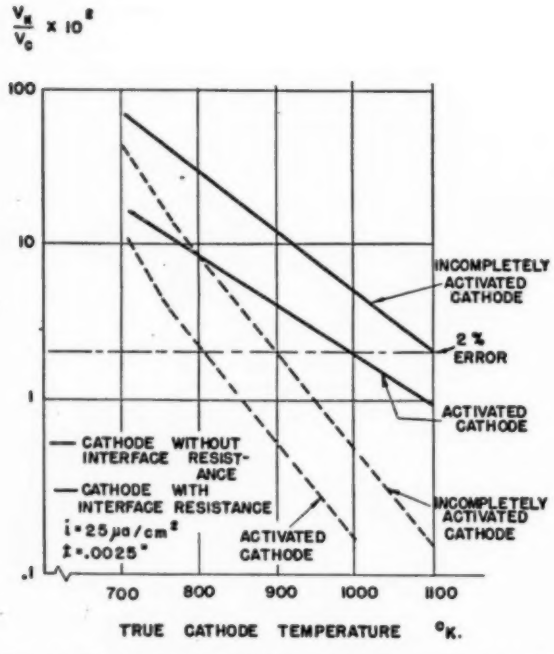

FIG. 1. Temperature dependence of the percent error in retarding potential current when the cathode resistance is neglected in the Maxwell-Boltzmann relation.

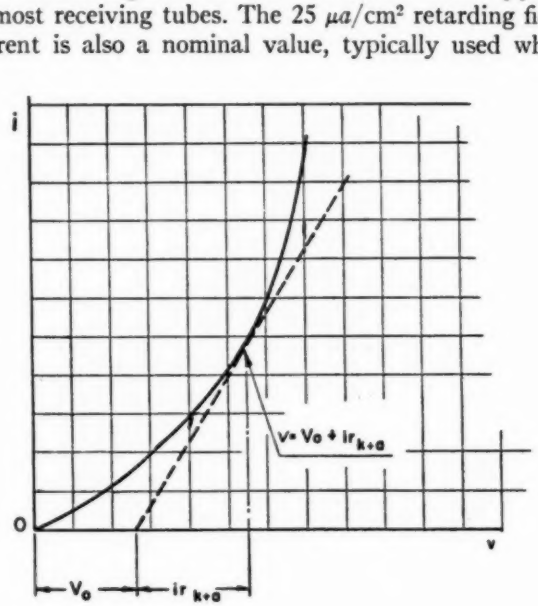

FIG. 2. Linear representation of a non-ohmic resistance.

The existence of an anode resistance which is independent of the cathode temperature would result in an upward displacement of all of the curves shown and a considerable error can exist for all values of cathode temperature. These errors can, however, be minimized by obtaining data at very low values of retarding potential currents. For the ohmic case where the sum of the cathode and anode resistances is r_{k+a}, the error

[15] I. L. Sparks and H. R. Philipp, J. Appl. Phys. 24, 453 (1953).
[16] G. C. Dalman, D.E.E. thesis, Polytechnic Institute of Brooklyn (1949).

will be less than 2 percent if

$$i<0.02(V_T/r_{k+a}), \tag{5}$$

where i is the retarding field current density. This condition is one which can be satisfied readily, in most practical cases when a modern ultrasensitive microammeter is used for the current measurement.

III. EFFECT OF ANODE AND CATHODE RESISTANCES ON TEMPERATURE DETERMINATION

It is interesting to consider as an example, the influence of non-ohmic anode and cathode resistance on the measurement of the cathode temperature.[1-3] For the purposes of the analysis, we can make the usual small signal approximation and apply the linear representation

$$V_{k+a}=V_0+ir_{k+a}; \tag{6}$$

therefore,

$$Vr=-V_a+V_{cp}+V_0+ir_{k+a}. \tag{7}$$

The significance of these relations is clear from Figs. 2 and 3.

Substituting Eq. (7) into Eq. (1), taking logarithms of both sides, and differentiating with respect to the anode voltage, we have for the slope of the retarding potential characteristics,

$$\frac{d\log_{10}i}{dV_a}=\frac{5040}{T}\left[1-r_{k+a}\frac{di}{dV_a}\right]; \tag{8}$$

also, we can obtain

$$di/dV_a=i/(V_T+ir_{k+a}). \tag{9}$$

In the ideal case, the value of r_{k+a} has usually been assumed zero so that the cathode temperature is given as 5040 ÷ the slope of the retarding potential characteristic. In the actual case, however, because of the factor within the bracket of Eq. (8) this calculation would yield an apparent temperature which would be in error. Defining T_e as this apparent temperature, then

$$T_e=\frac{5040}{\left(\frac{d\log_{10}i}{dV_a}\right)}, \tag{10}$$

and substitution of Eqs. (9) and (10) into Eq. (8) gives as a final result

$$T_e=T[1+ir_{k+a}/V_T]. \tag{11}$$

This equation shows that the apparent temperature as evaluated from the slope of the uncorrected retarding potential characteristic is equal to the true temperature T modified by the factor $1+ir_{k+a}/V_T$, where in this case r_{k+a} is the incremental cathode plus anode resistance. Thus if $ir_{k+a}\ll V_T$, then $T_e\approx T$. Equation (5) gives the condition for a 2 percent maximum error.

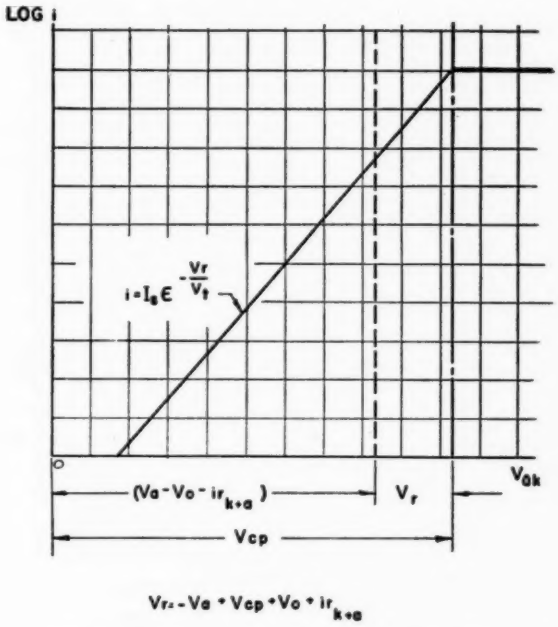

FIG. 3. Retarding potential characteristic of a diode.

Since the cathode resistance increases and V_T decreases with decreasing temperatures, it is evident that for fixed values of i, the ratio T_e/T is largest at the lower values of cathode temperatures.

In the method of temperature measurement proposed by MacDonald and Fürth[2] and Champeix[3] the temperature is given as

$$T=11\,600ir_d, \tag{12}$$

where i is the retarding field current and r_d is the measured small signal diode resistance. But by Eq. (9)

$$r_d=(V_T/i)+r_{k+a}, \tag{13}$$

so that if the effect of the anode and cathode resistances are to be included, Eq. (12) becomes

$$T=11\,600(r_d-r_{k+a})i. \tag{14}$$

Letting $T_e=11\,600ir_d$, and substituting into Eq. (14), we can obtain Eq. (11) again. Thus the same conditions for minimizing the errors apply. For low values of retarding field current, however, the diode resistance is very large and the errors in measurement increase considerably. It would appear that this method is most suitable provided $r_{k+a}\approx 0$.

IV. EXPERIMENTAL RESULTS

a. Effect of Cathode Resistance

A considerable amount of experimental data has been accumulated to show the validity of the analysis given. Much of the data are actually indirect evidence since direct measurements of the anode and cathode resistances were not feasible. However, it was possible in one case to determine the cathode resistance of a

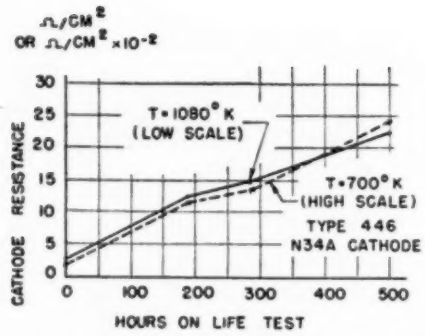

FIG. 4. Cathode resistance as a function of hours on life test for a triode having a high silicon nickel base metal.

particular triode tube, as a function of hours on life test, from an analysis of the measurements of the effective grid voltages required to maintain a 40-ma cathode current at the normal operating temperature of the cathode. At the same time, the cathode resistance was evaluated from the retarding potential characteristic of the tube connected as a diode, using

$$r_k = \Delta T / 11\,600 i, \tag{15}$$

where $\Delta T = T_c - T$. This equation is obtained from Eq. (11) assuming $r_a \approx 0$. This group of measurements was obtained at a low cathode temperature where large values of ΔT were obtainable.

The results of these measurements, obtained on a tube having a high silicon nickel base metal, are illustrated in Fig. 4. The two curves of the figure show the dependence of the cathode resistance upon hours of life tests, as evaluated by the two methods. At the higher cathode temperature the cathode resistance increased from about 2.5 ohms/sq cm to about 22 ohms/sq cm; whereas, at the low cathode temperature, the resistance increased from about 200 ohms/sq cm to about 2400 ohms/sq cm. A group of these tubes were studied in a similar manner, and Fig. 5 shows the correlation which existed between the low-temperature resistance and high-temperature resistance of the cathode as obtained by the two methods.

Clearly, the same factors which tend to increase the cathode resistance at high temperatures will produce similar effect at low temperatures. Thus the results obtained from the analysis of the retarding potential characteristics are consistent with the expected results.

The absence of anode resistance was detected by noting the lack of "anode poisoning" in these tubes when the grid is operated at a high positive potential at low cathode temperature. This will be discussed further below.

b. Effect of Anode Resistance

The author was very fortunate to be able to conduct the experiment, to be described below, using one of Lederer's original diodes[17] which he used to study the now well-known anode poisoning effect. Shown in the right side of Fig. 6 is a schematic diagram of the tube. The anode can be rotated by means of an external magnet so that various surfaces can be placed opposite the cathode such as pure nickel, pure platinum, nickel oxide, "activation spot" on nickel, etc.

The tests described here are confined to the pure platinum surface and activation spot on nickel surface. The latter surface is so-called to describe the discoloration on the anode which is sometimes a result of the cathode activation process. It is a high resistance layer believed to be largely barium oxide with some nickel oxide and pure barium. The cathode temperature was adjusted for a zero-field emission of 50 μa.

In order to show the effect of the anode resistance due to the activation spot, the retarding potential characteristics shown in Fig. 6 were obtained. So as not to decompose any of the oxides on the anode, all data were taken at low anode voltages, and the data were spot checked after the run to be sure that the readings were reproducible. Curve (1) was obtained for the case of the platinum anode opposite the cathode. Since no resistive film was on the platinum, the comparatively low slope of the characteristic is assumed to be due mainly to the effect of the cathode transverse resistance. In order to observe the effect of the anode film resistance on the retarding potential characteristics, the anode was rotated so as to expose the activation spot to the cathode, the cathode temperature being held constant. It is seen from the characteristics obtained, labeled curve (2), that the effect was to cause a considerable increase in the apparent temperature and a large displacement of the characteristic curve. Curve (1) was obtained again without time delay effects, when the anode was rotated so that the platinum was opposite the cathode.

While such a result is typical of "unhealthy" tubes, it is of importance, for studies of the resistances evaluated from Eq. (15), to determine if such anode effects are present. In order to accomplish this it is sufficient to test for "anode poisoning." By supplying anode voltages in excess of the energies corresponding to the heat of formation of the anode oxide, e.g., up to 25

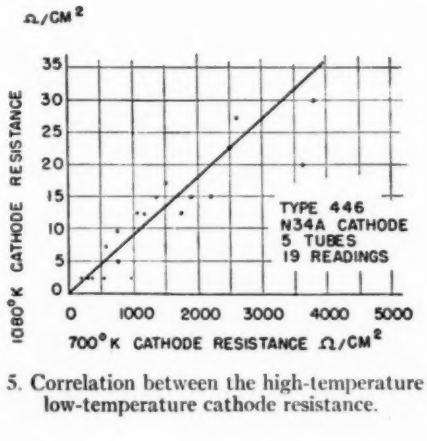

FIG. 5. Correlation between the high-temperature and low-temperature cathode resistance.

[17] L. B. Headrick and E. A. Lederer, Phys. Rev. **50**, 1094 (1936).

volts for aluminum oxide, if a poisoning effect is observed, then it can be assumed that an anode resistance layer is present. The voltage at which the poisoning occurs gives information regarding the type of oxide or oxides on the anode (or grid).

V. CONCLUSIONS

By accounting for the effects of the cathode and anode resistances it is possible to explain some of the anomalous results often obtained when the retarding potential characteristics of diodes having oxide cathodes are analyzed. Improvements in the known electronic methods for measuring cathode temperature have been indicated from the analysis. Similar improvements in the methods for measuring the true anode-cathode contact difference of potential and the thermionic constants of the cathode are clearly obtainable. The low-temperature resistance of the oxide cathode can be evaluated from an analysis of the retarding potential characteristics of parallel plane diodes. The possibility of the use of such measurements for quality control of the oxide cathodes of commercial type tubes is suggested.

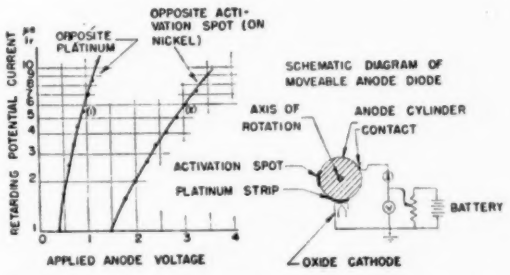

FIG. 6. Effect of anode resistance on the retarding potential characteristics of diodes.

The analysis given can be extended readily to the cylindrical diode case.

VI. ACKNOWLEDGMENT

The considerable help of Dr. H. J. Miller of R.C.A. is gratefully acknowledged as well as that of Dr. E. A. Lederer of Westinghouse for the use of his special diode and Professor E. Weber who guided the work on the diode analysis while the author was with the Polytechnic Institute of Brooklyn.

JOURNAL OF APPLIED PHYSICS VOLUME 25, NUMBER 10 OCTOBER, 1954

Theory of Strong Electromagnetic Waves in Massive Iron*†

WILLIAM MACLEAN
Polytechnic Institute of Brooklyn, Brooklyn 1, New York
(Received November 23, 1953)

A rigorous solution of Maxwell's equations is carried through for the case of a rectangular magnetization curve. Formulas for the depth of penetration and the wave impedance are derived yielding a theoretical power input formula which relates to the popular quasi-theoretical formula of Rosenberg by just the factor $4/\pi$.

IN iron, if the magnetizing force h is strong enough, the magnitude B_0 of the flux density b may be considered constant. Hence for strong alternating fields the rectangular magnetization curve of Fig. 1 becomes asymptotically almost exact.

Using precisely this curve let us consider an x-polarized plane wave propagating in the z direction. The electric field has only an x component e and the magnetic field and magnetizing force only y components, b and h. Under these conditions, Maxwell's equations reduce to

$$-\frac{\partial h}{\partial z}=\gamma e, \tag{1a}$$

$$\frac{\partial e}{\partial z}=-\frac{\partial b}{\partial t}, \tag{1b}$$

where γ is the conductivity. All variables are expressed in MKS units.

We consider a half-infinite sea of metal in the $z>0$ half-space and designate by the letters E, B, H the values at $z=0$ of the variables e, b, h. The wave enters the metal and penetrates with resulting attenuation. At the surface of the metal, i.e., at $z=0$, the magnetizing force H is given as a sinusoidal function of time:

$$H=H_0 \sin\omega t. \tag{2}$$

* This work was done under Contract No. AF33(616)-116 sponsored at the Polytechnic Institute of Brooklyn by the Wright Air Development Center of the U. S. Air Force and reported September 1952, as P.I.B. Aerolab Report No. 206.

† Since this work was submitted, a paper entitled "Penetration of an Electromagnetic Wave into a Ferromagnetic Material" by A. Papoulis in J. Appl. Phys. 25, 169–176 (1954) has appeared. It treats pulse phenomena in a manner similar to the treatment of sinusoidal phenomena adopted here.

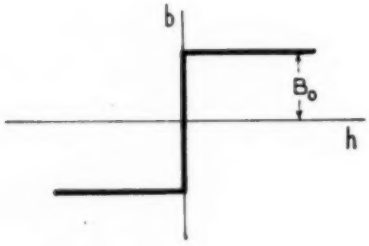

FIG. 1. Assumed magnetization curve.

At $z=\infty$ all fields are given as zero. These are the boundary conditions.

Due to the nature of the magnetization curve, $\partial b/\partial t$ might be infinite: therefore I choose to replace Eq. (1b) by its integral with respect to z. For this purpose I define:

$$\varphi=\int_z^\infty b\,dz, \tag{3}$$

whence Maxwell's equations may be given the alternate form

$$-\frac{\partial h}{\partial z}=\gamma e, \tag{4a}$$

$$e=\frac{\partial \varphi}{\partial t}. \tag{4b}$$

We seek the solution of (4a,b) compatible with Fig. 1 and the boundary conditions.

Rather than try to develop a solution from the equations by any process, I choose to present a hypothesis and prove it correct. I suppose that the solution is given by Fig. 2.

In Fig. 2, which is the proposed field configuration at a certain instant, the point $z=\delta$ is a fixed point, beyond which there are no fields at all. For $0<z<\delta$, the magnetic field has the values $b=\pm B$ as shown. The $\pm$ transition takes place at the point $z=\zeta(t)$, which is variable. The electric field has the values $e=E$ or 0 as shown, and $h(z)$ is linear to ζ and then zero as shown.

The value of B is taken as

$$B=B_0\,\mathrm{Sig}H. \tag{5}$$

"Sig$H$" means "sign of H," and is the unit square wave associated with the sinusoidal H. Equation (5) completes the hypothesis of b, which, together with that of h, does not contradict Fig. 1. Hence, since Fig. 2 obeys the boundary conditions, it remains only to check the hypothesis against Eqs. (4a,b).

Substituting from Fig. 2 into Eq. (4a), we find

$$\frac{H}{\zeta}=\gamma E, \tag{6}$$

as an equivalent equation. This is an equation in time only in which $\zeta(t)$ and $E(t)$ are unknown functions.

To make also a substitution into (4b), note first that

$$\frac{\partial \varphi}{\partial t}=2B\frac{d\zeta}{dt} \qquad z<\zeta,$$
$$\frac{\partial \varphi}{\partial t}=0 \qquad \zeta<z, \tag{7}$$

and also that

$$e=E \qquad z<\zeta,$$
$$e=0 \qquad \zeta<z. \tag{8}$$

So we can replace (4b) completely by

$$E=2B\frac{d\zeta}{dt}. \tag{9}$$

By these means we have replaced the Maxwell equations with the pair

$$\frac{H}{\zeta}=\gamma E, \tag{10a}$$

$$E=2B\frac{d\zeta}{dt}. \tag{10b}$$

These are dependent on time only, and $E(t)$ and $\zeta(t)$ are the unknown functions. Eliminating E between them yields

$$2\zeta\frac{d\zeta}{dt}=\frac{H}{\gamma B}, \tag{11}$$

or

$$\frac{d\zeta^2}{dt}=\frac{H_0}{\gamma B_0}|\sin\omega t|. \tag{12}$$

Choosing $\zeta(t)$ to satisfy the above and subsequently calculating $E(t)$ from (10a,b) will prove the hypothesis correct and fix all the quantities of Fig. 2 except the value of δ.

Equation (12) shows that the transition point ζ must always move to the right, a circumstance that seems at first to be strange if not impossible. But it is quite all right. ζ merely starts at the origin and moves to δ where it ceases to exist and a new ζ starts from the origin.

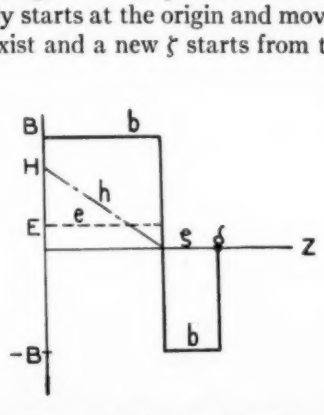

FIG. 2. Hypothesis of solution.

To see that this is so, consider any node of H. If ζ were not zero just after this instant, the sign reversal of H would cause a finite jump in b over a finite region and hence cause a finite jump in $\varphi(0)$ resulting [from (4b)] in $E=\infty$ which is clearly impossible. Consequently $\zeta=0$ just following each node of H.

From this consideration and from (12) we see that subsequent half-periods of $\zeta(t)$ are identical.

Let us calculate $\zeta(t)$ in the first half-period. There we may write

$$\frac{d\zeta^2}{dt}=\frac{H_0}{\gamma B_0}\sin\omega t,$$

whence

$$\zeta^2=\frac{H_0}{\gamma B_0}\frac{1-\cos\omega t}{\omega},$$

$$\zeta=\left(\frac{2H_0}{\omega\gamma B_0}\right)^{\frac{1}{2}}\sin\frac{\omega t}{2}\cdots 0<\omega t<\pi.$$

The value of δ is simply the extreme value of ζ which is attained at the end of each half-period:

$$\delta=\left(\frac{2}{\omega\gamma B_0/H_0}\right)^{\frac{1}{2}}. \tag{13}$$

This is the "depth of penetration" formula: δ is the extreme depth to which the fields penetrate. Since the ratio B_0/H_0 would be the permeability if the material were not ferromagnetic, we see that the formula (13) is formally the usual one for nonferrous materials also; but in the latter case, δ is the depth at which the fields are attenuated by one neper and no extreme depth exists.

My hypothesis will be fully proved if I can now calculate $E(t)$ from (10a,b). But (10a) can be written

$$E=-\frac{1}{\gamma}\frac{H_0\sin\omega t}{\delta\sin\frac{\omega t}{2}}\cdots 0<\omega t<\pi, \tag{14}$$

in the first half-period. Since in successive half-periods H reverses and ζ does not, (10a) shows that E does reverse and so derives easily from its values in the first half-period. Equation (14) can also be written

$$E=\frac{2H_0}{\gamma\delta}\cos\frac{\omega t}{2}\cdots 0<\omega t<\pi. \tag{15}$$

This completes the proof that Fig. 2 is the solution and determines the depth of penetration. A plot of $\zeta(t)$ and $E(t)$ is given in Fig. 3.

Often one would like to find the power loss per unit area into the metal. If we designate by $\bar{H}$ and $\bar{E}$ the peak complex amplitudes of H and the fundamental component of E, then the Poynting vector $\bar{N}$ into the metal would be

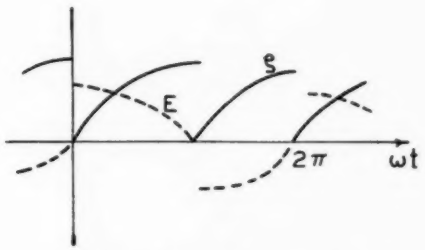

FIG. 3. Wave shapes of two variables.

$$\bar{N}=N+jM=\tfrac{1}{2}\bar{E}\bar{H}^*, \tag{16}$$

where the asterisk means complex conjugate. The real part N of $\bar{N}$ would be the power flow. (The harmonics of E do not contribute to the power flow.) A complex surface impedance (wave impedance at the surface) $\bar{\eta}$ is usually designated by

$$\bar{\eta}=r+jx=\frac{\bar{E}}{\bar{H}}, \tag{17}$$

which allows N to be written:

$$N=\tfrac{1}{2}rH_0^2. \tag{18}$$

Hence the power flow problem reduces to a determination of r which follows readily after the fundamental of E is calculated. To do this, put

$$E=2\sum_1^\infty(A_n\cos n\omega t+B_n\sin n\omega t), \tag{19}$$

wherein, by well-known formulas,

$$A_n=\frac{1}{T}\int_0^T E(t)\cos n\omega t\,dt,$$
$$B_n=\frac{1}{T}\int_0^T E(t)\sin n\omega t\,dt. \tag{20}$$

For $n=1$, by substituting $\omega t=\vartheta$ and using Fig. 3 and Eq. (15),

$$A_1=\frac{2H_0}{\gamma\delta}\frac{1}{2\pi}2\int_0^\pi\cos\frac{\vartheta}{2}\cos\vartheta\,d\vartheta, \tag{21}$$

$$B_1=\frac{2H_0}{\gamma\delta}\frac{1}{2\pi}2\int_0^\pi\cos\frac{\vartheta}{2}\sin\vartheta\,d\vartheta.$$

Or

$$A_1=\frac{H_0}{\gamma\delta\pi}\int_0^\pi\left(\cos\tfrac{3}{2}\vartheta+\cos\frac{\vartheta}{2}\right)d\vartheta=\frac{H_0}{\gamma\delta\pi}(-\tfrac{2}{3}+2),$$
$$B_1=\frac{H_0}{\gamma\delta\pi}\int_0^\pi\left(\sin\tfrac{3}{2}\vartheta+\sin\frac{\vartheta}{2}\right)d\vartheta=\frac{H_0}{\gamma\delta\pi}(\tfrac{2}{3}+2). \tag{22}$$

Consequently,

$$E=\frac{8H_0}{3\gamma\delta\pi}(\cos\omega t+2\sin\omega t)+\cdots. \tag{23}$$

So

$$\bar{E}=\frac{8H_0}{3\gamma\delta\pi}(1-2j). \tag{24}$$

But

$$\bar{H}=-jH_0, \tag{25}$$

whence the surface impedance becomes

$$\bar{\eta}=\frac{16}{3\pi}\frac{1}{\gamma\delta}(1+j\tfrac{1}{2}). \tag{26}$$

The resistance alone can then be written

$$r=\frac{16}{3\pi}\frac{1}{\gamma\delta}. \tag{27}$$

Or

$$r=\frac{16}{3\pi}\left(\frac{\omega B_0/H_0}{2\gamma}\right)^{\frac{1}{2}} \tag{28}$$

is the real part of the surface impedance of massive iron under high incident magnetic fields.

Again, since the ratio B_0/H_0 would be the permeability in the nonferrous case, it is interesting to compare this formula (28) with the known formula for the nonferrous case. This time the formulas are not formally identical since the nonferrous formula does not have the factor $16/3\pi$. This factor might be called the "rectangular multiplier." Also in the nonferrous case the phase angle is 45° and not as shown in (26).

The power input density may hence be estimated by the following rule. From the values of B_0, H_0 at the surface, calculate the nonferrous power. Multiplication by the "rectangular multiplier" $16/3\pi=1.70$ will give the correct result for a rectangular magnetization curve. This should be nearly correct for very strong fields. Since the true magnetization curve from H_0, B_0 down would lie between the linear and rectangular case it seems plausible to presume that the true "ferrous multiplier" shifts from unity to $16/3\pi$ with increasing saturation.

At complete saturation, the power input would be specifically

$$N=\frac{16}{3\pi}\frac{1}{2}\left(\frac{\omega B_0/H_0}{2\gamma}\right)^{\frac{1}{2}}H_0^2. \tag{29}$$

It is even more interesting to compare formula (28) with the work of Rosenberg.[1] In his pioneering paper the result for the power input density is given in mixed units. Surface impedance is not mentioned, but the resistance part can be implied from his formula. When this is done, and the notation and units of the present paper are used, one finds for his value

$$r_{\text{Rosenberg}}=\frac{\pi}{4}r.$$

In other words, Rosenberg's "ferrous multiplier" is 4/3.

Rosenberg's formula for the power input to massive iron has been in common use for three decades. It always gave good results, but it was often felt that his assumptions were numerous and obscure. Basically it was his intention to simplify to the extreme limit of complete rectangular saturation, but to avoid coping with the discontinuities so introduced, he used a flux density of constant amplitude although sinusoidal. He also neglected phase relations. All these laxities involved, at most, only numerical factors of the order of magnitude unity and together they tended to mitigate the harshness of the original simplification, so that in effect his "ferrous multiplier" comes out almost exactly halfway between the limits set above.

APPENDIX

The power input formula

$$N=\tfrac{1}{2}H_0^2\frac{16}{3\pi}\left(\frac{\omega B_0/H_0}{2\gamma}\right)^{\frac{1}{2}}=\tfrac{1}{2}H_0^2\frac{16}{3\pi}\frac{1}{\gamma\delta},$$

obtained from (18) and (28) should check with the total dissipation calculated from

$$N=\int_0^\infty \gamma\langle e^2\rangle dz,$$

where $\langle\ \rangle$ means time average. This latter calculation is more elaborate than the one presented, but it was made and does check.

[1] E. Rosenberg, Elektrotech. Z. **44**, 513 (1923); or, alternatively, Electrician **91**, 188 (August, 1923).

PPI Light Spot Brightness Probability Distributions*

GEORGE C. SPONSLER AND FERN L. SHADER†
Lincoln Laboratory, Massachusetts Institute of Technology, Lexington, Massachusetts
(Received November 30, 1953)

A mathematical study utilizing the statistics of noise theory is presented which derives light spot brightness probabilities for PPI target returns of various signal-to-noise ratios. An idealized model is employed which differs from similar previous ones by taking account of the cathode-ray tube's highlight brightness *vs* intensifier electrode voltage characteristic. For the 10KP7 cathode-ray tube this characteristic obeys an approximate 2.5 power law in typical operation. This law, together with a square law second detector, combine to form an over-all fifth power detector. The light spot brightness of the display is assumed to be formed by linear superposition of individual target returns resulting from the radar antenna scan. In the model, seven identical returns are so integrated.

Various mathematical methods of handling the problem are considered. The Edgeworth series approximation is found to give poor results compared with the Laguerre polynomial approximation. By the latter method the light brightness probabilities are found to be obtainable by interpolation from a table of the incomplete gamma function. Ancillary tables of statistical moments and selected values of the confluent hypergeometric function, ${}_1F_1(-5n/2; 1; -x)$, are included in the text.

INTRODUCTION

THE ability of radar sets to detect targets is generally expressed as a percentage likelihood of detection under certain conditions of operation. For every radar, this detection probability is found to be principally a function of the signal-to-noise ratio of the radio signal reflected by the target. In addition to the signal-to-noise ratio many other factors enter which reflect the manner of construction and operation of a particular radar. For example, the type of second detector and integration of the individual radar returns greatly affect the detection probability. A most thorough and extensive study of these factors has been made by Marcum.[1] He does not, however, include the nonlinear transfer characteristic of the cathode-ray tube display, but rather, as he states, analyzes a theoretically optimum performance. The following analysis of this paper, while treating in a similar fashion a similar idealized model of a radar, includes the highlight brightness, intensifier electrode voltage transfer characteristic and demonstrates, under certain assumptions, that the resultant over-all model may be represented as a fifth law detector followed by an integrator which adds individual target returns.

MATHEMATICAL DERIVATION

The following analysis considers only those portions of the radar receiver and display which are subsequent to the IF amplifier. The second detector is taken to be of the square law variety and the video amplifier is assumed to have infinite band width. The cathode-ray display tube is taken to be a 10KP7 which has a highlight brightness, intensifier electrode control voltage characteristic which follows an approximate 2.5 power law as typically operated (Fig. 1 shows the RCA Tube Handbook typical operation highlight brightness curve and a calculated 2.5 power curve scaled at the 45-volt intercept point).

For a single target return, the display light spot brightness is assumed to possess a probability function related to the amplitude probability function of the intensifier grid control voltage by the 2.5 power transfer function. The cathode-ray tube screen light persistence decay time is considered to be long compared to the time interval occupied by the total multiple returns received from the target during one scan period. The analysis does not take account of the actual pulse shape and considers the contribution to the light spot bright-

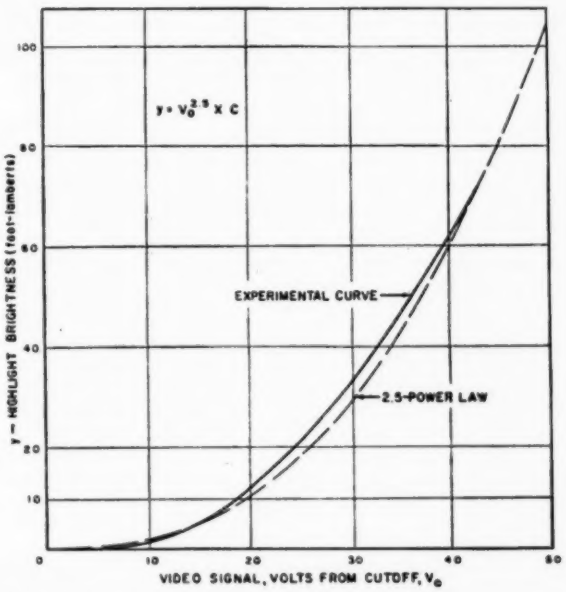

FIG. 1. Highlight brightness *vs* intensifier electrode voltage (10KP7, RCA Tube Handbook).

* The research in this document was supported jointly by the Army, Navy, and Air Force under contract with the Massachusetts Institute of Technology.

† Staff Members, Lincoln Laboratory, Massachusetts Institute of Technology, Lexington, Massachusetts.

[1] J. I. Marcum, "A Statistical Theory of Target Detection by Pulsed Radar, with Mathematical Appendix," Rand Reports RN 753 and 754, reissued 25 April, 1952.

ness by each target return to be formed during one instant of time. The analysis is thus of the so-called "one-point theory" type.[2]

The light brightness of each target return is assumed to be added linearly to the other individual target return contributions thereby forming a single, composite spot viewed by the observer. Thus, the individual returns are considered to be unresolved visually and no treatment is made of spot shape or dimensions. The preceding assumptions constitute the mathematical model as treated in this paper.

The signal at the input of the second detector is taken to be the usual sine wave $P\sin\omega t$ plus random Gaussian noise. The envelope of the combination possesses the amplitude probability density function developed by Rice.[3,4]

$$W(R)dR=\frac{R}{\psi_0}\exp\left[-\frac{R^2+P^2}{2\psi^0}\right]I_0\left(\frac{(RP)}{\psi_0}\right)dR, \quad R\geq 0$$
$$=0, \quad R<0. \tag{1}$$

The statistical problem is to determine the transformation effected upon this density function by the various elements of the radar model employed. In essence, there are only two such distinct operations involved: transformation by an nth order detector and linear superposition of similar signals. These two operations may be handled analytically in closed form or by use of infinite series approximations involving knowledge of the statistical moments of the distributions.

The analytical solution as determined with the aid of noise theory and of statistical mathematics is quickly outlined. If cognizance is taken that the probability density functions used here are zero for negative arguments then the rule for the transformation affected by nth law detector $y=\phi^n$ is[5]

$$W(y)dy=W(\phi)d\phi,$$

or

$$W(y)=\left.\frac{W(\phi)}{\left|\frac{dy}{d\phi}\right|}\right|_{\phi=y^{1/n}}, \quad \phi, y\geq 0 \tag{2}$$
$$=0, \quad y<0$$

where y and ϕ or bi-uniquely related.

The linear superposition of independent variables is a common statistical problem and can be handled analytically by use of the so-called characteristic functions[6] $F(\omega)$, where

$$F(\omega)=\int_{-\infty}^{\infty}W(y)e^{i\omega y}dy$$
$$W(y)=\frac{1}{2\pi}\int_{-\infty}^{\infty}F(\omega)e^{-i\omega y}d\omega. \tag{3}$$

These equations are recognized to be a Fourier transform pair. Thus, the superposition of N independent but statistically identical random variables may be treated by taking the nth power of their common characteristic function and then taking the inverse transform to find the composite distribution. Symbolically this process yields

$$W(y)=\frac{1}{2\pi}\int_{-\infty}^{\infty}[F(\omega)]^N e^{-i\omega y}d\omega. \tag{4}$$

Thus in theory the entire problem is readily solved. However, in practice, the transforms may lead to unrecognizable analytical expressions and ones difficult to handle even numerically. The transforms may be avoided by utilizing the convolution theorem which states that the inverse transform of the product of two transforms is the convolution of their individual inverse transforms, i.e.,

$$\frac{1}{2\pi}\int_{-\infty}^{\infty}F_1(\omega)F_2(\omega)e^{-i\omega y}d\omega=\int_{-\infty}^{\infty}W_1(y-\tau)W_2(\tau)\tau d. \tag{5}$$

The inverse transform of $[F(\omega)]^N$ may be considered to be an iterated convolution of the factors taken one at a time with the remaining factors grouped together.

Thus, if three statistical variables were to be added, the composite probability density of the three would be

$$W(y)=\int_{-\infty}^{\infty}W_1(y-\tau_1)\left\{\int_{-\infty}^{\infty}W_2(\tau_1-\tau_2)W_3(\tau_2)d\tau_2\right\}d\tau_1.$$

The lower limits are zero because the W_i's are zero for negative argument.

For the addition of "N" independent random variables, this iterated convolution may be generalized as

$$W(y)=\int\int_0^{\infty}\cdots\int W(\tau_{N-1})\prod_{i=1}^{N-1}W(\tau_{i-1}-\tau_i)d\tau_i, \tag{6}$$

where $y=\tau_0$ and the respective integrals are evaluated successively beginning with τ_{n-1} and working down to τ_1.

With the probability density of Eq. (1) and the radar model outlined, the expressions developed do not yield recognizable integrals with either the characteristic function or the iterated convolution method. Numerical evaluation of either method is quite complex

[2] J. L. Lawson and G. E. Uhlenbeck, *Threshold Signals* (McGraw-Hill Book Company, Inc., New York, 1950), Section 7.3.

[3] S. O. Rice, Bur. Standards Tech. J. **23**, 282–332 (1944); **24**, 46–156 (1945).

[4] For meaning of symbols not defined in the text consult the glossary at the end of the paper.

[5] W. B. Davenport, Jr., "Notes on an Introduction to Noise Theory," Mass. Inst. Technol. E. E. Lab. Sec. 2.3, 1952 (unpublished).

[6] H. Cramér, *Mathematical Methods of Statistics* (Princeton University Press, Princeton, 1946), pp. 89 *et seq.*

and most difficult to program for an automatic computer. The solution of the quandary is to employ a series approximation.[7,8]

All the infinite series approximation methods applicable depend upon knowledge of the statistical moments of the distribution to be expanded. Although the particular distribution function of the output of a circuit element may not be known or calculable, often the moments of this output are easily determined (as is the case here) and hence a series approximation can be made. Therefore, the first step in the development of any such series expansion is to determine the moments of the distribution to be expanded.

The expression for the probability density of the amplitude of the envelope of combined sine wave plus Gaussian noise as presented in Eq. (1) is simplified for analysis if the substitutions

$$v=\frac{R}{\sqrt{\psi^0}},\quad a=\frac{P}{\sqrt{\psi^0}},\quad x=\frac{a^2}{2} \tag{7}$$

are made. In this notation x is the signal to noise power ratio.

The output of the square law second detector is related to its input by

$$\begin{aligned} v_0&=v^2, \quad v\geq 0\\ &=0, \quad v<0. \end{aligned} \tag{8}$$

The proportionality constant has been taken to be unity for convenience. Actually, any proportionality constant could be employed as the analysis leads to ratios of parameters of equal powers in which the proportionality constants cancel in numerator and denominator. The analysis would thus require a scale factor to yield absolute values. These factors may be obtained by comparison with experiment or by inserting the particular proportionality constant desired at the appropriate points in the analysis and observing the resulting change in scale of the dependent variable.

A video amplifier of infinite band width does not alter the signal and so the input to the cathode-ray tube intensifier electrode is v_0. For the 10KP7 tube the light brightness is related to the intensifier voltage by an approximate 2.5 power law (a graph on semilog paper yields 2.6 as a better approximation, but 2.5 is more amenable to analysis), i.e.,

$$\begin{aligned} y&=v_0^{2.5}, \quad v_0\geq 0\\ &=0, \quad v_0<0, \end{aligned} \tag{9}$$

hence

$$\begin{aligned} y&=v^5, \quad v\geq 0\\ &=0, \quad v<0. \end{aligned} \tag{10}$$

Up to this point then, the radar model is thus that of an over-all fifth law detector.

The statistical moments of Eq. (1) have been determined by Rice.[3] As shown by Harrington[9] the nth moment of the output of a kth law detector is the same as the knth moment of the output of a linear detector. For a fifth law detector the expression for the moments as given by Harrington becomes

$$\langle y^n\rangle_{Av}=2^{5n/2}\Gamma[1+5n/2]\,{}_1F_1[-5n/2;1;-x]. \tag{11}$$

A table of the hypergeometric function

$${}_1F_1[-5n/2;1;-x]$$

is presented in Table I for certain selected values of x. To the authors' knowledge, no table of this function had been published for these particular parameter values.[10] The exact series expansion was employed for calculation of the values tabulated. This exact series is

$${}_1F_1\left[\frac{-5n}{2};1;-x\right]=\sum_{k=0}^{\infty}\frac{\left(\frac{-5n}{2}\right)\left(\frac{-5n}{2}+1\right)\left(\frac{-5n}{2}+2\right)\cdots\left(\frac{-5n}{2}+k-1\right)}{(k!)^2}(-x)^k. \tag{12}$$

A sufficient number of terms of this series was taken to assure 10 significant figures;[11] the number of terms depends upon n and ranges between 7 to 30. The tabulated values have been checked with a differencing machine.

Using Eq. (12) and tables of the gamma function, the moments of Eq. (11) are easily calculated.

The two series most generally used for the type of distribution to be expanded here are the Edgeworth series and the Laguerre series.[1,6] Both of these series employ central moments in their respective term coefficients. These central moments are defined by

$$\mu_n=\int_{-\infty}^{\infty}(y-\bar{y})^n W(y)dy. \tag{13}$$

The first few central moments are thus related to the moments of the distribution as given by Eq. (11) by

[7] W. M. Stone, J. Appl. Phys. **24**, 935 (1953).

[8] J. V. Harrington, "An Analysis of the Detection of Repeated Signals in Noise by Binary Integration," Technical Report No. 13, Lincoln Laboratory, Mass. Inst. Technol. (14 August, 1952).

[9] J. V. Harrington and T. S. Rogers, Proc. Inst. Radio Engrs. **38**, No. 10, 1198 (1950).

[10] For other values of this function, see D. Middleton and V. Johnson, "A Tabulation of Selected Confluent Hypergeometric Functions," NR-078-011, Harvard University, Cambridge, Massachusetts (Jan. 5, 1952).

[11] For n even the series reduces to a polynomial.

TABLE I. Tables of the confluent hypergeometric function ${}_1F_1[(-5n/2); 1; -x]$.

x^n	1	2	3	4	5
0	1.0	1.0	1.0	1.0	1.0
0.25	1.6844013	2.5893636	3.7615664	5.2550531	7.13216
0.50	2.4907866	4.9716146	8.8682725	14.742248	23.32511
0.75	3.4238235	8.3335205	17.3586439	32.915847	58.5102
1.00	4.4880471	12.8833333	30.544399	64.666620	126.7413
1.25	5.6878696	18.851766	50.054413	116.722757	249.244
1.50	7.0275883	26.492969	77.882853	198.12750	457.057
1.75	8.5113924	36.085506	116.441685	320.80346	794.395
2.00	10.1433703	47.933333	168.61775	500.21438	1322.877
2.5	13.86773	79.743490	328.11952	1113.55060	3319.56
3.0	18.231575	124.900000	591.45791	2265.1277	7520.52
3.5	23.264528	186.84818	1005.79830	4301.8614	15762.50
4.0	28.995073	269.53333	1633.1594	7736.8178	31059.1
4.5	35.450663	377.43203	2553.5603	13308.3426	58186.5
5.0	42.657815	515.58333	3868.5867	22054.640	1.044951×10^5
5.5	50.642196	689.62005	5705.4058	35406.682	1.81017×10^5
6.0	59.428694	905.80000	8221.2593	55302.690	3.03949×10^5
6.5	69.041485	1171.03724	11608.4683	84327.840	4.96620×10^5
7.0	79.504082	1492.9333	16099.978	125883.218	7.92054×10^5
7.5	90.839391	1879.8086	21975.477	184388.57	1.236290×10^6
8.0	103.069751	2340.7333	29568.125	265523.80	1.89262×10^6
8.5	116.21697	2885.5591	39271.918	376514.77	2.84698×10^6
9.0	130.30237	3524.9500	51549.732	526469.34	4.21467×10^6
9.5	145.34679	4270.4138	66942.069	726770.41	6.14879×10^6
10.0	161.37068	5134.3333	86076.554	991533.10	8.85069×10^6

the equations

$$\mu_2=\sigma^2=\langle y^2\rangle_{Nw}-\langle y^2\rangle_{Nw}=\langle y^2\rangle_{Nw}-m^2,$$
$$\mu_3=\langle y^3\rangle_{Nw}-\langle 3y^2\rangle_{Nw}m+2m^3, \quad (14)$$
$$\mu_4=\langle y^4\rangle_{Nw}-\langle 4y^3\rangle_{Nw}m+\langle 6y^2\rangle_{Nw}m^2-3m^4.$$

TABLE II. Tables of $\mu_{i,0}$ and $\mu_{i,p}$.

x	m_0	$\mu_{2,0}$	$\mu_{3,0}$	$\mu_{4,0}$
0	18.799712	3.4866×10^3	2.3372×10^4	3.5326×10^5
0.25	31.666259	8.9404×10^3	8.6752×10^4	1.86873×10^{10}
0.50	46.826072	1.68983×10^4	2.00533×10^7	5.1817×10^{10}
0.75	64.366895	2.7858×10^4	3.8454×10^7	1.14000×10^{11}
1.00	84.373992	4.2353×10^4	6.6277×10^7	2.2045×10^{11}
1.25	106.93031	6.0957×10^4	1.06386×10^8	3.9146×10^{11}
1.50	132.11664	8.4278×10^4	1.6215×10^8	6.5354×10^{11}
1.75	160.01173	1.12965×10^5	2.3750×10^8	1.04059×10^{12}
2.00	190.69244	1.4770×10^5	3.3694×10^8	1.5954×10^{12}
2.5	260.70935	2.3825×10^5	6.2953×10^8	3.4332×10^{12}
3.0	342.74835	3.6214×10^5	1.08997×10^9	6.7501×10^{12}
3.5	437.36642	5.2621×10^5	1.7811×10^9	1.23911×10^{13}
4.0	545.09903	7.3788×10^5	2.7804×10^9	2.1542×10^{13}
4.5	666.46226	1.00517×10^6	4.1816×10^9	3.5826×10^{13}
5.0	801.95464	1.3367×10^6	6.0964×10^9	5.7411×10^{13}
6.0	1117.24234	2.2300×10^6	1.20170×10^{10}	1.34711×10^{14}
7.0	1494.6539	3.4989×10^6	2.1874×10^{10}	2.8726×10^{14}
8.0	1937.6816	5.2338×10^6	3.7418×10^{10}	5.6836×10^{14}
9.0	2449.6470	7.5350×10^6	6.0888×10^{10}	1.05848×10^{15}
10.0	2732.4779	1.05124×10^7	9.5082×10^{10}	1.8748×10^{15}

x	m_p	$\mu_{2,p}$	$\mu_{3,p}$	$\mu_{4,p}$
0	131.598	2.4406×10^4	1.6361×10^7	2.6260×10^{10}
0.25	221.664	6.2583×10^4	6.0726×10^7	1.38686×10^{11}
0.50	327.7825	1.18288×10^5	1.40373×10^8	3.9156×10^{11}
0.75	450.568	1.9500×10^5	2.6918×10^8	8.7969×10^{11}
1.00	590.618	2.9647×10^5	4.6394×10^8	1.73848×10^{12}
1.25	748.512	4.2670×10^5	7.4470×10^8	3.1556×10^{12}
1.50	924.816	5.8995×10^5	1.13506×10^9	5.3847×10^{12}
1.75	1120.08	7.9075×10^5	1.6625×10^9	8.7623×10^{12}
2.00	1334.85	1.03390×10^6	2.3586×10^9	1.37260×10^{13}
2.5	1824.97	1.6677×10^6	4.4067×10^9	3.0809×10^{13}
3.0	2399.24	2.5350×10^6	7.6298×10^9	6.3099×10^{13}
3.5	3061.56	3.6835×10^6	1.24679×10^{10}	1.20489×10^{14}
4.0	3815.69	5.1651×10^6	1.9463×10^{10}	2.1758×10^{14}
4.5	4665.23	7.0362×10^6	2.9271×10^{10}	3.7531×10^{14}
5.0	5613.68	9.3570×10^6	4.2675×10^{10}	6.2291×10^{14}
6.0	7820.70	1.56103×10^7	8.4119×10^{10}	1.56136×10^{15}
7.0	10462.6	2.4492×10^7	1.53119×10^{11}	3.5382×10^{15}
8.0	13563.8	3.6637×10^7	2.6193×10^{11}	7.4039×10^{15}
9.0	17147.5	5.2745×10^7	4.2621×10^{11}	1.45206×10^{16}
10.0	21236.1	7.3587×10^7	6.6557×10^{11}	2.6982×10^{16}

Here we have called the mean "m" rather than $\langle y\rangle_{Nw}$.

Account has not yet been taken of the results of superimposing or adding the individual target echoes which make up a single target spot on the display tube. A model was taken wherein a total of 7 returns of equal intensity were to be added to form the spot. (These 7 returns on an equal energy basis correspond to 24 returns of binomially weighted intensity from a radar having a scan period of 15 seconds, a repetition rate of 3000 pps, and a beam width of about 1.75°.) Both the Edgeworth and the Laguerre series may be employed to represent the resultant or composite distribution arising from the superposition of these individual contributions if it is recognized that the central moments appearing in the individual term coefficients are the moments of the resultant or composite distribution rather than those of the individual or contributor distributions. The central moments of this composite distribution are obtainable from those of the contributor distributions with the aid of the so-called semi-invariants or cumulants.[6]

The first four semi-invariants are

$$X_1=m, \quad X_2=\sigma^2, \quad X_3=\mu_3, \quad X_4=\mu_4-3\sigma 4. \quad (15)$$

The semi-invariants have the property that the semi-invariants of the sum of a set of independent random variables are the sum of the respective semi-invariants of each individual random variable. Hence, if we superimpose N_p statistically identical but yet independent target returns on the face of the display tube to form a spot, the central moments ($\mu_{i,p}$) of the composite distribution function are related to the individual semi-

invariants ($\mu_{i,0}$) by

$$\mu_{i,p}=N_p\mu_{i,0},$$

or

$$m_p=N_pm_0,\quad \sigma_p=(N_p\sigma_0)^{\frac{1}{2}},\quad \mu_{3,p}=N_p\mu_{3,0},$$
$$\mu_{4,p}=N_p[\mu_{4,0}-3\sigma_0^4]+3N_p^2\sigma_0^4. \tag{16}$$

In the present situation, $N_p=7$. Table II presents a listing of the first few $\mu_{i,0}$ and $\mu_{i,p}$ for the fifth law detector and for selected values of the signal-to-noise ratio x. Thus, it is possible to compute the moments of the composite distribution; with them we can express the composite envelope amplitude density distribution by means of either an Edgeworth or Laguerre polynomial series.

The Edgeworth series is a rearranged Gram-Charlier series which expands the function in a set of orthogonal derivatives of the normal distribution or error function. The first three terms of the Edgeworth series are generally all that one uses and often are written as

$$W(y_i')dy_i'=\left\{\phi(y_i')-\frac{1}{3!}\frac{\mu_{3,i}}{\sigma_i^3}\phi^{(3)}(y_i')\right.$$
$$+\left[\frac{1}{4!}\left(\frac{\mu_{4,i}}{\sigma_i^4}-3\right)\phi^{(4)}(y_i')\right.$$
$$\left.\left.+\frac{10}{6!}\left(\frac{\mu_{3,i}}{\sigma_i^3}\right)\phi^{(6)}(y_i')\right]\right\}dy_i'. \tag{17}$$

The term involving $\phi^{(6)}$ is an approximation to the actual term and the entire series is asymptotic.

As the probability that the light spot brightness will exceed a given level is desired rather than the probability density, it is convenient to integrate the series with the aid of the relations

$$\int_{y_i}^{\infty}\phi^{(n)}(y_i')dy_i'=-\phi^{(n-1)}(y_i')$$

and

$$\phi^{(-1)}(y_i')=\int_{-\infty}^{y_i'}\phi(y_i')dy_i'.$$

The integral of Eq. (17) thus becomes

$$P(y\geq y_b)=\int_{y_b}^{\infty}W(y_i')dy_i'$$
$$=[1-\phi^{(-1)}(y_b')]+\frac{1}{3!}\frac{\mu_{3,i}}{\sigma_i^3}\phi^{(2)}(y_b')+$$
$$-\frac{1}{4!}\left(\frac{\mu_{4,i}}{\sigma_i^4}-3\right)\phi^{(3)}(y_b')$$
$$-\frac{10}{6!}\left(\frac{\mu_{3,i}}{\sigma_i^3}\right)^2\phi^{(5)}(y_b'). \tag{18}$$

In both Eqs. (17) and (18) the variables have been replaced by the standardized variable

$$y_i'\equiv\frac{y_i-m_i}{\sigma_i}. \tag{19}$$

Numerical computation demonstrated the Edgeworth series approximation gave a poor approximation of the composite distribution function. The asymptotic nature of the series is too apparent for such a low number of superpositions as is seven. The Edgeworth series approximation is shown in Fig. 3a for $x=0$ and again in Fig. 3b for $x=10$. The behavior expected of an asymptotic series, namely that for a fixed number of terms the sum approaches the true function value for large argument, is demonstrated by comparison of Figs. 3a and 3b. The approximation of Fig. 3b is seen to be much better than that of Fig. 3a.

Since the Edgeworth series gave poor results, recourse was taken to another orthogonal function series expansion which seems especially well suited for distribution functions having zero value for negative arguments.[12] This expansion is made with Laguerre polynomials such that

$$f(y)=\sum_{i=0}^{\infty}a_ie^{-y}y^{\alpha}L_i^{\alpha}(y). \tag{20}$$

Here the L_i^{α} are generalized Laguerre polynomials and the coefficients a_i are determined by

$$a_i=\frac{i!}{\Gamma(\alpha+i+1)}\int_0^{\infty}L_i^{\alpha}(y)f(y)dy. \tag{21}$$

Development in such a series with a change of variable permits the inclusion of two arbitrary parameters (α is one). By judicious choice of these two parameters, the second and third terms of the resulting series can be made to vanish and the first term alone becomes a good approximation. If such a choice is made and the appropriate light spot brightness moments employed, the resultant probability density function of light spot

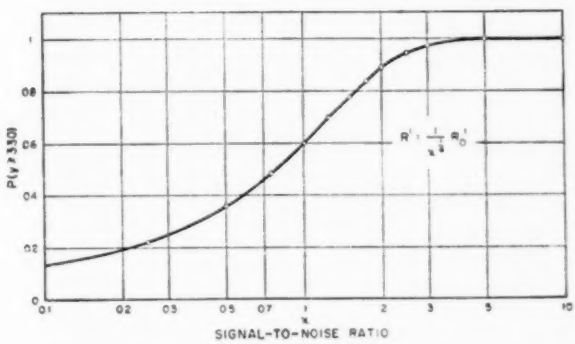

FIG. 2. Probability of signal amplitude exceeding arbitrary reference level 330 as a function of signal-to-noise ratio.

[12] See reference 6, pp. 35–37.

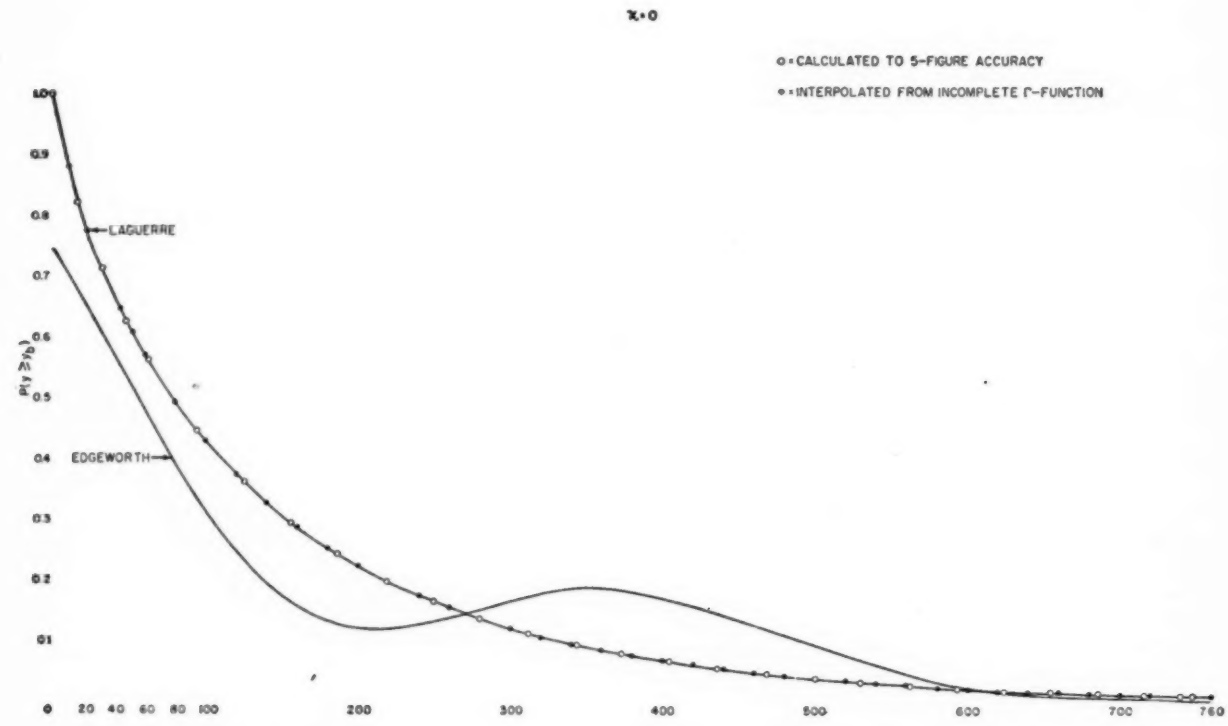

FIG. 3a. Probability that the received signal y will exceed detection level y_b for zero signal-to-noise ratio.

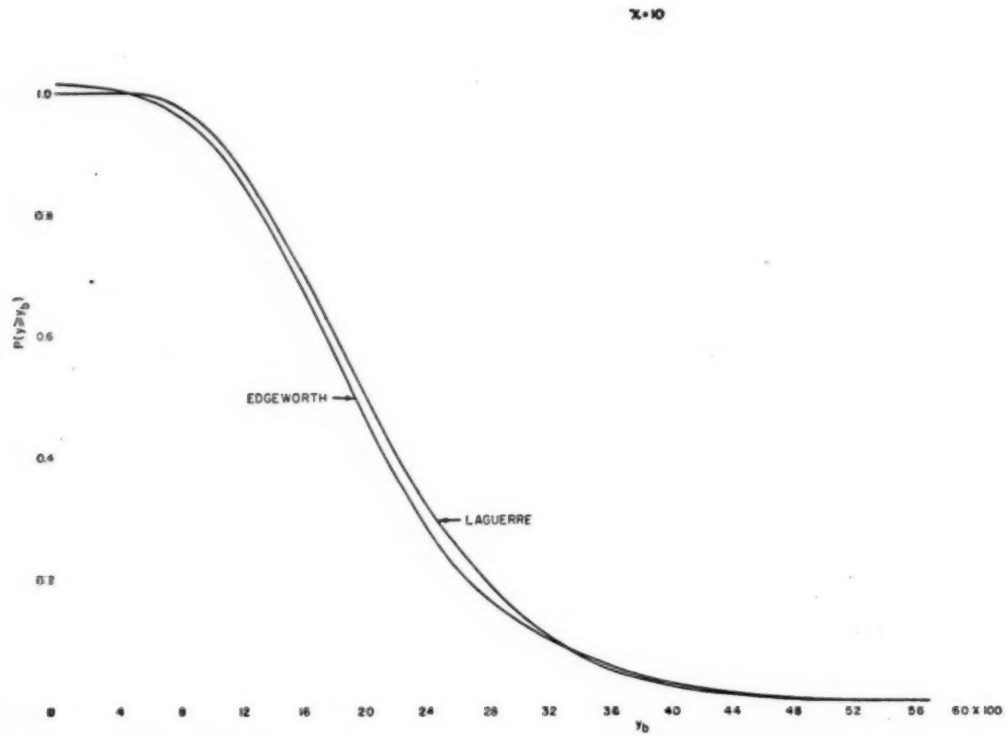

FIG. 3b. Probability that the received signal y will exceed detection level y_b for signal-to-noise ratio of 10.

brightness becomes

$$W(y)dy=\frac{m}{\sigma^2\Gamma[m^2/\sigma^2]}\left[\frac{m}{\sigma^2}y\right]^{[(m^2/\sigma^2)-1]}\exp\left[\frac{-m}{\sigma^2}y\right]dy. \tag{22}$$

The probability that the light spot brightness will exceed a certain level is the integral of this function, i.e.,

$$P(y\geq y_b)=\int_{Y_b}^{\infty}W(y)dy=1-I\left[\frac{y_b}{\sigma},\frac{m^2}{\sigma^2}-1\right]. \tag{23}$$

Here, $I(\mu,p)$ is the incomplete gamma function which is defined to be

$$I(\mu,p)\equiv\int_0^{\mu(p+1)^{\frac{1}{2}}}\frac{e^{-v}v^p}{p!}dv,$$

and has been tabulated by Pearson.[13] Figures 2‡, 3a, and 3b which present the probability that the light spot brightness will exceed a specified (nonabsolute) relative value, were obtained by linear interpolation of this table of incomplete gamma functions. Table III presents m_p, σ_p, and $(m_p/\sigma_p)^2-1$ for certain signal-to-noise ratios, x. These values may be employed to determine P of Eq. (23) by interpolation in the table of incomplete gamma functions.

TABLE III. Tables of m_p, σ_p, and $(m_p/\sigma_p)^2-1$.

x	m_p	σ_p	$(m_p/\sigma_p)^2-1$
0	131.598	156.224	−0.29042
0.25	221.664	250.166	−0.21488
0.50	327.7825	343.931	−0.091699
0.75	450.568	441.592	+0.041068
1.00	590.618	544.492	0.17661
1.25	748.512	653.220	0.31304
1.50	924.816	768.080	0.44977
1.75	1120.08	889.242	0.58657
2.0	1334.85	1016.81	0.72339
2.5	1824.97	1291.40	0.99704
3.0	2399.24	1592.16	1.27077
3.5	3061.56	1919.23	1.5447
4.0	3815.69	2272.69	1.8188
4.5	4665.23	2652.58	2.0932
5.0	5613.68	3058.92	2.3679
6.0	7820.70	3950.99	2.9181
7.0	10462.6	4948.95	3.4694
8.0	13563.8	6052.82	4.0216
9.0	17147.5	7262.59	4.5747
10.0	21236.1	8578.26	5.1284

[13] K. Pearson, *Tables of the Incomplete Gamma Function*, (Cambridge University Press, Cambridge, 1951).

‡ The 330 detection level of Fig. 2 corresponds to a 10 percent probability of detection of pure noise.

Figures 2, 3a, and 3b give the probability for a 10KP7 cathode-ray tube and for the radar model employed that the light spot brightness representing a target return will exceed certain selected relative values. The model is idealized and the probability predictions cannot be experimentally verified but must be considered as an estimate of the behavior of the actual radar.[14]

In conclusion, it should be noted that the analysis and results as here presented apply equally well to the determination of the composite envelope amplitude probability function of independent samples of sine wave plus Gaussian noise for any type of fifth law detector and subsequent N-fold signal superposition and are not confined simply to light spot brightness probabilities.

GLOSSARY OF SYMBOLS

${}_1F_1$	Confluent hypergeometric function.
$F(5)$	Characteristic function Fourier transform of $W(y)$.
(x)	Gamma function of X.
I_0	Modified Bessel function of first kind.
$I(\mu,p)$	Incomplete gamma function.
L_i^{α}	Generalized Laguerre polynomial.
m	Mean or average value.
N_p	Number of signals superimposed or added.
$\mu_{i,0}$	ith central moment of the individual contribution distribution.
$\mu_{i,p}$	ith central moment of composite distribution.
$P(y\geq y_b)$	Probability of y is equal to or greater than y_b.
$\phi^{(n)}(y')$,	nth derivative of the error function.
ψ_0	Mean noise power.
R	Amplitude of envelope of combined noise and sine wave.
R'	Range of target from radar.
R_0'	"Idealized" range.
σ	Standard deviation.
τ	Variable of integration.
v	Ratio of amplitude to root mean square noise power.
$W(R)$	Probability density function of R.
x	Signal to noise ratio.
y	Light spot brightness.
μ_i	i^{+3} central moment.
y_i'	Standardized variable.

[14] D. Middleton, J. Appl. Phys. **74**, 371, 379 (1953); **25**, 127, 128 (1954).

Direct Cellular Evaluation of the Density of States in Phase Space and the Accurate Calculation of Fermi Levels

LOUIS GOLD*
Massachusetts Institute of Technology, Cambridge, Massachusetts
(Received December 2, 1953)

A new procedure for rigorously deducing the energy distribution of states, formulated upon a direct summing of cells in k space, provides a sound basis for assessing the classical approximation so familiar in statistical mechanics. It is thus established that the latter approach underestimates the density of states to the extent that the conventional Fermi energy calculation for electrons in metals is a few percent too high.

IN dealing with the statistics of particles such as electrons, photons, phonons, etc., the spherical approximation[1] serves as a neat artifice for determining the distribution of states in phase space. Our purpose here is to demonstrate that the distribution can be evaluated directly by a technique that entails the explicit summing of cells and so avoids the introduction of an unknown degree of error. Accordingly a basis for appraising the spherical approximation is afforded in this rigorously exact calculation.

Preliminary reflection suggests that the spherical method tends toward a lower limit for the number of cells between the wave numbers k and $k+\Delta k$ since the actual surface, although approaching that of a sphere, is truly a puckered one, so that one really should have

$$c(k)\Delta k=\frac{4\pi}{8}\cdot\alpha k^2\Delta k, \tag{1}$$

where α is a correction factor presumably greater than unity, but whose magnitude remains to be ascertained by the analysis to follow. It will be of particular interest to learn how the Fermi energy calculation for electrons in metals is affected by such a correction.

THE SHELL TREATMENT OF THE CELLULAR CONFIGURATION IN k SPACE

We wish to develop a methodology for summing cells which are to be identified in terms of the indices k_x, k_y, k_z as they appear in the familiar energy relation

$$E=\frac{h}{8mV^{\frac{1}{3}}}(k_x^2+k_y^2+k_z^2)=\frac{h}{8mV^{\frac{1}{3}}}k^2. \tag{2}$$

Consider the number of cells in each succeeding shell of a cubic segment of the k space which includes all cells from (000) to (jjj).

One has the sequence of layers

1st shell — $\{000\}$
2nd shell — $\{100\}$, $\{110\}$, $\{111\}$
.
.
.
Jth shell $=j+1-\{jjj\}$, $\{jj-1j\}$, $\cdots\{j0j\}$
$\{jj-1j-1\}$, $\cdots\{jj-1\,0\}$
.
.
.
$\{j\,0\,j-1\}$, $\cdots\{j00\}$.

The curly bracket indicates that due allowance for multiplicity must be made such that

$\{k_xk_yk_z\}$ has 6-fold degeneracy for $k_x\neq k_y\neq k_z$
3-fold degeneracy for $k_x\neq k_y=k_z$.

The summing operation for the cells in the Jth$(j+1)$ shell is expedited if the various members are arranged systematically in the schematic array

Terms	Cell designations				Row totals
$j+1$	(jjj)	$(jjj-1)$	$(jjj-2)$	$\cdots(jj0)$	$1+3j$
j		$(jj-1\,j-1)$	$(jj-1\,j-2)\cdots(jj-1\,0)$		$3+6(j-1)$
$j-1$			$(jj-2\,j-2)\cdots(jj-2\,0)$		$3+6(j-2)$
.			.	.	.
.			.	.	.
.			.	.	.
1				$(j00)$	3

Here the *Term* column refers to the number of terms in each row, while the *Row totals* column lists the sums for each row with appropriate observance of the degeneracies.

There obtains then for the net number of cells in the jth index shell

$$c_j=1+3j+3\sum_{l=1}^{j}[1+2(j-l)]. \tag{3}$$

Making use of the explicit sums

$$\sum_{l=1}^{j}(j-l)=j^2-\sum_{l=1}^{j}l \tag{4}$$

and

$$\sum_{l=1}^{j}l=\frac{j(j+1)}{2} \tag{5}$$

the calculation of c_j yields

$$c_j=1+3j(1+j),\quad c_J=1+3J(J-1). \tag{6}$$

* Author's present address: 68 Standish Road, Watertown 72, Massachusetts.

[1] The spherical approximation is the conventional approach and may be found, for example, in Mayer and Mayer, *Statistical Mechanics* (John Wiley & Sons, Inc., New York, 1940), p. 54.

As for the grand sum, up to and including the nth layer, the evaluation derives from

$$c_n=\sum_{J=1}^{n} c_J=\sum_{J=1}^{n}[1+3J(J-1)], \tag{7}$$

whereby invoking the relation

$$\sum_{1}^{n} J^2=\frac{n}{6}(n+1)(2n+1) \tag{8}$$

leads to

$$\begin{aligned} c_n&=n+3\sum_{J=1}^{n} J(J-1)\\ &=n+3\cdot\left[\frac{n}{6}(n+1)(2n+1)-\frac{n}{2}(n+1)\right]\\ &=n^3. \end{aligned} \tag{9}$$

Now while one might have immediately inferred that the total number of cells in the cubical configuration is just the cube of the outermost shell layer, the foregoing in any event serves not only as a rigorous proof, but also as the background rationale for further elaboration of cellular calculations.

RIGOROUS TREATMENT OF THE EXTRA-CUBICAL CELLS

Unfortunately, the evaluation of the number of energy states associated with the k space cannot follow merely from the cubical shell calculation as carried out to this point; Eq. (9) in effect represents the minimal cells that correspond to a particular k value so it still remains to determine those cells which do not lie within the cube, but nevertheless accord with the condition

$$k_x^2+k_y^2+k_z^2\leq 3k_0^2,$$

where k_0 denotes the shell index.

Clearly those shells beyond k_0 contribute a portion of their cells for the prescribed energy state identified by k, and indeed the cellular identifications are derivable from

$$(k_0+\delta)^2+k_y^2+k_z^2\leq 3k_0^2,\quad \delta=1, 2, 3, \cdots \delta_m, \tag{10}$$

where δ designates the shell level beyond the cubical configuration with the maximum allowable value according to

$$\delta_m\leq(\sqrt{3}-1)k_0. \tag{11}$$

Thus for each of the δ shells, a grouped collection of cells can be composed from which the summation scheme can be deduced:

$$\begin{vmatrix} (k_0+\delta)00 & (k_0+\delta)10 & (k_0+\delta)20\cdots(k_0+\delta)x_10\\ & (k_0+\delta)11 & (k_0+\delta)21\cdots(k_0+\delta)x_21\\ & & (k_0+\delta)22\cdots(k_0+\delta)x_32\\ & & \vdots\\ & & (k_0+\delta)q_mq_m\cdots \end{vmatrix},$$

where since each member of the array fulfills condition stated in (10),

$$\begin{aligned} &(k_0+\delta)^2+x_1^2+0^2\leq 3k_0^2\\ &(k_0+\delta)^2+x_2^2+1^2\leq 3k_0^2\\ &\quad\vdots\\ &(k_0+\delta)^2+x_q^2+(q-1)^2\leq 3k_0^2. \end{aligned} \tag{12}$$

This latter result for the qth row translates into

$$x_q\leq(2k_0^2-2k_0\delta-\delta^2-(q-1)^2)^{\frac{1}{2}}, \tag{13}$$

whence the number of cells in the qth row is evidently

$$N_q=3T+6[x_q-(q-1)], \tag{14}$$

where $T=1$ or 2 accordlng to whether $x_q\leq k_0+\delta$. For the total number of cells in each δ shell, we must sum N_q up to q max, i.e.,

$$(k_0+\delta)^2+2q_m^2\leq 3k_0^2$$

or

$$q_m\leq\frac{\sqrt{2}}{2}(2k_0^2-2k_0\delta-\delta^2)^{\frac{1}{2}}. \tag{15}$$

Hence each δ shell contains

$$N_{t,q}=\sum_{q=1}^{q_m} N_q=3Tq_m+6\sum_{q=1}^{q_m}[x_q-(q-1)] \tag{16}$$

cells.

Finally the grand sum of all extra-cubical cells follows directly from relation (16) by now summing over all δ, i.e., from $\delta=1$ to $\delta=\delta_m$, *viz.*,

$$N_T=\sum_{\delta} N_{t,q}=3T\sum_{\delta=1}^{\delta_m} q_m+6\sum_{\delta=1}^{\delta_m}\sum_{q=1}^{q_m}[x_q-(q-1)]. \tag{17}$$

This is a rigorously correct finding which can be readily applied in the domain $k_0\to 0$ with only integers of all quantities having meaning.

THE EXTRA-CUBICAL CELL CALCULATION IN THE REALM OF STATISTICAL MECHANICS

In the domain $k_0\to\infty$ which is appropriate for statistical mechanics where k_0 may be well in excess of 10^6, Eq. (17) no longer retains its discrete character, i.e., integer values are without meaning, i.e., the sums may be replaced by integrals with impunity. The dominant contribution comes from the double sum; the first term in (17) is of order k_0^2, whereas the latter term is of order k_0^3 thereby giving to all practical purposes the exact formula

$$N_T=6\int_{x=1}^{\delta_m}\int_{q=1}^{q_m}(2k_0^2-2k_0x-x^2-q^2)^{\frac{1}{2}}dqdx -6\sum_{\delta}\sum_{q}(q-1). \tag{18}$$

Performing the summing operation, we have

$$\sum_{\delta}\sum_{q}(q-1)=\sum_{\delta}\left[\frac{q_m}{2}(q_m+1)-q_m\right]=\tfrac{1}{2}\sum q_m(q_m-1)$$

where since $q_m^2\gg q_m$

$$\tfrac{1}{2}\sum_{\delta} q_m(q_m-1)\cong\tfrac{1}{2}\sum_{\delta} q_m^2=\tfrac{1}{2}\sum_{\delta=1}^{\delta_m}\frac{2}{4}(2k_0^2-2k_0\delta-\delta^2)$$

with the outcome

$$\sum_{\delta}\sum_{q}(q-1)=\tfrac{1}{4}\left[2k_0^2\delta_m-2k_0\frac{\delta_m}{2}(\delta_m+1)-\frac{\delta_m}{6}(\delta_m+1)(2\delta_m+1)\right]$$
$$\cong\tfrac{1}{4}\delta_m(2k_0^2-k_0\delta_m-\tfrac{1}{3}\delta_m^2). \quad (19)$$

This result is clearly good to an accuracy of several parts per million for $k_0\sim10^6$.

Next the integration with respect to q entails

$$\int_{q=1}^{q_m}(A^2-q^2)^{\frac{1}{2}}dq, \quad A^2\equiv 2k_0^2-2k_0x-x^2$$

so that the solution is

$$\frac{1}{2}\left\{\frac{\sqrt{2}}{2}(2k_0^2-2k_0x-x^2)^{\frac{1}{2}}\times(2k_0^2-2k_0x-x^2-\tfrac{1}{2}(2k_0^2-2k_0x-x^2))^{\frac{1}{2}}+(2k_0^2-2k_0x-x^2)\sin^{-1}\frac{\sqrt{2}}{2}-(2k_0^2-2k_0x-x^2-1)^{\frac{1}{2}}-(2k_0^2-2k_0x-x^2)\sin^{-1}\frac{1}{(2k_0^2-2k_0x-x^2)^{\frac{1}{2}}}\right\}. \quad (20)$$

The contribution from the lower limit $q=1$ is virtually zero as the isolated term $(2k_0^2-2k_0x-x^2)^{\frac{1}{2}}$ is of higher order than the two preceding ones and also the arcsine term is of order $\sin^{-1}1/k_0$ which for $k_0\to\infty$ has the limit zero.

Hence the solution for N_T reduces to

$$N_T=6\cdot\tfrac{1}{2}\left(\frac{\sqrt{2}}{2}\cdot\frac{1}{\sqrt{2}}+\sin^{-1}\frac{\sqrt{2}}{2}\right)\times\int_{x=1}^{\delta_m}(2k_0^2-2k_0x-x^2)dx$$
$$-\tfrac{3}{2}\delta_m(2k_0^2-k_0\delta_m-\tfrac{1}{3}\delta_m^2), \quad (21)$$

where again the lower limit $x=1$ makes essentially no contribution, whence it follows that

$$N_T=3\left(\tfrac{1}{2}+\frac{\pi}{4}\right)\delta_m(2k_0^2-k_0\delta_m-\tfrac{1}{3}\delta_m^2)-\tfrac{3}{2}(2k_0^2-k_0\delta_m-\tfrac{1}{3}\delta_m^2)$$
$$=\tfrac{3}{4}\pi\delta_m(2k_0^2-k_0\delta_m-\tfrac{1}{3}\delta_m^2). \quad (22)$$

Now for numerical evaluation we have

$$\delta_m(2k_0^2-k_0\delta_m-\tfrac{1}{3}\delta_m^2)=(\sqrt{3}-1)[2-(\sqrt{3}-1)-\tfrac{1}{3}(\sqrt{3}-1)^2]k_0^3$$
$$=0.798k_0^3$$

and

$$N_T=0.599\pi k_0^3=1.881k_0^3. \quad (23)$$

Thus the extra-cubical cells, in the limit of $k_0\to\infty$, contribute almost twice as many cells as those within the cube k_0.

THE FERMI ENERGY AND THE DISTRIBUTION OF STATES

The total number of cells in phase space corresponding to a specified wave vector k is given by

$$c(k)=2.881/(3\sqrt{3})k^3=0.553k^3, \quad (24)$$

from which the energy of electrons in the uppermost level of the distribution at the absolute zero (Fermi energy) can be found with dispatch. Thus, if in a volume of metal V there are N electrons occupying all states with two electrons in each cell to allow as usual for the two possible spin orientations, then

$$N/2=c(k)=0.553k^3. \quad (25)$$

Next it follows from the energy expression (2) that

$$E_{\max}=\left[\frac{N}{(2)(0.553)}\right]^{\frac{2}{3}}\frac{h^2}{8mV^{\frac{2}{3}}}=\frac{h^2}{8m}\left(\frac{N}{1.106V}\right)^{\frac{2}{3}}, \quad (26)$$

whereby comparison with the classical result

$$\mu_0=\frac{h^2}{8m}\left(\frac{3}{\pi}\cdot\frac{N}{V}\right)^{\frac{2}{3}} \quad (27)$$

reveals essential agreement, with a distinguishable difference manifest to the extent:

$$\frac{E_{\max}}{\mu_0}=\left(\frac{\pi}{3}\cdot\frac{1}{1.106}\right)^{\frac{2}{3}}=(0.947)^{\frac{2}{3}}=0.964. \quad (28)$$

Evidently the spherical approximation allows Fermi level calculations to within an accuracy of a few percent.

As for the actual energy distribution of the states between k and $k+\Delta k$ discussed earlier, the cellular computational method gives via Eq. (25)

$$c(k)\Delta k=1.65_9k^2\Delta k, \quad (29)$$

which compares quite favorably with the spherical result with α in Eq. (1) equal to 1.06.

JOURNAL OF APPLIED PHYSICS VOLUME 25, NUMBER 10 OCTOBER, 1954

Focusing of a Long Cylindrical Electron Stream by Means of Periodic Electrostatic Fields

PING KING TIEN
Bell Telephone Laboratories, Inc., Murray Hill, New Jersey
(Received December 4, 1953)

This paper presents a theory of focusing long cylindrical electron streams by means of electric fields which vary periodically along the stream. The use of a bifilar helix or a series of annular rings to produce periodic electric fields is considered.

The potential distribution at the position of the electrons is expanded in a power series, and an equation of electron motion is written. The solutions obtained indicate that the flow of electrons is essentially parallel, provided that the electrons enter the focusing structure practically without transverse velocities and are distributed across the stream such that the space charge fields decrease radially toward the axis in a manner similar to that of the periodic electric fields.

The method of periodic electrostatic focusing is of particular interest in connection with traveling wave tubes. The possibility of using a bifilar helix as both the slow wave and the focusing structure is discussed.

1. INTRODUCTION

SINCE the discovery of the "Strong Focusing"[1] at the Brookhaven National Laboratory, more attention has been given, from the point of view of the traveling wave tubes, to the focusing of a long cylindrical electron stream by means of electric fields which vary periodically along the stream. In this laboratory, periodic electrostatic focusing by thin lenses has been studied by Pierce.[2] Clogston and Heffner[3] have studied periodic focusing using the paraxial ray equation. Experimentally, Quate has successfully focused an electron stream by means of periodic electric field of quadrupole type. Recently the author has obtained a 78 percent current transmission through a 10 in. helix in a traveling wave tube using bifilar helix as the focusing structure.[4]

Before analyzing the problem in detail, we may explain the principles of periodic focusing by a rather simplified picture. Consider a layer of electrons at the boundary of an electron stream. Figure 1 shows the radial electron motion caused by the periodic electric fields which are strongest close to the surface of the focusing structure and decrease radially away from the structure. It is seen that, because of the motion of the electrons, the electrons are in a stronger field when the field is focusing, and in a weaker field when the field is defocusing. This gives to the electrons a net focusing force which should be balanced by the space charge force of the stream for a parallel flow. Because the periodic electric fields vary radially, in order to maintain this equilibrium condition over the entire cross section of the stream, we must use an electron stream in which the space charge fields vary radially in a similar manner. This kind of electron stream, although it is not physically unrealizable, may require an electron gun of special design.

In this paper, the potential distribution at the position of the electrons is expanded in a power series, and an equation of the electron motion is written. Solutions corresponding to an essentially parallel electron flow are analyzed in detail, as this is the case of particular interest in most applications. During the course of the discussions, numerical examples are given and equations which may be useful in the practical designs are provided.

2. PERIODIC ELECTRIC FIELDS

An approximate sinusoidal potential distribution along an electron stream can be obtained by using a series of annular rings connected alternatively with potentials V_0+V_f and V_0-V_f, where V_0 is the average dc potential of the focusing structure measured with respect to the cathode and V_f, the potential used to produce periodic electrostatic fields. V_f will be denoted in this paper as the "focusing potential." A similar potential distribution may also be produced by a bifilar helix with V_0+V_f applied to one helical wire and with V_0-V_f to the other.

Consider a bifilar tape helix of radius a, with tape width δ, and a pitch $2p$. If the gap between the tapes is narrow, the electric field across the gap may be assumed constant and the potential distribution at

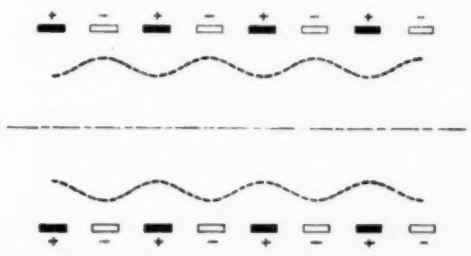

FIG. 1. The radial electron motion of a stream focused inside a series of annular rings.

[1] Courant, Livingston, and Snyder, Phys. Rev. **88**, 1190 (1952).
[2] J. R. Pierce, "Confining Electron Flow by Means of Thin Lenses" (unpublished).
[3] A. M. Clogston and H. Heffner, "Focusing of an Electron Beam by Periodic Fields," J. Appl. Phys. **25**, 437 (1954).
[4] P. K. Tien, "Bifilar Helix for Backward Wave Oscillators," submitted to Proc. Inst. Radio Engr.

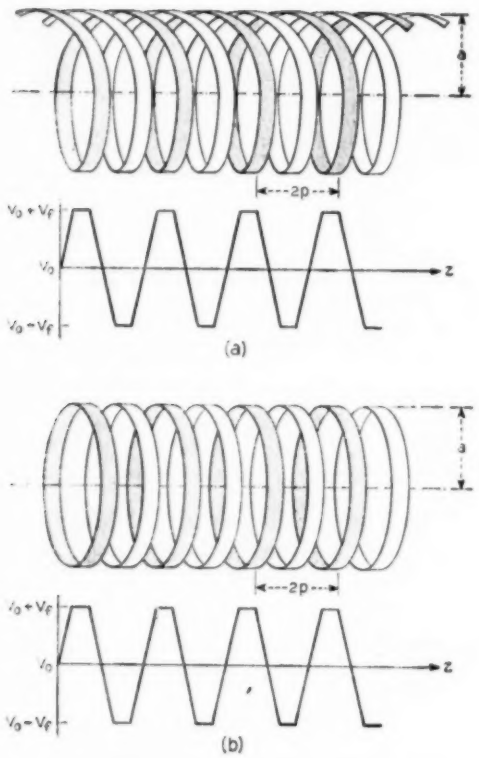

FIG. 2. Approximate potential distribution at $r=a$. (a) the bifilar helix, (b) the annular rings.

$r=a$ may be approximated by that shown in Fig. 2a. Inside the helix, the potential field must satisfy Laplace's equation. We thus have

$$V(r,z,\theta)=V_0+\sum_m \frac{4V_f}{m\pi}\frac{\sin\frac{m\pi}{2}\left(1-\frac{\delta}{p}\right)}{\frac{m\pi}{2}\left(1-\frac{\delta}{p}\right)} \times\frac{I_m\left(\frac{m\pi r}{p}\right)}{I_m\left(\frac{m\pi a}{p}\right)}\sin m\left(\frac{\pi}{p}z-\theta\right). \quad (1a)$$

It is assumed that the helix is wound so that θ increases in following the wire. Cylindrical coordinates r, z, and θ, and M. K. S. units are used throughout this paper. I_m is the modified Bessel function of the mth order of the first kind. In their effect on the electron stream, the terms in (1a) except that for $m=1$ can be generally neglected. This is because fields with larger m vary with the modified Bessel functions of higher order and of larger arguments. We thus have approximately

$$V(r,z,\theta)\cong V_0+\frac{4V_f}{\pi}\left[\frac{\sin\frac{\pi}{2}\left(1-\frac{\delta}{p}\right)}{\frac{\pi}{2}\left(1-\frac{\delta}{p}\right)}\right]\frac{I_1\left(\frac{\pi r}{p}\right)}{I_1\left(\frac{\pi a}{p}\right)}\sin\left(\frac{\pi z}{p}-\theta\right), \quad (1b)$$

where the factor $4/\pi(\ )$ will be denoted as F for convenience. F depends only upon the ratio of δ/p.

Similarly, the potential distribution inside a series of annular rings of pitch $2p$ (Fig. 2b) is approximately

$$V(r,z)\cong V_0+FV_f\frac{I_0\left(\frac{\pi}{p}r\right)}{I_0\left(\frac{\pi}{p}a\right)}\sin\frac{\pi}{p}z. \quad (2)$$

The field in this case is axial symmetrical. The potential distribution outside the structure can be obtained from (1b) or (2) by replacing I_m function by K_m function, where K_m is the modified Bessel function of the second kind.

3. A SIMPLIFIED EQUATION OF ELECTRON MOTION

When an electron stream is focused inside a series of annular rings, the periodic electrostatic fields are axial symmetrical and the electron motion in the θ direction may be assumed prohibited. As shown in (2), the potential distribution is in a form of

$$V(r,z)=V_0+V(r)\cos\frac{\pi}{p}z. \quad (3)$$

Consider a layer of electrons at the boundary of an electron stream of an average radius of r_0. The electron motion may be described as

$$r(z)=r_0+r_1(z). \quad (4)$$

For a well-focused electron stream, $r_1(z)$ must be a periodic function in z and has a magnitude much smaller than r_0. $r_1(z)$ will be abbreviated as r_1 for convenience.

By expanding $V(r)$ of (3) in Maclaurin series at $r=r_0$,

$$V(r)=V(r_0)+V'(r_0)r_1+\tfrac{1}{2}V''(r_0)r_1^2+\cdots, \quad (5)$$

and neglecting the terms higher than the r_1^2 term, the radial component of the electric field at the vicinity of $r=r_0$ is

$$E_r(r,z)=-\frac{\partial V(r,z)}{\partial r}=(-V'-V''r_1)\cos\frac{\pi}{p}z, \quad (6)$$

where in (5), $V(r_0)$, $V'(r_0)$, and $V''(r_0)$ are, respectively, the electric potential, and the derivative and the second

derivative of the electric potential with respect to the radial coordinate at $r=r_0$. $V(r_0)$, $V'(r_0)$, and $V''(r_0)$ are abbreviated as V, V', and V'' in (6).

In addition to the radial component of electric field produced by the focusing structure, the electron stream exerts a space charge force of

$$\frac{eI_0}{v_0 2\pi r_0 \epsilon}$$

on the boundary electrons, where e is the electron charge ϵ the dielectric constant I_0 the beam current, and v_0, the average axial velocity of the stream. v_0 is evidently related to V_0 in (1) by

$$v_0=\left(\frac{2eV_0}{m}\right)^{\frac{1}{2}}. \tag{7}$$

The thermal velocities of the electrons are neglected.

In this section we will assume that the axial electron velocity v_0 is constant. A more accurate analysis will be given in the next section to include the variation of the axial electron velocity caused by the axial component of the periodic electric fields. The equation prescribing the motion of a boundary electron is

$$\frac{d^2r_1}{dt^2}=\eta(V'+V''r_1)\cos\frac{\pi}{p}z+\eta\frac{I_0}{v_0 2\pi r_0\epsilon}, \tag{8}$$

where η is the ratio of the electron charge to the electron mass. Replacing d^2r_1/dz^2 by $v_0^2(d^2r_1/dt^2)$ and after some manipulations, we have

$$\frac{d^2r_1}{dz^2}-\frac{V''}{2V_0}\left(\cos\frac{\pi}{p}z\right)r_1=\frac{V'}{2V_0}\cos\frac{\pi}{p}z+\frac{I_0}{r_0 4\pi(2\eta)^{\frac{1}{2}}V_0^{\frac{1}{2}}\epsilon}. \tag{9}$$

As will be justified later, the space charge field is generally much smaller than the periodic focusing fields. Since r_1 is small, the variation of the space charge field due to the radial motion of the electrons for a well behaved electron stream must be a quantity small in the second order. The space charge force in (8) and (9) is therefore evaluated at $r=r_0$ and is assumed constant irrespective of the motion of the electrons. In order to simplify the solution of the equation, we will *further assume* that the quantities $V/2V_0$, $(p/\pi)\times(V'/2V_0)$ and $(p/\pi)^2(V''/2V_0)$ are small compared with unity. That is, the focusing potential V_f is assumed small compared with the average potential V_0. This is the condition generally preferred in most applications.

Equation (9) has a homogeneous part in a form of the Mathieu equation[5]

$$\frac{d^2y}{dx^2}+(a-2q\cos 2x)y=0, \tag{10}$$

where y is r_1, $x=(\pi/2p)z$, $q=(p/\pi)^2(V''/V)$, and $a=0$. A study of the "Butterfly diagram"[5] of the Mathieu equation shows that the solutions may be stable or not depending upon the value of q. Methods for numerical calculation of those solutions are available.[6] We may, however, as in the case of the "Brillouin flow focusing,"[7] avoid setting up the solutions of the homogeneous equation by properly choosing the initial conditions. As we are interested in the values of q inside the stable region of the Butterfly diagram ($q<0.8$ as assumed later), the particular solution of (9) is evidently a pure cosine series of the form[8]

$$r_1=\sum a_m\cos m\frac{\pi}{p}z, \tag{11}$$

where $a_0=0$, because the electron stream is supposed to be confined at $r=r_0$. It should be emphasized here, that the particular solution only satisfies a special set of initial conditions which will be discussed in detail later.

To evaluate a_m's of (11), substituting (11) in (9) and equating the corresponding terms, we have for the constant term,

$$\frac{V''}{4V_0}a_1=-\frac{I_0}{4\pi r_0(2\eta)^{\frac{1}{2}}V_0^{\frac{1}{2}}\epsilon}, \tag{12a}$$

for the $\cos(\pi/p)z$ term,

$$\frac{V'}{2V_0}=-\left(\frac{\pi}{p}\right)^2 a_1-\frac{V''}{4V_0}a_2, \tag{13}$$

and for the general term $\cos m(\pi/p)z$ with $m\geq 2$,

$$m^2a_m+\frac{V''}{4V_0}\left(\frac{p}{\pi}\right)^2(a_{m-1}+a_{m+1})=0. \tag{14}$$

To be the particular solution of (9), the series (11) must converge, otherwise the solution is meaningless. Stated more specifically, if the particular solution in the form of (11) exists and when m is made very large, a_{m+1} in (11) and so in (14) should approach zero and may be neglected. Remembering that $(P/\pi)^2(V''/2V_0)$ is a quantity small compared with unity, we have after some manipulations,

$$a_1=-\frac{I_0}{\pi r_0(2\eta)^{\frac{1}{2}}V_0^{\frac{1}{2}}\epsilon V''} \tag{12a}$$

$$a_m\cong-\frac{V''}{2V_0}\left(\frac{p}{\pi}\right)^2\frac{a_{m-1}}{2m^2},\quad m\geq 2. \tag{15}$$

As seen from (15), the series (11) converges rapidly. This justifies the procedure used in evaluating a_m's.

[5] N. W. McLachlan, *Theory and Application of Mathieu Functions* (Oxford University Press, London, 1947), p. 79.

[6] N. W. McLachlan, Phil. Mag. 36, 403 (1945).

[7] J. R. Pierce, *Theory and Design of Electron Beams* (D. Van Nostrand Company, Inc., New York, 1949), p. 152.

[8] M. Golomb and M. Shanks, *Elements of Ordinary Differential Equations* (McGraw-Hill Book Company, Inc., New York, 1950), p. 272.

The radial electron motion can be computed from (12a),

$$r_1 \cong -\frac{I_0}{V''\pi r_0(2\eta)^{\frac{1}{2}}V_0^{\frac{1}{2}}\epsilon}\cos\frac{\pi}{p}z,$$

or from (13),

$$r_1 \cong -\left(\frac{p}{\pi}\right)^2\frac{V'}{2V_0}\cos\frac{\pi}{p}z. \tag{12b}$$

The terms in (11) except $a_1\cos(\pi/p)z$ can generally be neglected.

Using (15) and eliminate a_1 from (12a) and (13), we obtain an important relation, that is,

$$V'V'' = \left(\frac{\pi}{p}\right)^2\frac{\sqrt{2}V_0^{\frac{1}{2}}I_0}{\pi r_0\sqrt{\eta\epsilon}}. \tag{16}$$

The term at the left-hand side of the equation can be calculated from (2) and is proportional to the square of V_f. The term at the right-hand side of the equation contains I_0 and V_0 which are known for a given stream. We thus obtain a relation which can be used to calculate the amount of the focusing potential required for a given physical system.

We can easily give a physical picture of what we calculated. Consider first the sizes of the quantities contained in Eq. (9). $(V'/2V_0)(p/\pi)$ and $(V''/2V_0)(p/\pi)^2$ are quantities small compared with unity. d^2r_1/dz^2 and $V'/2V_0\cos(\pi/p)z$, which are of the order of $(V'/2V_0)\times(p/\pi)$ are much larger than $(V''/2V_0)[\cos(\pi/p)z]r_1$ and $I_0/[4\pi r_0(2\eta)^{\frac{1}{2}}V_0^{\frac{1}{2}}\epsilon]$, which are of the order of $[(V'/2V_0)(p/\pi)][(V''/2V_0)(p^2/\pi^2)]$. Neglecting the small quantities in Eq. (9), we obtain an equation,

$$\frac{d^2r_1}{dz^2} = \frac{V'}{2V_0}\cos\frac{\pi}{p}z, \tag{17}$$

which can be used to solve for the radial motion of the electrons. For the initial conditions,

$$\left.\begin{aligned}\frac{dr_1}{dz} &= 0,\\ r_1 &\cong -\left(\frac{p}{\pi}\right)^2\frac{V'}{2V_0}\end{aligned}\right\}\quad \text{at}\quad z=0$$

we have

$$r_1 = -\frac{V'}{2V_0}\left(\frac{P}{\pi}\right)^2\cos\frac{\pi}{p}z. \tag{18}$$

Equation (17) gives exactly the same solution as (12b). The radial electron motion is seen to be primarily due to the periodic focusing fields, as it should be. The electron motion is plotted in Fig. 1. It may be seen that the electrons are closer to the surface of the focusing structure where the field is stronger when the field is focusing, and are further away from the structure when the field is defocusing. This, as mentioned in the first section, gives a net focusing force. Substituting (18) into the term $-(V''/2V_0)[\cos(\pi/p)z]r_1$ of Eq. (9), we get

$$-\frac{1}{2}\left[\frac{V''}{2V_0}\frac{V'}{2V_0}\right]\left(\frac{p}{\pi}\right)^2+\frac{1}{2}\left[\frac{V''}{2V_0}\frac{V'}{2V_0}\right]\left(\frac{p}{\pi}\right)^2\cos\frac{2\pi}{p}z. \tag{19}$$

The first term of (19) must be equal to the space charge term $I_0/[4\pi r_0(2\eta)^{\frac{1}{2}}V_0^{\frac{1}{2}}\epsilon]$ of Eq. (9), as they are the only comparable constant terms in the equation. This gives a relation exactly like (16). The second term of Eq. (19) sets up a second harmonic motion which is small compared with that given by Eq. (18) and may be thus neglected. Thus, in the particular solution, the focusing force is just balanced by the space charge force of the stream and so the net average radial force applied to the electrons is equal to zero. Later in a numerical example, we will show that the periodic motion shown in (18) is extremely small. The electron flow is therefore essentially parallel.

4. FOCUSING BY ANNULAR RINGS

In the previous section, the axial velocity of the boundary electrons is assumed constant irrespective of the positions of the electrons. Actually the axial electron velocity v_z varies with axial component of the periodic electric field and may be expanded as

$$v_z = \left[2\eta\left(V_0+V\cos\frac{\pi}{p}z\right)\right]^{\frac{1}{2}} \cong v_0\left(1+\frac{V}{2V_0}\cos\frac{\pi}{p}z+\cdots\right), \tag{20}$$

where $V/2V_0$ is small compared with unity as assumed previously.

Substituting v_0 in (8) by v_z and d^2r_1/dt^2 by $v_z^2(d^2r_1/dz^2)+v_z(dv_z/dz)(dr_1/dz)$, we get an equation similar to (9),

$$\frac{d^2r_1}{dz^2}+\frac{dr_1}{dz}\frac{1}{v_z}\frac{dv_z}{dz}-r_1\eta\frac{V''}{v_z^2}\cos\frac{\pi}{p}z = \eta\frac{V'}{v_z^2}\cos\frac{\pi}{p}z+\eta\frac{1}{v_z^2}\frac{I_0}{v_0 2\pi r_0\epsilon}. \tag{21}$$

Again by inspection, the particular solution of (21) is a pure cosine series as given in (11). The term $(dr_1/dz)\times(1/v_z)(dv_z/dz)$ is small compared with d^2r_1/dz^2 and may be dropped in solving the radial motion of the electrons. The radial electron motion is thus approximately given by the equation

$$\frac{d^2r_1}{dz^2} = \frac{V'}{2V_0}\cos\frac{\pi}{p}z,$$

which gives again the first-order solution

$$r_1 = -\left(\frac{p}{\pi}\right)^2\frac{V'}{2V_0}\cos\frac{\pi}{p}z, \tag{22}$$

like that given in (12b) and (18).

After substituting (22) in (21), and properly expanding all the terms, we arrive at a relation similar to (16), by equating the constant terms of the equation, that is

$$V'\left[V+V''\left(\frac{p}{\pi}\right)^2\right]=\frac{\sqrt{2}I_0V_0^{\frac{1}{2}}}{\pi r_0\sqrt{\eta\epsilon}}. \tag{23}$$

Comparing (23) with (16), we find that the effect of the axial component of the periodic electric fields is to give an additional term to the focusing force. This has been pointed out by Pierce.[2]

By means of (2), (22) and (23) become, respectively,

$$\frac{(FV_f)^2}{I_0^2\left(\frac{\pi a}{p}\right)}[I_0'(\xi_0)I_0(\xi_0)+I_0'(\xi_0)I_0''(\xi_0)]\xi_0 = 1.212\times10^5 I_0V_0^{\frac{1}{2}}, \tag{24}$$

$$\frac{r_{1\max}}{r_0}\cong\frac{FV_f}{2V_0}\frac{I_0'(\xi_0)}{\xi_0 I_0\left(\frac{\pi a}{p}\right)}, \tag{25}$$

where $\xi_0=\pi r_0/p$. I_0' and I_0'' are, respectively, the derivative and the second derivative of I_0 with respect to the argument. Equations (24) and (25) are useful in the practical designs.

5. FOCUSING BY BIFILAR HELIX

When an electron stream is focused inside a bifilar helix, there is a θ component of electric fields and therefore a θ component of electron motion. With the potential distribution in the form of

$$V(r,z,\theta)=V_0+V(r)\cos\left(\frac{\pi}{p}z-\theta\right),$$

the equations of the electron motion become

$$\frac{d^2r_1}{dt^2}-r_0\left(\frac{d\theta}{dt}\right)^2=\eta\frac{\partial V(r,z,\theta)}{\partial r}+\eta\frac{I_0}{2\pi r_0 v_z\epsilon} \tag{26}$$

$$r_0\frac{d^2\theta}{dt^2}+2\frac{d\theta}{dt}\frac{dr_1}{dt}=\frac{1}{r_0}\eta\frac{\partial V(r,z,\theta)}{\partial\theta}. \tag{27}$$

By inspection, we find that the radial component of the electron motion may be approximately solved from (26) by dropping the term $r_0(d\theta/dt)^2$ and the θ component of the electron motion, from (27) by dropping the term $2(d\theta/dt)(dr_1/dt)$. We thus have

$$r_1\cong-\left(\frac{p}{\pi}\right)^2\frac{V'}{2V_0}\cos\left(\frac{\pi}{p}z-\theta_0\right), \tag{28}$$

similar to (22) given before, and

$$\theta\cong-\frac{1}{r_0^2}\left(\frac{p}{\pi}\right)^2\frac{V}{2V_0}\left[\sin\left(\frac{\pi}{p}z-\theta_0\right)\right]+\theta_0, \tag{29}$$

where θ_0 defines the angular position of the electron at $z=0$ and the initial conditions

$$\left.\begin{aligned} r_1&\cong-\left(\frac{p}{\pi}\right)^2\frac{V'}{2V_0}\\ \frac{dr_1}{dz}&=0\\ \theta-\theta_0&=0\\ \frac{d\theta}{dz}&\cong-\frac{1}{r_0^2}\left(\frac{p}{\pi}\right)\frac{V}{2V_0}\end{aligned}\right\}\ \text{at}\ \begin{cases}z=0\\ \theta_0=0\end{cases}$$

are assumed.

Expanding $V(r)$ and v_z in (26) and (27) as before, and remembering that r_1 and $\theta-\theta_0$ are small quantities, we obtain a relation similar to (23) by equating the constant terms of the equations, that is

$$\left(\frac{p}{\pi}\right)^2V'V''+VV'+\left(\frac{p}{\pi r_0}\right)^2VV' - \frac{1}{r_0}\left(\frac{p}{\pi r_0}\right)^2V^2=\frac{\sqrt{2}I_0V_0^{\frac{1}{2}}}{\pi r_0(\eta)^{\frac{1}{2}}\epsilon}. \tag{30}$$

Again, we have an equation, the left-hand side of which is proportional to the square of V_f, and the right-hand side of which is dependent on the physical quantities of the electron stream. The first, second, and the third terms at the left-hand side of (30) are, respectively, the focusing action caused by the radial, axial, and the θ component of the periodic electric fields; the fourth term is from the centrifugal force of the electrons. From (1b), (28), and (30), we obtain

$$\frac{(FV_f)^2}{I_1^2(\cot\psi)}\left[I_1'(\xi_1)I_1(\xi_1)+I_1'(\xi_1)I_1''(\xi_1) +\frac{1}{\xi_1^2}I_1'(\xi_1)I_1(\xi_1)-\frac{1}{\xi_1^3}I_1^2(\xi_1)\right]\xi_1 = 1.212\times10^5 I_0V_0^{\frac{1}{2}}, \tag{31}$$

$$\frac{r_{1\max}}{r_0}=\frac{FV_f}{2V_0}\frac{I'(\xi_1)}{\xi_1 I_1(\cot\psi)}, \tag{32}$$

where $\xi_1=(r_0/a)\cot\psi$, and ψ is the angle between the helical conductor and the circumference of the helical cylinder. Equations (31) and (32) will be used for numerical calculations in the next section.

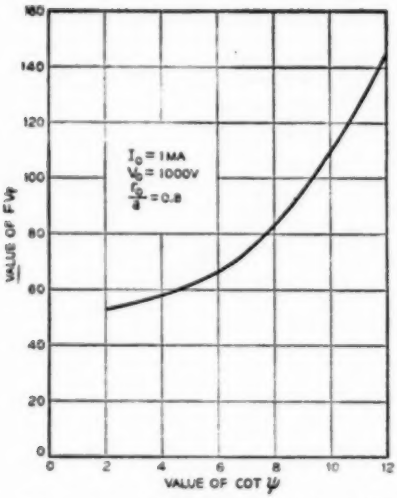

FIG. 3. FV_f *versus* cot ψ for the case of the bifilar helix. $I_0=1$ milliampere. $V_0=1000$ volts.

6. NUMERICAL RESULTS

Focusing voltages are computed from (24), (25), (31), and (32) for an electron stream of $I_0=1$ milliampere $V_0=1000$ volts, and of $r_0/a=0.8$. The results are compared in Table I, in which the focusing by a quadruple-wire helix is also included for completeness. The value of FV_f is plotted *versus* cotψ in Fig. 3 for the case of the bifilar helix. In traveling wave tubes, the bifilar helix seems preferable, because it is simpler in construction as a structure inside the vacuum envelope, and the same structure may be used both for the slow wave and for the focusing circuit. We will return to this point later.

7. CONDITIONS FOR A PARALLEL FLOW

In the previous sections, the particular solution of the equation of electron motion is found for the electrons at the boundary of the stream. The electron trajectory is essentially a straight line parallel to the axis with very small ripples. In order to avoid exciting the solutions of the homogeneous equation mentioned in section I, electrons must enter the focusing structure practically without transverse velocities, and the value V_f must be just right to balance the space charge force according to (24) for the annular rings and according to (31) for the bifilar helix. For a solid stream, we may divide the cross section into circular rings of infinitely small thickness, and electrons inside each circular ring are considered as the boundary electrons of a smaller stream. If the conditions described above can be fulfilled anywhere inside the stream, the flow is essentially rectilinear, and laminar.

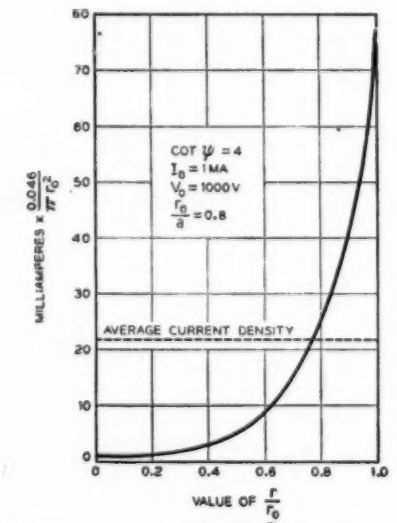

FIG. 4. Electron current density *versus* radius for an electron stream focused by a bifilar helix, cot $\psi=4$, $I_0=1$ milliampere. $V_0=1000$ volts.

From (1b) and (2), we find that for a given V_f, the periodic electric field decreases with the radius according to the modified Bessel functions and so with the quantities at the left-hand sides of the Eqs. (24) and (31). The current enclosed inside a circle of radius r must decrease accordingly in order to satisfy the relation (24) or (31) at any radius inside a solid stream. We thus determine the proper distribution of the electron current density necessary for a parallel flow. For the annular rings we have

$$\rho(r)=4.12\times10^{-6}\frac{(FV_f)^2\left(\frac{\pi r_0}{p}\right)^2}{I_0^2\left(\frac{\pi a}{p}\right)V_0^{\frac{1}{2}}\pi r_0^2}\left\{\frac{1}{\xi}[I_1(\xi)+\xi I_1'(\xi)][I_1'(\xi)+I_0(\xi)]+I_1(\xi)[I_1''(\xi)+I_1(\xi)]\right\}, \quad (33)$$

and for the bifilar helix,

$$\rho(r)=4.12\times10^{-6}\frac{(FV_f)^2\left(\frac{r_0}{a}\cot\psi\right)^2}{I_1^2(\cot\psi)V_0^{\frac{1}{2}}\pi r_0^2}\left\{\frac{1}{\xi_1}[I_1'(\xi_1)+\xi_1 I_1''(\xi_1)]\left[I_1''(\xi_1)+I_1(\xi_1)+\frac{1}{\xi_1^2}I_1(\xi_1)\right]+I_1'(\xi_1)\left[I_1'''(\xi_1)+I_1'(\xi_1)+\frac{1}{\xi_1^2}I_1'(\xi_1)-\frac{2}{\xi_1^3}I_1(\xi_1)\right]-\frac{2}{\xi_1^3}I_1(\xi_1)I_2(\xi_1)\right\}, \quad (34)$$

where $\rho(r)$ is the electron current density at the radius r, and $\xi=\pi r/p$. Equation (34) is plotted in Fig. 4 for an electron stream of $I_0=1$ milliampere, $V_0=1000$ volts, and of $r_0/a=0.8$. The average current density is

also shown in the figure as the dotted line for comparison. It may be seen that the current density decreases rapidly from the boundary and is generally only few percent of the average value at the center of the stream.

8. THE COMPLETE SOLUTIONS

The complete solution of (9) is in the form of

$$r_1 = C_1 ce_\beta(z,q) + C_2 se_\beta(z,q) + \sum_{m=1}^{\infty} a_m \cos m\frac{\pi}{p} z \qquad (35)$$

where C_1 and C_2 are constants associated with the solutions. The first two terms of (35) are the solutions of the homogeneous equation (10) mentioned in section 2. They are Mathieu functions of real fractional order[5] and can be computed in the series forms as

$$ce_\beta(z,q) = \sum_{r=-\infty}^{+\infty} A^\beta_{2r} \cos(2r+\beta)\frac{\pi}{2p} z, \qquad (36)$$

$$se_\beta(z,q) = \sum_{r=-\infty}^{+\infty} A^\beta_{2r} \sin(2r+\beta)\frac{\pi}{2p} z. \qquad (37)$$

The functions are stable if the value of q is inside the stable region of the Butterfly diagram[5] (Fig. 5). The third term of (35) is the particular solution that we have discussed in the previous sections.

The initial conditions for the homogeneous equation are: (i) the value of $(2p/\pi)(dr_1/dz)$ at $z=0$, and (ii) the difference between the radius at which the electron actually enters the focusing structure and the radius which the electron would have, to satisfy the condition (24) or (31). If the initial condition (i) is zero, only the Mathieu function $Ce_\beta(z,q)$ is excited, and if (ii) is zero, the other Mathieu function is excited. If both are zero, only the particular solution exists.

The Mathieu functions have been calculated for several values of q. They are plotted in Figs. 6a and b for the initial condition (i) equal to γ, and the initial condition (ii) equal to α. It may be seen that in these solutions, the electrons may oscillate radially with a much larger period and amplitude as compared with those described in the particular solution. In general, when the focusing potential is larger than that required for the particular solution, and the value of q is inside the stable region of the Butterfly diagram, the electron motion is confined inside a well defined radial boundary. Although we may confine the electron stream in this way, because of the presence of the solutions of the homogeneous equation, the electron trajectories starting at different radii inside the stream cross each other and the space charge field is distorted badly, unless a thin hollow stream is used. When the electron radial motion is large enough so that r_1 becomes comparable to r_0, the expansion (5) does not hold. To this extent, the equations discussed in this paper no longer apply. Fortunately this is not the case of interest in most of the practical applications.

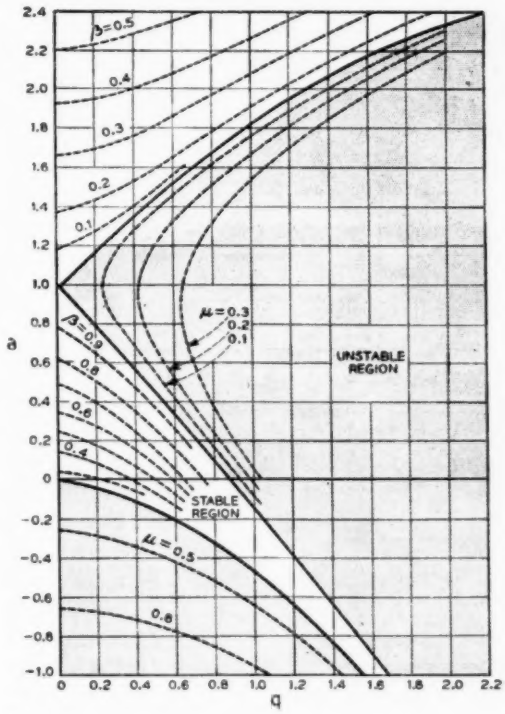

FIG. 5. The "Butterfly" diagram of the Mathieu equation.

9. THE BIFILAR HELIX AS THE SLOW WAVE AND THE FOCUSING CIRCUIT

In considering to use the same bifilar helix as the slow wave and the focusing circuit, we notice from Fig. 3 that the focusing potential increases with the value of $\cot\psi$. As a slow wave circuit in the traveling wave amplifier, $\cot\psi$ is generally larger than 12. The focusing potential for that value of $\cot\psi$ seems to be excessive, if the beam current is more than several milliamperes. We thus have to design the traveling

TABLE I.

	Bifilar helix	Quadruple wire helix	Rings
$\cot\psi$	4	2	
$\frac{\pi a}{p}$	4	4	4
FV_f	57.6[v]	50.4[v]	57.4[v]
$\frac{r_{1\max}}{r_0}$	0.0038	0.0036	0.0037

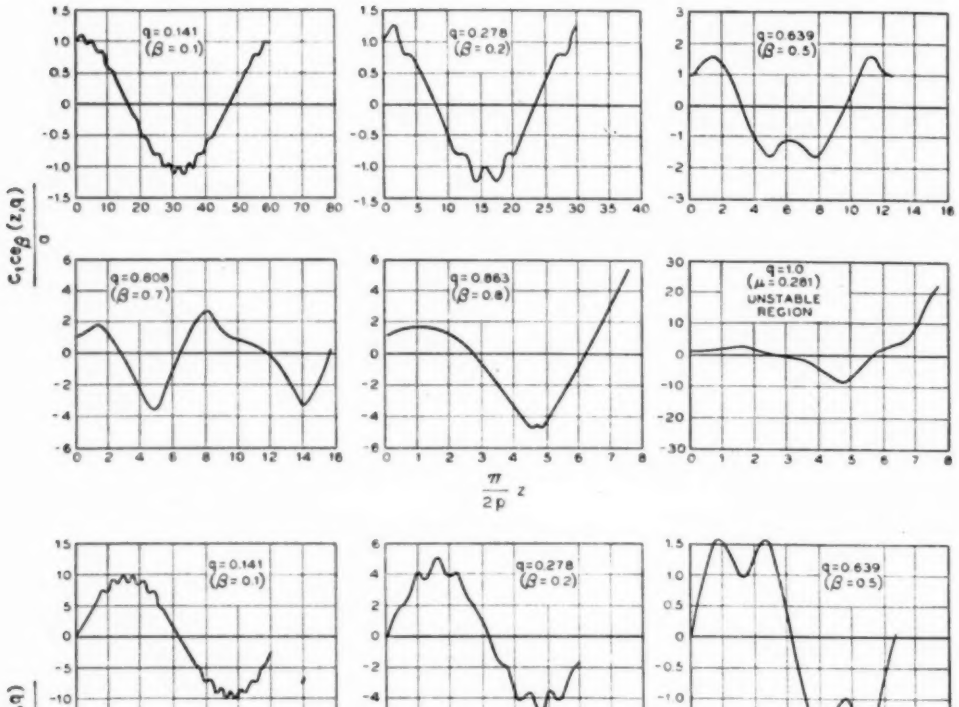

FIG. 6. Solutions of the homogeneous equation
(a) $c_1 ce_\beta(z,q)$,
(b) $c_2 se_\beta(z,q)$.

wave tubes with high beam voltage so that the value of $\cot\psi$ is small or with low beam current to limit the focusing potential to a reasonable value. We may also use a larger value of r_0/a, although this requires skillful construction techniques. Another alternative is to operate the helix at a space harmonic component. This seems particularly suitable for backward wave oscillators,[9] although in this case, means are needed to vary the focusing potential with the average beam voltage.

10. ACKNOWLEDGMENT

The Mathieu functions used in this paper were calculated by Miss M. C. Gray.

[9] R. Kompfner and N. T. Williams, Proc. Inst. Radio Engr. 41, 1602 (1953).

JOURNAL OF APPLIED PHYSICS VOLUME 25, NUMBER 10 OCTOBER, 1954

Transient Flow of Non-Ideal Gases in Porous Solids—One-Dimensional Case

J. S. Aronofsky and O. D. Ferris
Magnolia Petroleum Company, Field Research Laboratories, Dallas, Texas
(Received December 7, 1953)

Calculations of pressure and production histories are presented for one-dimensional flow of non-ideal gases through porous media. The non-ideal properties considered in this paper are the gas viscosity and deviation factor (compressibility factor) which are assumed to vary as simple functions of pressure. The effect of each of these parameters is investigated independently as well as in combination. The results demonstrate that pressure declines and production histories in linear gas-flow systems are markedly influenced by variations in these parameters. Numerical solutions of the flow equations were obtained by solving the corresponding difference equations on an electronic digital computer.

INTRODUCTION

THIS paper is an extension of work presented in a previous paper,[1] which gave solutions of the problem of one-dimensional gas flow through porous media for an ideal gas with constant viscosity. These solutions are extended here to include gases which do not obey the ideal gas law, and which have pressure-dependent viscosities.

Several articles have appeared in the literature which deal with transient gas flow in porous solids, where such properties as viscosity, deviation factor, and gas permeability are considered to be constants. A modified analytical solution has been presented by Roberts.[2] Green and Wilts[3] used an electrical network analog in solving the problem for constant terminal pressures. Approximating finite difference equations were solved numerically by Bruce, Peaceman, Rachford, and Rice,[4] and by Aronofsky and Jenkins;[1] the former employing the implicit, and the latter the explicit type difference equation.

The current study considers a long porous sample of constant cross section, sealed at one end and filled with a non-ideal gas at an initial uniform pressure P_m. Calculations are made to determine the changes in pressure distribution with time after the open end pressure is reduced to $P_0=P_i/10$, and maintained at that value. Parameters are introduced to describe the variation of viscosity and deviation factor with pressure, and a series of solutions is presented to demonstrate the influence of these parameters on the gas production rate history and pressure history of the system.

A condition that has not been considered in this study is the pressure dependence of permeability due to gas slip effects. For depletion problems of the type described above, it has been indicated[5] that gas slip effects are of lesser importance at sufficiently high pressures. However, it is shown in this paper that the variations of viscosity and deviation factor with pressure produce effects which are of considerable magnitude when pressures are high. These considerations justify the present assumption that permeability is constant (no slip effect) while the other factors are allowed to change with pressure. If desired, a study could be made where variations in all three parameters are taken into consideration in the same calculation.

FLOW EQUATIONS

The general equation for one-dimensional fluid flow in a porous medium is[6]

$$\frac{\partial}{\partial x}\left(\frac{k}{\mu}\frac{\partial P}{\partial x}\right)=\phi\frac{\partial \rho}{\partial t}, \tag{1}$$

(see symbols list at end of paper).

In this investigation the permeability k is assumed to be independent of pressure. However, the viscosity μ is taken to be a linear function of the pressure: $\mu=nP+d$. This relation is approximately true for many gases in the pressure range of interest. A factor expressing the non-ideality of real gases is also introduced into the equation. The general relationship between pressure and density for non-ideal gases is obtainable from the equation $(PV)/Z=RT$, and is expressed as

$$\rho=\frac{\rho_s Z_s}{P_s}\left(\frac{P}{Z}\right), \tag{2}$$

for the constant temperature case. The quantity Z describes the deviation from the ideal gas law and is therefore referred to as the deviation factor (also called compressibility factor). This factor approaches unity in the vicinity of P_s (a low pressure used as a standard); hence for the purposes of this discussion Z_s is assumed

[1] J. S. Aronofsky and R. Jenkins, "Unsteady flow of gas through porous media, one-dimensional case," Proc. First U. S. Natl. Cong. Appl. Mech., Am. Soc. Mech. Engrs. New York (1952).
[2] Richard C. Roberts, "Unsteady flow of a gas through a porous medium," Proc. First U. S. Natl. Cong. Appl. Mech., Am. Soc. Mech. Engrs. New York (1952).
[3] L. Green, Jr. and C. H. Wilts, "Nonsteady flow of gas through a porous wall," Proc. First U. S. Natl. Cong. Appl. Mech., Am. Soc. Mech. Engrs., New York (1952).
[4] Bruce, Peaceman, Rachford, and Rice, Trans. Am. Inst. Mining Met. Engrs. **198**, 79 (1953).
[5] J. S. Aronofsky, J. Appl. Phys. **25**, 48 (1954).
[6] M. Muskat, *Flow of Homogeneous Fluids Through Porous Media* (J. Edwards, Inc., Ann Arbor, Michigan, 1946).

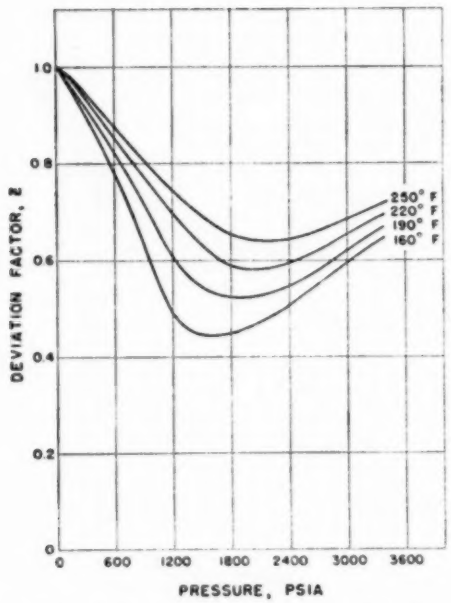

FIG. 1. Deviation factor *versus* pressure for ethane.

equal to unity. Figure 1 shows the deviation factor for ethane as a function of pressure, for various temperatures.[6] Note that in the region of lower pressures (e.g., below 1200 psi on the 160°F curve) a straight line representation is a reasonable approximation to the curve. Deviation-factor graphs will be different for every gas, but they will all show the same general character. Thus we assume $Z=1-mP$.

Making the appropriate substitutions in Eq. (1) yields

$$\frac{\partial}{\partial x}\left[\frac{Pk}{(1-mP)(nP+d)}\frac{\partial P}{\partial x}\right]=\phi\frac{\partial}{\partial t}\left(\frac{P}{1-mP}\right), \quad (3)$$

where ρ and μ have been expressed in terms of pressure. Upon introducing the dimensionless pressure $p=P/P_i$ and the dimensionless parameters $\alpha=nP_i/d$ and $\beta=mP_i$, we obtain

$$2p[(\alpha-\beta)p-2\alpha\beta p^2]\frac{\partial^2 p}{\partial x^2}+(1+\alpha\beta p^2)\frac{\partial^2 p^2}{\partial x^2}=\frac{2\phi d}{kP_i}(1+\alpha p)^2\frac{\partial p}{\partial t}. \quad (4)$$

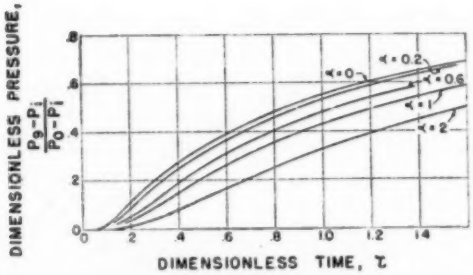

FIG. 2. Dimensionless pressure-time curves for $\beta=0$.

The quantities α and β are introduced as a means of characterizing the pressure dependence of the deviation factor and viscosity. Equation (4) can be approximated by the difference equation

$$p_j'=p_j+\frac{kP_i\Delta t}{2\phi d(\Delta x)^2(1+\alpha p_j)^2}\times\{2p_j[(\alpha-\beta)p_j-2\alpha\beta p_j^2](p_{j+1}+p_{j-1}-2p_j)+(1+\alpha\beta p_j^2)(p_{j+1}^2+p_{j-1}^2-2p_j^2)\}, \quad (5)$$

where the prime indicates the pressure value for the next time step, and the subscript j indicates a particular value of x at which the pressure is evaluated. The above difference Eq. (5) is of a type that becomes unstable for large time steps. Numerical stability was insured in this case by restricting the size of time steps by the following relationship:

$$\frac{kP_i\Delta t}{2\phi d(\Delta x)^2}=\frac{(1+\alpha)^2}{4(1+\alpha+\beta+2\alpha\beta)}. \quad (6)$$

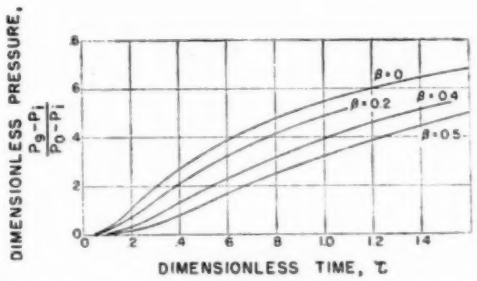

FIG. 3. Dimensionless pressure-time curves for $\alpha=0$.

Substituting the above condition in Eq. (5) gives the relationship

$$p_j'=p_j+\frac{(1+\alpha)^2}{4(1+\alpha+\beta+2\alpha\beta)(1+\alpha p_j)^2}\times\{2p_j[(\alpha-\beta)p_j-2\alpha\beta p_j^2](p_{j+1}+p_{j-1}-2p_j)+(1+\alpha\beta p_j^2)(p_{j+1}^2+p_{j-1}^2-2p_j^2)\}, \quad (7)$$

which is used in the numerical calculations.

For the application of the numerical procedure, the porous sample is divided into nine segments of equal length Δx, bounded by pressure measuring stations at $j=0, 1, \cdots, 9$. Thus it is necessary to solve Eq. (7) ten times for each time step. This procedure was carried out, using IBM's Type 604 Electronic Calculating Punch, at the rate of approximately five time steps per minute.

PRESSURE HISTORIES

The numerical solutions of Eq. (7) were obtained subject to the following initial and boundary conditions: the sample is considered to be sealed at station $j=9$, and charged with gas to an initial uniform pressure P_i;

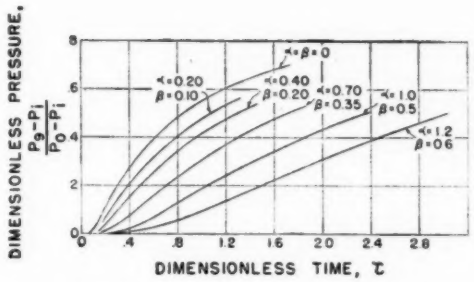

FIG. 4. Dimensionless pressure-time curves for $\beta/\alpha=\frac{1}{2}$.

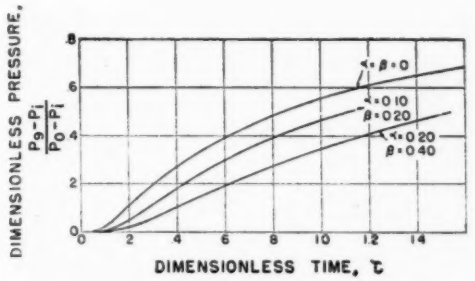

FIG. 6. Dimensionless pressure-time curves for $\beta/\alpha=2$.

the pressure at $j=0$ is suddenly reduced to $P_0=P_i/10$ and held constant at that value.

The first solutions to be considered were for the case of a gas with a pressure dependent viscosity and $Z=1$. Setting β equal to zero is equivalent to making Z equal to unity and Eq. (7) reduces to the case where only the viscosity is pressure dependent. The resulting curves for various values of α are shown in Fig. 2. These are plots, in dimensionless form, of $(P_9-P_i)/(P_0-P_i)$ as a function of time. The form of the plot is such that the ordinate for all curves is initially zero and approaches unity as the dimensionless time parameter $\tau=(kP_it)/(\phi dL^2)$ increases. The curves of Fig. 2 show a systematic shift for increasing values of α. This shift is indicative of the influence of the value of α on the solutions. The curve for $\alpha=0$ represents the ideal gas case, the solution of which was presented in a previous paper.[5]

A similar family of curves, shown in Fig. 3, illustrates solutions of Eq. (7) for the case of pressure independent viscosity and varying deviation factor. These assumptions are the equivalent of setting $\alpha=0$ and permitting varying values of β. The curves of Fig. 3 corresponding to this case are shifted in the direction of increasing τ for increasing values of β. In Fig. 4, both α and β are varied, but the ratio β/α is held at the constant value $\frac{1}{2}$. It should be noted that, since both parameters α and β are directly proportional to P_i, the ratio $\beta/\alpha=(md)/n$ is solely a property of the gas and is independent of the initial pressure P_i. This family of curves corresponds to a series of isothermal laboratory flow experiments starting at different initial pressures using the same gas. It would be necessary to conduct such experiments at constant temperature since both α and β may be temperature sensitive. Indeed, this temperature dependence may prove to be a practical means of varying either α or β in a controlled experiment. The results of other calculations for β/α ratios of 1 and 2 are shown in Figs. 5 and 6.

A study of Figs. 4, 5, and 6 shows the effect of the ratio β/α on the pressure histories. This effect is more clearly demonstrated in Fig. 7, which is essentially a cross plot of Figs. 4, 5, and 6. Figure 7 is a plot of $\bar{\tau}$ *versus* β/α for several values of α. The quantity $\bar{\tau}$ is the specific value of τ for which the pressure P_9 has declined to $0.55P_i$. By following one curve it is possible to see how changes in β affect the decline time $\bar{\tau}$ for any specified α. The horizontal straight line represents the limit which is approached as both α and β approach zero.

CUMULATIVE PRODUCTION

The rate of gas flow at $j=0$ may be obtained from the previously described numerical solutions for the pressure distributions. A quantity of perhaps more importance is the cumulative mass of fluid withdrawn, evaluated from the initial time to some time t. The initial mass in the porous solid is represented by

$$M_i=\phi AL\rho_i, \tag{8}$$

and the mass at any time t can be expressed as

$$M(t)=\phi AL\rho_a(t), \tag{9}$$

where ρ_a is defined as the average gas density which would result if flow at $j=0$ were stopped and the pressure in the porous solid allowed to stabilize. The cumu-

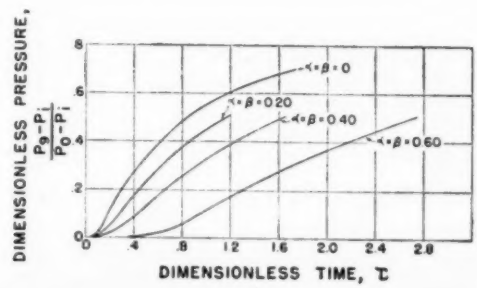

FIG. 5. Dimensionless pressure-time curves for $\beta/\alpha=1$.

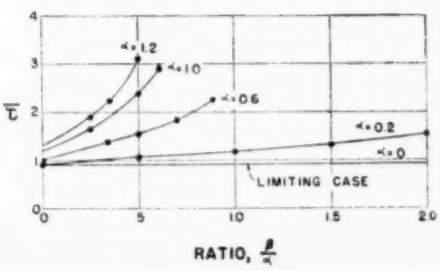

FIG. 7. Effects of α and β on pressure decline times.

lative production is defined as

$$C(t)=M_i-M(t)=\phi AL\rho_i[1-(\rho a/\rho_i)], \quad (10)$$

or

$$\bar{C}(t)=1-(\rho_a/\rho_i), \quad (11)$$

where $\bar{C}$ is a dimensionless quantity and represents the fraction of the initial mass that has been produced up to the time t. The mass $M(t)$ may also be expressed as

$$M(t)=\phi AL\int_0^1 \rho(t)d(x/L), \quad (12)$$

where $\rho(t)$ is the instantaneous density distribution throughout the porous medium. The elimination of $M(t)$ from Eqs. (9) and (12) gives

$$\rho_a/\rho_i=(1-\beta)\int_0^1 [p/(1-\beta p)]d(x/L), \quad (13)$$

where p is the instantaneous dimensionless pressure distribution. Equations (11) and (13) are combined so that

$$\bar{C}/(1-N)=(1-N)^{-1} \times\left\{1-(1-\beta)\int_0^1 [p/(1-\beta p)]d(x/L)\right\}. \quad (14)$$

The quantity $\bar{C}/(1-N)$ represents the mass fraction of gas produced at any time to the total amount that is produced in an infinite time, where N represents the ratio of terminal to initial pressure. This quantity can now be calculated from the pressure distribution by numerically integrating the right-hand side of Eq. (14). Two such calculations are illustrated in Fig. 8, which is a plot of $\bar{C}/(1-N)$ *versus* τ. One curve was evaluated for $N=\frac{1}{10}$, $\alpha=\beta=0$, and the other gas curve was evaluated for $N=\frac{1}{10}$, $\alpha=1.2$, and $\beta=0.6$. Similar curves could be prepared for all the other values of α and β discussed in the previous section, but these two curves demonstrate how the cumulative production is influenced by the parameters α and β.

A comparison is made in Fig. 8 of the two gas curves with a corresponding curve for an ideal liquid system.

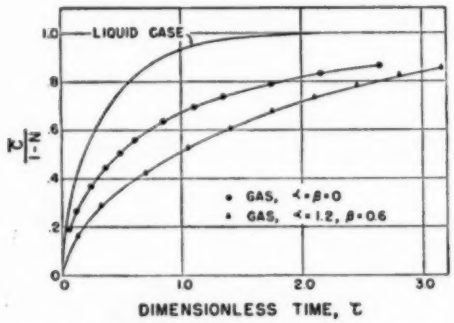

FIG. 8. Production histories for liquid and gas cases.

This corresponding liquid system is defined to have the same initial and boundary conditions as the previously described gas case. The pressure distribution in such a liquid system is simply the solution of the classical diffusion equation,[6] and the analytical solution is well known.[7]

$$\frac{p-1}{1-N}=1-\sum_{n=0}^{\infty}\frac{2}{\alpha_n^2}e^{-\alpha_n^2\tau}\sin[\alpha_n(x/L)], \quad (15)$$

where $\alpha_n=\pi(n+1)/2$ and $n=0, 1, 2$, etc. The term τ is now the analogous dimensionless time for a liquid system and is defined in the symbols list. The cumulative production for this liquid system reduces to

$$\bar{C}=\int_0^\tau\left(\frac{\partial p}{\partial(x/L)}\right)d\tau. \quad (16)$$

Differentiating Eq. (15) with respect to x/L and substituting in Eq. (16) will yield

$$\frac{\bar{C}}{1-N}=1-2\sum_{n=0}^{\infty}\frac{e^{-\alpha_n^2\tau}}{\alpha_n^2}. \quad (17)$$

The solution of Eq. (17) is plotted in Fig. 8 in order to make a comparison of this liquid case with the two gas cases. It should be noted that the liquid curve is invariant for different values of $N=P_0/P_i$, whereas the gas curves are quite sensitive to changes in the ratio N. It can be shown that the two gas curves should approach the liquid curve in the limit as $\alpha=\beta=0$ and N approaches unity.

ACKNOWLEDGMENT

The authors are indebted to the management of the Magnolia Petroleum Company for permission to publish this material.

SYMBOLS LIST

A = cross sectional area of core, cm²
d = a constant representing the intercept of viscosity-pressure plot, centipoises
k = permeability, darcys
L = length of core, cm
M = mass of gas, grams
m = slope of straight line of gas deviation-pressure plot, atmos^{-1}
N = ratio of terminal to initial pressure (P_0/P_i)
n = slope of the straight line on the viscosity-pressure plot, centipoises/atmos
P = pressure, atmos (unless specifically stated otherwise)
P_i = initial and also maximum pressure in system, atmos
p = pressure ratio P/P_i
T = temperature

[7] H. Carslaw and J. Jaeger, *Conduction of Heat in Solids* (Clarendon Press, Oxford, 1947).

t = time, seconds
V = specific volume, cm³/gram
x = distance along core, cm
Z = deviation (compressibility) factor, dimensionless
α = dimensionless ratio $(NP_i)/d$
β = dimensionless quantity mP_i
μ = viscosity, centipoises
ρ = density, grams/cm³
τ = for gas systems, a dimensionless time parameter $(kP_it)/(\phi dL^2)$
τ = for liquid systems, a dimensionless time parameter $(kt)/(\phi dL^2\gamma)$
$\bar{\tau}$ = a specific value of τ for which $P_9 = 0.55P_i$
ϕ = porosity, fraction
γ = a constant for liquid, change in volume per unit volume per atmos.

JOURNAL OF APPLIED PHYSICS VOLUME 25, NUMBER 10 OCTOBER, 1954

The Effect of a Transverse Electric Field on Carrier Diffusion in the Base Region of a Transistor

J. S. S. KERR, J. S. SCHAFFNER, AND J. J. SURAN
General Electric Electronics Laboratory, Syracuse, New York

(Received December 1, 1953)

A solution for the density of minority carriers is obtained for a semiconductor device having a two-dimensional rectangular geometry and a transverse field. The solution is developed for a variety of boundary conditions and the current-gain factor α of the corresponding semiconductor devices is obtained from this solution.

I. INTRODUCTION

THE performance characteristics of semiconductor devices depend upon the flow of electrons and holes inside the semiconductor materials. This flow is governed by a system of partial differential equations.

In this report the following customary assumptions are made:

1. The flow distribution is studied only in the base region of the device, the effect of the emitter and collector regions entering as boundary conditions on the base region.

2. The base region contains an overwhelming majority of one type of carrier. Under this condition the relevant variable describing the flow is the density of minority carriers as a function of position and time, and the partial differential equation governing this function becomes linear.

Figure 1 shows a transistor with a transverse field in the base region. It is assumed that this field is uniform and has a component in the y direction only. It is furthermore assumed that the minority carrier density is constant in the z direction. A solution for the density of minority carriers is developed for a variety of boundary conditions specified below and the current transport factor β is obtained from this solution ($\beta \cong \alpha$).

II. BASIC EQUATIONS

The flow of minority carriers in the base region of a transistor is governed by the following differential equations:[1]

$$\mathbf{i} = \mu q m \mathbf{E} - qD \operatorname{grad} m, \tag{1}$$

$$-\frac{\partial m}{\partial t} = -\frac{1}{q}\operatorname{div}\mathbf{i} + \frac{m-m_e}{\tau}, \tag{2}$$

[1] W. Shockley, *Electrons and Holes in Semiconductors* (D. Van Nostrand Company, Inc., New York, 1950).

where i is the current density, μ the mobility, q the charge, m the density, and D the diffusion constant of the minority carriers. τ is the lifetime and m_e the thermal equilibrium density of the minority carriers. By combining Eqs. (1) and (2) one obtains

$$\frac{\partial(m-m_e)}{\partial t} = D\nabla^2(m-m_e) - \mu\nabla[\mathbf{E}(m-m_e)] - \frac{m-m_e}{\tau}. \tag{3}$$

As stated in the introduction, it is assumed that the field has a component E_y in the y direction only and that $\partial m/\partial z = 0$. It is furthermore assumed that E_y and m_e are constant in space and time.

The density function m may be separated into a dc part and an ac part so that

$$m = M_0(x,y) + M_1(x,y)\exp j\omega t, \tag{4}$$

where $M_0(x,y)$ is the space distribution of the dc part of m and $M_1(x,y)$ is the space distribution of the ac part. Therefore

$$\frac{\partial}{\partial t}(M_0 + M_1 e^{j\omega t}) = D\left[\frac{\partial^2(M_0+M_1e^{j\omega t})}{\partial x^2} + \frac{\partial^2(M_0+M_1e^{j\omega t})}{\partial y^2}\right] - \mu E_y\frac{\partial}{\partial y}(M_0+M_1e^{j\omega t}) - \frac{1}{\tau}(M_0+M_1e^{j\omega t}-m_e). \tag{5}$$

This can be separated into the following two independent differential equations:

$$\frac{\partial^2 M_0}{\partial x^2} + \frac{\partial^2 M_0}{\partial y^2} - \frac{\mu E_y}{D}\cdot\frac{\partial M_0}{\partial y} - \frac{M_0 - m_e}{D\tau} = 0, \tag{6}$$

$$\frac{\partial^2 M_1}{\partial x^2} + \frac{\partial^2 M_1}{\partial y^2} - \frac{\mu E_y}{D}\cdot\frac{\partial M_1}{\partial y} - \frac{M_1}{D}\left(\frac{1}{\tau} + j\omega\right) = 0. \tag{7}$$

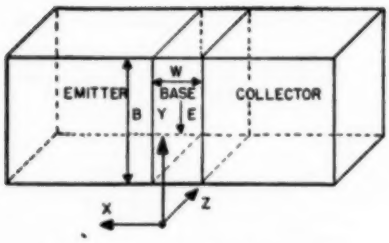

FIG. 1. The transistor geometry.

Only the ac part of the minority carrier density is of interest here and therefore only Eq. (7) will be solved.

III. BOUNDARY CONDITIONS

The potential V across the collector junction ($x=0$) is prescribed. Because of Boltzmann's relation,

$$m=m_e \exp\left(-\frac{qV}{kT}\right), \tag{8}$$

this means that m is prescribed. Since in practice $qV/kT\gg 1$ it can be assumed that $m=0$ and hence that $M_1=0$. Experiments on diodes indicate that metallic contacts lead to the boundary condition $m=m_e$. The boundary condition for $y=0$ is therefore $M_1=0$.

On the emitter surface ($x=W$) the current is prescribed. This means that $\partial m/\partial x$ is prescribed. Since we are only interested in the steady-state ac solution we assume that

$$\frac{\partial M_1}{\partial x}=F(y), \tag{9}$$

where $F(y)$ is any function of y which can be expanded in a Fourier series.

Prescribing the potential on the emitter surface rather than the current distribution determines m rather than $\partial m/\partial x$. The form of the solution obtained for the boundary condition $M_1=F(y)$ does not readily lend itself to an estimate of the current-gain factor α. For that reason this boundary condition is not considered in the present report.

Finally there remains the boundary condition for the base surface defined by $y=B$. The exact condition at this surface has not been determined and so a rather general boundary condition has been applied to this surface. It is

$$\frac{\partial M_1}{\partial y}+hM_1=0. \tag{10}$$

Here h is a parameter depending on the surface condition. The condition $h\to\infty$ corresponds to a strong surface recombination rate while the condition $h=0$ corresponds to a weak surface recombination rate, so that the value of h may be thought of as a measure of the surface recombination rate.

IV. THE GENERAL SOLUTION

The boundary conditions for M_1 are

$$\begin{aligned} &M_1(0,y)=0, \quad \frac{\partial M_1}{\partial y}(x,y)\bigg|_{y=B}+hM_1(x,B)=0, \\ &M_1(x,0)=0, \quad \frac{\partial M_1}{\partial x}(x,y)\bigg|_{x=W}=F(y). \end{aligned} \tag{11}$$

The following symbols will be used for the solution of Eq. (7):

$$L^2=D\tau,$$

$$L^{*2}=L^2/(1+j\omega\tau),$$

$$p=\frac{-\mu E_y B}{2D}.$$

Equation (7) may be solved by the separation of variables technique. Let

$$M_1(x,y)=X(x)Y(y).$$

With the aid of the preceding relations the differential Eq. (7) separates into Eqs. (12) and (13) where k^2 is the separation constant:

$$X''-k^2X=0, \tag{12}$$

$$Y''+\frac{2p}{B}Y'+\left(k^2-\frac{1}{L^{*2}(\omega)}\right)Y=0. \tag{13}$$

Taking into account the boundary conditions $M_1(0,y)=0$ and $M_1(x,0)=0$ we get

$$\begin{aligned} X&=C_1\sinh kx, \\ Y&=C_2e^{-py/B}\sin\frac{ay}{B}, \end{aligned} \tag{14}$$

where

$$\left(\frac{a}{B}\right)^2=k^2-\frac{1}{L^{*2}(\omega)}-\left(\frac{p}{B}\right)^2.$$

Therefore

$$M_1(x,y)=Ce^{-py/B}\sinh kx\sin\frac{ay}{B} \tag{15}$$

and

$$\frac{\partial M_1}{\partial y}=Ce^{-py/B}\sinh kx\left[\frac{-p}{B}\sin\frac{ay}{B}+\frac{a}{B}\cos\frac{ay}{B}\right]. \tag{16}$$

From Eqs. (15) and (16) and the boundary condition

$$\frac{\partial M_1}{\partial y}(x,y)\bigg|_{y=B}+hM_1(x,B)=0,$$

there results

$$\tan a=\frac{a}{p-hB}. \tag{17}$$

Let the roots of this equation be a_n, where $n=1, 2, 3, \cdots$, where the first root is the one nearest the origin, the second root is the next nearest, etc. (the root $a=0$ is excluded). Now define $L_n^*(\omega)$ by

$$\frac{1}{L_n^{*2}(\omega)}=\left(\frac{a_n}{B}\right)^2+\left(\frac{p}{B}\right)^2+\frac{1}{L^{*2}(\omega)}$$
$$=\left(\frac{a_n}{B}\right)^2+\left(\frac{p}{B}\right)^2+\frac{1}{L^2}+j\frac{\omega}{D}. \quad (18)$$

Now, to each a_n there corresponds a special solution of the differential equation, namely,

$$C_n e^{-py/B}\sinh\left(\frac{x}{L_n^*(\omega)}\right)\sin\frac{a_n y}{B}.$$

The linear superposition of these special solutions for all positive integers n results in the general solution

$$M_1(x,y)=e^{-py/B}\sum_{n=1}^{n=\infty}C_n\sinh\frac{x}{L_n^*(\omega)}\sin\frac{a_n y}{B}. \quad (19)$$

The values of the C_n must be determined from the boundary condition

$$\left.\frac{\partial M_1(x,y)}{\partial x}\right|_{x=W}=F(y)$$

or

$$\sum_{n=1}^{\infty}\frac{C_n}{L_n^*(\omega)}\cosh\frac{W}{L_n^*(\omega)}\sin\frac{a_n y}{B}=F(y)e^{py/B}.$$

It may be shown[2] that

$$\frac{C_n}{L_n^*(\omega)}\cosh\frac{W}{L_n^*(\omega)}=\frac{2B_n}{B}\int_0^B F(y)e^{py/B}\sin\frac{a_n y}{B}dy,$$

where

$$B_n=\frac{a_n^2+(hB-p)^2}{a_n^2+(hB-p)\cdot(1+hB-p)}. \quad (20)$$

Substituting the values of C_n into (19) there finally results

$$M_1=e^{-py/B}\sum_{n=1}^{\infty}G_n L_n^*(\omega)\,\mathrm{sech}\frac{W}{L_n^*(\omega)}\sinh\frac{x}{L_n^*(\omega)}\sin\frac{a_n y}{B},$$

where

$$G_n=\frac{2B_n}{B}\int_0^B F(y)e^{py/B}\sin\frac{a_n y}{B}dy \quad (21)$$

and a_n, L_n^* and B_n are defined by (17) and (18), and (20), respectively.

V. THE CURRENT AMPLIFICATION FACTOR α

The current amplification factor α is defined as the ratio of the current at the collector to the current at the emitter. Now the amplitude of the ac current passing through any plane $x=x_1$ is given by

$$i_T(x_1)=qD\int_0^B\left.\frac{\partial M_1(x,y)}{\partial x}\right|_{x_1}dy$$
$$=qD\sum_{n=1}^{\infty}\frac{G_n\cosh(x_1)/[L_n^*(\omega)]}{\cosh(W)/[L_n^*(\omega)]}\times\int_0^B e^{-py/B}\sin\frac{a_n y}{B}dy$$
$$=\sum_{n=1}^{\infty}\frac{B}{p^2+a_n^2}[a_n-e^{-p}(p\sin a_n+a_n\cos a_n)]G_n\frac{\cosh(x_1)/L_n^*(\omega)]}{\cosh W/[L_n^*(\omega)]}. \quad (22)$$

Therefore

$$\alpha=\frac{i_T(0)}{i_T(W)}$$
$$=\frac{\sum_{n=1}^{\infty}\frac{G_n B}{a_n^2+p^2}[a_n-e^{-p}(p\sin a_n+a_n\cos a_n)]\,\mathrm{sech}W/[L_n^*(\omega)]}{\sum_{n=1}^{\infty}\frac{G_n B}{a_n^2+p^2}[a_n-e^{-p}(p\sin a_n+a_n\cos a_n)]} \quad (23)$$

$$=\frac{\sum_{n=1}^{\infty}\frac{G_n B}{a_n^2+p^2}[a_n-e^{-p}(p\sin a_n+a_n\cos a_n)]\,\mathrm{sech}W/[L_n^*(\omega)]}{\int_0^B F(y)dy}. \quad (24)$$

Thus the expression for α is given by a sum of terms each having the same form as the solution for the one dimensional transistor triode.[3]

[2] W. E. Byerly, *An Elementary Treatise on Fourier's Series and Spherical, Cylindrical, and Ellipsoidal Harmonics* (Ginn and Company, New York, 1893), Articles 67 and 68, pp. 117–121.
[3] E. L. Steele, Proc. Inst. Radio Engrs. **40**, 1424 (1952).

VI. THE JUNCTION TRANSISTOR TRIODE

For a junction transistor triode it can be assumed that $E_y=0$ and that the current density across the emitter I_e is independent of y. Therefore, $p=0$ and $F(y)=I_e/qD$. Only the cases $h=0$ and $h\to\infty$ will be considered. The current amplification factor is then for $h=0$:

$$\alpha=\frac{\sum_{n=1}\frac{8}{\pi^2(2n-1)^2}\operatorname{sech}\frac{W}{L}\left[1+\left(\frac{(2n-1)\pi}{2}\right)^2\left(\frac{L}{B}\right)^2+j\omega\tau\right]^{\frac{1}{2}}}{\sum_{n=1}^{\infty}\frac{8}{\pi^2(2n-1)^2}}$$

$$=\sum_{n=1}^{\infty}\frac{8}{\pi^2(2n-1)^2}\operatorname{sech}\frac{W}{L}\left[1+\left(\frac{(2n-1)}{2}\frac{\pi L}{B}\right)^2+j\omega\tau\right]^{\frac{1}{2}}, \tag{25}$$

and for $h=\infty$:

$$\alpha=\sum_{n=1}^{\infty}\frac{8}{\pi^2(2n-1)^2}\operatorname{sech}\frac{W}{L}\times\left[1+\left(\frac{(2n-1)\pi L}{B}\right)^2+j\omega\tau\right]^{\frac{1}{2}}. \tag{26}$$

The two solutions are identical if the value of B in Eq. (26) is twice as large as the value of B in (25). This may have been anticipated from the geometrical symmetries involved in the two cases.

VII. EXPONENTIAL CURRENT DISTRIBUTION

(a) $E_y=0$. Let us assume the emitter current distribution is of the form of an exponential along the emitter surface (with the greater current near the base).

$$F(y)=Ke^{-ry/B};$$

then, if Eq. (23) is written in the form

$$\alpha=\frac{\sum_{n=1}^{\infty}U_n\operatorname{sech}W/[L_n^*(\omega)]}{\sum_{n=1}^{\infty}U_n},$$

the values of the coefficients U_n are

$$U_n=[1+e^{-r}]\frac{4BK}{\pi^2(2n-1)^2+r^2}. \tag{27}$$

The coefficients of the series are different from those of Eq. (26) but the "sech" terms are not, since L_n^* is independent of r. Multiplying a constant emitter current distribution by the factor $e^{-ry/B}$ merely makes the convergence of the series slower so that the $\operatorname{sech}W/[L_n^*(\omega)]$ terms for larger n now have more effect on the answer.

(b) $E_y\neq 0$. We restrict the discussion to the case where the boundary condition at the boundary $y=B$ is $m=m_e$ (i.e., $h\to\infty$ or strong surface recombination). In that case the solution for U_n becomes (Eq. (23))

$$U_n=\frac{2n\pi}{(n\pi)^2+p^2}[1+(-1)^{n-1}e^{-p}]\times\int_0^B F(y)e^{py/B}\sin\frac{n\pi y}{B}dy. \tag{28}$$

For

$$F(y)=Ke^{-ry/B},$$

U_n becomes

$$U_n=\frac{2KBn\pi}{(n\pi)^2+p^2}\left[\frac{n\pi}{(n\pi)^2+(p-r)^2}\times[1+(-1)^{n+1}e^{-p}][1+(-1)^{n+1}e^{p-r}]\right]. \tag{29}$$

If r approaches zero so that the alternating portion of the injected current becomes independent of y, the value of U_n reduces to

$$U_n=\frac{4KBn^2\pi^2}{[(n\pi)^2+p^2]^2}[1+(-1)^{n+1}\cosh p]. \tag{30}$$

Suppose, now, that instead of letting r approach zero, we make r very much larger than unity. In fact, let us set $r=p$. Then U_n reduces to

$$U_n=\frac{4KB(1+e^{-p})}{\pi^2(2n-1)^2+p^2}. \tag{31}$$

VIII. STEP FUNCTION

Let us assume a step in emitter current density:

$$F(y)=K,\quad 0<y<y_1,$$

$$F(y)=0,\quad y_1<y<B.$$

The values of the factors U_n are then, for $h\to\infty$,

$$U_n=\frac{2\pi nKB[1-(-1)^ne^{-p}]}{[(n\pi)^2+p^2]^2}\cdot\left[e^{py/B}\left(p\sin\frac{n\pi}{B}y_1-n\pi\cos\frac{n\pi}{B}y_1\right)+n\pi\right].$$

The value of α is

$$\alpha=\frac{\sum_{n=1}^{\infty} U_n \operatorname{sech}\frac{W}{L}\left[1+\left(\frac{n\pi L}{B}\right)^2+\left(\frac{pL}{B}\right)^2+j\omega\tau\right]^{\frac{1}{2}}}{y_1 K}.$$

For $y=B$ this reduces to

$$\alpha=4\pi^2\sum_{n=1}^{\infty}\frac{n^2[1-(-1)^n\cosh p]\operatorname{sech}\frac{W}{L}\left[1+\left(\frac{n\pi L}{B}\right)^2+\left(p\frac{L}{B}\right)^2+j\omega\tau\right]^{\frac{1}{2}}}{[(n\pi)^2+p^2]^2}.$$

This is the current amplification factor for uniform current density at the emitter and transverse field.

The authors would like to acknowledge suggestions from Dr. J. S. Saby and Dr. P. Weiss. The work was supported by the U. S. Air Force Air Research and Development Command, Army Signal Corps, and Navy Bureau of Ships under contract AF 33 (600)-17793.

JOURNAL OF APPLIED PHYSICS VOLUME 25, NUMBER 10 OCTOBER, 1954

Analyses of Basic Dielectric Amplifier Circuits

SHOU-HSIEN CHOW
Burroughs Corporation Research Center, Philadelphia, Pennsylvania

(Received December 16, 1953)

Dielectric amplifiers with high-input impedance and low-output impedance have high power gain and slow response. Analyses of two basic types of dielectric amplifier circuits, i.e., parallel and series, are given here. Both steady-state and transient responses are studied.

I. INTRODUCTION

DIELECTRIC amplifiers offer a solution to the problem of obtaining high-power amplification of signals from a source with a high internal resistance. In this paper mathematical analyses of two basic types of dielectric amplifiers, i.e., parallel-connected and series-connected circuits, are given. The basis of a mathematical analysis of a nonlinear circuit is the faithful representation of the characteristics of the nonlinear element in the circuit. For a nonlinear capacitance the voltage V across the capacitance is not a single-valued function of the charge Q accumulated because of the presence of hysteresis. To make a mathematical analysis possible, the $Q-V$ characteristics will be represented by a single-valued function. This representation is a good one when the hysteresis loop is narrow.

A power series can faithfully represent a single-valued $Q-V$ characteristic to any degree of accuracy, depending on how many terms are being used in the series. A typical $Q-V$ characteristic of a nonlinear capacitance is shown in Fig. 1. In the analysis of the parallel-connected circuit, this characteristic will be represented by

$$Q(V)=k_1V-k_3V^3+k_5V^5-k_7V^7+\cdots; \qquad (1)$$

and in the analysis of the series-connected circuit, the characteristic will be represented by

$$V(Q)=k_1'Q+k_3'Q^3+k_5'Q^5+\cdots. \qquad (2)$$

In Eq. (1) many terms are necessary to represent a $Q-V$ characteristic, whereas in Eq. (2) two or three terms are sufficient.

II. BASIC DIELECTRIC AMPLIFIER CIRCUITS

The basic mechanism of dielectric amplifiers depends on some degree of isolation of the input and output

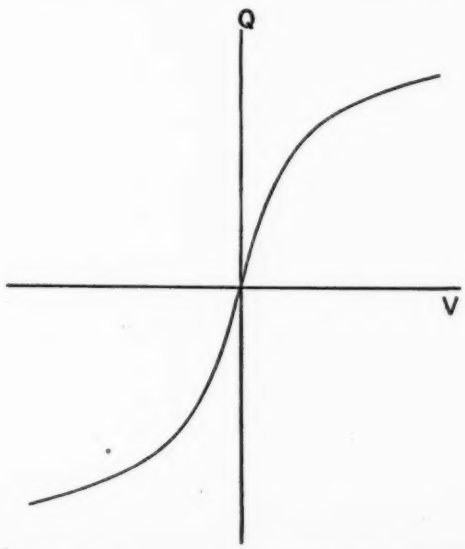

FIG. 1. $Q-V$ characteristic of a nonlinear capacitor.

circuits. This can be achieved by a push-pull or balanced connection. Figures (2) and (3) show the two basic types of push-pull connections. Figure (2) shows a parallel-connected circuit[1] in which two nonlinear capacitances $C_{\rm I}$ and $C_{\rm II}$ in parallel are connected to the ac carrier source. Figure (3) shows a series-connected circuit, in which $C_{\rm I}$ and $C_{\rm II}$ in series are connected to the ac carrier source. In both circuits, V_0 is the input voltage, R_0 the input resistance, $V_m \sin\omega t$ the ac carrier voltage, and R_l the load resistance.

III. PARALLEL-CONNECTED AMPLIFIER

In the circuit shown in Fig. 2, $C_1=C_2=C$ are two linear capacitances which serve to balance the circuit. The capacitance C must be a high capacitance so that its reactance is very low in the ac circuit. When this is true, there are negligible ac voltages across C_1 and C_2 and therefore the ac current through R_0 is negligible. The circuit equations are

$$V_m \sin\omega t = i_l R_l + v_{\rm I} + V_1, \tag{3a}$$

$$V_m \sin\omega t = i_l R_l + v_{\rm II} + V_2, \tag{3b}$$

where $v_{\rm I}$ and $v_{\rm II}$ are voltages across the nonlinear capacitors $C_{\rm I}$ and $C_{\rm II}$, respectively, and V_1 and V_2 are voltages across the linear capacitors C_1 and C_2, respectively, with $-V_1=V_2=V_0/2$. Therefore,

$$v_{\rm I} = v + \frac{V_0}{2}, \tag{4a}$$

$$v_{\rm II} = v - \frac{V_0}{2}, \tag{4b}$$

where v is a periodic function to be determined. On substituting Eqs. (4), Eqs. (3) both become

$$V_m \sin\omega t = i_l R_l + v, \tag{5}$$

or

$$-\frac{V_m}{\omega}\cos\omega t = q_l R_l + \int v\,dt, \tag{6}$$

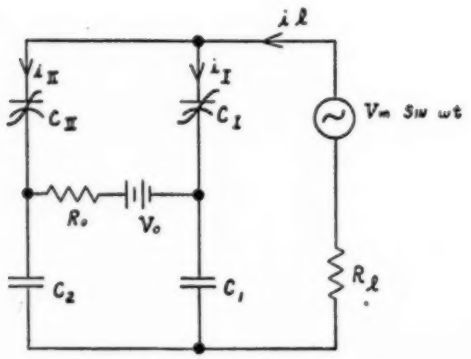

FIG. 2. Parallel-connected dielectric amplifier.

[1] A. M. Vincent, Electronics **24**, 84 (1951).

where

$$q_l = \int i_l dt = \int (i_{\rm I} + i_{\rm II})dt = q_{\rm I} + q_{\rm II}, \tag{7}$$

and $q_{\rm I}$, $q_{\rm II}$ are related to $v_{\rm I}$, $v_{\rm II}$ by the $Q-V$ characteristic (1). On combining Eqs. (1), (4), (6), and (7) it is found that

$$-\frac{V_m}{\omega}\cos\omega t = \int v\,dt + 2R_l\left[\frac{dQ(V)}{dV}\bigg|_{V=V_0/2}\right]v + 2R_l\sum_{n=1}^{\infty}\left\{\frac{1}{(2n+1)!}\left[\frac{d^{2n+1}Q(V)}{dV^{2n+1}}\bigg|_{V=V_0/2}\right]v^{2n+1}\right\}$$

$$= \int v\,dt + 2R_l C_V v + 2R_l\Phi(v), \tag{8}$$

where

$$C_V = \frac{dQ(V)}{dV}\bigg|_{V=V_0/2},$$

and

$$\Phi(v) = \sum_{n=1}^{\infty}\left\{\frac{1}{(2n+1)!}\left[\frac{d^{2n+1}Q(V)}{dV^{2n+1}}\bigg|_{V=V_0/2}\right]v^{2n+1}\right\}.$$

Equation (8) can be solved for v by using the Laplace transformation. The method has been used by Pipes in solving a similar equation of this type[2] and discussed by the author.[3] Take the Laplace transform of Eq. (8):

$$\frac{-V_m p}{\omega(p^2+\omega^2)} = \frac{\bar{v}-A}{p} + 2R_l C_V \bar{v} + 2R_l L[\Phi(v)], \tag{9}$$

where p is the Laplace variable, L the Laplace operator, $L(v)=\bar{v}(p)=\bar{v}$, and A is a constant. On rearranging Eq. (9) it is found that

$$\bar{v} = -\frac{V_m m}{\omega}\frac{p^2}{(p^2+\omega^2)(p+m)} + \frac{Am}{p+m} - \frac{1}{C_V}\left[1-\frac{m}{p+m}\right]\{L[\Phi(v)]\}, \tag{10}$$

where

$$m = \frac{1}{2R_l C_V}.$$

Take the inverse transform of Eq. (10). Since only the steady-state response is of interest here, the transient part of the inverse transform will be neglected. By the use of the Faltung theorem of the Laplace transforma-

[2] L. A. Pipes, J. Appl. Phys. **23**, 625 (1952).
[3] S. H. Chow, J. Appl. Phys. **25**, 216 (1954).

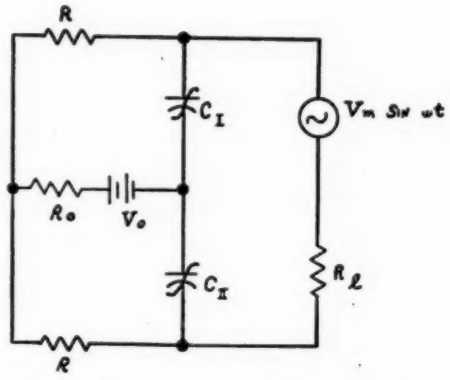

FIG. 3. Series-connected dielectric amplifier.

tion[4] the inverse transform of Eq. (10) is

$$v=\frac{V_m m}{(m^2+\omega^2)}(m\sin\omega t-\omega\cos\omega t)-\frac{1}{C_V}\Phi(v)+\frac{m}{C_V}\int_0^t \epsilon^{-m(t-u)}\cdot\Phi[v(u)]du. \quad (11)$$

The integral equation Eq. (11) can be solved by the method of successive approximations. By taking the first approximation of v as

$$v^{(1)}=\frac{V_m m}{(m^2+\omega^2)}(m\sin\omega t-\omega\cos\omega t), \quad (12)$$

the second approximation is

$$v^{(2)}=v^{(1)}-\frac{1}{C_V}\Phi[v^{(1)}]+\frac{m}{C_V}\int_0^t \epsilon^{-m(t-u)}\cdot\Phi[v^{(1)}(u)]du, \quad (13)$$

etc. Although $\Phi(v)$ occurring in Eq. (8) is an infinite series, a finite number of terms will be sufficient. The number of terms necessary depends on the accuracy desired, and the amplitude of V_0 and V_m. When V_0 and V_m are small only a few terms are necessary. The load current i_l is

$$i_l=\frac{1}{R_l}(V_m\sin\omega t-v). \quad (14)$$

On carrying out the details of the suggested procedure, the steady-state solution can be found to any desired degree of accuracy.

The response time of the parallel-connected dielectric amplifier depends mainly on the time constant $R_0C/2$, or the time necessary to charge the linear capacitors in series. The nonlinear capacitances, on account of their low values compared with C, affect the response time but little. The circuit is inherently a slow-response circuit. In order to avoid interactions between input and output circuits, either R_0 or C has to be high, and therefore the time constant is long.

It is desirable that the load resistance be low. The reason can be visualized in the following manner. When the infinite series $\Phi(v)$ is neglected in Eq. (8), the circuit equation is simply that of a resistance R_l and a linear capacitance $2C_V$ in series. When V_0 is zero, $2C_V$ is a high capacitance whose value will be denoted by C_h; and when V_0 is high, $2C_V$ is a low capacitance whose value will be denoted by C_l. For a high-gain amplifier, the difference in the power delivered to R_l when the capacitance is high and when the capacitance is low is given by

$$\Delta P=\frac{R_l}{2}\left[\frac{E_m^2}{\left(R_l^2+\frac{1}{\omega^2C_h^2}\right)}-\frac{E_m^2}{\left(R_l^2+\frac{1}{\omega^2C_l^2}\right)}\right], \quad (15)$$

which should be high. By neglecting the second term in Eq. (15) and differentiating the resulting equation with respect to R_l, it is found that ΔP is a maximum when $R_l=1/\omega C_h$. Therefore, R_l should be a low resistance.

When a shorter response time is desired, either R_0 or C should be low. In this case, the current through R_0 will be appreciable. The interaction between input and output circuits will then reduce the effectiveness of the input voltage in controlling the value of the nonlinear capacitances. This interaction may be called "inherent negative feedback."

IV. SERIES-CONNECTED AMPLIFIER

Figure 3 shows a series-connected dielectric amplifier. In this circuit R_0 should be high to avoid interaction between input and output circuits. A step input voltage V_0 will charge the nonlinear capacitors C_I and C_{II} to V_0 and $-V_0$, respectively. When a steady state sets in the current through R_0 is insignificant and will be neglected. Therefore, the steady-state circuit reduces to that

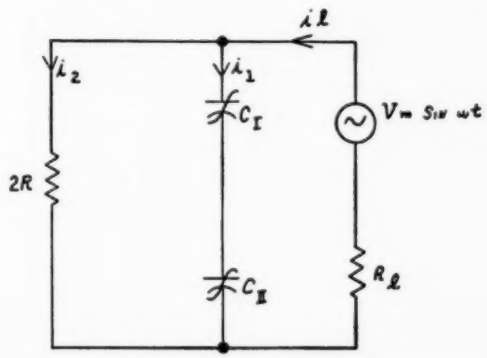

FIG. 4. Steady-state circuit of a series-connected dielectric amplifier.

[4] See, for instance, L. A. Pipes, *Applied Mathematics for Engineers and Physicists* (McGraw-Hill Book Company, Inc., New York, 1946), Chap. XXI.

shown in Fig. 4. The circuit equations read

$$V_m \sin\omega t = v_I + v_{II} + i_l R_l, \tag{16a}$$

$$V_m \sin\omega t = 2Ri_2 + i_l R_l, \tag{16b}$$

$$i_l = i_1 + i_2, \tag{16c}$$

where v_I, v_{II} are the voltages across C_I and C_{II}, respectively, and are related to the charges on C_I and C_{II} by the $Q-V$ characteristic (2). Since the same ac current flows through C_I and C_{II}, the charges on C_I and C_{II} are

$$q_I = q_1 + Q_0, \tag{17a}$$

$$q_{II} = q_1 - Q_0, \tag{17b}$$

where Q_0 is given by V_0 on the $Q-V$ characteristic (2), and $q_1 = \int i_1 dt$ is a periodic function to be determined. On combining Eqs. (2), (16), and (17) it is found that

$$\frac{2R}{2R+R_l} V_m \sin\omega t = \frac{2RR_l}{2R+R_l}\frac{dq_1}{dt} + 2\left[\frac{dV(Q)}{dQ}\bigg|_{Q=Q_0}\right] q_1 + 2\sum_{n=1}^{\infty}\left\{\frac{1}{(2n+1)!}\left[\frac{d^{2n+1}V(Q)}{dQ^{2n+1}}\bigg|_{Q=Q_0}\right] q_1^{2n+1}\right\}, \tag{18}$$

or

$$V_m' \sin\omega t = R_{11}\frac{dq_1}{dt} + 2Sq_1 + 2\Psi(q_1), \tag{19}$$

where

$$V_m' = \frac{2R}{2R+R_l} V_m,$$

$$R_{11} = \frac{2RR_l}{2R+R_l},$$

$$S = \frac{dV(Q)}{dQ}\bigg|_{Q=Q_0},$$

and

$$\Psi(q_1) = \sum_{n=1}^{\infty}\left\{\frac{1}{(2n+1)!}\left[\frac{d^{2n+1}V(Q)}{dQ^{2n+1}}\bigg|_{Q=Q_0}\right] q_1^{2n+1}\right\}.$$

Equation (19) can be transformed into an integral equation by the same procedure used in obtaining Eqs. (9), (10), and (11). The resultant integral equation is

$$q_1 = \frac{V_m'}{R_{11}(m'^2+\omega^2)}[m' \sin\omega t - \omega\cos\omega t] - \frac{2}{R_{11}}\int_0^t \epsilon^{-m'(t-u)} \cdot \Psi[q_1(u)]du, \tag{20}$$

where $m' = 2S/R_{11}$. By taking the first approximation of q_1 as

$$q_1^{(1)} = \frac{V_m'}{R_{11}(m'^2+\omega^2)}[m' \sin\omega t - \omega\cos\omega t], \tag{21}$$

the second approximation is

$$q_1^{(2)} = q_1^{(1)} - \frac{2}{R_{11}}\int_0^t \epsilon^{-m'(t-u)} \cdot \Psi[q_1^{(1)}(u)]du, \tag{22}$$

etc. Although $\Psi(q_1)$ has been expressed as an infinite series, one or two terms will prove to be sufficient. From Eq. (16) the load current i_l is

$$i_l = \frac{V_m}{2R+R_l}\sin\omega t + \frac{2R}{2R+R_l}\frac{dq_1}{dt}. \tag{23}$$

On carrying out the details of the suggested procedure, the steady-state solution can be found to any desired degree of accuracy.

The transient response of the series circuit may be studied with the ac voltage short-circuited. This device has been used by the author[3] in the transient analysis of a parallel-connected magnetic amplifier. Such a simplification proves to be necessary when the Laplace transformation is used in solving nonlinear equations. If the ac voltage is included in the analysis, the resultant transient is the transient excited when both the input voltage V_0 and the ac voltage $V_m \sin\omega t$ are suddenly applied to the circuit at the instant $t=0$. Such is not the case in practice, since the ac voltage is always present. Furthermore, neglecting the ac voltage introduces only a small error. The reasoning here is the same as that stated in reference 3. The simplified transient circuit then becomes that shown in Fig. 5, where $C_I(=C_{II})$ is the nonlinear capacitance. The charging of the nonlinear capacitance when a step input voltage V_0 is applied is

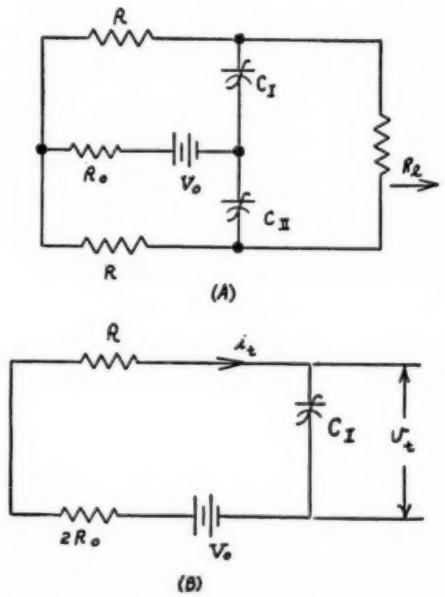

FIG. 5. Transient circuit of a series-connected dielectric amplifier.

governed by the following equation:

$$V_0=(2R_0+R)i_t+v_t=(2R_0+R)\frac{dq_t}{dt}+v(q_t), \quad (24)$$

where $v(q_t)$ is given by Eq. (2). Equation (24) may be transformed into an integral equation by the same procedure used in obtaining Eqs. (9), (10), and (11). The resultant integral equation is

$$q_t=\frac{V_0}{(2R_0+R)m''}+\left[Q_i-\frac{V_0}{(2R_0+R)m''}\right]\epsilon^{-m''t}$$
$$-\frac{1}{2R_0+R}\int_0^t \epsilon^{-m''(t-u)}$$
$$\cdot[k_3'q_t^3(u)+k_5'q_t^5(u)+\cdots]du, \quad (25)$$

where $m''=k_1'/(2R_0+R)$ and Q_i is the initial dc charge on the nonlinear capacitor. By taking the first approximation of q_t as

$$q_t^{(1)}=\frac{V_0}{(2R_0+R)m''}+\left[Q_i-\frac{V_0}{(2R_0+R)m''}\right]\epsilon^{-m''t}, \quad (26)$$

the second approximation is

$$q_t^{(2)}=q_t^{(1)}-\frac{1}{2R_0+R}\int_0^t \epsilon^{-m''(t-u)}\{k_3'[q_t^{(1)}(u)]^3$$
$$+k_5'[q_t^{(1)}(u)]^5+\cdots\}du, \quad (27)$$

etc. The charging of a nonlinear capacitor by a dc voltage can be visualized in the following manner. Initially the nonlinear capacitor has been charged to a dc potential V_i, corresponding to a dc charge Q_i. The differential capacitance of C_I is

$$C_i=\frac{1}{\left.\frac{dV(Q)}{dQ}\right|_{Q=Q_i}}. \quad (28)$$

When the nonlinear capacitor is then charged to V_0, corresponding to a dc charge Q_0, the differential capacitance is

$$C_0=\frac{1}{\left.\frac{dV(Q)}{dQ}\right|_{Q=Q_0}}. \quad (29)$$

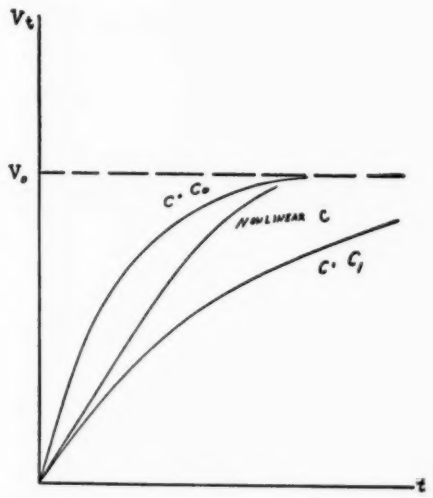

FIG. 6. Charging of a nonlinear capacitor by a dc voltage.

If the transient response curves of two linear series RC circuits with a resistance $(2R_0+R)$ and one with a capacitance C_i and the other with a capacitance C_0 are plotted, the transient voltage wave form of the nonlinear circuit must lie between the two curves. Figure 6 shows a case when $Q_i=0$.

In the series-connected amplifier the input resistance should be high and the load resistance should be low for the reasons mentioned in the analysis of the parallel-connected amplifier. If the input resistance is not high, the interaction between input and output circuits will cause an "inherent negative feedback" as in the parallel-connected circuit.

V. CONCLUSION

Dielectric amplifiers, with high input resistance and low load resistance, are inherently devices with high power gain and slow response. In the present paper, the steady-state response of both parallel- and series-connected dielectric amplifiers has been studied. By a series of successive approximations, the steady-state solution can be carried out to a high degree of accuracy. The transient response has also been studied. The entire analysis assumes a single-valued relation connecting Q and V of the nonlinear capacitors. Interactions between input and output circuits, which are negligible in high-gain, slow-response dielectric amplifier circuits, have been neglected. Certain of the engineering aspects of dielectric amplifiers may be found in reference 1 and will not be repeated here.

Applications of the Dirac Delta Function to the Evaluation of Certain Integrals

MURRAY R. SPIEGEL
Rensselaer Polytechnic Institute, Troy, New York
(Received December 24, 1953)

The evaluation of certain integrals is attained by use of ordinary linear differential equations having inputs that depend on the Dirac delta function. The method is illustrated by several examples.

I. INTRODUCTION

IN a recent article,[1] the author demonstrated how one could sum Fourier series by use of the Dirac delta function $\delta(x)$ which is usually defined by the property

$$\int_{-\infty}^{\infty}\delta(x-a)F(x)dx=F(a), \tag{1}$$

irrespective of the functions $F(x)$. The method given there was heuristic but gave results which could then be verified by other means. In the present article, we wish to exploit further the properties of the delta function to obtain results often desired in practice by physicists and engineers. Most of these results require for their rigorous derivations the theory of functions of a complex variable, in particular methods of contour integration and the theory of residues.

II. THE FOURIER INTEGRAL THEOREM

Fourier's Integral Theorem states that under suitable restrictions[2] on $f(x)$

$$f(x)=\frac{1}{2\pi}\int_{-\infty}^{\infty}e^{iux}du\int_{-\infty}^{\infty}e^{-iut}f(t)dt. \tag{2}$$

This theorem is sometimes given in terms of Fourier transforms in the symmetric form

$$f(x)=\frac{1}{\sqrt{2\pi}}\int_{-\infty}^{\infty}e^{iux}g(u)du, \tag{3}$$

$$g(u)=\frac{1}{\sqrt{2\pi}}\int_{-\infty}^{\infty}e^{-iut}f(t)dt. \tag{4}$$

It is easily shown that Eqs. (3) and (4) are equivalent to Eq. (1). Furthermore, it is not difficult to show from the above results that

$$f(x)=\int_{0}^{\infty}\{A(\lambda)\cos\lambda x+B(\lambda)\sin\lambda x\}d\lambda, \tag{5}$$

where

$$\begin{Bmatrix}A(\lambda)\\B(\lambda)\end{Bmatrix}=\frac{1}{\pi}\int_{-\infty}^{\infty}f(u)\begin{Bmatrix}\cos\lambda u\\\sin\lambda u\end{Bmatrix}du. \tag{6}$$

This is an analog of Fourier series where, instead of a summation being taken over a discrete set of values, we have an integration over a continuous set of values. From the fact that we had success in summing Fourier series by use of the Dirac delta function it would seem likely that one could evaluate integrals by a similar approach, i.e., one making use of the Dirac delta function.

III. SOME PRELIMINARY REMARKS

We proceed in a formal manner, assuming that Fourier's Integral Theorem holds for $f(x)\equiv\delta(x)$, the Dirac delta function. Accordingly, we obtain from Eqs. (5) and (6)

$$\delta(x)=\int_{0}^{\infty}\{A(\lambda)\cos\lambda x+B(\lambda)\sin\lambda x\}d\lambda, \tag{7}$$

where

$$\begin{Bmatrix}A(\lambda)\\B(\lambda)\end{Bmatrix}=\frac{1}{\pi}\int_{-\infty}^{\infty}\delta(u)\begin{Bmatrix}\cos\lambda u\\\sin\lambda u\end{Bmatrix}du. \tag{8}$$

According to Eq. (8) and the property (1) of the delta function [letting $a=0$ and $F(x)=\cos\lambda x$ and $\sin\lambda x$, respectively], it would seem plausible to take

$$A(\lambda)=\frac{1}{\pi}\int_{-\infty}^{\infty}\delta(u)\cos\lambda u du=\frac{1}{\pi} \tag{9}$$

and

$$B(\lambda)=\frac{1}{\pi}\int_{-\infty}^{\infty}\delta(u)\sin\lambda u du=0, \tag{10}$$

so that from Eq. (7) we have

$$\int_{0}^{\infty}\cos\lambda x dx=\pi\delta(\lambda) \tag{11}$$

but no similar relation exists for

$$\int_{0}^{\infty}\sin\lambda x dx. \tag{12}$$

We may write

$$\int_{-\infty}^{\infty}\cos\lambda x dx=2\pi\delta(\lambda) \tag{13}$$

$$\int_{-\infty}^{\infty}\sin\lambda x dx=0, \tag{14}$$

[1] M. R. Spiegel, J. Appl. Phys. **23**, 906 (1952).
[2] E. C. Titchmarsh, *Introduction to the Theory of Fourier Integrals* (Oxford University Press, London, 1937).

since $\cos\lambda x$ and $\sin\lambda x$ are even and odd functions of x, respectively.

IV. ILLUSTRATIVE EXAMPLES

The process of evaluating certain types of integrals making use of the relations (11) or (13) involving the delta function will now be demonstrated by the use of some illustrative examples.

Example 1

Evaluate

$$\int^{\infty} \frac{\sin x}{x} dx. \tag{15}$$

We first replace the x in $\sin x$ by λx to obtain

$$F(\lambda)=\int_0^{\infty} \frac{\sin\lambda x}{x} dx. \tag{16}$$

Differentiating formally with respect to λ, we obtain

$$F'(\lambda)=\frac{d}{d\lambda}\int_0^{\infty} \frac{\sin\lambda x}{x} dx$$

$$=\int_0^{\infty} \frac{\partial}{\partial\lambda}\left(\frac{\sin\lambda x}{x}\right) dx$$

$$=\int_0^{\infty} \cos\lambda x dx=\pi\delta(\lambda).$$

Hence,

$$F'(\lambda)=\pi\delta(\lambda). \tag{17}$$

Although the differential equation (17) (and similar differential equations of the future illustrative examples) may be solved by the methods of linear ordinary differential equations with constant coefficients, the author prefers the Laplace transform technique as yielding results more easily, in general.

Taking the Laplace transform of

$$F'(\lambda)=\pi\delta(\lambda) \tag{18}$$

with respect to λ, we have

$$\mathfrak{L}[F'(\lambda)]=\pi\mathfrak{L}[\delta(\lambda)] \tag{19}$$

or

$$sf(s)-F(0)=\frac{\pi}{2}, \tag{20}$$

where $f(s)$ is the Laplace transform of $F(\lambda)$. Since $F(0)=0$ as can be seen from Eq. (16), we have from Eq. (20)

$$sf(s)=\frac{\pi}{2}, \quad f(s)=\frac{\pi}{2s},$$

and thus

$$F(\lambda)=\frac{\pi}{2} \quad \lambda>0, \tag{21}$$

upon inversion.

From Eq. (16) we may deduce further that

$$F(\lambda)=\begin{cases} \frac{\pi}{2} & \lambda>0 \\ 0 & \lambda=0 \\ -\frac{\pi}{2} & \lambda<0. \end{cases} \tag{22}$$

The required integral (15) thus has the value $\pi/2$.

Example 2

Evaluate

$$\int_0^{\infty} \frac{\cos x}{x^2+4} dx. \tag{23}$$

Replacing $\cos x$ by $\cos\lambda x$ we have

$$F(\lambda)=\int_0^{\infty} \frac{\cos\lambda x}{x^2+4} dx. \tag{24}$$

Hence,

$$F'(\lambda)=\int_0^{\infty} \frac{-x\sin\lambda x}{x^2+4} dx \tag{25}$$

$$F''(\lambda)=\int_0^{\infty} \frac{-x^2\cos\lambda x}{x^2+4} dx. \tag{26}$$

From Eqs. (24) and (26) we obtain

$$F''(\lambda)-4F(\lambda)=\int_0^{\infty} \frac{-(x^2+4)\cos\lambda x}{x^2+4} dx$$

$$=-\int_0^{\infty} \cos\lambda x dx$$

$$=-\pi\delta(\lambda), \tag{27}$$

so that

$$F''(\lambda)-4F(\lambda)=-\pi\delta(\lambda). \tag{28}$$

Taking the Laplace transform we have

$$s^2f(s)-sF(0)-F'(0)-4f(s)=-\frac{\pi}{2}. \tag{29}$$

From Eq. (24) we have

$$F(0)=\int_0^{\infty} \frac{dx}{x^2+4}=\tfrac{1}{2}\arctan\frac{x}{2}\Big|_0^{\infty}=\frac{\pi}{4}. \tag{30}$$

Similarly we obtain from Eq. (25) $F'(0)=0$. Thus Eq. (29) becomes

$$(s^2-4)f(s)-\frac{\pi}{4}s=-\frac{\pi}{2},$$

or

$$f(s)=\frac{\frac{\pi s}{4}-\frac{\pi}{2}}{s^2-4}=\frac{\pi}{4}\left(\frac{s-2}{s^2-4}\right)=\frac{\pi}{4(s+2)}, \tag{31}$$

so that upon inversion we obtain

$$F(\lambda)=\frac{\pi}{4}e^{-2\lambda} \quad \lambda>0. \tag{32}$$

If in particular $\lambda=1$ we have the required integral evaluated to be

$$\int_0^\infty \frac{\cos x\,dx}{x^2+4}=\frac{\pi}{4e^2}. \tag{33}$$

In general we may easily show by the above technique that

$$\int_0^\infty \frac{\cos\lambda x}{x^2+a^2}dx=\begin{cases}\dfrac{\pi}{2a}e^{-a\lambda} & \lambda>0\\[2ex] \dfrac{\pi}{2a} & \lambda=0\\[2ex] \dfrac{\pi}{2a}e^{a\lambda} & \lambda<0,\end{cases} \tag{34}$$

where we assume $a>0$.

Example 3

Evaluate

$$\int_0^\infty \frac{x\sin x}{x^4+4}dx. \tag{35}$$

Consider

$$F(\lambda)=\int_0^\infty \frac{\cos\lambda x}{x^4+4}dx. \tag{36}$$

We have

$$F'(\lambda)=\int_0^\infty \frac{-x\sin\lambda x}{x^4+4}dx \tag{37}$$

$$F''(\lambda)=\int_0^\infty \frac{-x^2\cos\lambda x}{x^4+4}dx \tag{38}$$

$$F'''(\lambda)=\int_0^\infty \frac{x^3\sin\lambda x}{x^4+4}dx \tag{39}$$

$$F^{(iv)}(\lambda)=\int_0^\infty \frac{x^4\cos\lambda x}{x^4+4}dx. \tag{40}$$

From Eqs. (36) and (40) we have

$$F^{(iv)}(\lambda)+F(\lambda)=\int_0^\infty \cos\lambda x\,dx=\pi\delta(\lambda). \tag{41}$$

Taking the Laplace transform we obtain

$$s^4f(s)-s^3F(0)-s^2F'(0)-sF''(0)-F'''(0)+f(s)=\frac{\pi}{2}. \tag{42}$$

From Eqs. (37) and (39), we have $F'(0)=0$ and $F'''(0)=0$, so that Eq. (42) becomes

$$(s^4+1)f(s)-s^3F(0)-sF''(0)=\frac{\pi}{2}. \tag{43}$$

It will be noticed that $F(0)$ and $F''(0)$ remain undetermined. It can be seen from Eqs. (36) and (38) that

$$F(0)=\int_0^\infty \frac{dx}{x^4+4} \tag{44}$$

and

$$F''(0)=-\int_0^\infty \frac{x^2dx}{x^4+4}. \tag{45}$$

The present method would not be as useful if one had to determine the values of the integrals in (44) and (45) although they are not difficult to evaluate.[3]

The device now to be described enables us to avoid explicit evaluation of the integrals in (44) and (45). We solve for $f(s)$ in Eq. (43) to obtain

$$f(s)=\frac{\pi}{2(s^4+1)}+\frac{s}{s^4+1}F''(0)+\frac{s^3}{s^4+1}F(0). \tag{46}$$

Referring to a table of Laplace transforms and inverting we obtain

$$F(\lambda)=\frac{\pi}{8}\{\sin\lambda\cosh\lambda-\cos\lambda\sinh\lambda\}+\frac{F''(0)}{2}\sin\lambda\sinh\lambda+\frac{F(0)}{2}\cos\lambda\cosh\lambda. \tag{47}$$

By inspection of the terms in Eq. (47) we see that it may be written in the form

$$F(\lambda)=e^\lambda\left\{\frac{\pi}{16}\sin\lambda-\frac{\pi}{16}\cos\lambda+\frac{F''(0)}{4}\sin\lambda+\frac{F(0)}{4}\cos\lambda\right\}+\text{a similar term involving } e^{-\lambda}. \tag{48}$$

This in turn may be written

$$F(\lambda)=e^\lambda\left\{\left[\frac{F''(0)}{4}+\frac{\pi}{16}\right]\sin\lambda+\left[\frac{F(0)}{4}-\frac{\pi}{16}\right]\cos\lambda\right\}+\text{a similar term involving } e^{-\lambda}. \tag{49}$$

[3] In fact, they are special cases of the well-known result

$$\int_0^\infty \frac{x^{p-1}}{1+x}dx=\frac{\pi}{\sin p\pi} \quad 0<p<1.$$

Since $F(\lambda)$ must remain bounded (in fact it can be shown that it goes to zero) as $\lambda\to\infty$, we must necessarily have from Eq. (49)

$$\frac{F''(0)}{4}+\frac{\pi}{16}=0 \tag{50}$$

and

$$\frac{F(0)}{4}-\frac{\pi}{16}=0, \tag{51}$$

from which

$$F''(0)=-\frac{\pi}{4},\quad F(0)=\frac{\pi}{4}, \tag{52}$$

which incidentally evaluates the integrals (44) and (45).

From Eq. (47) we can now obtain the main result, namely,

$$\int_0^\infty \frac{\cos\lambda x}{x^4+4}dx=\frac{\pi}{8}\{\sin\lambda\cosh\lambda-\cos\lambda\sinh\lambda\} -\frac{\pi}{8}\sin\lambda\sinh\lambda+\frac{\pi}{8}\cos\lambda\cosh\lambda, \tag{53}$$

which reduces upon simplification to

$$\int_0^\infty \frac{\cos\lambda x}{x^4+4}dx=\frac{\pi}{8}e^{-\lambda}\{\sin\lambda+\cos\lambda\}. \tag{54}$$

Differentiation with respect to λ and placing $\lambda=1$ we obtain the required integral

$$\int_0^\infty \frac{x\sin x}{x^4+4}dx=\frac{\pi}{4e}\sin 1. \tag{55}$$

Example 4

Evaluate

$$\int_{-\infty}^{\infty}\frac{\sin 2x}{x^2+x+1}dx. \tag{56}$$

If we begin with the related integral

$$F(\lambda)=\int_{-\infty}^{\infty}\frac{\sin\lambda x}{x^2+x+1}dx \tag{57}$$

and compute

$$F'(\lambda)=\int_{-\infty}^{\infty}\frac{x\cos\lambda x}{x^2+x+1}dx \tag{58}$$

and

$$F''(\lambda)=\int_{-\infty}^{\infty}\frac{-x^2\sin\lambda x}{x^2+x+1}dx, \tag{59}$$

we find that it is impossible to combine the Eqs. (57), (58), and (59) so as to obtain a suitable linear differential equation with constant coefficients for $F(\lambda)$. It therefore seems, at first sight, that our method is inapplicable. However if we make use of form (2) of Fourier's Integral Theorem or the equivalent forms (3) and (4) we find by letting $f(x)\equiv\delta(x)$ that

$$\delta(x)=\frac{1}{(2\pi)^{\frac{1}{2}}}\int_{-\infty}^{\infty}e^{iux}g(u)du, \tag{60}$$

where

$$g(u)=\frac{1}{(2\pi)^{\frac{1}{2}}}\int_{-\infty}^{\infty}e^{-iut}\delta(t)dt=\frac{1}{(2\pi)^{\frac{1}{2}}}, \tag{61}$$

so that Eq. (60) gives

$$\delta(x)=\frac{1}{(2\pi)^{\frac{1}{2}}}\int_{-\infty}^{\infty}e^{iux}\frac{1}{(2\pi)^{\frac{1}{2}}}du \tag{62}$$

or

$$\delta(x)=\frac{1}{(2\pi)^{\frac{1}{2}}}\int_{-\infty}^{\infty}e^{iux}du, \tag{63}$$

i.e.,

$$\int_{-\infty}^{\infty}e^{iux}du=2\pi\delta(x). \tag{64}$$

This same result could have been arrived at by using

$$\int_{-\infty}^{\infty}(\cos\lambda x+i\sin\lambda x)d\lambda=2\pi\delta(\lambda) \tag{65}$$

from Eqs. (13) and (14) so that

$$\int_{-\infty}^{\infty}e^{i\lambda x}dx=2\pi\delta(\lambda). \tag{66}$$

Consider now instead of (57)

$$F(\lambda)=\int_{-\infty}^{\infty}\frac{e^{i\lambda x}}{x^2+x+1}dx. \tag{67}$$

By differentiation we obtain

$$F'(\lambda)=\int_{-\infty}^{\infty}\frac{ixe^{i\lambda x}}{x^2+x+1}dx \tag{68}$$

$$F''(\lambda)=\int_{-\infty}^{\infty}\frac{-x^2e^{i\lambda x}}{x^2+x+1}dx. \tag{69}$$

From Eqs. (67), (68), and (69) we obtain

$$-F''(\lambda)-iF'(\lambda)+F(\lambda)=\int_{-\infty}^{\infty}\frac{(x^2+x+1)e^{i\lambda x}}{x^2+x+1} =\int_{-\infty}^{\infty}e^{i\lambda x}dx=2\pi\delta(\lambda), \tag{70}$$

so that

$$F''(\lambda)+iF'(\lambda)-F(\lambda)=-2\pi\delta(\lambda). \tag{71}$$

Taking the Laplace transform we have

$$s^2f(s)-sF(0)-F'(0)$$
$$+i[sf(s)-F(0)]-f(s)=-\pi. \tag{72}$$

From (67) we find

$$F(0)=\int_{-\infty}^{\infty}\frac{dx}{x^2+x+1}=\int_{-\infty}^{\infty}\frac{dx}{(x+\frac{1}{2})^2+\frac{3}{4}}$$
$$=\frac{2}{(3)^{\frac{1}{2}}}\arctan\frac{2x+1}{(3)^{\frac{1}{2}}}\Bigg|_{-\infty}^{\infty}$$
$$=\frac{2\pi}{(3)^{\frac{1}{2}}}. \tag{73}$$

Similarly

$$F'(0)=i\int_{-\infty}^{\infty}\frac{xdx}{x^2+x+1}=i\int_{-\infty}^{\infty}\frac{(x+\frac{1}{2})}{(x+\frac{1}{2})^2+\frac{3}{4}}dx$$
$$-\tfrac{1}{2}i\int_{-\infty}^{\infty}\frac{dx}{x^2+x+1}=0-\tfrac{1}{2}i\cdot\frac{2\pi}{(3)^{\frac{1}{2}}}=-\frac{\pi i}{(3)^{\frac{1}{2}}}, \tag{74}$$

since

$$\int_{-\infty}^{\infty}\frac{(x+\frac{1}{2})dx}{(x+\frac{1}{2})^2+\frac{3}{4}}=0$$

in the Cauchy principal-value sense.

If the integrals had not been so simple to evaluate, a method analogous to that used in example 3 could have been employed.

From Eq. (72) and the results (73) and (74) we obtain

$$f(s)=\frac{\dfrac{2\pi s}{(3)^{\frac{1}{2}}}-\dfrac{\pi i}{(3)^{\frac{1}{2}}}+\dfrac{2\pi i}{(3)^{\frac{1}{2}}}-\pi}{s^2+is-1}$$
$$=\frac{\dfrac{2\pi}{(3)^{\frac{1}{2}}}\left(s+\dfrac{i}{2}\right)}{\left(s+\dfrac{i}{2}\right)^2-\frac{3}{4}}-\frac{\pi}{\left(s+\dfrac{i}{2}\right)^2-\frac{3}{4}}. \tag{75}$$

Inversion yields

$$F(\lambda)=\frac{2\pi}{(3)^{\frac{1}{2}}}\exp-\frac{i\lambda}{2}\cosh\frac{(3)^{\frac{1}{2}}}{2}\lambda-\frac{2\pi}{(3)^{\frac{1}{2}}}\exp-\frac{i\lambda}{2}\sinh\frac{(3)^{\frac{1}{2}}}{2}\lambda$$
$$=\frac{2\pi}{(3)^{\frac{1}{2}}}\exp-\frac{i\lambda}{2}\left(\cosh\frac{(3)^{\frac{1}{2}}}{2}\lambda-\sinh\frac{(3)^{\frac{1}{2}}}{2}\lambda\right)$$
$$=\frac{2\pi}{(3)^{\frac{1}{2}}}\exp-\frac{(3)^{\frac{1}{2}}\lambda}{2}\left(\cos\frac{\lambda}{2}-i\sin\frac{\lambda}{2}\right). \tag{76}$$

Hence,

$$\int_{-\infty}^{\infty}\frac{e^{i\lambda x}}{x^2+x+1}dx=\frac{2\pi}{(3)^{\frac{1}{2}}}\exp-\frac{(3)^{\frac{1}{2}}\lambda}{2}\left(\cos\frac{\lambda}{2}-i\sin\frac{\lambda}{2}\right), \tag{77}$$

so that by equating real and imaginary parts we obtain

$$\int_{-\infty}^{\infty}\frac{\cos\lambda x}{x^2+x+1}dx=\frac{2\pi}{(3)^{\frac{1}{2}}}\exp-\frac{(3)^{\frac{1}{2}}\lambda}{2}\cos\frac{\lambda}{2}\quad\lambda>0 \tag{78}$$

$$\int_{-\infty}^{\infty}\frac{\sin\lambda x}{x^2+x+1}dx=-\frac{2\pi}{(3)^{\frac{1}{2}}}\exp-\frac{(3)^{\frac{1}{2}}}{2}\sin\lambda\frac{\lambda}{2}\quad\lambda>0. \tag{79}$$

Hence, the value of the required integral is

$$\int_{-\infty}^{\infty}\frac{\sin 2x}{x^2+x+1}dx=-\frac{2\pi}{(3)^{\frac{1}{2}}}\exp-(3)^{\frac{1}{2}}\sin 1. \tag{80}$$

Compression Wave Velocity Experiments with Copper

JACOB SAVITT, R. H. STRESAU, AND L. E. STARR
U. S. Naval Ordnance Laboratory, White Oak, Maryland

(Received January 4, 1954)

A method for obtaining experimental compression wave velocities in metals is described. Measurements of the compression wave velocity in copper were made and found to be in good agreement with theoretical predictions. It is suggested that the discrepancy between the velocity (4730 m/sec) reported herein and that reported by Rinehart and Pearson (3600 m/sec) is associated with the different geometries of the two sets of experiments.

INTRODUCTION

WHEN a heavy walled metal cylinder is loaded internally with explosive it is sometimes observed that geometrically interesting failure patterns of the body of the cylinder are produced when the explosive is detonated from one end. Such distortions are shown in Figs. 1 and 2. In Fig. 1, the explosive was detonated at the back end of the cylinder and a cone torn off the front end of the brass cylinder. For the copper cylinder shown in Fig. 2, the ratio of the outside to the inside diameter of the heavy walled cylinder was greater than the corresponding ratio for the cylinder shown in Fig. 1. In this case the explosive was initiated at the left end of the cylinder. It was observed that no cone was torn from the cylinder and except for the change in its inside diameter its distortion was negligible. A longitudinal cross-sectional cut of the cylinder which was polished and etched in acid is shown in Fig. 2. The forces which tore the cone out, as in Fig. 1 were only large enough to distort the metal of Fig. 2.

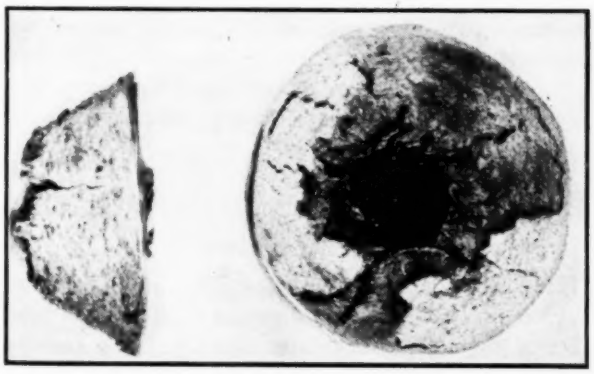

FIG. 1. Distortion of internally loaded brass cylinder. The explosive was initiated at the far end and a cone blown out of the near end.

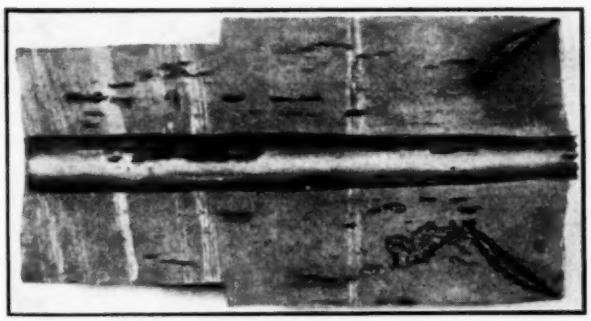

FIG. 2. A polished and etched longitudinal cross section of an internally loaded copper cylinder. The explosive was initiated at the left end.

THEORY

It is helpful to consider the following simplified description of the distortion producing phenomena. When the cylindrical explosive column (see Fig. 3) is detonated at one end, a high pressure impulse travels down the interior axis of the metal cylinder with the detonation velocity, v_E. In the metal, however, the compression wave travels with a velocity v_M which is less than v_E. The result is as illustrated. The front of the wave in the metal is inclined to the axis of the cylinder at an angle θ. If we assume negligible velocity attenuation, the wave front is conical and it is easily seen that

$$v_M = v_E \sin\theta. \tag{1}$$

When the compression wave in the metal reaches the surface of the cylinder, part of it is reflected back as a tension wave. The tension wave reflected from the forward end face of the cylinder and the tension wave

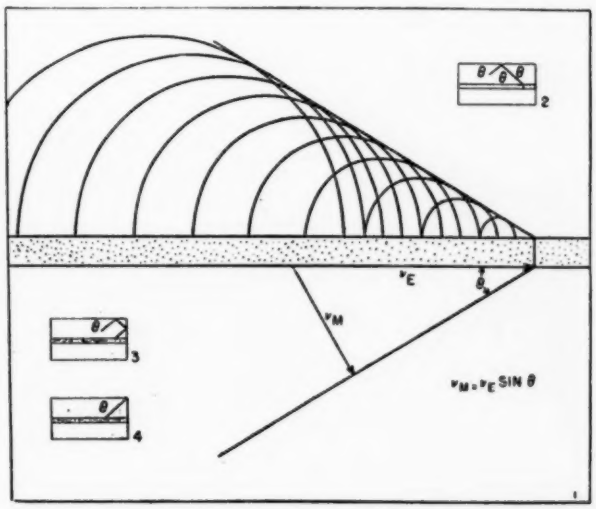

FIG. 3. A simplified description of the distortion produced by compression and tension wave interaction.

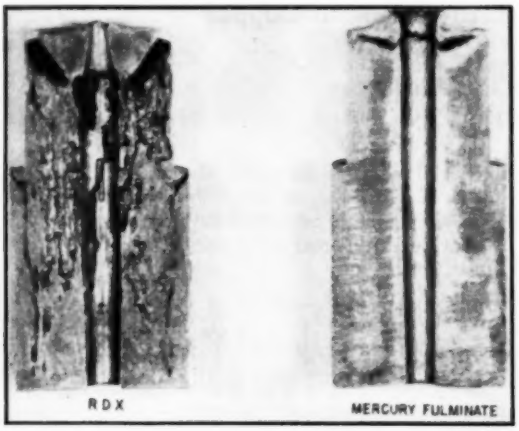

FIG. 4. Distortion of copper cylinders produced by the detonation of RDX and mercury fulminate when loaded internally under a pressure of 32 000 psi. The explosive was initiated at the bottom end.

reflected back from the side meet (as shown in the insets 2, 3, and 4). Since the maximum tensile stress associated with each of these waves is that immediately behind the front and since the stresses of the two colliding waves are additive, the material in the conical surface indicated by this line is subjected to a higher tensile stress than any other part of the nearby bar. If these stresses are large enough the metal tears along the line at the angle θ as shown. This crack in the metal is easily observed and if the detonation velocity of the explosive v_E is known, it is possible to calculate v_M using Eq. (1).

It is to be noted however, as shown in Fig. 2, there are actually two conical cracks in the metal, only one of which is straight. According to the simple theory presented however, only one crack should be observed and it should be straight. The straight conical crack will be discussed first, after which a few comments about the curved crack will be made.

The velocities v_L of longitudinal compression waves in elastic media are easily calculated. For unbounded

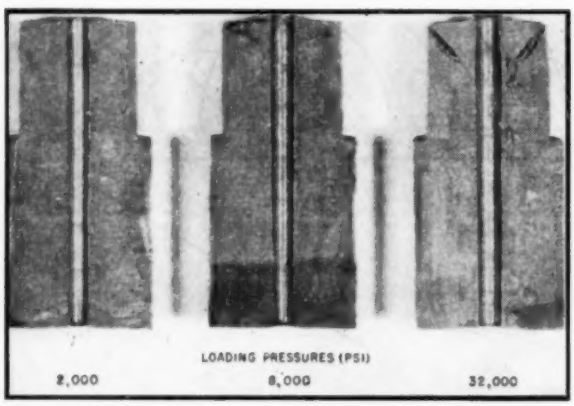

FIG. 5. Distortion of copper cylinders produced by the detonation of TNT when loaded internally at various pressures.

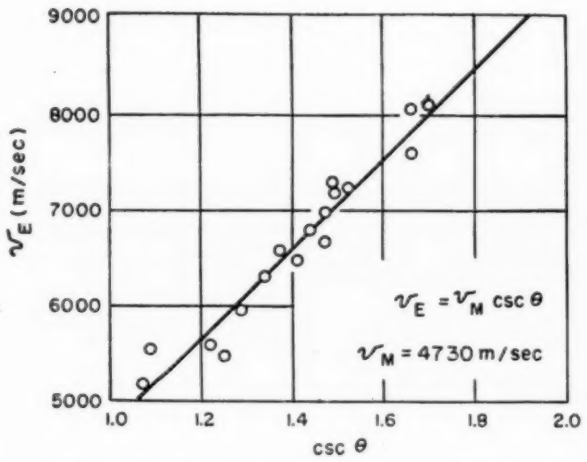

FIG. 6. Determination of compression wave velocity in copper from detonation velocity and spalling angle data.

media

$$v_L=[E(1-\sigma)/\rho(1+\sigma)(1-2\sigma)]^{\frac{1}{2}}. \quad (2)$$

For thin elastic bars

$$v_L=(E/\rho)^{\frac{1}{2}} \quad (3)$$

where

E is Young's modulus for the medium
σ is Poisson's ratio for the medium, and
ρ is its density.

For copper, the material used in the experiments to be described,

$$E=12.85\times10^{11} \text{ dynes/cm}^2$$
$$\sigma=0.35 \text{ and } \rho=8.9 \text{ g/cm}^3.$$

Accordingly $v_L=4800$ meters per second for unbounded media and 3600 meters per second for thin bars.

OBSERVATIONS

If the theory presented is essentially correct, different angles of crack should be observed for explosives having different detonation velocities. In Fig. 4, we see that this is the case. The explosives RDX and mercury fulminate were loaded into copper cylinders two inches

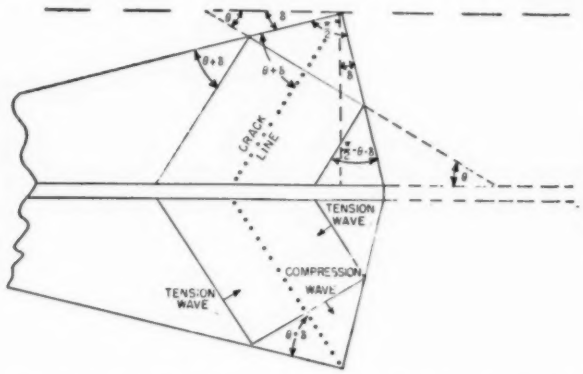

FIG. 7. A simplified description of the distortion produced by compression and tension wave interactions showing the effect of tapering the external diameter of the cylindrical explosive containers.

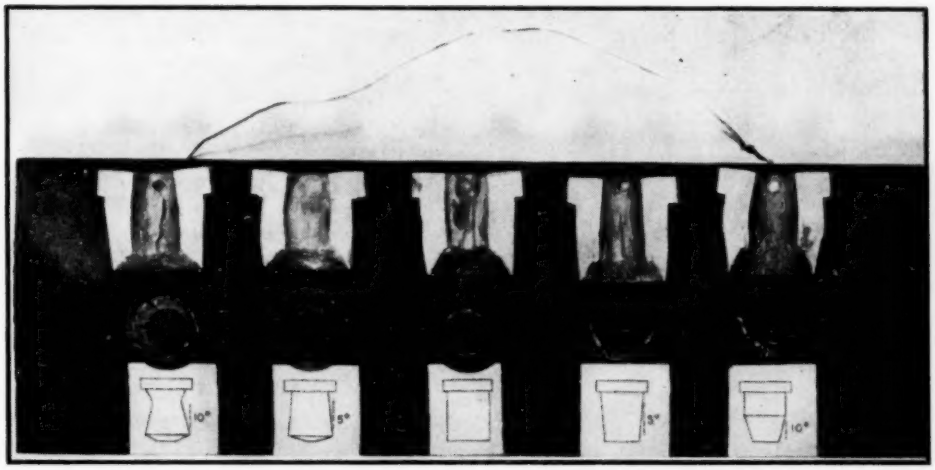

FIG. 8. Effect of tapered cylinders upon the fracture angle.

long and one inch in outside diameter. The inside diameter and the diameter of the explosive column were 0.075 inch. These explosive columns were initiated at the bottom using a special electric detonator containing about $\frac{1}{2}$ gram of lead azide. In Fig. 5, the distortions produced using TNT in the copper cylinders are shown. Many measurements of the angle θ were made using a large number of explosives loaded at the three pressures indicated in Fig. 5.

If the compression wave velocity in the copper is independent of the detonation pressure of the explosive then we should expect [see Eq. (1)] that if v_E is plotted against $\csc\theta$ as shown in Fig. 6, a straight line will be obtained, the slope of which is v_M, the compression wave velocity in the copper. Note that this seems to be the case, and that the observed compression wave velocity is 4730 meters per second. This is in good agreement with the prediction of Eq. (3), for the velocity in unbounded media.

It will be noted that the proposed mechanism whereby the failures are produced involves the interaction of relaxation waves reflected from the surfaces of the right cylindrical container. An obvious extension of the theory to containers with conical external surfaces would predict that a conical container whose diameter increases in the direction of detonation propagation should have a shallower fracture with a larger included angle, i.e., $\theta+\delta$ instead of θ and conversely a cone whose diameter decreases in the direction of propagation should have a deeper fracture with a smaller included angle. The extension of the theory is graphically illustrated in Fig. 7. A series of conical containers were made and loaded with tetryl which was detonated. The results, Fig. 8, support the extended theory and, in turn, provide further support for the application to the untapered cylindrical case.

DISCUSSION

Rinehart and Pearson[1] have performed similar experiments. The ratio of their copper cylinder diameter to the explosive column diameter was about 5 to 1 instead of the 13 to 1 of our system. For their system cones like that shown in Fig. 1 were blown out of the ends of their cylinders and θ was determined by measurements on this cone. They observe that the compression wave velocity in copper is about 3600 meters per second. This is in agreement with the velocity calculated using the bulk modulus (as they have done) as well as with the velocity calculated using Young's modulus. One possibility for the observed discrepancy between their observation of the compression wave velocity and ours is that their system is analogous to the propagation in thin bars (their cylinder walls are relatively thin compared to ours) while ours is analogous to propagation in unbounded media. Of course the fact that their explosive charges are of a much larger diameter than ours and their wall thicknesses are relatively thin suggests that their contention that the velocities which they measure are velocities associated with the bulk modulus of the copper is also reasonable.

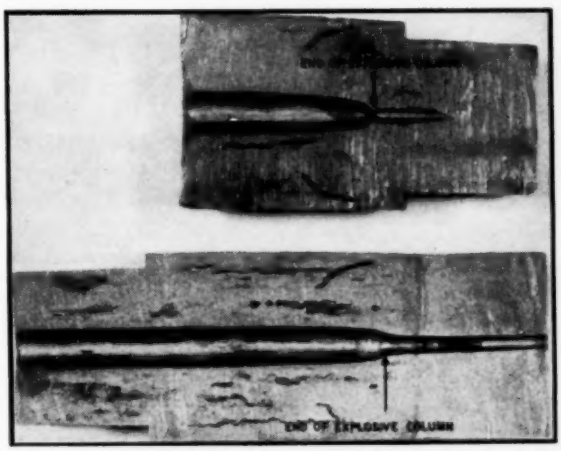

FIG. 9. The curved cracks associated with the end of the explosive column. The explosive was initiated at the left end of the cylinders.

[1] J. S. Rinehart and J. Pearson, J. Appl. Phys. **23**, 685 (1952).

It is of considerable interest to observe (see Fig. 9) that the curved conical crack previously mentioned (see Fig. 2) can be produced alone without the straight one. This was accomplished by loading the copper cylinders of Fig. 9 only as far as the position indicated. The straight cracks which we associate with the meeting of the relaxation waves reflected from both the side and the end of the cylinder are absent but the curved crack appears in the same position relative to the end of the explosive column. We conclude then that the curved cracks are associated only with the end of the explosive column while the straight cracks are the result of the interaction mechanism which depends upon the position and geometry of the metal cylinder surfaces.

JOURNAL OF APPLIED PHYSICS VOLUME 25, NUMBER 10 OCTOBER, 1954

Stationary Temperature Distribution in an Electrically Heated Conductor*

CHARLES A. DOMENICALI
Franklin Institute Laboratories, Philadelphia, Pennsylvania
(Received January 11, 1954)

The thermodynamic theory of irreversible processes as developed by Onsager, de Groot, and Callen is used to derive in a straightforward way the partial differential equation for the stationary temperature distribution in an electrically heated, chemically inhomogeneous conductor. It is shown that the form of this differential equation given in 1900 by Diesselhorst (for homogeneous media) in terms of the electrical potential gradient $\nabla\phi$ is incorrect. Diesselhorst's equation reads $\nabla\cdot\kappa\nabla T+\sigma\tau\nabla T\cdot\nabla\phi+\sigma(\nabla\phi)^2=0$, in which κ is the thermal conductivity (for zero electrical current), T the temperature, σ the isothermal electrical conductivity, and τ the Thomson coefficient. The correct form of the equation, for the special case of a chemically homogeneous conductor, is $\nabla\cdot\kappa\nabla T+(1/\sigma)J^2-\tau\mathbf{J}\cdot\nabla T=0$, where $\mathbf{J}$ is the electrical current density. The correct form can be obtained from Diesselhorst's equation by substitution of the "isothermal Ohm's law" $\mathbf{J}=-\sigma\nabla\phi$, which, however, is not valid in a nonisothermal medium. The apparent difficulty is resolved by the method of Onsager-de Groot-Callen, and it is shown that the correct differential equation expressed in terms of electrical potential is much more complicated than the form given by Diesselhorst.

WE wish to show how the thermodynamic theory of Onsager,[1] Callen,[2] and de Groot[3] leads in a straightforward way to the differential equation describing the stationary distribution of temperature in an electrically heated conductor. This differential equation, easy to derive in the usual way by considering heat production rates and heat transfer within the conducting medium, has on occasion been expressed incorrectly in terms of the electrical potential gradient $\nabla\phi$. The form often referred to is that of Diesselhorst,[4] namely

$$\nabla\cdot\kappa\nabla T+\sigma\tau\nabla T\cdot\nabla\phi+\sigma(\nabla\phi)^2=0, \tag{1}$$

in which κ is the thermal conductivity (for zero electrical current), T is the absolute temperature, σ and τ are, respectively, the (isothermal) electrical conductivity and the Thomson coefficient. We shall show that the correct equation expressed in terms of the electrical potential gradient is quite complicated and in fact consists of seven terms.

One of the advantages of the Onsager-de Groot-Callen theory is that it represents a kind of "field theory" of thermodynamics in the sense that one can describe irreversible phenomena in terms of vector functions which depend in general on position and on the time. Thus, in the present problem of finding the partial differential equation describing the *stationary* temperature distribution in an inhomogeneous, electrically heated conductor, one needs only to set the divergence of the total energy vector $\mathbf{W}$ equal to zero, where[5]

$$\mathbf{W}=-(1/e)(TS^*+\tilde{\mu})\mathbf{J}-\kappa\nabla T,$$

$-e$ is the electron charge, T the absolute temperature, S^* the entropy transported per particle (electron), $\mathbf{J}$ the electrical current density, and κ the thermal conductivity (at zero electrical current). In the steady state there can be no accumulation of energy within any arbitrary region of the current-carrying medium and the divergence of $\mathbf{W}$ must vanish.

$$\begin{aligned}0\equiv\nabla\cdot\mathbf{W}&=-(1/e)\mathbf{J}\cdot\nabla(TS^*+\tilde{\mu})-\nabla\cdot\kappa\nabla T\\&=-(1/e)\mathbf{J}\cdot(T\nabla S^*+S^*\nabla T+\nabla\tilde{\mu})-\nabla\cdot\kappa\nabla T.\end{aligned} \tag{2}$$

Now in an isotropic but inhomogeneous medium the parameter S^* depends not only on temperature but also on position, $S^*=S^*(x,y,z;T)$, so that the gradient ∇S^* has the form $\nabla S^*=(\partial S^*/\partial T)_{x_i}\nabla T+\nabla_T S^*$, where the subscript x_i indicates that the derivative $(\partial S^*/\partial T)_{x_i}$ is to be taken at a fixed point $x_i(=x,y,z)$, and the subscript T indicates that the gradient $\nabla_T S^*$ is to be taken at fixed temperature. In a homogeneous material this latter gradient vanishes.

* This work has been supported by the Squier Signal Laboratory, Fort Monmouth, New Jersey.
[1] L. Onsager, Phys. Rev. **38**, 2265 (1931); Ann. New York Acad. Sci. **46**, 241 (1945).
[2] H. B. Callen, Phys. Rev. **73**, 1349 (1949).
[3] S. R. de Groot, *Thermodynamics of Irreversible Processes* (Interscience Publishers, Inc., New York, 1951).
[4] H. Diesselhorst, Ann. Physik **1**, 312 (1900).
[5] C. A. Domenicali, Phys. Rev. **92**, 877 (1953).

It has been shown,[5,6] that in a nonisothermal medium the usual form of Ohm's law, $\nabla\phi=-(1/\sigma)\mathbf{J}$, must be replaced by the "generalized Ohm's law"

$$\nabla\bar{\mu}=\nabla\mu-e\nabla\phi=(e/\sigma)\mathbf{J}-S^*\nabla T, \tag{3}$$

in which the electrochemical potential $\bar{\mu}$ is separated into a chemical part (the chemical potential μ) and an electrical part (the electrical potential ϕ); *viz.*, $\bar{\mu}=\mu-e\phi$. If we then make use of Eq. (3) and the separation of ∇S^* into a spatial and a temperature part as described in the previous paragraph, Eq. (2) becomes

$$\begin{aligned}0&=-(1/e)\mathbf{J}\cdot[T(\partial S^*/\partial T)_{x_i}\nabla T+T\nabla_T S^*\\&\qquad+S^*\nabla T+(e/\sigma)\mathbf{J}-S^*\nabla T]-\nabla\cdot\kappa\nabla T\\&=-(1/e)T(\partial S^*/\partial T)_{x_i}\mathbf{J}\cdot\nabla T-(1/e)T\mathbf{J}\cdot\nabla_T S^*\\&\qquad-(1/\sigma)\mathbf{J}^2-\nabla\cdot\kappa\nabla T.\end{aligned} \tag{4}$$

The coefficient of $\mathbf{J}\cdot\nabla T$ in Eq. (4) is called[2,3,5,7] the Thomson coefficient τ, and $-(1/e)S^*\equiv S^{\text{abs}}=-\Pi^{\text{abs}}/T$, where S^{abs} and Π^{abs} are, respectively, the absolute thermoelectric power and the absolute Peltier coefficient of the material at point x_i at temperature T. Inserting these quantities into Eq. (4) we find the required differential equation specifying the stationary temperature distribution in an electrically heated, inhomogeneous conductor,

$$\nabla\cdot\kappa\nabla T+(1/\sigma)J^2+\mathbf{J}\cdot\nabla_T\Pi^{\text{abs}}-\tau\mathbf{J}\cdot\nabla T=0. \tag{5}$$

The third term in (5) represents an "inhomogeneity Peltier heat" which vanishes in a homogeneous conductor, so that for this latter kind of medium (5) takes the simpler form

$$\nabla\cdot\kappa\nabla T+(1/\sigma)\mathbf{J}^2-\tau\mathbf{J}\cdot\nabla T=0. \tag{6}$$

If one substitutes $\mathbf{J}$ in terms of $\nabla\phi$ from Eq. (3) into (6), one finds the complicated equation,

$$\begin{aligned}&\nabla\cdot\kappa\nabla T+\sigma\left(\tau-\frac{2S^*}{e}\right)\nabla\phi\cdot\nabla T+\sigma(\nabla\phi)^2\\&\quad-\frac{\sigma}{e}\left(\tau-\frac{2S^*}{e}\right)\nabla\mu\cdot\nabla T-\frac{S^*\sigma}{e}\left(\tau-\frac{S^*}{e}\right)(\nabla T)^2\\&\quad+\frac{\sigma}{e^2}(\nabla\mu)^2-\frac{2\sigma}{e}\nabla\mu\cdot\nabla\phi=0.\end{aligned} \tag{7}$$

Thus the correct equation, expressed in terms of the electrical potential gradient, contains five extra terms in addition to the three given by Diesselhorst's equation (1). On the other hand, comparison of (6) and (1) shows that the incorrect Eq. (1) leads to the correct relation (6) upon substitution of the incorrect (in a nonisothermal region) expression $\mathbf{J}=-\sigma\nabla\phi$. The explanation of this difficulty is as follows. Substitution of $\nabla\phi$ from (3) into (7) leads back to the form (6) and not, of course, to the Diesselhorst form (1). On the other hand, if we start with (1) and use the incorrect relation $\nabla\phi=-(1/\sigma)\mathbf{J}$, we are neglecting exactly all the terms in $\nabla\mu$ and $-S^*\nabla T$ in both (3) and (7), which make (7) reduce to (1) and which make $\nabla\mu-e\nabla\phi=(e/\sigma)\mathbf{J}-S^*\nabla T$ reduce to $\nabla\phi=-(1/\sigma)\mathbf{J}$.

The correct Eq. (7) expressed in terms of $\nabla\phi$ is not only complicated but is rather useless because little is known about the chemical potential μ in actual substances. We should, therefore, prefer to use the relation (6) in practice. If the current density distribution is known, (6) can be used (in principle) to find the actual stationary temperature distribution in a conducting region subject to given boundary conditions.

[6] H. B. Callen, Phys. Rev. **85**, 16 (1952).

[7] Callen and de Groot use a positive charge in their definitions whereas we use $-e$; this accounts for the difference in sign of the Thomson coefficient. On the other hand, the *electrical* current and the particle current in our case are in opposite directions, so that our equations involving τ are identical with those of Callen and de Groot.

Method for Determining the Viscoelastic Properties of Dilute Polymer Solutions at Audio-Frequencies

KARL SITTEL, PRINCE E. ROUSE, JR.,* AND EMERSON D. BAILEY†
The Franklin Institute Laboratories for Research and Development, Philadelphia, Pennsylvania
(Received January 20, 1954)

A sensitive instrument for the measurement of the viscoelastic properties of dilute polymer solutions is described. It makes use of torsion pendulums with resonant frequencies in the range between 200 cps and 2300 cps. The test liquid is contained in a hollow oscillating disk. The shearing stress which is exerted at the liquid-metal interface alters the frequency and rate of decay of the free oscillations of the pendulum. By means of an optical system, the oscillations of the pendulum are caused to modulate the light striking the cathode of a phototube. The frequency and the rate of decay of the resulting alternating voltage are measured electronically.

The operation of the instrument and the factors affecting the precision of measurement are analyzed.

INTRODUCTION

MEASUREMENT of the viscoelastic properties of dilute solutions of coiling polymeric molecules requires very sensitive instruments. The first technique suitable for work in this field was introduced by Mason;[1] it makes use of torsionally oscillating, cylindrical piezoelectric crystals. It is useful at frequencies from about 20 kc to about 100 kc. However, the dynamic properties of polymeric systems are known to vary with frequency over several decades of frequency. Furthermore, the location of the dispersion region is different for each system. Consequently, the study of this phenomenon requires the widest possible extension of the range of frequency over which measurements can be made. The instrument described here was developed to extend the range down to frequencies of the order of 100 cps. It has recently been used, together with quartz torsion crystals, in a study of the properties of dilute solutions of linear polymers.[2]

PRINCIPLES OF MEASUREMENT

The viscoelastic properties of a liquid may be studied by bringing the liquid into contact with a plane surface which executes a simple harmonic motion in its own plane with the angular frequency $\omega=2\pi f$. A shearing wave is propagated in the liquid. It will be assumed that the liquid extends to infinity in the direction of z-positive and that the plane surface is infinite in extent. When a steady state has been established, the transverse velocity of the liquid at the distance z from the surface is[3]

$$v=v_0e^{-\Gamma z}e^{i\omega t} \tag{1}$$

$$\Gamma=(i\omega\rho/\eta)^{\frac{1}{2}} \tag{1a}$$

where $i^2=-1$, v_0 is the maximum velocity of the oscillating surface, and η and ρ are, respectively, the viscosity and the density of the liquid. If the liquid is viscoelastic, the gradient of velocity is not in phase with the shearing stress. Under steady-state conditions, the phase difference can be taken into account by use in Eq. (1) of a complex viscosity, $\eta^*=\eta_1-i\eta_2$. In this complex representation a liquid with no shear elasticity has a value of $\eta_2=0$.

In a liquid of low viscosity, the amplitude of the wave described by Eq. (1) decreases rapidly with increasing values of z. At a frequency of 100 cps the transverse velocity in a liquid with a viscosity of ten centipoise and a density of one gram per cubic centimeter is reduced by a factor of 10^{-3} in approximately 1.2 mm. As Eq. (1) shows, the attenuation becomes even more rapid with increasing frequency or decreasing viscosity.

The rapid attenuation of the wave generated in the liquid prevents direct measurements of the phase and amplitude of the transmitted wave. The alternative is to measure the shearing stress exerted by the liquid upon the oscillating surface. This stress is

$$\begin{aligned}S&=-\eta^*(\partial v/\partial z)_{z=0}\\&=\eta^*\Gamma v_0e^{i\omega t}=(i\omega\rho\eta^*)^{\frac{1}{2}}v_{z=0}.\end{aligned}$$

The complex impedance per unit area Z of the liquid is defined as the ratio of the shearing stress to the particle velocity; it is related to the complex viscosity of the liquid by the equation

$$Z=R+iX=(i\omega\rho\eta^*)^{\frac{1}{2}}. \tag{2}$$

For a simple liquid, i.e., one for which $\eta_2=0$, real and imaginary parts of the impedance are equal and $Z=(1+i)(\pi f\rho\eta)^{\frac{1}{2}}$. For a viscoelastic liquid Eq. (2) can be solved for the components η_1 and η_2 of the complex viscosity to give

$$\eta_1=2RX/\omega\rho, \tag{3a}$$

$$\eta_2=(R^2-X^2)/\omega\rho. \tag{3b}$$

The instrument described here measures R by measuring the damping action of the liquid upon the free

* Now at Department of Chemistry and Chemical Engineering, University of Illinois, Urbana, Illinois.
† Now at The Budd Manufacturing Company, Philadelphia, Pennsylvania.
[1] W. P. Mason, Trans. Am. Soc. Mech. Engrs. **69**, 359 (1947).
[2] P. E. Rouse, Jr., and K. Sittel, J. Appl. Phys. **24**, 690 (1953).
[3] H. Lamb, *Hydrodynamics* (Dover Publications, New York, 1945), p. 619.

oscillations of a torsionally oscillating pendulum. The small decrease in the frequency of the free oscillations provides the means of measuring X. The pendulum consists of a hollow disk suspended below a massive disk by a torsion rod. The liquid is enclosed in the hollow disk. The free oscillations of the pendulum obey the differential equation

$$I\ddot{\theta}+Z_t\dot{\theta}+C^{-1}\theta=0, \tag{4}$$

where θ is the angular displacement of the hollow disk from its position at rest, I is the effective moment of inertia of the disk, and C is the effective moment of compliance of the torsion rod. The term $Z_t=R_i+(R_e+iX_e)$ is the sum of R_i, the moment of resistance resulting from internal frictional effects in the metal, and (R_e+iX_e) the moment of impedance of the liquid. The latter quantity is given by the integral over the internal surface of the hollow disk of the product $(R+iX)r^2dA$, where r is the distance of the infinitesimal area dA from the axis of rotation.

The appropriate solution of the differential Eq. (4) is

$$\theta=\theta_0e^{-\alpha t}e^{i\omega t}. \tag{5}$$

When the pendulum contains no liquid, $Z_t=R_i$. Then

$$\alpha=\alpha_0=R_i/2I, \tag{6a}$$

$$\omega^2=\omega_0^2=(IC)^{-1}-\alpha_0^2\cong(IC)^{-1}. \tag{6b}$$

Even with the most viscous liquids used in this study, the values of α and $\Delta\omega=\omega_0-\omega$ are both less than $0.005\,\omega$. Under these conditions the relations of α and $\Delta\omega$ to the components of the impedance of the liquid in the pendulum are given with sufficient accuracy by

$$\alpha=(R_i+R_e)/2I=\alpha_0+K_aR_M, \tag{7a}$$

$$\Delta\omega=X_e/(2I)=K_\omega X_M, \tag{7b}$$

$$K_a=K_\omega=\pi a^3(a+2h)/2I, \tag{7c}$$

where a is the radius of the hollow disk and h is the height of its lateral surface. These equations provide a means of obtaining values of R and X from which η_1, and η_2 can be calculated.

It will be noted that the experimental conditions differ in several details from those assumed in the derivation of Eq. (1). First, the liquid does not extend to infinity. This causes no difficulty since the shear wave is attenuated very rapidly. Even under the adverse conditions of the example discussed above ($f=100$ cps, $\eta=0.1$ poise) the wave would be attenuated by a factor of 10^{-24} in one centimeter, the shortest internal dimension of the disk.

Second, the surface presented to the liquid is not plane. The rapid attenuation of the wave also minimizes this difficulty. The relation of Z_e, the complex impedance presented by a liquid to a cylindrical surface which executes rotational oscillations about its axis, is related to Z, the impedance which the liquid presents to a plane surface, by the equation[4]

$$Z_e=Z[1-(3/2a\Gamma)+\cdots] \quad \text{if} \quad |a\Gamma|>10,$$

where a is the radius of the cylinder. Under the adverse conditions of viscosity and frequency considered above, the value of $|Z_e|$ is within one percent of $|Z|$ if a is greater than 1.4 cm. The hollow disk of each pendulum used in this work had a radius of 3.0 cm.

A more serious divergence of the experimental conditions from the assumption of a plane surface occurs at the joints between the lateral cylindrical surface and the approximately plane top and bottom of the disk. Rapid attenuation of the wave also reduces the importance of this factor. The residual effects were compensated, insofar as possible, by empirical calibration of each pendulum against a series of simple liquids of known viscosity and density.

The third difference between the experimental conditions and the assumptions upon which Eq. (1) is based is the substitution of a damped oscillation for a steady-state oscillation. The use of the concepts of complex viscosity and complex impedance under these conditions requires justification. For this purpose the decaying oscillations of the pendulum can be considered to be the sum of a continuous spectrum of steady-state oscillations. The effective values of R and X are then some sort of weighted averages of the values of R and X at each of the frequencies in the continuous spectrum. By application of the method of Fourier integration it can be shown that the square of the amplitude of the oscillation of frequency s is proportional to A^2, where

$$A^2=[\alpha^2+(\omega-2\pi s)^2]^{-1}.$$

This quantity has a maximum value at $s=f$, the resonant frequency. The frequencies at which A^2 has one percent of its maximum value are given by $s=(\omega-10\alpha)/2\pi$. For the liquids used in this work, experimental values of α are less than 0.005ω. Thus the spectrum of frequencies present in the decaying oscillations of the pendulum contains no appreciable contribution with frequencies more than 5 percent greater or 5 percent less than the resonant frequency of the loaded pendulum. At frequencies outside of the regions of dispersion of viscosity, R and X increase with frequency in proportion to the square root of the frequency, while in regions of dispersions the rate of increase is even smaller. Accordingly, it is a good approximation to take the values of R and X obtained from Eqs. (7a) and (7b) as the true values at the resonant frequency of the loaded pendulum.

DESCRIPTION OF THE INSTRUMENT

The torsion pendulum is shown in Fig. 1. The upper part of the lower disk, the torsion rod, and the cylindrical insert in the upper disk were machined from a single piece of stainless steel. The insert was held in

[4] H. J. McSkimin, J. Acoust. Soc. Am. **24**, 355 (1952).

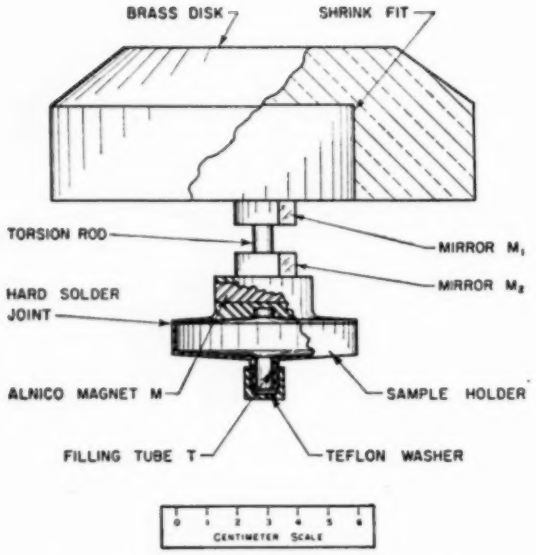

FIG. 1. Schematic drawing of torsion pendulum.

the large upper disk by a "shrink fit." The upper disk was of brass and had a moment of inertia about 700 times that of the lower disk. The large moment of inertia of the upper disk kept the amplitude of its oscillations very small. This, together with the small torsional stiffness of the 0.010-in. steel wire by which the upper disk was suspended, prevented transmission of energy from the oscillating pendulum to the support.

The hollow disk inside which the liquid sample was placed for measurement was constructed by silver soldering the lower and upper parts together at the joint indicated in Fig. 1. The soldering operation was performed with uniform heating on a constantly rotating turntable to prevent distortion of the thin walls (0.5 mm) of the disk. Oxidation of the internal surfaces during the soldering operation was prevented by introducing a stream of helium through the tube T. The top and the bottom of the disk were conically shaped to prevent distortion. The conical shape of the top also served to guide any bubbles in the liquid to the small indentation in the center of the top. A bubble contained in this indentation had a negligible effect upon the oscillations of the pendulum. The tube T through which the sample was introduced was closed by a threaded cap sealed with a Teflon gasket.

The torsional oscillations of the pendulum were excited by means of a horizontal, alternating magnetic field between two coils. The action of the field upon the Alnico V magnet M, which had been forced into a snugly fitting hole in the upper part of the oscillating disk, produced an alternating torque about the vertical axis of the pendulum. The purely torsional character of the forces exerted on the pendulum by the magnetic field was assured by the symmetry of the arrangement. The diameter of the coils was 20 cm and the distance between the coils 10 cm. The coils were wound of 19-gauge copper wire and had sufficient turns to give a cross section of 6.85 cm^2. The magnet M in the oscillating disk was horizontal and perpendicular to the lines of force between the coils. The pendulum was suspended midway between the coils and at a height which placed the magnet approximately on the horizontal line between the centers of the coils.

The vibrations were detected optically by means of two coplanar mirrors. One of the mirrors, designated M_1 in Fig. 1, was fixed to the massive upper disk and the other, M_2, was mounted on the oscillating disk. The use of two mirrors was made necessary by the low torsional stiffness of the fine wire by which the assembly was suspended. The suspended mass could undergo rotational oscillations about the suspension wire at a low frequency. The optical system was designed to prevent these unwanted oscillations from interfering with the detection of the torsional oscillations of the hollow disk about the torsion rod. An image of the source was focused on M_1. The light reflected from this mirror fell on a stationary spherical mirror which produced an image of the source on M_2. After reflection from M_2 the light entered the detecting system. As a result the direction of the emergent beam was changed only if M_1 and M_2 rotated with respect to each other.

The optical detecting system is depicted in Fig. 2. Light emitted by the Western Union 100-watt zirconium arc source was focused on a stop by means of a lens. The stop was used to cut off light from the outer part of the source, which was influenced by an unsteady gas arc. A second lens formed a parallel beam, and, together with a third lens, focused an image of the stop on the reference mirror M_1. Between the second and third lenses a semicircular aperture cut the light beam in half. The distance of the aperture from the third lens was adjusted to bring it into focus on the spherical mirror. The third lens, then, would have superposed an image of the semicircular aperture directly upon the aperture itself. Instead, by the interposition of two adjustable mirrors, the image was brought into focus upon a similar aperture in which the opening was on the opposite side. This second aperture cut off all but a narrow vertical sliver of the beam. By means of a fixed mirror and a lens this sliver was brought into focus on the cathode of a Type 931-A photomultiplier tube. In practice the two semicircular apertures

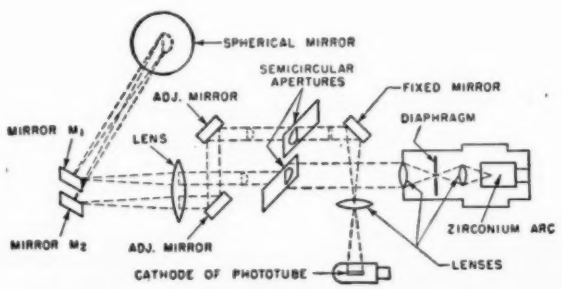

FIG. 2. Optical system.

were replaced with grids, each of which had opaque lines 0.5 mm wide separated by clear spaces 0.5 mm wide. This increased the sensitivity in the detector by increasing the amount of modulated light striking the photomultiplier cathode. However, the use of grids with more than about ten lines per centimeter was found to be impractical because of diffraction.

The natural frequencies of the pendulums had a temperature coefficient of about 240×10^{-6} per degree centigrade. A temperature change of 1°C would change the frequency by an amount comparable to the change caused by a liquid such as toluene. This made it necessary to hold the temperature of the pendulum as nearly constant as possible during a measurement and to measure this temperature with a precision of ±0.005°C.

For control of the temperature the pendulum and the driving coils were mounted in a closed chamber provided with windows for the passage of the light beam. The chamber had hollow brass walls through which water was circulated from a thermostatic water bath. The temperature of the water was controlled at 30.35°C ±0.05°C. A centrifugal fan was used to agitate the air inside the box to accelerate the attainment of thermal equilibrium. When the pendulum reached the proper temperature the fan was stopped. Under these conditions the pendulum was well insulated against the short-term fluctuations of the temperature of the metal walls of the chamber.

The temperature of the pendulum was measured by means of a platinum resistance thermometer inserted in the massive upper disk. The resistance of the thermometer was measured with a simple bridge in which the ratio arms were two matched 100-ohm resistors. The measuring arm consisted of a fixed nichrome resistor, with a resistance of 4.015 ohms, connected in series with a parallel combination of a 25.02-ohm wire-wound resistor and a decade resistance box (General Radio Type 602-N). All components of the bridge except the resistance box were placed inside the temperature-controlled chamber. The bridge balance was obtained by varying the setting of the resistance box, using a sensitive galvanometer (Leeds and Northrup No. 2284) as the detector. In this way changes in the temperature of the pendulum were measurable with a precision of ±0.005°C.

Since disturbances such as external shock waves or vibrations would set the suspended pendulum assembly into vibration, the pendulum, driving coils, and optical system were mounted on a concrete pillar. A heavy plate of slate served as a top for the pillar and a similar plate was supported upon it by rubber shock mounts. Upon this mechanically insulated base the apparatus was assembled.

ASSOCIATED ELECTRONIC EQUIPMENT

The oscillations of the pendulum were translated by the optical system and photomultiplier into an alternating voltage whose frequency and rate of decay were measured by the electronic system the block diagram of which is given in Fig. 3. The output of the photomultiplier was amplified by the voltage amplifier and fed into the driving amplifier, which has a maximum output of 50 watts. When the output of this amplifier was connected to the driving coils and the phase shift around the loop was adjusted to a small value, the pendulum went into oscillation. The amplitude of the oscillations was limited by adjustment of a variable resistor in series with the coils; thus the intensity of the magnetic field was adjusted to compensate for the damping of the liquid in the pendulum. To make a measurement, the coils were connected and the oscillations allowed to build up until the output of the voltage amplifier exceeded 70 v rms. It was experimentally determined that this voltage corresponds to an amplitude of oscillation of the pendulum of about 10^{-4} radian.

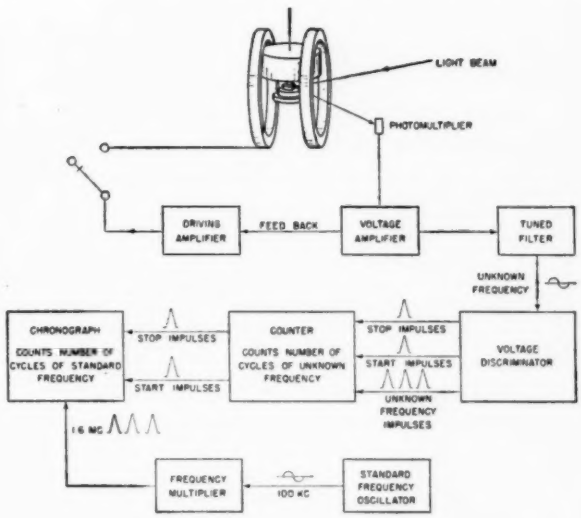

FIG. 3. Block diagram of electronic circuits.

The coils were then disconnected from the amplifier and the oscillations of the pendulum allowed to decay. The noise in the output of the photomultiplier made it necessary to pass the voltage representing the decaying oscillations through a filter tuned to the resonant frequency of the pendulum. The band width of the filter was adjusted to reduce the noise voltage to about 0.1 v rms. Under these conditions the rate of decay of the oscillations of the filter was still very large compared to that of the oscillations of the pendulum. This condition was necessary in order to avoid significant alteration by the filter of the rate of decay of the oscillating voltage.

The decaying voltage was finally applied to a voltage discriminator,[5] a schematic diagram of which is given in Fig. 4. The discriminator makes use of five Schmitt trigger circuits.[6] The important property of the Schmitt

[5] The electronic discriminator was designed by Professor W. C. Elmore of Swarthmore College.

[6] W. C. Elmore and M. Sands, *Electronics; Experimental Techniques* (McGraw-Hill Book Company, Inc., New York, 1949).

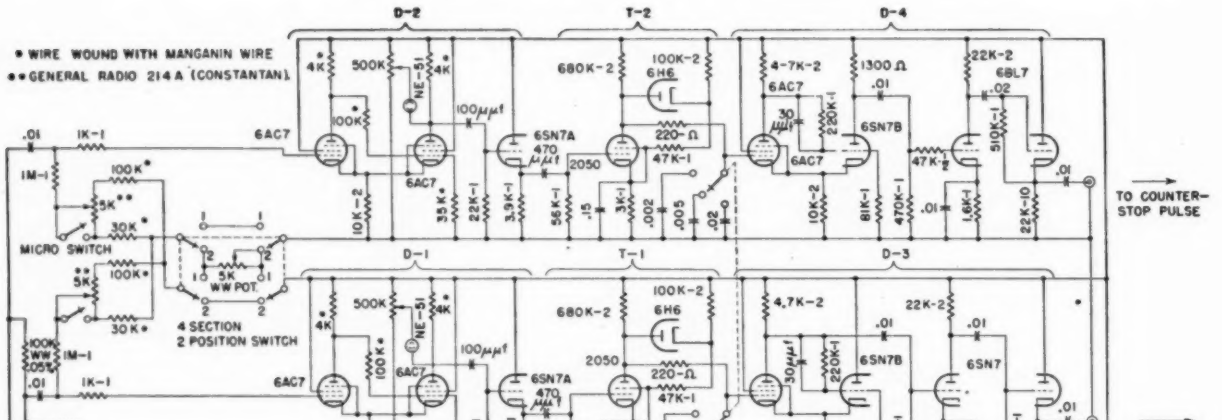

FIG. 4. Discriminator circuit.

trigger circuit in this application is that it produces a pulse as the instantaneous voltage at its grid rises above a value which can be precisely predetermined.

One of the trigger circuits, *D*-0, was used to produce a pulse for each oscillation of the pendulum, namely, each time the input voltage rose above zero. In this way the phase relationship between these pulses and the oscillations of the pendulum was independent of the amplitude of oscillation.

The trigger circuits *D*-1 and *D*-2 were adjusted to operate at the same voltage, approximately 9 v. The output of the filter was attenuated by a factor of 11 before being applied to the input of *D*-1. Thus *D*-1 ceased producing pulses when the amplitude of the voltage at the output of the filter dropped below about 100 v. The pulses from *D*-1 were applied to the grid of the thyratron tube (see Fig. 4), each pulse causing the thyratron to become conducting, and to discharge the condenser connected between its plate and the ground. The condenser then was recharged through the resistor connected in series with the condenser across the plate voltage supply. The thyratron circuit is indicated as *T*-1 in Fig. 4.

The time constant of the resistor-condenser combination was adjusted to approximately one-third the period of the pendulum. As long as the amplitude of the output of the filter remained above 100 v, the pulses produced by *D*-1 prevented the voltage on the condenser from rising to the critical voltage of discriminator *D*-3, another Schmitt trigger circuit. When *D*-1 missed one pulse, as it did if the input signal did not rise to the critical voltage, the voltage on the condenser rose above the critical voltage of *D*-3. The resulting pulse from *D*-3 opened the gating circuit of the counter (Potter Instrument Company, Model 3025) and prepared it for counting the pulses from *D*-0. The next pulse from *D*-0, in addition to being registered by the counter, caused the gating circuit to produce a pulse that started the chronograph (Potter Instrument Company, Model 450A) which counted pulses generated at a standard frequency of 1.6 megacycles.

The output of the filter was applied directly to the grid of *D*-2; thus *D*-2 continued to produce pulses until the amplitude of the signal fell below about 9 v. At that point *D*-4 produced a "stop" pulse in the same way that *D*-3 produced the "start" pulse. The "stop" pulse closed the gating circuit of the counter. The next pulse of *D*-0 caused the gating circuit of the counter to produce a pulse which stopped the chronograph.

The operation of these electronic circuits produced two numerical data, namely, the number of cycles, n, registered by the counter, and the count registered by the chronograph. The first represents the integral number of *maxima* of the voltage ouput of the filter that occurred between the first maximum to fall below E_a (approximately 100 v) and the first maximum to fall below E_b (approximately 9 v). The second represents the integral number of pulses, m, of the standard frequency, 1.6 megacycles, that occurred between the first pulse of *D*-0 following the "start" pulse and the first pulse of *D*-0 following the "stop" pulse. From these two numbers, values of the frequency f and the

decay constant α of the free oscillations of the pendulum can be calculated by means of the equations

$$f = f_0 n/m, \tag{8}$$

$$\alpha = f_0 \ln x/m. \tag{9}$$

In these equations f_0 is the standard frequency (1.6 mc) and $x = E_a/E_b$, the ratio of the voltages at which discriminators D-1 and D-2 were adjusted to operate.

MEASUREMENTS AND CALIBRATION

For each filling of the pendulum two sets of measurements separated by an interval of about one hour were made. About fifteen minutes were required to make forty measurements in each set and to record the forty pairs of values of m and n that were obtained. A value of α was calculated from each set of measurements by averaging the values of m and substituting this average in Eq. (9). An analysis of the sources of error, which is discussed below, showed that the expectation of the value of α obtained in this way is the true value of α.

The values of n obtained in a set of measurements varied over a range that depended on the values of α and f. Because of these variations it was expedient to calculate a value of f from each pair of values of m and n. The analysis of the sources of error showed that the expectation of the mean of these values was related to the true value of the frequency by the equation

$$\left\langle \frac{f_0 n}{m} \right\rangle_{Av} = f\left[1 + \frac{\sigma_f^2}{f^2} + \cdots\right],$$

where σ_f is the root-mean-square deviation of the single values of f from the mean. This result indicates that the error introduced by averaging in this way is insignificant in comparison with the experimental errors.

An empirical calibration was carried out with each pendulum, including measurements with air and with liquids of different viscosities. The constants of the pendulums are given in Table I. Measurements on the largest number of liquids were made in the 900-cycle pendulum, the calibration curves of which are shown in Fig. 5.

The degree to which the operation of the instrument conforms to the assumptions upon which Eqs. (7a) and (7b) are based can be seen by comparing the empirical values of the constants K_α and K_ω to those predicted by Eq. (7c). Values of I, the moment of inertia of the oscillating disk, were estimated for each of the three pendulums by means of the equation

$$I = \frac{\mu r^4}{8\pi f^2 l},$$

where μ is the torsional modulus of the torsion rod (7.3×10^{11} dynes/cm^2 for stainless steel), r and l are the radius and length, respectively, of the torsion rod, and f is the resonant frequency of the pendulum. For each of the pendulums a was 3 cm and h was 1 cm. The calculated constant of the 220-cycle pendulum was 0.67, that of the 900-cycle pendulum 0.54, and that of the 2300-cycle pendulum 0.45. The agreement with the empirical values given in Table I is reasonably satisfactory.

TABLE I. Empirical values of the constants of the pendulums.

f_0	K_ω	α_0	K_α
220.75	0.690	0.123	0.640
898.88	0.520	0.400	0.545
2305.5	0.525	1.50	0.590

PRECISION OF MEASUREMENT

Values of α and f calculated from experimental data obtained by this technique were subject to errors arising from the following sources: (1) the presence of "noise" voltage in the signal produced by the photomultiplier, (2) the fixed phase relationship between the pulses produced by the discriminators and the oscillations of the signal voltage, (3) the ability of the chronograph to register only integral numbers of pulses, (4) uncontrolled variations in the operating voltages of the discriminator circuits, (5) variations in the standard frequency f_0.

The effect of the last factor was made insignificant by the use of a secondary frequency standard, the output of which was often compared with the 5-mc carrier frequency transmitted by Station WWV. In this way the variations in f_0 were restricted to about one part in 5×10^6.

The variability of the operating voltages of the discriminators was minimized by use of well-regulated power supplies. In addition, resistors wound with manganin wire were used at all points in the circuit at

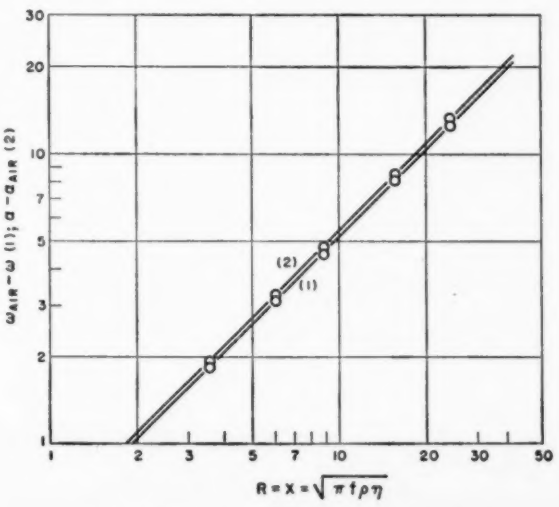

FIG. 5. Calibration of the 900-cycle pendulum.

which change in the resistance would affect the operating voltage. Before each series of measurements the operating voltages of D-1 and D-2 were set by comparison with the same dc voltage of about 9 v, which was obtained from the regulated high voltage supply of the discriminator circuits. The data indicate that these precautions reduced the variations in the ratio of the operating voltages of the discriminators to such an extent that they were less important than the noise voltages in the signal applied to the discriminators.

A detailed analysis has been made of the effects of the first three factors listed above upon the experimental precision. The bases and results of this analysis will be presented here but the details of the analysis will be omitted.

The character of the "noise" produced by the photomultiplier was greatly modified by the action of the band-pass filter through which the signal passed before being applied to the discriminators. It has been shown[7] that, if random noise such as that produced by the "shot effect" is applied to the input of a relatively narrow band-pass filter, the noise voltage at the output of the filter can be represented by an equation of the form

$$\Delta E=\Delta E_1\cos\omega_m t-\Delta E_2\sin\omega_m t, \qquad (10)$$

where ω_m is roughly equal to 2π times the midband frequency of the filter. This equation resolves the output noise into two components, which are ninety degrees out of phase. The amplitudes ΔE_1 and ΔE_2 undergo independent, random fluctuations, which obey a Gaussian distribution law:

$$P(\Delta E_i)d(\Delta E_i)=\frac{h}{\pi^{\frac{1}{2}}}\exp[-h^2(\Delta E_i)^2]d(\Delta E_i), \qquad (11)$$

where $i=1, 2$. The frequency of the fluctuations can be expressed in terms of the number of maxima of the *envelope* of the noise voltage which can be expected to occur in one second. To calculate this number the power distribution curve of the filter must be known. The filter used in this work consisted of a single resonant circuit. The power distribution curve of such a nonideal filter can be approximated by a Gaussian function

$$w(f)=\frac{1}{\sigma(2\pi)^{\frac{1}{2}}}\exp\left[-\frac{(f-f_m)^2}{2\sigma^2}\right].$$

The value of σ can be obtained by determining the frequency $f_{\frac{1}{2}}$ at which the power output is one-half the output at the midband frequency. Thus

$$\sigma=0.849|f_{\frac{1}{2}}-f_m|;$$

the expected number of maxima per second is then

$$\nu=2.52\sigma=2.14|f_{\frac{1}{2}}-f_m|.$$

[7] S. O. Rice, Bell System Tech. J. **23**, 282 (1944); **24**, 46 (1945).

The values of ν calculated from the measured band width of the filter are: $\nu=22$ at 220 cps; $\nu=27$ at 900 cps; $\nu=60$ at 2300 cps. These values indicate that the frequency of fluctuation is small compared to the frequency of the applied signal.

The noise voltages affected the experimental data by altering the timing of the pulses produced by the trigger circuits. If the first component, $\Delta E_1\cos\omega_m t$, is considered to be exactly in phase with the applied signal, it is found that the timing of D-1 and D-2, which operated when the amplitude dropped below predetermined levels, was affected by this component only. Furthermore, the timing of D-0, which was adjusted to operate as the instantaneous voltage rose above zero, was affected only by the out-of-phase component of the noise. Because of the low frequency of fluctuation of the noise voltages it was permissible to assume that in any one measurement the noise voltage that affected the timing of any particular output pulse had a definite value, the probability of which was given by Eq. (11). Since the "start" and "stop" pulses were separated by many cycles of the applied signal, the noise voltages that affected the "stop" pulse were independent of those that affected the "start" pulse. From these considerations it is clear that the probability of any particular pulse being advanced or delayed by any particular time can be calculated from the probability of the corresponding noise voltage.

In addition to the noise, the fixed phase relationship between the pulses of D-1 and D-2 and the oscillations of the signal voltage also affected the time m/f_0 registered by the chronograph. If, in a particular measurement, the time required for the *envelope* of the combined signal and noise voltages to decay from E_1 to E_2 corresponded to $N+p$ periods of the pendulum (N being an integer and p a fraction less than unity), the chronograph would register a time corresponding approximately to either N or $N+1$ periods of the pendulum. The probability of registering a time corresponding to N periods was equal to $1-p$, while the probability of registering a time corresponding to $N+1$ periods was equal to p. For a group of measurements in each of which the envelope of the combined signal and noise voltages decayed from E_1 to E_2 in $N+p$ periods, the expected means of the times registered by the chronograph was

$$\frac{N(1-p)}{f}+\frac{(N+1)p}{f}=\frac{N+p}{f}.$$

The third source of error considered in the analysis was the ability of the chronograph to register only an integral number of pulses of the standard frequency. In a group of measurements in each of which the time between the first pulse of D-0 following the "start" pulse and the first pulse of D-0 following the "stop" pulse corresponded to $M+q$ periods of the standard frequency, f_0, the expected mean of the time registered

by the chronograph was

$$\frac{M(1-q)}{f_0}+\frac{(M+1)q}{f_0}=\frac{M+q}{f_0}.$$

The analysis of the effects of these factors upon the experimental data resulted in the conclusion that only the in-phase component of the noise and the fixed phasing of the "start" and "stop" pulses had a significant effect upon the values of m and, consequently, of α. The result also indicated that the effect of these factors upon the values of n were proportional to their effect upon m. Accordingly, the precision of the frequency was affected significantly only by the out-of-phase component of the noise and the ability of the chronograph to register only integral numbers of pulses.

The analysis discussed above produced equations which predict the precision of the experimental values of α and f. The mean-square deviation of the single values of α is given by the equation

$$\sigma_\alpha=\frac{\alpha}{\ln x}\left[\frac{x^2+1}{2h^2E_a^2}+\frac{\alpha^2}{4f^2}\right]^{\frac{1}{2}}. \tag{12}$$

The first term in the brackets is caused solely by the in-phase component of the noise voltages. The second term represents the maximum effect of the fixed-phase relationship between the discriminator pulses and the applied voltage; the maximum value is given because the interaction of this effect and the noise voltages produces an integral which cannot be evaluated.

The mean-square deviation of the single values of f is given by the equation

$$\sigma_f=\frac{\alpha}{2\ln x}\left[\frac{x^2+1}{2\pi^2h^2E_a^2}+\frac{f^2}{f_0^2}\right]^{\frac{1}{2}}. \tag{13}$$

In this equation the first term in the brackets is caused by the out-of-phase component of the noise voltages. The second term arises from the fact that the chronograph can register only an integral number of pulses. Here again the maximum value is given because the interaction of this effect with the noise produces an unintegrable expression.

In the measurements reported here the value of x, the ratio of the critical voltages for discriminators D-1 and D-2, was $x=11$. It was found that, under these conditions, the second term on the right-hand side of Eq. (12) was negligible in comparison with the experimental value of σ_α, indicating that the deviations were almost entirely caused by the noise. The corresponding statement was true of Eq. (13).

By means of Eqs. (12) and (13) the experimental values of the mean-square deviations can be used to obtain values of h, the "precision index" of the noise voltages. This result can also be expressed in terms of the root-mean-square noise voltage, $\sigma_{\Delta E}$, which is related to h by the equation

$$\sigma_{\Delta E}^2=\tfrac{1}{2}h^2=\sigma_{\Delta E_1}^2=\sigma_{\Delta E_2}^2.$$

TABLE II. Values of the root-mean-square noise voltages calculated from the root-mean-square deviations of the frequency and the attenuation constant for a variety of experimental conditions.

f	α	$\sigma_f\times10^3$	$\sigma_\alpha\times10^2$	$\sigma_{\Delta E_1}$	$\sigma_{\Delta E_2}$
220.5645	1.250	0.9	0.7	0.10	0.11
220.5138	2.083	2.2	1.3	0.14	0.13
219.9078	5.105	4.8	3.5	0.13	0.11
219.5580	7.260	5.7	5.7	0.11	0.11
898.5896	2.302	1.4	0.7	0.08	0.07
898.4073	3.581	1.7	1.0	0.06	0.06
897.5943	8.920	3.4	3.7	0.06	0.08
897.1436	12.810	5.8	4.7	0.06	0.07
2305.0751	4.854	3.4	1.8	0.09	0.08
2304.9848	5.790	5.1	2.8	0.11	0.10
2304.595	8.782	6	3.5	0.09	0.09
2303.376	16.34	11	10	0.08	0.12

The root-mean-square value of the in-phase component of the noise voltage was calculated by means of Eq. (12) for several sets of measurements; with results as given in Table II. Similar calculations of the out-of-phase component of the noise were made by the use of Eq. (13), with results also given in Table II. The two sets of values are seen to be in good agreement.

If the value of h is known, Eqs. (12) and (13) furnish a means of selecting the values of x that will make either σ_α or σ_f a minimum for any particular pair of values of α and f. The value of $x=11$ (see above) was larger than these optimum values in most instances. However, since the minima of σ_α and σ_f with respect to x are rather broad, the adverse effect upon the precision of the data was small.

The precision of the values of η_1 and η_2 can be estimated from the experimental values of σ_α and σ_f. In the work on polymer solutions[2] the calibration was based on measurements made on the pure solvent and on an oil with a viscosity of 10 cp. Under these conditions the relative values of the standard deviations of η_1 and η_2 are given by

$$\frac{\sigma_{\eta_1}}{\eta_1}=\left[\frac{\sigma_{R_c}^2}{R_c^2}+\frac{\sigma_{X_c}^2}{X_c^2}\right]^{\frac{1}{2}},$$

$$\frac{\sigma_{\eta_2}}{\eta_2}=\frac{2}{R_c^2-X_c^2}\left[R_c^2\sigma_{R_c}^2+X_c^2\sigma_{X_c}^2\right]^{\frac{1}{2}},$$

$$\sigma_{R_c}=\frac{1}{K_a}\left[\sigma_{ac}^2+\frac{R_b^2\sigma_{aa}^2+R_a^2\sigma_{ab}^2R_c^2(\sigma_{aa}^2+\sigma_{ab}^2)}{(R_b-R_a)^2}\right]^{\frac{1}{2}},$$

$$\sigma_{X_c}=\frac{2\pi}{K_\omega}\left[\sigma_{fc}^2+\frac{X_b^2\sigma_{fa}^2+X_a^2\sigma_{fb}^2+X_c^2(\sigma_{fa}^2+\sigma_{fb}^2)}{(X_b-X_a)^2}\right]^{\frac{1}{2}},$$

TABLE III. The precision of the experimental values of the components of the complex viscosity of several polymer solutions.

Polymer[a]	Solvent	Conc. g/100 ml	f	a	R_c	X_c	η_1	η_2	$\frac{\sigma_{\eta_1}}{\eta_1}$	$\frac{\sigma_{\eta_2}}{\eta_2}$
A	Toluene	0.144	220.5138	2.083	3.00	2.25	0.0113	0.0039	0.018	0.07
B	Oil[b]	1.21	219.580	7.260	11.1	10.9	0.200	0.003	0.015	0.7
A	Toluene	0.101	898.5662	2.958	4.69	3.75	0.0073	0.0017	0.013	0.06
B	Oil	1.21	897.1436	12.810	22.7	21.2	0.196	0.013	0.009	0.13
A	Toluene	0.144	2305.0251	5.951	7.53	6.3	0.0076	0.0014	0.020	0.11
C	Toluene	1.37	2304.5953	8.782	12.2	11.1	0.0218	0.0021	0.016	0.17

[a] Polymer *A* was a polystyrene fraction, which had a molecular weight of 6.2×10^6. Polymer *B* was a polyisobutylene fraction, molecular weight = 136 000. Polymer *C* was a polystyrene fraction, molecular weight = 460 000.
[b] Oil had viscosity of 0.099 poise.

where the terms with subscript *a* refer to the solvent, those with subscript *b* refer to the oil, and those with subscript *c* refer to the solution.

In Table III values are given which illustrate the precision of the components of the complex viscosity. Each set is the result of the single group of measurements with a particular pendulum, i.e., a set of measurements (eighty individual determinations) made with a single filling of the pendulum with toluene, a similar set with the polymer solution, and a third set with the oil. Although η_1 and η_2 have an absolute precision of the same order of magnitude, the relative precision of η_2 is poorer than that of η_1, because η_2 is much smaller than η_1 for these systems.

The reproducibility of the data obtained in this work was insufficient to take full advantage of the precision attained. This is illustrated by the data obtained in fourteen separate sets of measurements on toluene in the 900-cycle pendulum. The average value of the attenuation constant was 2.327. The root-mean-square deviation of the mean of a single set of eighty measurements from the mean of all the sets was 0.008. Comparison of this value with the data in Table II leads to the conclusion that in this case, at least, the precision and the reproducibility of the attenuation constant were approximately equal. However, the root-mean-square deviation of the values of the frequency for the single sets from the mean value of 898.5854 for all the sets was 0.0054. Thus the reproducibility of the frequency was about four times poorer than the precision. Time did not permit the isolation and elimination of the causes of this lack of satisfactory reproducibility. The most probable cause was a lack of exact knowledge of the temperature of the pendulum. This difficulty could be reduced greatly by the use of a Mueller bridge with the resistance thermometer, and by replacing the stainless steel torsion rod of the pendulum with a metal having a much smaller thermal coefficient of modulus.

ACKNOWLEDGMENT

The authors wish to acknowledge the help of Professor W. C. Elmore, who designed the electronic discriminator circuits. The construction and several contributions to the design of the electronic circuits was the work of Mr. J. H. Kratz. In the design and construction of the mechanical and optical components the authors were materially aided by Mr. R. J. Gibson.

This work was performed as a part of the research project sponsored by the Reconstruction Finance Corporation, Office of Synthetic Rubber, in connection with the Government Synthetic Rubber Program.

JOURNAL OF APPLIED PHYSICS VOLUME 25, NUMBER 10 OCTOBER, 1954

Torsion of a Shaft with a Toroidal Cavity*

G. WEISS,† *U. S. Naval Ordnance Laboratory, White Oak, Maryland*

AND

L. E. PAYNE,‡ *Institute for Fluid Dynamics and Applied Mathematics, University of Maryland, College Park, Maryland*

(Received February 1, 1954)

This paper gives the solution to the torsion problem for a near-cylindrical shaft of circular section having a toroidal cavity. Since the interpretation of the axially symmetric problem as a flow problem in 5 dimensions is well known, the first part of the paper is devoted to developing a method for handling the flow problem about an n dimensional ring-shaped body of general cross section. In the second part of the paper this method is applied to the case of an n dimensional torus ring. The case $n=3$ then yields the solution to the classical flow problem, and $n=5$ gives the solution to the torsion problem under consideration.

INTRODUCTION

THE torsion problem for axially symmetric beams has received considerable attention in literature.[1,2] In 1916 Arndt[3] showed that this problem was analogous to an axially symmetric flow problem in a space of 5 dimensions. Subsequently, Weinstein[4] extended the methods of Arndt in considering the torsion problem for certain hollow shafts and introduced the method of generalized electrostatics[5,6] in treating the torsion problem for certain near circular shafts with prescribed cracks or cavities. This latter method is applicable only to cases in which the meridian section of the crack or cavity is simply connected. In this paper we shall extend the method of generalized electrostatics and remove the limitation that the cavity have a simply connected section. The solution to the torsion problem for a shaft with a toroidal cavity will be given as an example.

It is well known that the torsion problem for a near cylindrical beam with a sufficiently small axially symmetric cavity is equivalent to the flow problem about a 5- dimensional axially symmetric body having the same meridian profile as that of the cavity.[6] Since flow problems in 2, 3, and 5 dimensions have immediate physical interpretations, it is natural then to first develop the method for obtaining the flow about an n dimensional axially symmetric body with a multiply connected meridian section. This procedure will then give simultaneously a means for solving two and three dimensional flow problems as well as the torsion problem. We shall be concerned here only with a single body (cavity) having a doubly connected section. The methods to be developed can be easily extended to handle problems involving two or more such bodies.

GENERAL FORMULATION OF THE PROBLEM

In this paper we restrict our consideration to the problem of an n dimensional axially symmetric body in a uniform stream of a nonviscous incompressible fluid flowing parallel to the axis of symmetry of the body. It will be shown later precisely how the solution of this problem in five dimensions is related to the torsion of a beam with an axially symmetric cavity. For the present we give the solution of this more abstract n-dimensional problem.

Since the problem involves axial symmetry we need only define two coordinates, x and y, in order to give the solutions. Thus, in an n-dimensional Cartesian coordinate system $(x_1, x_2, \cdots, x_n)$ we choose

$$\begin{aligned} x &= x_1, \\ y &= (x_2^2+x_3^2+\cdots+x_n^2)^{\frac{1}{2}}, \end{aligned} \tag{1}$$

where the x axis is the axis of symmetry. In view of the axial symmetry we shall in our calculations limit our considerations to the meridian half plane $y \geqq 0$, where we shall designate the section of the n-dimensional body as B, its boundary as C, and its complement in the half plane $y \geqq 0$ as D (see Fig. 1). We see then that a profile C in the x, y plane designates a body in any number of dimensions, $n \geqq 2$. The n-dimensional flow potential

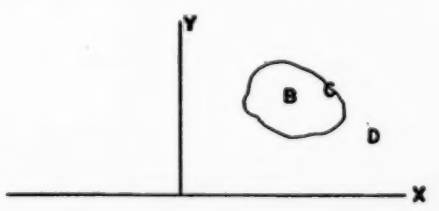

FIG. 1.

* This research was supported in part by the United States Air Force under contract No. AF18(600)-573 monitored by the Office of Scientific Research.

† Physicist, U. S. Naval Ordnance Laboratory, White Oak, Maryland.

‡ Assistant Research Professor, Institute for Fluid Dynamics and Applied Mathematics, University of Maryland.

[1] S. Sokolnikoff, *Mathematical Theory of Elasticity* (McGraw-Hill Book Company, Inc., New York, 1946).

[2] S. Timoshenko and J. N. Goodier, *Theory of Elasticity* (McGraw-Hill Book Company, Inc., New York, 1951).

[3] W. Arndt, "Die Torsion von Wellen mit achsensymmetrischen Bohrungen und Hohlräumen," dissertation, Göttingen, 1916 (unpublished).

[4] A. Weinstein, *On Generalized Potential Theory and on the Torsion of Shafts*. Studies and Essays presented to R. Courant (Interscience Publishers, Inc., New York, 1948), p. 108.

[5] A. Weinstein, Bull. Am. Math. Soc. **59**, 20 (1953).

[6] A. Weinstein, Quart. Appl. Math. **10**, 77 (1952).

$\phi(x,y)$ is a solution of the equation

$$\frac{\partial}{\partial x}\left[y^{n-2}\frac{\partial \phi\{n\}}{\partial x}\right]+\frac{\partial}{\partial y}\left[y^{n-2}\frac{\partial \phi\{n\}}{\partial y}\right]=0. \tag{2}$$

The notation $\phi\{n\}$ is used to signify that $\phi(x,y)$ is a potential in a space of n dimensions. An associate or stream function $\psi(x,y)$ may be defined in the following way:

$$y^{n-2}\frac{\partial \phi\{n\}}{\partial x}=\frac{\partial \psi\{n\}}{\partial y}, \quad y^{n-2}\frac{\partial \phi\{n\}}{\partial y}=-\frac{\partial \psi\{n\}}{\partial x}. \tag{3}$$

Hence, $\psi\{n\}$ satisfies the equation

$$\frac{\partial}{\partial x}\left[y^{-(n-2)}\frac{\partial \psi\{n\}}{\partial x}\right]+\frac{\partial}{\partial y}\left[y^{-(n-2)}\frac{\partial \psi\{n\}}{\partial y}\right]=0. \tag{4}$$

In the classical flow problem one is interested in obtaining a stream function $\psi\{3\}$ which is constant on the profile of the body and corresponds to a uniform flow in the x direction at infinity. The problem to be considered here is that of obtaining the stream function $\psi\{n\}$ defined in the half-plane $y\geqq 0$, which corresponds to such a flow about an n-dimensional body A with doubly connected section. Whenever the meridian section B of A is simply connected, $\psi\{n\}$ must vanish on C, the upper half of the meridian profile of the body. However, this is not the case if the meridian section of A (B and its reflection in the x axis) is doubly connected. The stream function $\psi\{n\}$ cannot vanish on C if the flow is to be circulation free, since this would mean that there could be no flow between the x axis and the body.

The method for obtaining the flow about the n-dimensional body whose section is simply connected is essentially this.[5,7] The stream function $\Psi_s\{n\}$ characterizing the flow is defined in the meridian half-plane $y\geqq 0$ as follows:

$$\Psi_s\{n\}=(n-1)^{-1}y^{n-1}-\psi_1\{n\}, \tag{5}$$

where $\psi_1\{n\}$ assumes the value $(n-1)^{-1}y^{n-1}$ on the boundary C of B and vanishes at infinity. We make use of a correspondence relation, introduced by Weinstein,[8]

$$\psi_1\{n\}=ky^{n-1}\phi^*\{n+2\}, \tag{6}$$

which relates a stream function in n dimensions to a potential in two more dimensions. By the proper choice of the artibrary constant k we are able to express the function $\Psi_s\{n\}$ in the form

$$\Psi_s\{n\}=(n-1)^{-1}y^{n-1}[1-\phi^*\{n+2\}]. \tag{7}$$

Thus, the problem of determining $\Psi\{n\}$ is reduced to one of determining a potential $\phi^*\{n+2\}$ which takes the value unity on C and vanishes at infinity; but this is precisely the electrostatic potential of the $n+2$ dimensional body having the same meridian profile as A. Hence the flow problem in n dimensions is reduced to an electrostatics problem in two more dimensions. This method of handling the flow problem is known as the method of generalized electrostatics. It has been employed by Payne[7] to obtain the flows about a spindle and a lens.

If, however, the meridian section of A is doubly connected, Eq. (7) will yield a flow with circulation if $\phi^*\{n+2\}$ is chosen to be equal to unity on C. In fact the circulation will be such that there is no resultant flow between the x axis and the body. Hence, if we wish to obtain a circulation free flow we must modify (7) by the addition of a function $\psi_2\{n\}$, i.e.,

$$\Psi\{n\}=(n-1)^{-1}y^{n-1}[1-\phi^*\{n+2\}]+\psi_2\{n\}, \tag{8}$$

where $\psi_2\{n\}$ represents a pure circulatory flow. In other words, $\psi_2\{n\}$ vanishes on the axis of symmetry and at infinity and assumes the value $k\{n\}$ on C. The problem is thus reduced to the determination of two functions $\phi^*\{n+2\}$ and $\psi_2\{n\}$ which satisfy essentially the same conditions. Both assume constant values on the body and vanish at infinity.

In our formulation the constant $k\{n\}$ still remains unspecified. However, this quantity can be solved for by the requirement that the total circulation $\Omega\{n\}$ vanish. That is

$$\Omega\{n\}=\oint_C \frac{\partial \Phi\{n\}}{\partial s}ds=\oint_C y^{-(n-2)}\frac{\partial \Psi\{n\}}{\partial \nu}ds=0, \tag{9}$$

where $\partial/\partial\nu$ designates the outward normal derivative. Since the term $(n-1)^{-1}y^{n-1}$ contributes nothing to the circulation we have

$$\oint_C y^{-(n-2)}\left[\frac{\partial \psi_1\{n\}}{\partial \nu}-\frac{\partial \psi_2\{n\}}{\partial \nu}\right]ds=0, \tag{10}$$

and if we write

$$\psi_2\{n\}=k\{n\}\psi_2'\{n\}, \tag{11}$$

where $\psi_2'\{n\}$ assumes the value unity on C, we obtain

$$k\{n\}=\frac{\oint_C y^{-(n-2)}\dfrac{\partial \psi_1\{n\}}{\partial \nu}ds}{\oint_C y^{-(n-2)}\dfrac{\partial \psi_2'\{n\}}{\partial \nu}ds}. \tag{12}$$

We see then that the problem of obtaining the flow about a body A whose meridian section is doubly connected is completely solved if we determine a potential $\phi^*\{n+2\}$ and a stream function $\psi_2'\{n\}$ each of which takes the value unity on C and vanishes at infinity. (It is easily shown that if $\psi_2'\{n\}$ vanishes at infinity it vanishes everywhere along the x axis).

[7] L. E. Payne, Quart. Appl. Math. **10**, 197 (1952).
[8] A. Weinstein, Trans. Am. Math. Soc. **63**, 342 (1948).

The virtual mass of an n-dimensional body of revolution A is defined as follows,[9]

$$M\{n\}=\omega_{n-1}\iint_D y^{-(n-2)}\left[\left(\frac{\partial\psi\{n\}}{\partial x}\right)^2+\left(\frac{\partial\psi\{n\}}{\partial y}\right)^2\right]dxdy, \quad (13)$$

where

$$\omega_n=2\pi^{n/2}/\Gamma(n/2), \quad (14)$$

and $\psi\{n\}$ is determined from (8) as

$$\psi\{n\}=\Psi\{n\}-(n-1)^{-1}y^{n-1}=-\psi_1\{n\}+\psi_2\{n\}. \quad (15)$$

In (13) the uniform velocity at infinity and the density have been taken as unity. If we divide $M\{n\}$ by the square of the uniform velocity and multiply by the density of the fluid ρ, we obtain the true virtual mass. It should be remembered in (15) that

$$\psi_1\{n\}=(n-1)^{-1}y^{n-1}\phi^*\{n+2\}. \quad (16)$$

The n-dimensional volume and capacity of A are defined as

$$V\{n\}=\omega_{n-1}\iint_B y^{n-2}dxdy$$

$$C\{n\}=\frac{\omega_{n-1}}{\omega_n}\iint_D y^{n-2}\left[\left(\frac{\partial\phi^*\{n\}}{\partial x}\right)^2+\left(\frac{\partial\phi^*\{n\}}{\partial y}\right)^2\right]dxdy, \quad (17)$$

where $\phi^*\{n\}$ is the electrostatic potential of A. i.e., $\phi^*\{n\}$ assumes the value unity on the boundary of A and vanishes at infinity. Payne and Weinstein[9] obtained the following expression for $M\{n\}$ which is valid whenever the meridian section of A is simply connected

$$M\{n\}=\pi^{n/2}[(n-1)\Gamma(n/2+1)]^{-1}C\{n+2\}-V\{n\}, \quad (18)$$

where $C\{n+2\}$ is the capacity of the $(n+2)$ dimensional body having the same meridian section as A. In our case we must determine

$$M\{n\}=\omega_{n-1}\left\{\iint_D y^{-(n-2)}\left[\left(\frac{\partial\psi_1}{\partial x}\right)^2+\left(\frac{\partial\psi_1}{\partial y}\right)^2\right]dxdy-2\iint_D y^{-(n-2)}\left[\frac{\partial\psi_1}{\partial x}\frac{\partial\psi_2}{\partial x}+\frac{\partial\psi_1}{\partial y}\frac{\partial\psi_2}{\partial y}\right]dxdy+\iint_D y^{-(n-2)}\left[\left(\frac{\partial\psi_2}{\partial x}\right)^2+\left(\frac{\partial\psi_2}{\partial y}\right)^2\right]dxdy\right\}, \quad (19)$$

where we understand that ψ denotes $\psi\{n\}$. But the first integral in (19) obviously yields the same result as in the simply connected case, and hence reduces to the right-hand side of Eq. (18). By Green's theorem we have

$$\iint_D y^{-(n-2)}\left[\frac{\partial\psi_1}{\partial x}\frac{\partial\psi_2}{\partial x}+\frac{\partial\psi_1}{\partial y}\frac{\partial\psi_2}{\partial y}\right]dxdy=-\oint_C y^{-(n-2)}\psi_2\frac{\partial\psi_1}{\partial\nu}ds-\iint_D y^{-(n-2)}\psi_2\left[\frac{\partial^2\psi_1}{\partial x^2}+\frac{\partial^2\psi_1}{\partial y^2}-\frac{(n-2)}{y}\frac{\partial\psi_1}{\partial y}\right]dxdy. \quad (20)$$

From (4) we see that the last integral on the right of (20) vanishes. Also, $\psi_2=k\{n\}$ on C. Thus

$$\iint_D y^{-(n-2)}\left[\frac{\partial\psi_1}{\partial x}\frac{\partial\psi_2}{\partial x}+\frac{\partial\psi_1}{\partial y}\frac{\partial\psi_2}{\partial y}\right]dxdy=-k\{n\}\oint_C y^{-(n-2)}\frac{\partial\psi_1}{\partial\nu}ds. \quad (21)$$

Similarly, the last integral of (19) may be expressed as

$$\iint_D y^{-(n-2)}\left[\left(\frac{\partial\psi_2}{\partial x}\right)^2+\left(\frac{\partial\psi_2}{\partial y}\right)^2\right]dxdy=-k\{n\}\oint_C y^{-(n-2)}\frac{\partial\psi_2}{\partial\nu}ds. \quad (22)$$

Thus if we substitute expressions (21) and (22) in (19) and make use of (10), we obtain

$$M\{n\}=\pi^{n/2}[(n-1)\Gamma(n/2+1)]^{-1}C\{2n+2\}-V\{n\}+\frac{2\pi^{(n-1)/2}k\{n\}}{\Gamma\left(\frac{n-1}{2}\right)}\Omega_1\{n\}, \quad (23)$$

where

$$\Omega_1\{n\}=\oint_C y^{-(n-2)}\left(\frac{\partial\psi_1}{\partial\nu}\right)ds=\oint_C y^{-(n-2)}\left(\frac{\partial\psi_2}{\partial\nu}\right)ds, \quad (24)$$

and $k\{n\}$ may be found from (12). It is obvious from Gauss's theorem that the value of either integral in (24) is independent of the path for any closed curve about C. We will often find it convenient to choose as our curve of integration a semicircle consisting of the

[9] L. E. Payne and A. Weinstein, Pacific J. Math. **2**, 633 (1952).

x axis, $-\infty<x<\infty$ and a semicircular arc at infinity. An alternate expression for (24) is thus given by

$$\Omega_1\{n\}=-\int_{-\infty}^{\infty}\phi^*(x,0)dx, \tag{25}$$

where it is understood that $\phi^*=\phi^*\{n+2\}$.

It can be easily verified that $k\{n\}$ and $\Omega_1\{n\}$ are of opposite sign,§ as is to be expected from the nature of the physical problem. It is thus apparent from (23) that the virtual mass in the case of no circulation is less than that with circulation.

FORMULATION OF THE TORSION PROBLEM

Thus far a treatment of the general flow problem has been given. It remains now to show how the general results are specifically applicable to the torsion of a beam containing a ring shaped cavity. In order to treat this problem we use a cylindrical coordinate system (y,θ,x), where x is the axis of symmetry. The components of the displacement vector are denoted by (u,v,w). The displacement of any particle is assumed to be purely tangential (u, $w\equiv 0$). On account of the axial symmetry v will not depend on the angle θ. Thus, the nonvanishing stresses are given by

$$\tau_{y\theta}=G\left(\frac{\partial v}{\partial y}-\frac{v}{y}\right),\qquad \tau_{x\theta}=G\frac{\partial v}{\partial x}, \tag{26}$$

where G is the shear modulus. If we let $v=y\Phi$ we find that the equilibrium conditions require that Φ satisfy the equation

$$\frac{\partial^2\Phi}{\partial x^2}+\frac{\partial^2\Phi}{\partial y^2}+\frac{3}{y}\frac{\partial\Phi}{\partial y}=0. \tag{27}$$

It is easily verified that this equation is just the generalized axially symmetric Laplace Eq. (2), for $n=5$. Thus the nonvanishing stresses may be expressed as

$$\tau_{y\theta}=Gy\frac{\partial\Phi}{\partial y}=-Gy^{-2}\frac{\partial\Psi}{\partial x},\qquad \tau_{x\theta}=Gy\frac{\partial\Phi}{\partial x}=Gy^{-2}\frac{\partial\Psi}{\partial y}, \tag{28}$$

where Ψ is defined as in Eq. (3) for $n=5$. We note that any surface on which the normal component of the shearing stress vanishes must be a line of constant Ψ. Similarly, any line $\Psi=$constant may be taken as the boundary of a shaft. Consider the stream function

$$\Psi_s\{5\}=\frac{y^4}{4}-\psi_1\{5\}. \tag{29}$$

If we require that $\psi_1\{5\}$ vanish at infinity, a line $\Psi_s\{5\}=a^2$ (a constant) will be asymptotic to the line $y=(2a)^{\frac{1}{2}}$ as $x\to\infty$. Similarly for large values of y, a line $\Psi_s\{5\}=$constant will be essentially a line parallel to the x axis for all values of x. Let us again make use of the correspondence principle (6) and rewrite (29) as

$$\Psi_s\{5\}=\frac{y^4}{4}[1-\phi^*\{7\}]. \tag{30}$$

If we now choose for $\phi^*\{7\}$ the electrostatic potential of a certain axially symmetric body A in 7 dimensions we obtain a solution to the torsion problem for a shaft with a cavity whose boundary has the same meridian profile as A, where any line $\Psi_s\{5\}=$constant may be used to define the outer boundary of the shaft. If the meridian section of the cavity is simply connected Eq. (30) represents the complete solution to the torsion problem for a near cylindrical beam with the prescribed cavity. On the other hand, if the meridian section is doubly connected, the corresponding potential $\Phi_s\{5\}$ will obviously not be single-valued, but will have a jump of constant value along some surface represented by a line in the meridian plane joining a point on C to a point on the x axis. Since $v=y\Phi_s$, this jump represents a dislocation along such a surface. Hence, Eq. (30) yields in this case the solution to a torsion problem with a dislocation. The problem of eliminating the dislocation is precisely the problem of eliminating the circulation in the flow about the analogous five dimensional body. Thus, for a body with a doubly connected section we choose

$$\Psi\{5\}=\Psi_s\{5\}+\psi_2\{5\}. \tag{31}$$

Now, if $\phi^*\{7\}$ and $\psi_2\{5\}$ are chosen as indicated in the preceding section, and the line $\Psi\{5\}=$a moderately large constant is taken as the outer boundary of the beam, Eq. (31) will give the solution to the torsion problem for a near cylindrical beam with the prescribed cavity. Since $\phi^*\{7\}$ is of order r^{-5} and $\psi_2\{5\}$ is of order r^{-1} at infinity ($r^2=x^2+y^2$), it is obvious that the line $\Psi\{5\}=$a moderately large constant will deviate only slightly from a line parallel to the x axis. Hence in this case one has a very good approximation to the torsion problem for a circular cylindrical shaft with a prescribed cavity.

We mention in passing that the strain energy developed in an infinite medium due to an axially sym-

§ The right-hand side of (24) may be rewritten in the form $-k\{n\}\int\int_D y^{-(n-2)}\left[\left(\frac{\partial\psi_2'}{\partial x}\right)^2+\left(\frac{\partial\psi_2'}{\partial y}\right)^2\right]dxdy$. Since the integral is always positive, $\Omega_1\{n\}$ and $k\{n\}$ are of opposite sign i.e., $k\{n\}$ is always positive and $\Omega_1\{n\}$ always negative.

metric distribution of stress on the boundary of a cavity of revolution is given by

$$E=\frac{4\pi}{G}\int\int_D y[(\tau_{x\theta})^2+(\tau_{y\theta})^2]dxdy$$
$$=4\pi G\int\int_D y^{-3}\left[\left(\frac{\partial\psi}{\partial x}\right)^2+\left(\frac{\partial\psi}{\partial y}\right)^2\right]dxdy, \quad (32)$$

which for the proper distribution of stress is proportional to the virtual mass of the analogous five dimensional body. In other words, if $\tau_{n\theta}$, the normal component of the stress on the cavity, is given as

$$\tau_{n\theta}=Gy\frac{\partial\Phi}{\partial n}=-Gy\frac{\partial x}{\partial n}, \quad (33)$$

then

$$E=\left(\frac{2G}{\pi}\right)M\{5\}. \quad (34)$$

FLOW ABOUT AN N-DIMENSIONAL TORUS

We shall now apply the methods developed in the preceding sections and solve the torsion problem for a near cylindrical shaft with a toroidal cavity. We shall first obtain the flow about an n-dimensional torus (n odd). The cases $n=3$ and $n=5$ then yield the solutions to the flow problem and the torsion problem.

Let us introduce the toroidal transformation

$$x+iy=-b\cot\tfrac{1}{2}(\xi+i\eta), \quad (35)$$

where b is a positive constant, and the range of variables is chosen as $0\leq\eta<\infty$, $-\pi<\xi\leq\pi$. The relations between the (x,y) coordinates and the toroidal coordinates are given by

$$x=-b\frac{\sin\xi}{\cosh\eta-\cos\xi}, \qquad y=b\frac{\sinh\eta}{\cosh\eta-\cos\xi}. \quad (36)$$

A surface $\eta=\eta_0$ defines the boundary of a torus, and the region exterior to the torus is given by the inequality $\eta\leq\eta_0$. Simple computation shows that in this coordinate system (2) becomes in $n+2$ dimensions

$$\frac{\partial}{\partial\eta}\left[\left(\frac{\sinh\eta}{s-t}\right)^n\frac{\partial\phi^*\{n+2\}}{\partial\eta}\right]+\frac{\partial}{\partial\xi}\left[\left(\frac{\sinh\eta}{s-t}\right)^n\frac{\partial\phi^*\{n+2\}}{\partial\xi}\right]=0, \quad (37)$$

where $s=\cosh\eta$ and $t=\cos\xi$. By making a substitution $\phi^*\{n+2\}=(s-t)^{n/2}U$, we are able to separate variables and obtain the following general solution for $\phi^*\{n+2\}$:

$$\phi^*\{n+2\}=\frac{(s-t)^{n/2}}{\sinh^{(n-1)/2}\eta}[A\cos m\xi+B\sin m\xi]\times[CP_{m-1/2}{}^{(n-1)/2}(s)+DQ_{m-1/2}{}^{(n-1)/2}(s)], \quad (38)$$

where the P and Q functions are the associated Legendre functions.[10] Since the Q function becomes infinite as $\eta\to0$, D must be taken as zero. Also since $\phi^*\{n+2\}$ is to be the electrostatic potential in $n+2$ dimensions, it will be an even function of ξ. Hence, we choose

$$\phi^*\{n+2\}=\frac{(s-t)^{n/2}}{\sinh^{(n-1)/2}\eta}\times\sum_{m=0}^{\infty}A_mP_{(m-1)/2}{}^{(n-1)/2}(s)\cos m\xi. \quad (39)$$

To satisfy the boundary condition that $\phi^*\{n+2\}=1$ for $\eta=\eta_0$, we consider the following expansion,

$$\frac{1}{[\mu_0-(\mu_0^2-1)^{\frac{1}{2}}\cos\xi]^{n/2}}=(\sinh\eta_0)^{\frac{1}{2}}\times\sum_{m=0}^{\infty}A_mP_{m-1/2}{}^{(n-1)/2}(s_0)\cos m\xi, \quad (40)$$

where $\mu_0=\coth\eta_0$, and the subscript 0 indicates that the term is evaluated on the profile. We may consider (40) as a Fourier expansion of the left-hand term and thus evaluate the constants A_m. We therefore find

$$(\sinh\eta_0)^{\frac{1}{2}}P_{m-1/2}{}^{(n-1)/2}(s_0)A_m=\frac{2}{\pi}\int_0^{\pi}\frac{\cos m\xi\,d\xi}{(\mu_0-(\mu_0^2-1)^{\frac{1}{2}}\cos\xi)^{n/2}}=\frac{\Gamma\left(\frac{n}{2}+m\right)}{\Gamma\left(\frac{n}{2}\right)}P_{(n/2)-1}{}^{-m}(u_0), \quad (41)$$

$$(\sinh\eta_0)^{\frac{1}{2}}P_{-1/2}{}^{(n-1)/2}(s_0)A_0=\frac{1}{\pi}\int_0^{\pi}\frac{d\xi}{(\mu_0-(\mu_0^2-1)^{\frac{1}{2}}\cos\xi)^{n/2}}=\tfrac{1}{2}P_{(n/2)-1}(u_0).$$

From Whipple's relation [see reference 10, Eq. (92), p. 245], we have

$$P_{(n/2)-1}{}^{-m}(\mu_0)=\left(\frac{2}{\pi}\right)^{\frac{1}{2}}\frac{\exp\frac{(n-1)\pi i}{2}(\sinh\eta_0)^{\frac{1}{2}}}{\Gamma\left(m-\frac{n}{2}+1\right)}\times Q_{m-1/2}{}^{-(n-1)/2}(s_0), \quad (42)$$

[10] E. W. Hobson, *The Theory of Spherical and Ellipsoidal Harmonics* (Cambridge University Press, London, 1931).

and using the relationship

$$Q_{m-1/2}{}^{-(n-1)/2}(s_0)=e^{-(n-1)\pi i}\frac{\Gamma\left(m-\frac{n}{2}+1\right)}{\Gamma\left(m+\frac{n}{2}\right)}\times Q_{m-1/2}{}^{(n-1)/2}(s_0) \quad (43)$$

we find finally for A_m when n is odd

$$A_m=\frac{(-1)^{(n-1)/2}2^{\frac{1}{2}}}{\sqrt{\pi}\Gamma\left(\frac{n}{2}\right)}\frac{Q_{m-1/2}{}^{(n-1)/2}(s_0)}{P_{m-1/2}{}^{(n-1)/2}(s_0)}. \quad (44)$$

The expression for $\phi^*\{n+2\}$ then becomes

$$\phi^*\{n+2\}=\frac{(-1)^{(n-1)/2}2^{\frac{1}{2}}}{\sqrt{\pi}\Gamma\left(\frac{n}{2}\right)}\frac{(s-l)^{n/2}}{\sinh^{(n-1)/2}\eta}\times\sum_{m=0}^{\infty}{}'\frac{Q_{m-1/2}{}^{(n-1)/2}(s_0)}{P_{m-1/2}{}^{(n-1)/2}(s_0)}P_{m-1/2}{}^{(n-1)/2}(s)\cos m\xi, \quad (45)$$

where the prime indicates that the term with zeroth subscript must be multiplied by $\frac{1}{2}$. Using (7) we obtain the following expression for $\Psi_s\{n\}$,

$$\Psi_s\{n\}=\frac{b^{n-1}\sinh^{n-1}\eta}{(n-1)(s-l)^{n-1}}-\frac{(-1)^{(n-1)/2}2^{\frac{1}{2}}}{(n-1)\sqrt{\pi}\Gamma\left(\frac{n}{2}\right)}\frac{b^{n-1}\sinh^{(n-1)/2}\eta}{(s-l)^{n/2-1}}\times\sum_{m=0}^{\infty}{}'\frac{Q_{m-1/2}{}^{(n-1)/2}(s_0)}{P_{m-1/2}{}^{(n-1)/2}(s_0)}P_{m-1/2}{}^{(n-1)/2}(s)\cos m\xi. \quad (46)$$

We wish now to determine a function $\psi_2'\{n\}$ satisfying the conditions

$$\psi_2'\{n\}=0, \quad \eta=0, \qquad \psi_2'\{n\}=1, \quad \text{on } C. \quad (47)$$

The function $\psi_2'\{n\}$ will be of the form

$$\psi_2'\{n\}=\frac{\sinh^{(n-1)/2}\eta}{(s-l)^{n/2-1}}\sum_{m=0}^{\infty}{}'A_m'P_{m-1/2}{}^{(n-1)/2}(s)\cos m\xi. \quad (48)$$

In order that the second of conditions (47) be fulfilled, the following must be true for $\eta=\eta_0$:

$$(\sinh\eta_0)^{\frac{1}{2}}P_{m-1/2}{}^{(n-1)/2}(s_0)A_m'=\frac{2}{\pi}\int_0^{\pi}[\mu_0-(\mu_0^2-1)^{\frac{1}{2}}\cos\xi]^{(n/2)-1}\cos m\xi\,d\xi. \quad (49)$$

From this equation we determine the coefficients A_m' to be

$$A_m'=\frac{(-1)^{(n-1)/2}2^{\frac{1}{2}}}{\sqrt{\pi}\Gamma\left(1-\frac{n}{2}\right)}\frac{Q_{m-1/2}{}^{-(n-1)/2}(s_0)}{P_{m-1/2}{}^{(n-1)/2}(s_0)}. \quad (50)$$

Therefore the expression for $\psi_2\{n\}$ is

$$\psi_2\{n\}=k\{n\}\psi_2'\{n\}=\frac{(-1)^{(n-1)/2}2^{\frac{1}{2}}k\{n\}\sinh^{(n-1)/2}\eta}{\sqrt{\pi}\Gamma\left(1-\frac{n}{2}\right)(s-l)^{n/2-1}}\times\sum_{m=0}^{\infty}{}'\frac{Q_{m-1/2}{}^{-(n-1)/2}(s_0)}{P_{m-1/2}{}^{(n-1)/2}(s_0)}P_{m-1/2}{}^{(n-1)/2}(s)\cos m\xi. \quad (51)$$

All that remains now in order to get the complete solution is the evaluation of the constant $k\{n\}$ which is the value of the stream function on the boundary of the torus. We require that $\Omega\{n\}=0$. In case of the torus this gives us the condition that

$$\Omega\{n\}=-\int_{-\pi}^{\pi}\frac{\partial\Phi\{n\}}{\partial\xi}d\xi=-\int_{-\pi}^{\pi}\frac{1}{y^{n-2}}\frac{\partial\Psi\{n\}}{\partial\eta}d\xi=0. \quad (52)$$

By use of (11) we obtain the following expression for $k\{n\}$,

$$k\{n\}=\frac{\int_{-\pi}^{\pi}\frac{1}{y^{n-2}}\frac{\partial\psi_1\{n\}}{\partial\eta}d\xi}{\int_{-\pi}^{\pi}\frac{1}{y^{n-2}}\frac{\partial\psi_2'\{n\}}{\partial\eta}d\xi}, \quad (53)$$

The circulation must be zero around any closed curve enclosing one cross section of the torus in the x,y plane. In particular it must vanish on $\eta=0$ along which contour we shall perform the integration because of the simplicity of computation. Along this curve we may neglect any terms involving $\sinh\eta$, and for the combination

$$\frac{P_{m-1/2}{}^{(n-1)/2}(s)}{\sinh^{(n-1)/2}\eta}, \quad (54)$$

which occurs in both integrands, we use the fact that

$$\frac{P_{m-1/2}{}^{(n-1)/2}(s)}{\sinh^{(n-1)/2}\eta}=\frac{\Gamma\left(m+\frac{n}{2}\right)F\left(\frac{n}{2}-m,\frac{n}{2}+m,\frac{n+1}{2},\frac{1-s}{2}\right)}{2^{(n-1)/2}\Gamma\left(\frac{n+1}{2}\right)\Gamma\left(1+m-\frac{n}{2}\right)}, \quad (55)$$

(see reference 10, p. 189). Passing to the limit $\eta=0$, we find

$$\lim_{\eta\to 0}\frac{P_{m-1/2}{}^{(n-1)/2}(s)}{\sinh^{(n-1)/2}\eta}=\frac{\Gamma\left(m+\frac{n}{2}\right)}{2^{n-1}\Gamma\left(\frac{n+1}{2}\right)\Gamma\left(1+m-\frac{n}{2}\right)}. \quad (56)$$

The constant $k\{n\}$ is therefore given by

$$k\{n\}=\frac{b^{n-1}\Gamma\left(1-\frac{n}{2}\right)\sum_{m=0}^{\infty}{}'\beta_m\{n\}\int_{-\pi}^{\pi}\sigma_m d\xi}{(n-1)\Gamma\left(\frac{n}{2}\right)\sum_{m=0}^{\infty}{}'\beta_m{}^*\{n\}\int_{-\pi}^{\pi}\sigma_m d\xi}, \quad (57)$$

where we have used the notation

$$\beta_m\{n\}=\frac{Q_{m-1/2}{}^{(n-1)/2}(s_0)}{P_{m-1/2}{}^{(n-1)/2}(s_0)},$$

$$\beta_m{}^*\{n\}=\frac{Q_{m-1/2}{}^{-(n-1)/2}(s_0)}{P_{m-1/2}{}^{(n-1)/2}(s_0)}, \quad (58)$$

$$\sigma_m=\left\{\frac{1}{y^{n-2}}\frac{\partial}{\partial\eta}\left[\frac{\sinh^{(n-1)/2}\eta}{(s-t)^{n/2-1}}P_{m-1/2}{}^{(n-1)/2}(s)\right]\right\}_{\eta=0}\cos m\xi.$$

It is obvious from (57) that any factors which depend only on n in $\int_{-\pi}^{\pi}\sigma_m d\xi$ will cancel. Taking account of this fact we find

$$\int_{-\pi}^{\pi}\sigma_m d\xi\ \alpha\ \frac{\Gamma\left(m+\frac{n}{2}\right)}{\Gamma\left(1+m-\frac{n}{2}\right)}\int_{-\pi}^{\pi}(1-\cos\xi)^{(n/2)-1}\cos m\xi d\xi$$

$$=\frac{\pi\cos m\pi}{\Gamma\left(\frac{n}{2}-m\right)\Gamma\left(1+m-\frac{n}{2}\right)}. \quad (59)$$

Substituting $z=(n/2)-m$ in the identity

$$\Gamma(z)\Gamma(1-z)=\frac{\pi}{\sin\pi z}, \quad (60)$$

we find from Eq. (59)

$$\int_{-\pi}^{\pi}\sigma_m d\xi\ \alpha\ \sin\frac{\pi n}{2}. \quad (61)$$

Hence, the contributions from $\int_0^{2\pi}\sigma_m d\xi$ cancel out from Eq. (57) and we find for $k\{n\}$,

$$k\{n\}=\frac{b^{n-1}(-1)^{(n-1)/2}\pi\sum_{m=0}^{\infty}{}'\beta_m\{n\}}{(n-1)\left[\Gamma\left(\frac{n}{2}\right)\right]^2\sum_{m=0}^{\infty}{}'\beta_m{}^*\{n\}}. \quad (62)$$

This is the value of the stream function $\psi_2\{n\}$ on the boundary of the torus.

By a simple calculation we obtain the following expression for the quantity $\Omega_1\{n\}$ defined by (24),

$$\Omega_1\{n\}=\frac{-2^{4-n}\Gamma(n-1)b}{\sqrt{\pi}\Gamma\left(\frac{n+1}{2}\right)\Gamma\left(\frac{n}{2}\right)}\sum_{m=0}^{\infty}{}'\beta_m\{n\}. \quad (63)$$

We may now specialize to $n=5$, the case of the toroidal cavity in the near-cylindrical beam.

The stream function is found by inserting (46) and (51) in (31). This gives

$$\Psi\{5\}=\frac{y^4}{4}-\frac{2}{3\pi}\frac{b^4\sinh^2\eta}{(s-t)^{\frac{1}{2}}}\sum_{m=0}^{\infty}{}'\frac{Q^2_{m-1/2}(s_0)}{P^2_{m-1/2}(s_0)}$$

$$\times P^2_{m-1/2}(s)\cos m\xi+\frac{3k\{5\}}{\pi\sqrt{2}}\frac{\sinh^2\eta}{(s-t)^{\frac{1}{2}}}$$

$$\times\sum_{m=0}^{\infty}{}'\frac{Q^{-2}_{m-1/2}(s_0)}{P^2_{m-1/2}(s_0)}P^2_{m-1/2}(s)\cos m\xi, \quad (64)$$

where

$$k\{5\}=\frac{4}{9}b^4\frac{\sum_{m=0}^{\infty}{}'\frac{Q^2_{m-1/2}(s_0)}{P^2_{m-1/2}(s_0)}}{\sum_{m=0}^{\infty}{}'\frac{Q^{-2}_{m-1/2}(s_0)}{P^2_{m-1/2}(s_0)}}. \quad (65)$$

The potential $\Phi\{5\}$ associated with $\Psi\{5\}$ [see Eq. (28)] may be easily determined in double series form from the relations

$$y^3\frac{\partial\Phi}{\partial\xi}=\frac{\partial\Psi}{\partial\eta},\quad y^3\frac{\partial\Phi}{\partial\eta}=-\frac{\partial\Psi}{\partial\xi}, \quad (66)$$

by employing expansions of type (40).

We note that the stress function

$$\Psi'\{5\}=\psi_1\{5\}-\psi_2\{5\}, \quad (67)$$

characterizes the problem of the toroidal cavity in an infinite medium on whose profile $\tau_{n\theta}$ is of form (33). Hence the strain energy developed in the medium is

given in this case by (34) and (23). We find for $V\{5\}$

$$V\{5\}=2\pi^3\int\int_B y^3dxdy$$

$$=b^5\left(\frac{\pi^3}{2}\right)\coth\eta_0\,\mathrm{csch}^2\eta_0[4+7\,\mathrm{csch}^2\eta_0]. \quad (68)$$

The capacity $C\{7\}$ in (23) can be found from the relation

$$C\{7\}=5\lim_{r\to\infty}r^5\phi_1\{7\}, \quad (69)$$

and is given by

$$C\{7\}=(\tfrac{5}{6}\pi)b^5\sum_{m=0}^{\infty}{}'\beta_m\{5\}[16m^4-40m^2+9]. \quad (70)$$

The term $\Omega_1\{5\}$ is obtained from (63),

$$\Omega_1\{5\}=-\frac{2b}{\pi}\sum_{m=0}^{\infty}{}'\beta_m\{5\}. \quad (71)$$

Substitution of these expressions in (23) yields when $n=5$

$$E=\left(\frac{2}{9}\right)Gb^5\sum_{m=0}^{\infty}{}'\beta_m\{5\}[16m^4-40m^2+9-36b^{-4}k\{5\}]$$

$$-\pi^2Gb^5\cosh\eta_0\,\mathrm{csch}^2\eta_0[4+7\,\mathrm{csch}^2\eta_0]. \quad (72)$$

The stress function $\psi_2\{5\}$ is the solution to the problem of an infinite medium with an unstressed toroidal cavity, having a torsional dislocation across the portion of the plane $x=0$, characterized by a line through the origin joining the centers of the circles in the meridian section of the torus. In this case the strain energy E'' is given by

$$E''=8Gk\{5\}b\sum_{m=0}^{\infty}{}'\beta_m\{5\}. \quad (73)$$

Finally we should point out that for $n=3$, Eqs. (46) and (51) give the solution to the problem of flow about a torus. This solution agrees with that recently obtained in a different manner by Sternberg and Sadowsky.[11] The value of C given in their Eq. (68) is equivalent to our $k\{3\}$ in (62). We need only use the relation

$$Q^{-1}{}_{m-1/2}(s)=4(4m^2-1)^{-1}Q^1{}_{m-1/2}(s) \quad (74)$$

to establish the equivalence. The virtual mass of the torus in three dimensions is found by (23) to be

$$M\{3\}=4b^3\sum_{m=0}^{\infty}{}'\beta_m\{3\}[1-2b^{-2}k\{3\}-4m^2]$$

$$-2\pi^2b^3\cosh\eta_0\,\mathrm{csch}^2\eta_0. \quad (75)$$

This agrees with the results given by Schiffer and Szegö.[12]

[11] E. Sternberg and M. A. Sadowsky, J. Appl. Mech. **20**, 393 (1953).

[12] M. Schiffer and G. Szegö, Trans. Am. Math. Soc. **67**, 130 (1949).

Thickness-Shear and Flexural Vibrations of a Circular Disk*

R. D. MINDLIN AND H. DERESIEWICZ
Department of Civil Engineering, Columbia University, New York, New York

(Received February 4, 1954)

Equations governing the coupled thickness-shear and flexural vibrations of isotropic, elastic plates are solved for the case of a circular disk with free edges. The results of computations are given for the resonant frequencies analogous to those which would be excited in an AT-cut quartz disk with full electrode coating. A marked difference is observed between the frequency spectrum of the disk and the spectrum of cylindrical vibrations of a rectangular plate. The difference is due to the presence of thickness-twist modes of motion, in the disk, which, along with the thickness-shear modes, are coupled to the flexural modes.

INTRODUCTION

THIS is the seventh in a series of papers on vibrations of plates. The first paper[1] contained a derivation of isotropic plate equations which accommodate the phenomenon of coupling between flexural and thickness-shear modes of motion. These equations were later extended to take into account crystal plates,[2] piezoelectric crystal plates, plates of varying thickness, plates with incomplete electrodes, and plates with specially shaped electrodes. (The first[1] and second[2] papers are referred to as I and II in the sequel.) The solutions of the various equations, given as illustrative examples in these papers, were all confined to cylindrical motions, that is, to one-dimensional problems.

We return, now, to the simplest (isotropic) form of the equations to solve a two-dimensional problem. We have in mind the antisymmetric modes of motion that are excited in an AT-cut quartz disk. However, the additional mathematical complexities introduced by the circular shape of the plate make it advisable to consider, first, the corresponding motions of an isotropic disk. It seems likely that the modes of motion and the frequency spectrum of the isotropic disk will be found to differ insignificantly from those of the quartz disk. This is because the two controlling parameters are the shape of the plate and the ratio of the plate-flexure modulus to the thickness-shear modulus. The former is the same for the two cases, and the latter has been made identical, in the computations, simply by choosing Poisson's ratio, for the isotropic material, to give the modulus ratio appropriate to the AT-cut of quartz. The lateral elastic constants, it is true, are not quite the same, but the discrepancy is small, and its influence on the motion is probably slight.

We give, here, the exact solutions of the equations for the isotropic, free disk and the results of detailed computations of the frequencies in the neighborhood of the thickness-shear frequency of an infinite plate. The frequency spectrum of the disk is found to have a different character from that obtained in II for the cylindrical vibrations of a rectangular plate. At first glance, it appears that the thickness-shear fundamental and its overtones are multivalued, i.e., corresponding to the fundamental and to each overtone of thickness-shear in the rectangular plate, there appears to be more than one resonant frequency in the disk. Upon closer examination, it develops that the additional resonances are due to the presence of a thickness-twist mode and its overtones, in which the displacement is a twist about an axis normal to the plate. The complete frequency spectrum is the result of coupling between thickness-shear and flexure and between thickness-twist and flexure.

PLATE EQUATIONS

In I and II, the plate equations were deduced from the three-dimensional equations of elasticity, referred to a rectangular coordinate system. The resulting equations may be transformed to a polar coordinate system, appropriate to the circular disk, but it is simpler to rederive the plate equations in the new system of coordinates. Thus, the assumed form of the displacements, in place of I(10) or II(5), is

$$u_r \approx y\psi_r(r,\theta,t), \quad u_\theta \approx y\psi_\theta(r,\theta,t), \quad u_y \approx \eta(r,\theta,t), \tag{1}$$

where r and θ are polar coordinates defined by $x=r\cos\theta$, $z=r\sin\theta$, i.e., the y axis is normal to the plane of the plate.

The derivation of the plate equations proceeds as before. Thus, corresponding to I(14,15) or II(10), we have plate-stress equations of motion

$$\begin{aligned}
&\frac{\partial M_r}{\partial r}+\frac{1}{r}\frac{\partial M_{r\theta}}{\partial \theta}+\frac{M_r-M_\theta}{r}-Q_r=\frac{\rho h^3}{12}\frac{\partial^2\psi_r}{\partial t^2}\\
&\frac{\partial M_{r\theta}}{\partial r}+\frac{1}{r}\frac{\partial M_\theta}{\partial \theta}+\frac{2M_{r\theta}}{r}-Q_\theta=\frac{\rho h^3}{12}\frac{\partial^2\psi_\theta}{\partial t^2}\\
&\frac{\partial Q_r}{\partial r}+\frac{1}{r}\frac{\partial Q_\theta}{\partial \theta}+\frac{Q_r}{r}=\rho h\frac{\partial^2\eta}{\partial t^2},
\end{aligned} \tag{2}$$

where ρ is the density, h is the thickness of the plate and the plate-stress components are given in terms of the

* This investigation was supported by the U. S. Army Signal Corps and the U. S. Office of Naval Research.

[1] R. D. Mindlin, J. Appl. Mech. **18**, 31–38 (1951).
[2] R. D. Mindlin, J. Appl. Phys. **22**, 316–323 (1951).

plate-displacements by

$$M_r=D\left[\frac{\partial\psi_r}{\partial r}+\frac{\nu}{r}\left(\psi_r+\frac{\partial\psi_\theta}{\partial\theta}\right)\right]$$

$$M_\theta=D\left[\frac{1}{r}\left(\psi_r+\frac{\partial\psi_\theta}{\partial\theta}\right)+\nu\frac{\partial\psi_r}{\partial r}\right]$$

$$M_{r\theta}=\frac{D}{2}(1-\nu)\left[\frac{1}{r}\left(\frac{\partial\psi_r}{\partial\theta}-\psi_\theta\right)+\frac{\partial\psi_\theta}{\partial r}\right] \tag{3}$$

$$Q_r=\kappa^2\mu h\left(\psi_r+\frac{\partial\eta}{\partial r}\right)$$

$$Q_\theta=\kappa^2\mu h\left(\psi_\theta+\frac{1}{r}\frac{\partial\eta}{\partial\theta}\right),$$

where $D=Eh^3/12(1-\nu^2)$, E, μ, ν are Young's modulus, the shear modulus and Poisson's ratio, respectively, and $\kappa^2=\pi^2/12$.

If (3) were substituted in (2) the resulting plate-displacement equations of motion would be those corresponding to I(16) or II(11). However, in the present case it is more convenient to work with the alternative formulation of the equations given by I(62,63). In polar coordinates, again omitting a factor e^{ipt}, these become

$$\psi_r=(\sigma_1-1)\frac{\partial\eta_1}{\partial r}+(\sigma_2-1)\frac{\partial\eta_2}{\partial r}+\frac{1}{r}\frac{\partial H}{\partial\theta}$$

$$\psi_\theta=(\sigma_1-1)\frac{\partial\eta_1}{r\partial\theta}+(\sigma_2-1)\frac{\partial\eta_2}{r\partial\theta}-\frac{\partial H}{\partial r} \tag{4}$$

$$\eta=\eta_1+\eta_2,$$

$$(\nabla^2+\delta_1^2)\eta_1=0$$

$$(\nabla^2+\delta_2^2)\eta_2=0 \tag{5}$$

$$(\nabla^2+\omega^2)H=0,$$

where

$$\delta_1^2,\ \delta_2^2=\tfrac{1}{2}\delta_0^4\{R+S\pm[(R-S)^2+4\delta_0^{-4}]^{\frac{1}{2}}\}, \tag{6}$$

$$\sigma_1,\ \sigma_2=(\delta_2^2,\delta_1^2)(R\delta_0^4-S^{-1})^{-1}, \tag{7}$$

$$\omega^2=2(R\delta_0^4-S^{-1})/(1-\nu), \tag{8}$$

$$R=h^2/12,\quad S=D/\kappa^2\mu h,\quad \delta_0^4=\rho p^2h/D. \tag{9}$$

SOLUTION OF EQUATIONS OF MOTION

In view of the modes of motion of interest in the present case, the appropriate solutions of (5) are

$$\eta_1=A_1J_1(\delta_1r)\cos\theta$$
$$\eta_2=A_2J_1(\delta_2r)\cos\theta \tag{10}$$
$$H=A_3J_1(\omega r)\sin\theta,$$

where $J_1(x)$ is Bessel's function of the first kind, of order unity, and A_1, A_2, A_3 are arbitrary constants. These are the modes of circumferential order unity. There are also modes of higher and lower circumferential order in which, for example, $\eta_1=A_1J_n(\delta_1r)\cos n\theta$, $n=0,1,2,\cdots$, but we are not concerned with them here.

For the vibrations of a plate with free edges, the boundary conditions are

$$M_r=M_{r\theta}=Q_r=0 \quad \text{at} \quad r=a, \tag{11}$$

where a is the radius of the disk. By using (3), (4), and (10), Eqs. (11) become

$$\left[\left(2-\frac{\delta_1^2a^2}{1-\nu}\right)J_1(\delta_1a)-\delta_1aJ_0(\delta_1a)\right](\sigma_1-1)A_1$$
$$+\left[\left(2-\frac{\delta_2^2a^2}{1-\nu}\right)J_1(\delta_2a)-\delta_2aJ_0(\delta_2a)\right](\sigma_2-1)A_2$$
$$+[\omega aJ_0(\omega a)-2J_1(\omega a)]A_3=0,$$
$$[\delta_1aJ_0(\delta_1a)-2J_1(\delta_1a)](\sigma_1-1)A_1$$
$$+[\delta_2aJ_0(\delta_2a)-2J_1(\delta_2a)](\sigma_2-1)A_2$$
$$+\left[\left(2-\frac{\omega^2a^2}{2}\right)J_1(\omega a)-\omega aJ_0(\omega a)\right]A_3=0, \tag{12}$$
$$[\delta_1aJ_0(\delta_1a)-J_1(\delta_1a)]\sigma_1A_1$$
$$+[\delta_2aJ_0(\delta_2a)-J_1(\delta_2a)]\sigma_2A_2+J_1(\omega a)A_3=0.$$

FREQUENCY EQUATION

Equations (12) comprise a system of three homogeneous, algebraic equations in the unknowns A_1, A_2, A_3. The vanishing of the determinant of their coefficients yields an equation for the determination of the frequency p through δ_1, δ_2, and ω. This secular equation, expressed in a form convenient for desk-calculator computation, reads

$$(1-\beta^2)\gamma^2\Gamma_1\Gamma_2+\frac{1-g\beta^2}{1+g}\left[\frac{2(1+\beta^2)}{(1-\nu)(1+g)}\right]^{\frac{1}{2}}\gamma^2\Gamma_1\Gamma_3$$
$$-\frac{1}{\beta}\frac{1-g\beta^2}{1+g}\left(3+\frac{1+\beta^2}{1+g}+\frac{g-\beta^2}{1-g\beta^2}-\frac{\beta^2}{1-\nu}\gamma^2\right)\gamma\Gamma_1$$
$$+\frac{1}{\beta}\frac{g-\beta^2}{1+g}\left[\frac{2(1+\beta^2)}{(1-\nu)(1+g)}\right]^{\frac{1}{2}}\gamma^2\Gamma_2\Gamma_3$$
$$-\frac{g-\beta^2}{1+g}\left(3+\frac{1}{\beta^2}\frac{1+\beta^2}{1+g}+\frac{1-g\beta^2}{g-\beta^2}-\frac{\gamma^2}{1-\nu}\right)\gamma\Gamma_2$$
$$-\frac{1-g\beta^2}{1+g}\left(1+\frac{1}{\beta^2}\frac{g-\beta^2}{1-g\beta^2}\right)\left[\frac{2(1+\beta^2)}{(1-\nu)(1+g)}\right]^{\frac{1}{2}}\gamma\Gamma_3$$
$$+\frac{1-\beta^2}{\beta}\left[4-\frac{g(1+\beta^2)}{(1-\nu)(1+g)}\gamma^2\right]=0, \tag{13a}$$

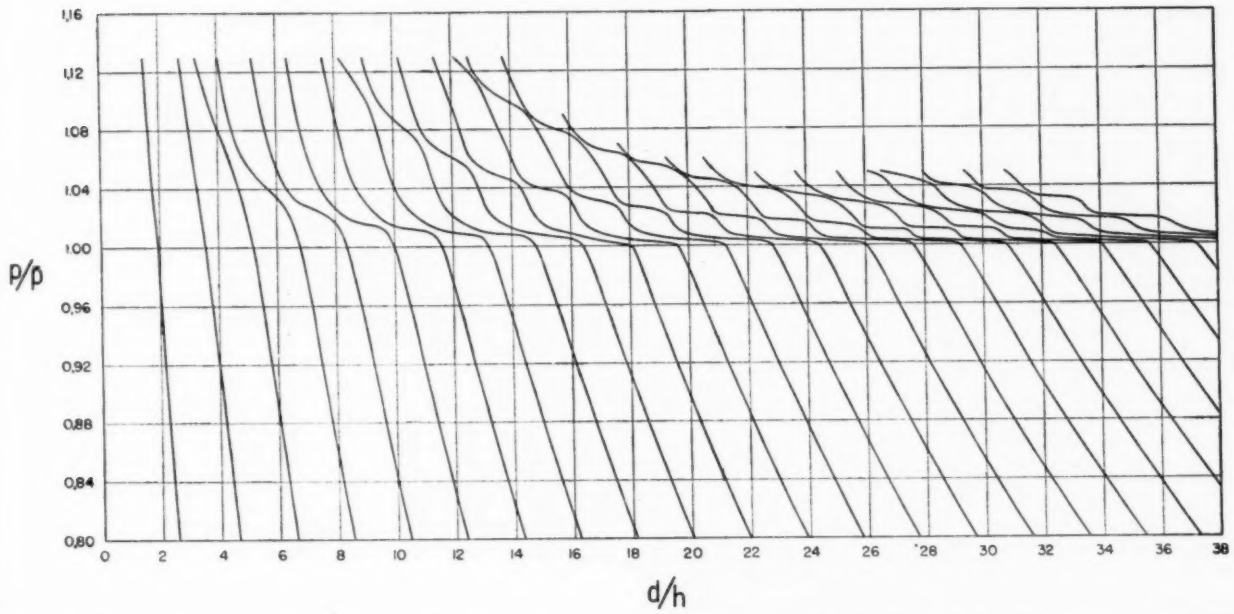

FIG. 1. Resonant frequencies of modes of vibration of circumferential order unity of a circular disk ($\nu=0.312$) as computed from Eqs. (13), (14), and (15). The ordinate is the ratio of the resonant frequency (p) to the frequency ($\bar{p}$) of the first thickness-shear mode of an infinite plate. The abscissa is the ratio of the diameter (d) to the thickness (h) of the disk.

where

$$\beta=\delta_2/\delta_1, \quad \gamma=\delta_1 a, \quad g=R/S$$

$$\Gamma_i=J_0(c_i\gamma)/J_1(c_i\gamma), \quad i=1, 2, 3$$

$$c_1=1, \quad c_2=\beta, \quad c_3=\beta\left[\frac{2(1+g)}{(1-\nu)(1+\beta^2)}\right]^{\frac{1}{2}}.$$

Now, $\delta_1^2>0$ for all values of $p>0$ while $\delta_2^2\gtrless 0$ according as $p\gtrless\bar{p}$, where $\bar{p}=\pi(\mu/\rho)^{\frac{1}{2}}/h$ is the frequency of the first thickness-shear mode of an infinite plate. Hence, β will be real or imaginary according as $p\gtrless\bar{p}$. Equation (13a) is a useful form for $p\gtrsim\bar{p}$. In the range $p<\bar{p}$, let $\beta=i\beta_1$, so that the frequency equation reads

$$\begin{aligned}
&(1+\beta_1^2)\gamma^2\Gamma_1G_2+\frac{1+g\beta_1^2}{1+g}\left[\frac{2(1-\beta_1^2)}{(1-\nu)(1+g)}\right]^{\frac{1}{2}}\gamma^2\Gamma_1G_3\\
&-\frac{1}{\beta_1}\frac{1+g\beta_1^2}{1+g}\left(3+\frac{1-\beta_1^2}{1+g}+\frac{g+\beta_1^2}{1+g\beta_1^2}+\frac{\beta_1^2}{1-\nu}\gamma^2\right)\gamma\Gamma_1\\
&-\frac{1}{\beta_1}\frac{\beta_1^2+g}{1+g}\left[\frac{2(1-\beta_1^2)}{(1-\nu)(1+g)}\right]^{\frac{1}{2}}\gamma^2G_2G_3\\
&-\frac{\beta_1^2+g}{1+g}\left(3-\frac{1}{\beta_1^2}\frac{1-\beta_1^2}{1+g}+\frac{1+g\beta_1^2}{g+\beta_1^2}-\frac{\gamma^2}{1-\nu}\right)\gamma G_2\\
&+\frac{1+g\beta_1^2}{1+}\left(-1+\frac{1}{\beta_1^2}\frac{\beta_1^2+g}{1+g\beta_1^2}\right)\left[\frac{2(1-\beta_1^2)}{(1-\nu)(1+g)}\right]^{\frac{1}{2}}\gamma G_3\\
&+\frac{1+\beta_1^2}{\beta_1}\left[4-\frac{g(1-\beta_1^2)}{(1-\nu)(1+g)}\gamma^2\right]=0, \quad (13b)
\end{aligned}$$

where

$$G_2=I_0(\beta_1\gamma)/I_1(\beta_1\gamma),$$

$$G_3=I_0(c'\gamma)/I_1(c'\gamma),$$

$$c'=\beta_1\left[\frac{2(1+g)}{(1-\nu)(1-\beta_1^2)}\right]^{\frac{1}{2}},$$

and $I_0(x)$, $I_1(x)$ are modified Bessel's functions of the first kind.

From the relation $\beta=\delta_2/\delta_1$ and Eq. (6), explicit expressions for the frequency may be obtained. Thus,

$$\begin{aligned}
p/\bar{p}&=[1-\beta^2(1+g)^2/g(1+\beta^2)^2]^{-\frac{1}{2}}, \quad p>\bar{p}\\
p/\bar{p}&=[1+\beta_1^2(1+g)^2/g(1-\beta_1^2)^2]^{-\frac{1}{2}}, \quad p<\bar{p}.
\end{aligned} \quad (14)$$

Further, from the relation $\gamma=\delta_1 a$,

$$\begin{aligned}
d/h&=\gamma(\bar{p}/p)[(1+\beta^2)/3(1+g)]^{\frac{1}{2}}, \quad p>\bar{p}\\
d/h&=\gamma(\bar{p}/p)[(1-\beta_1^2)/3(1+g)]^{\frac{1}{2}}, \quad p<\bar{p},
\end{aligned} \quad (15)$$

where d is the plate diameter.

COMPUTATION OF FREQUENCIES

Equations (13), (14), and (15) constitute the solution of the problem. For a given material the values of ν and g are fixed. Choosing a value of β or β_1 fixes $p/\bar{p}$ by (14) and determines an infinite set of roots γ of (13). For the particular β or β_1 each of these roots determines a ratio d/h, thus giving an infinite set of d/h corresponding to every value of $p/\bar{p}$.

For the isotropic plate, the ratio of the thickness-shear modulus to the plate flexure modulus is

$$g=\pi^2(1-\nu)/24,$$

while, for the AT-cut of quartz,

$$g=\frac{\pi^2 c_{66}}{12(c_{11}-c_{12}^2/c_{22})},$$

where the elastic constants are referred to the coordinates of the (rotated) AT section. For this cut of quartz, $g=0.283$. Hence, an isotropic plate with $\nu=0.312$ gives the same value of g as an AT quartz plate. The computations were made for this value of ν.

To facilitate the task of finding the roots γ of Eqs. (13), for a series of values of $p/\bar{p}$, tables were computed of the functions:

$$J_0(x)/J_1(x) \quad 0(0.01)100$$

$$I_0(x)/I_1(x) \quad \text{and} \quad 0(0.01)10,\ 10(0.02)16,\ 16(0.1)20,\ 20(1)37$$

to six decimals.[3] The subsequent numerical work, carried out on a desk calculator, yielded the resonant frequencies of vibration depicted in Fig. 1.

The flexural modes, in the lower part of Fig. 1, are those of even order $r=2,4,6,\cdots$, and are similar to those in the lower part of Fig. 1 of II. However, the upper parts ($p/\bar{p}>1$) of the two figures are different. For example, in the case of the rectangular plate the thickness-shear fundamental couples with every even flexural mode in turn, but, in the disk, the thickness-shear fundamental appears to couple only with alternate, even, flexural modes. As a result, the thickness-shear fundamental appears to be double-valued.

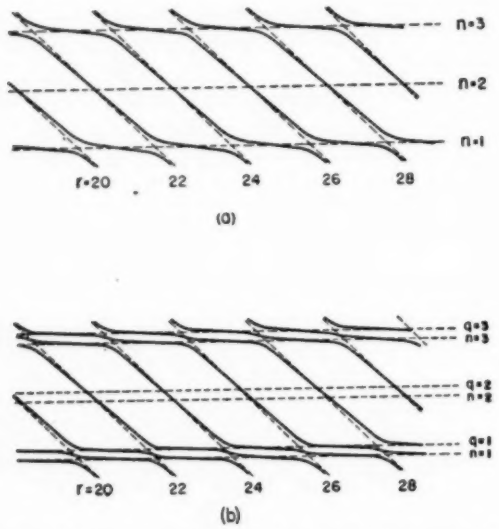

FIG. 2. (a) Frequency spectrum for coupling between thickness-shear and flexural modes. (b) Frequency spectrum for coupling between thickness-shear and flexural modes and between thickness-twist and flexural modes, with no coupling between shear and twist modes.

[3] The computation of the tables of $J_0(x)/J_1(x)$ was performed by S. Poley on equipment made available by the Watson Scientific Computing Laboratory of the International Business Machines Corporation. Both tables are stored in the files of the Department of Civil Engineering, Columbia University.

The apparent anomaly is resolved when it is recognized that there is present a set of thickness-twist modes in addition to thickness-shear and flexural modes. Mathematically, the additional modes derive from the solenoidal, retarded potential H. Their uncoupled frequencies may be obtained, approximately, by setting $\eta=0$, in the equations, so that H is the only potential left. Then we have

$$(\nabla^2+\omega^2)H=0$$

$$\psi_r=-\frac{1}{r}\frac{\partial H}{\partial\theta}, \quad \psi_\theta=-\frac{\partial H}{\partial r}$$

$$M_{r\theta}=-\frac{D(1-\nu)}{2}\left(2\frac{\partial^2}{\partial r^2}+\omega^2\right)H$$

$$=-D(1-\nu)\omega^2 A_3 f(\omega r)\sin\theta,$$

where

$$f(\omega r)=\left(\frac{2}{\omega^2 r^2}-\frac{1}{2}\right)J_1(\omega r)-\frac{1}{\omega r}J_0(\omega r).$$

Applying only the boundary condition $M_{r\theta}=0$ on $r=a$, we obtain the secular equation $f(\omega a)=0$, or

$$2c_3\gamma\Gamma_3=4-c_3^2\gamma^2. \tag{16}$$

The roots of (16), in conjunction with (14) and (15), give the approximate frequency spectrum ($p/\bar{p}$ *vs* d/h) of the thickness-twist modes. The curves are asymptotic to $p/\bar{p}=1$ and are very nearly tangent to the almost horizontal portions of the curves in Fig. 1. That is, the thickness-twist modes have frequencies very close to those of the corresponding thickness-shear modes. The effect, of two such neighboring families, on the coupling with the flexural modes is illustrated in Fig. 2. In Fig. 2a is shown the usual spectrum resulting from the coupling of a family of odd thickness-shear modes ($n=1, 3, \cdots$) and even flexural modes ($r=20, 22, \cdots$). In Fig. 2b a family of thickness-twist modes ($q=1, 3, \cdots$), closely paralleling the thickness-shear modes, is added. If the result were to be interpreted as coupling between flexure and thickness-shear alone, it would appear that the thickness-shear modes are double-valued and couple only with alternate flexure modes. This would be especially so if the coupling were strong enough to smooth out the kinks in the almost horizontal portions of the curves, as is the case in Fig. 1. However, when the presence of the thickness-twist modes is taken into account, there are no anomalies.

It should be observed that the case described here is a degenerate one of coupling of three families of modes, because, although there is coupling between thickness-shear and flexure and between thickness-twist and flexure, there is no coupling between thickness-shear and thickness-twist. An example in which there is full coupling of the three families will be described in a subsequent paper.

Low-Energy Electron Diffraction Investigation of Chemisorbed Gases on the (100) Faces of Copper and Nickel Single Crystals

R. E. SCHLIER*† AND H. E. FARNSWORTH
Brown University, Providence, Rhode Island‡

(Received February 1, 1954)

The use of low-energy (10–250 ev) electron diffraction as a method of studying the chemisorption of gases on metal single crystals is described. The apparatus permits controlling the temperature of the crystal in the range from liquid nitrogen to room temperatures during observation. Outgassing the crystal is effected by strong heating using electron bombardment. The residual gas structures on the (100) faces of copper and nickel single crystals are determined to be: (1) a monolayer with a single-spaced square array, found on both copper and nickel after heating at temperatures slightly below the minimum temperature for observable evaporation; and (2) a double-spaced, face-centered square array, found after heating at or above this temperature. Nitrogen adsorbs on the (100) face of a copper single crystal at 25°C and −78°C into an incomplete single-spaced square array. Most of the adsorption at 25°C occurs in a pressure range of 10^{-4} to 10^{-1} mm Hg in a ten-minute interval, with little change occurring between 10^{-1} and 8 mm Hg. At −78°C, the corresponding pressure range is 10^{-4} to 10^{-3} mm Hg with little adsorption occurring between 10^{-3} and 1 mm. At room temperature, oxygen adsorbs into a complete, single-spaced, square array at a pressure of 2×10^{-3} mm Hg in a ten-minute interval. At higher pressures, additional oxygen adsorbs into a thicker layer of no regular structure.

INTRODUCTION

THE early work in the field of low-energy electron diffraction[1,2] indicated that surface phenomena, such as the adsorption of gases, could be profitably investigated by this method as a consequence of the small penetration of low-energy electrons into the surface under investigation. For example, Farnsworth[3] found that 90 percent of the diffracted electrons arise from the first two atomic layers of silver, for electron energies under 300 electron volts.

Although diffraction maxima caused by an adsorbed gas lattice have been observed by the above investigators, little work of a systematic nature has been carried out, using the low-energy electron diffraction technique, on the adsorption of gases on solids.

This paper presents the results obtained by using this method to investigate the (100) faces of copper and nickel single crystals over wide ranges of temperature and pressure. The investigation includes the adsorption of gases on a copper single crystal, and the determination of the residual gas structures on both copper and nickel single crystals. Adsorption data on nickel were not obtained, because of the recrystallization of the nickel crystal.

APPARATUS AND PROCEDURE

The apparatus is shown in Fig. 1, and is a conventional low-energy electron diffraction tube,[2] with modifications for controlling the temperature of the metal crystals under investigation. In the present apparatus, electrons from the filament are accelerated, deflected so as to pass through a collimating tube[4] and strike the face of the metal single crystal under investigation at normal incidence. Some of the electrons scattered by the crystal enter a one-mm diameter hole in a Faraday collector. The electron current to the collector is measured with a dc amplifier. The collector may be rotated by a magnetic control, so that the hole in the collector moves in an arc about the point of incidence of the beam on the crystal, and in a plane containing the incident beam. The crystal may also be rotated about the axis of the incident electron beam. Thus, electrons scattered into nearly the entire forward hemisphere about the crystal may be investigated, by suitable combinations of crystal rotation and collector motion. Electron diffraction beams are observed by measuring the current to the Faraday collector as a function of collector angle. The energy and current of the primary beam are held constant.

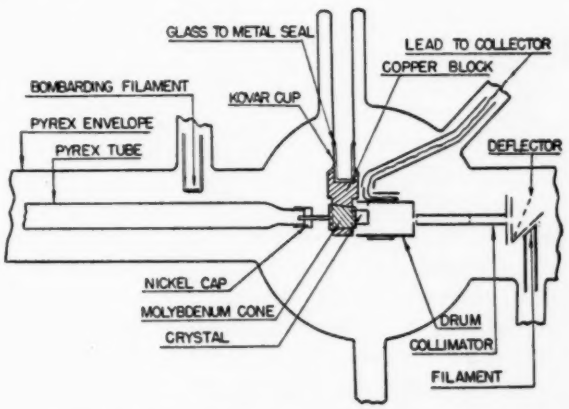

FIG. 1. Experimental tube.

* Charles A. Coffin Fellow, 1950–1951.

† Part of a dissertation submitted in partial fulfillment of the requirements for the degree of Doctor of Philosophy in Brown University. Part of this paper was presented at a meeting of the American Physical Society, Phys. Rev. **90**, 351 (1953).

‡ Assisted by the Office of Naval Research and Research Corporation.

[1] C. Davisson and L. H. Germer, Phys. Rev. **30**, 705 (1927).

[2] H. E. Farnsworth, Phys. Rev. **34**, 679 (1929).

[3] H. E. Farnsworth, Phys. Rev. **49**, 605 (1936).

[4] H. E. Farnsworth, Rev. Sci. Instr. **21**, 102 (1950).

The crystal is mounted on a molybdenum cone by means of molybdenum hooks passing through the cone, and seating in slots in the crystal. The cone in turn is attached to a Pyrex tube. The tube is supported on Chromel bearings, so that rotation or translation of the tube, cone, and crystal is possible. When the crystal is in the forward position (for diffraction measurements), the cone seats in a copper block, which is attached by means of a glass-to-Kovar seal to a re-entrant tube in the Pyrex envelope. Thus, by using a suitable coolant in the re-entrant tube, the temperature of the block, cone, and crystal can be controlled. Finally, the cone and crystal may be withdrawn into a side tube for strong heating by electron bombardment.

The Pyrex experimental tube is evacuated by a three-stage oil diffusion pump. Cold traps are placed on each side of the pump. In addition, a one-stage oil diffusion pump is used to evacuate the fore volume of the system. A pressure of less than 1×10^{-8} mm Hg can be attained after the experimental tube is baked at 350°C for several hours in two intervals with an increase in the trap temperature to 25°C for 15 minutes between baking intervals.

The effect of adsorbed gas on the electron diffraction beams is observed using the following procedure. The crystal is outgassed by strong heating in a high vacuum, and the electron diffraction beams characteristic of the outgassed surface are observed. Then, a gas is allowed to enter the experimental tube at a known pressure for a definite period of time. The tube is re-evacuated, and the electron diffraction beams are again observed. A higher pressure is next used, and so on. The pressure in the experimental tube is controlled by allowing a gas, previously introduced into the fore volume of the vacuum system, to diffuse into the tube through the diffusion pumps. This is accomplished by decreasing the power to the diffusion pump heaters. Liquid nitrogen is used as a refrigerant for the vapor traps between the diffusion pumps and the tube when the adsorption studies are being made. After completing an adsorption run, the crystal is again outgassed.

RESIDUAL GAS STRUCTURES ON OUTGASSED CRYSTAL SURFACES

Before adsorption investigations were undertaken, the crystals being investigated were outgassed for several hundred hours at red-heat temperatures in a high vacuum. The pressure in the experimental tube, under best conditions, was lower than 1×10^{-8} mm Hg. During the outgassing procedure, the pressure was kept below 1×10^{-6} mm Hg in the initial stages and below 1×10^{-7} in the later stages. Final outgassing was carried out with the pressure in the tube at about 3×10^{-8} mm Hg, while the crystal was hot. During the course of the outgassing, the surface structures were determined as a function of outgassing temperatures.

The following information was obtained for the (100) faces of nickel and copper single crystals.

Copper

After initial outgassing at temperatures below 700°C no electron diffraction beams could be observed from the (100) face of the copper crystal. This fact indicates that the (100) face was covered with chemisorbed gas, at least several molecular layers in thickness, the outer layers of which had no regular structure.

After outgassing at temperatures between 700°C and 900°C, the (100) face was covered with a residual gas lattice, probably a monolayer, in a single-spaced, square array of the same orientation as the underlying copper atoms. After outgassing at temperatures at which the copper evaporated (above 900°C), the residual gas structure was predominantly a double-spaced, face-centered monolayer, with perhaps some of the single-spaced, square array still present. Intensities of the diffraction beams from the double-spaced structure could not be reduced to less than about $\frac{2}{3}$ of their maximum values, even after prolonged heating at temperatures above 900°C at the lowest pressure. These results are in agreement with those reported earlier by Farnsworth.[2,5,6]

Nickel

Similar results were obtained with the (100) face of the nickel single crystal. Several hours of outgassing at 600°C were required to produce diffraction beams. After outgassing at temperatures between 600°C and 1000°C, the surface was covered with a residual gas lattice composed of a single-spaced, simple square array. Immediately after outgassing at temperatures between 1000°C and 1050°C, diffraction beams characteristic of the double-spaced, face-centered structure were observed. These beams weakened and disappeared within an hour. Outgassing at 1100°C was necessary to develop a stable double-spaced, face-centered residual gas structure. This structure could not be removed by prolonged heating at temperatures above the evaporation temperature (1100°C). It should be noted that the outgassing temperature required to first produce electron diffraction maxima from nickel is only 600°C while that required to produce diffraction beams from copper is 700°C. However, the temperature required to form the double-spaced, face-centered residual gas structure on nickel (1100°C) is higher than that for copper (900°C).

ADSORPTION OF GASES ON THE (100) FACE OF A COPPER SINGLE CRYSTAL

The copper crystal was outgassed at temperatures higher than the one at which copper evaporated from the crystal, and until the experimental tube pressure

[5] H. E. Farnsworth, Phys. Rev. **40**, 684 (1932).
[6] H. E. Farnsworth, Phys. Rev. **35**, 1131 (1930).

was below 3×10^{-8} mm Hg when the crystal was hot. The effect of adsorbed gases on the diffraction beams from the (100) face of a well-outgassed copper single crystal was observed. Nitrogen was adsorbed at room and dry ice-acetone crystal temperatures, and oxygen was adsorbed at room temperature. Before making the adsorption studies, the residual gas structure on the surface of the crystal was the above-mentioned double-spaced, face-centered square structure.

The results of the investigations are shown in Fig. 2. Peak diffraction beam current is plotted against the logarithm (base 10) of the pressure in mm Hg. Changes in the maximum diffraction beam current arising from the copper lattice can be used as an indication of changes in adsorption, since adsorbed gas weakens the beam. The maximum diffraction beam current from a gas structure is a measure of the amount of that structure present.

The upper set of curves are the results obtained with nitrogen adsorbed on the crystal at room temperature. As the pressure is increased, the diffraction beam current from the copper structure decreases, and appears to be approaching a limiting value at the highest pressure used, which is about 8 mm Hg. The diffraction beam current for the double-spaced, face-centered structure increases as the pressure is increased; it then decreases and approaches a limiting value as the pressure is increased to 8 mm Hg. Finally, the diffraction beam current from the single-spaced, square structure increases as the pressure is increased above 10^{-4} mm Hg, and approaches a limiting value as the pressure is increased to 8 mm Hg. The approach of the diffraction beams to a limiting value indicates that the adsorption reaction is nearly complete at the higher pressure.

The observed variation of the beams can be explained if initially the crystal surface is covered with an incomplete double-spaced, face-centered, square array of adsorbed gas atoms. As the pressure is increased, the adsorbed gas atoms first complete the double-spaced structure, thus causing the observed increase in beam current for that structure. Then, as further gas is added, the double-spaced structure is partially converted into the single-spaced structure by the addition of atoms in interstitial positions in the two dimensional, double-spaced, face-centered gas lattice. When the pressure is increased to the highest value used (8 mm Hg), the reaction appears to be nearly complete, although the presence of the diffraction beam from the double-spaced lattice indicates that the single-spaced, square structure has not been completed. The surface gas layer, therefore, is probably still less than a single-spaced monolayer. It is noted that the pressure, for which the adsorption reaction is approximately one-half completed, is about 3×10^{-3} mm Hg.

The middle set of curves in Fig. 2 is for nitrogen, with the crystal at dry ice-acetone temperature. As the pressure is increased, the currents of the beams for both the copper and the double-spaced gas lattices

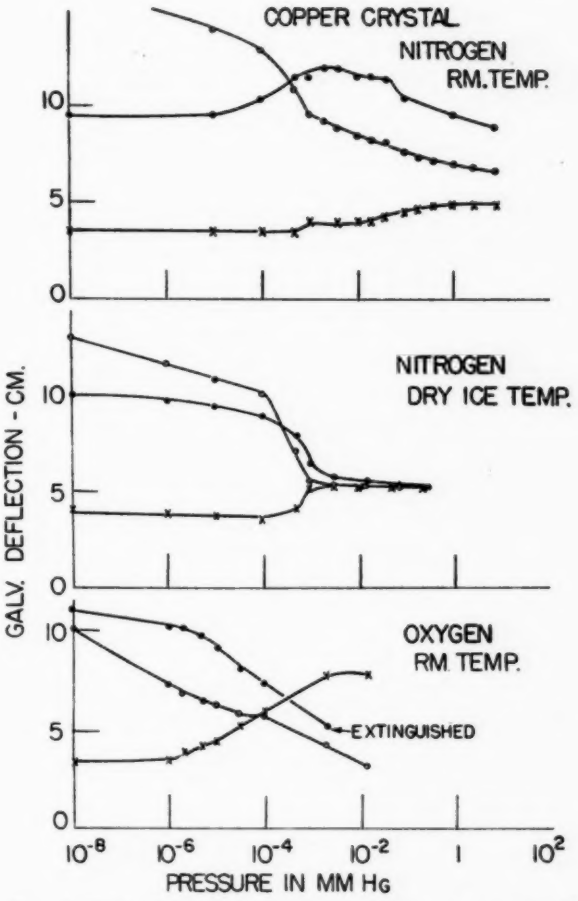

FIG. 2. Peak diffraction beam current *versus* pressure. The diffraction beam current for a given pressure was obtained after exposing the crystal to that pressure for ten minutes, and re-evacuating the tube. The beam currents are not corrected for background scattering. ○ Copper structure (multiply ordinate by 3). The background is approximately 0.2 cm on the scale shown in the figure. ● Double-spaced, face-centered square structure. The background is approximately 3 cm. × Single-spaced, square structure. The background is approximately 1.5 cm.

decrease, and approach limiting values at pressures above 10^{-2} mm Hg. Most of the effect of the gas on the beams occurs at pressures between 10^{-4} and 10^{-3} mm Hg. Over the same pressure range, the diffraction beam current from the single-spaced structure increases, and approaches a limiting value at pressures above 10^{-2} mm Hg. Again, the observed results are accounted for if the crystal is initially covered with a *complete* double-spaced, face-centered square array of residual gas atoms. Then, as gas is adsorbed, the atoms are adsorbed interstitially in this lattice, converting it to a single-spaced square lattice. At pressures above 10^{-2} mm Hg, when the adsorption reaction appears to be completed, the single-spaced structure is still incomplete, since the diffraction beams from the double-spaced structure are still present, and the adsorbed gas layer is therefore probably less than a single-spaced monolayer.

The amount of the single-spaced structure present

when the reaction is complete at the dry ice-acetone temperature is greater than the amount present at room temperature, when the reaction is complete. This is shown by the relatively greater decrease of the diffraction beam from the double-spaced structure, and the greater increase of the beam from the single-spaced structure, at the lower temperature. The pressure at which the adsorption reaction is approximately one-half completed is about 3×10^{-4} mm Hg.

The last set of curves in Fig. 2 is for oxygen, with the crystal at room temperature. In this case, the effect of oxygen on the diffraction beams is considerably different from that of nitrogen. There is no approach to a limit by the diffraction beams as the pressure is increased. In fact, at sufficiently high pressures (a few millimeters) all the diffraction beams are extinguished (this is not shown in Fig. 2, but has been observed).

As the pressure is increased, the diffraction beams from both the copper and the double-spaced, face-centered lattices decrease, and the beam from the double-spaced structure is no longer detectable at a pressure of 2×10^{-3} mm Hg. At the same pressure, the diffraction beam from the single-spaced structure has reached a maximum value.

In this case, if the crystal is initially covered with a complete double-spaced, face-centered array, the interstitial spaces in this array are subsequently completely filled by adsorbed oxygen atoms at a pressure of 2×10^{-3} mm Hg, so that the gas structure at this pressure is a complete single-spaced, square array. As the pressure is further increased, the further decrease in the diffraction beam current for the copper structure indicates that further adsorption is occurring, and thus the adsorbed gas layer at the higher pressure is probably more than a monolayer in thickness. At still higher pressures (not shown) the continued decrease and extinction of all the diffraction beams are indicative of an adsorbed oxygen layer several monolayers in thickness, of which the upper layers have no oriented lattice structure.

JOURNAL OF APPLIED PHYSICS VOLUME 25, NUMBER 10 OCTOBER, 1954

On the Flicker Noise Generated in an Interface Layer*

H. J. HANNAM AND A. VAN DER ZIEL
Department of Electrical Engineering, University of Minnesota, Minneapolis, Minnesota
(Received February 8, 1954)

It is shown that a large amount of flicker noise is generated in tubes that have developed a high-resistance interface layer between the cathode-nickel and the oxide coating. The equivalent noise resistance R_n of this effect can be represented by the equation $R_n=KI_p^2R_i^2/f^\alpha$, where K is a constant, I_p the plate current, R_i the interface resistance, and f the frequency whereas α varies between 1.1 (for low R_i) and 1.5 (for high R_i). All evidence suggests that the noise is generated in the interface layer; this was subsequently proved by a direct experiment. The current dependence suggests that the noise is caused by spontaneous fluctuations in the resistance R_i. Experiments up to 1.5 mc indicate a change in the exponent α from 1.1 to 1.6 at high frequencies, indicating that the interface impedance cannot be represented by a fixed resistance R_i and a fixed capacitance C_i in parallel.

1. INTRODUCTION

PRELIMINARY data obtained by Lindemann and van der Ziel[1] indicate that a high-resistance interface layer of Ba_2SiO_4, which develops in many tube types after aging, gives rise to a large increase in flicker noise. This paper presents a more detailed study of the noise characteristics of the interface layer.

It is generally believed that free barium is necessary for the high emission of an oxide-coated cathode. Silicon and other suitable impurities in the cathode nickel act as "reducing agents," reducing some of the BaO of the coating to free barium; these impurities are therefore essential for obtaining active cathodes. Many of the reaction products between the impurities and the oxide coating form an interface layer, but not all these interface layers are detrimental to the operation of the tube. The Ba_2SiO_4 interface layer caused by the silicon in the cathode nickel, however, has a high resistance and this gives rise to undesirable feedback effects. The interface resistance may either be caused by the properties of bulk Ba_2SiO_4 or by a rectifying barrier at the interface. Experimental evidence seems to favor the latter point of view.[2]

The rate of development of the interface resistance depends upon the amount of silicon present in the cathode nickel. If the silicon content of the cathode nickel is high (0.2–0.3 percent), an appreciable interface resistance develops after a few hundred hours of aging. If the silicon content of the nickel is low (<0.05 percent) it takes a few thousand hours of aging before some interface resistance has developed and the values of

* Work performed under U. S. Signal Corps Contract.
[1] W. W. Lindemann and A. van der Ziel, J. Appl. Phys. 23, 1410 (1952).
[2] A. S. Einstein, "Oxide coated cathodes," *Advances in Electronics* (Academic Press, Inc., New York, 1948), Vol. 1, pp. 1–69.

this resistance never becomes as high as in the previous case.

The interface resistance decreases strongly with increasing temperature and this decrease is instantaneous; this should be expected for a semiconductor with a relatively large gap between the donor levels and the conduction band. The interface resistance also decreases strongly with increasing tube current. The latter effect may be explained by assuming that the flow of current through the layer causes donors to flow into the interface layer (current activation). This decrease in resistance is not instantaneous, but it takes several minutes or even longer before a new equilibrium condition has set in.

The interface resistance increases with further aging and is especially large if the tube is aged under cut-off conditions. This is not because no interface is formed if the tube is drawing current, but because the interface layer is then "current activated." If the interface resistance has been partially destroyed by drawing current and if the tube is then aged under cut-off conditions it takes a few hours before a new equilibrium condition has set in.

The interface resistance is not completely destroyed by drawing a large current. In fact, we found that for high values of the interface resistance some 12SN7 tubes could be operated without filament power as long as the tube current was larger than 20 ma; apparently the heating of the cathode coating by the tube current was enough to maintain the emission current at a reasonable level.

Most of the experiments were performed on 12SN7 tubes donated by the Minneapolis Honeywell Regulator Company; these tubes developed an appreciable interface resistance after 200 hours of aging under cut-off conditions. The rapid development of interface resistance speeded up the research considerably.†

The noise measurements were carried out with a 7-channel noise spectrum analyzer, which allowed to measure a spectrum between 10–10 000 cycles in 5 minutes.[3] The noise in a frequency interval df may be represented by an equivalent noise emf $(\langle e^2\rangle_{Av})^{\frac{1}{2}}$ in series with the input of the tube. It is common practice to compare this noise emf with the thermal noise emf of a resistance R_n at room temperature by equating

$$\langle e^2\rangle_{Av}=4kTR_n df.$$

R_n is called the noise resistance of the tube.

The interface resistance was measured by a pulse technique described by Wagner.[4]

2. EXPERIMENTAL RESULTS

Figure 1 shows the noise resistance R_n at 30 cycles for tube 12SN7 No. 309B as a function of the plate current I_p for various stages of aging (the tubes were aged without drawing current); these curves are representative for most of those 12SN7 tubes that rapidly developed a high-resistance interface. The interface resistance R_i was 50 ohms after 200 hours of aging and 240 ohms after 850 hours of aging. Five tubes were followed through this aging period.

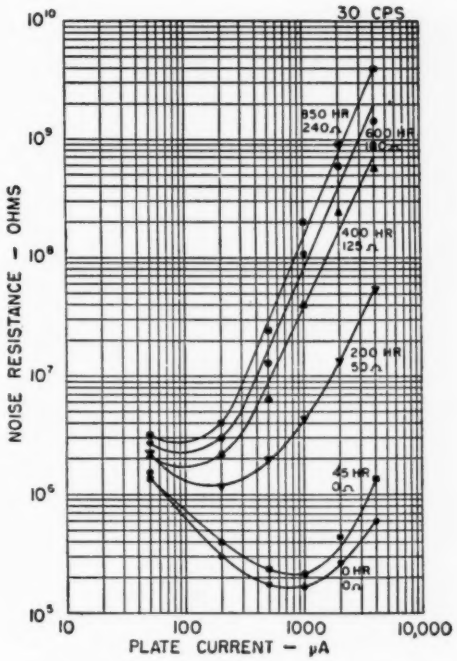

FIG. 1.

The noise resistance does not change very much during the first stages of aging. After the interface resistance has reached a reasonable value, the noise due to the interface resistance completely masks the other sources of flicker noise of the tube except at very small currents, where the other noise sources may still predominate. The flicker noise resistance due to the interface effect varies as I_p^2, whereas the flicker noise resistance of a tube without interface resistance shows quite a different current dependence. If the noise resistance at a plate current $I_p=1$ ma is plotted against the interface resistance R_i, it is found that R_n varies approximately as R_i^2 (Fig. 5). Only one tube showed deviations in the dependence of R_n upon I_p and upon R_i.

Figure 2 shows the results for a Philips EF40 tube in which the cathode nickel has a very low silicon content. This tube showed a noticeable interface resistance only after a few thousand (not hundred) hours of aging. R_n showed little variation with aging after the cathode was well activated; this continued until an interface resistance was formed.

Figure 3 shows the noise resistance of tube 12SN7 No. 347B at 1 ma plate current as a function of the frequency for various values of the interface resistance R_i. Here the interface resistance was changed by drawing varying amounts of plate current and waiting until

† The authors are indebted to Mr. E. Rexer, Minneapolis Honeywell Regulator Company, for making this donation possible.

[3] E. G. Nielsen and A. van der Ziel (to be published).

[4] H. M. Wagner, Proc. Natl. Electronics Conf. 8, 553 (1952).

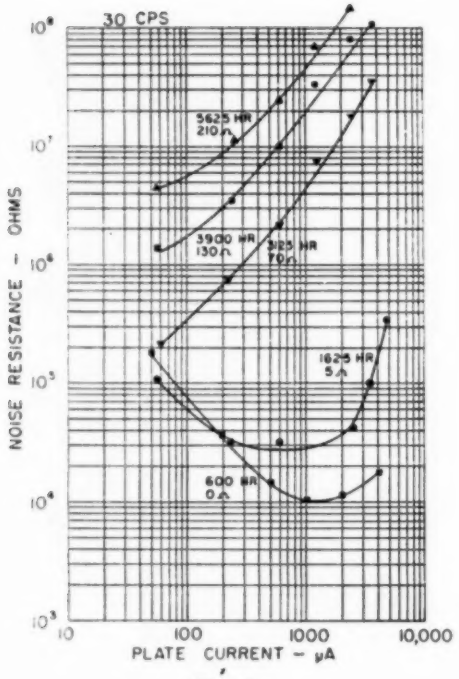

FIG. 2.

an equilibrium had set in (current activation). The measurements had to be carried out rapidly to prevent a change in the state of activation of the interface layer during the measurement. As these curves indicate, R_n varies as $1/f^\alpha$; α is about 1.1 for tubes having an interface resistance R_i of a few hundred ohms. For higher values of R_i the exponent α increases slightly with increasing R_i; for a tube for which $R_i = 13\,000$ ohms we found $\alpha = 1.5$. If R_n is plotted *versus* R_i at 30 cycles, it is again found that R_n varies as R_i^2 (Fig. 5). At least five tubes were measured this way and only one of them gave a different dependence of R_n upon R_i (exponent >2).

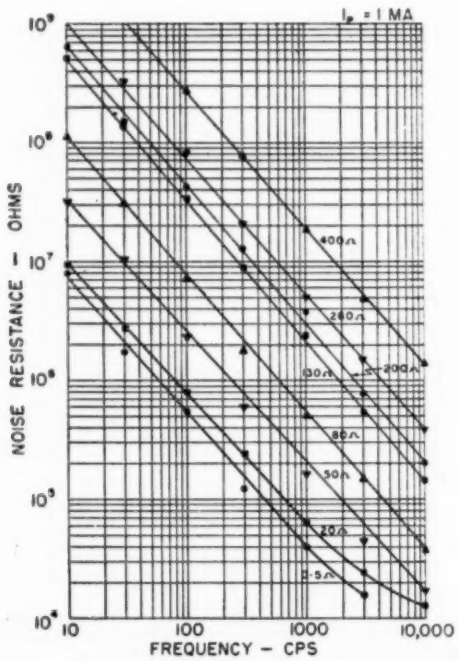

FIG. 3.

In the next experiment the interface resistance was varied by varying the filament voltage from 6 v to 18 v, thus changing the cathode temperature. In Fig. 4 the noise resistance R_n for tube 12SN7 No. 341A at 1 ma plate current is plotted against the frequency f. The flicker noise varies as $1/f^\alpha$ where α varies from 1 to 1.3 and R_n at 10 cycles varies from 10^6 to 10^{12} ohms if R_i

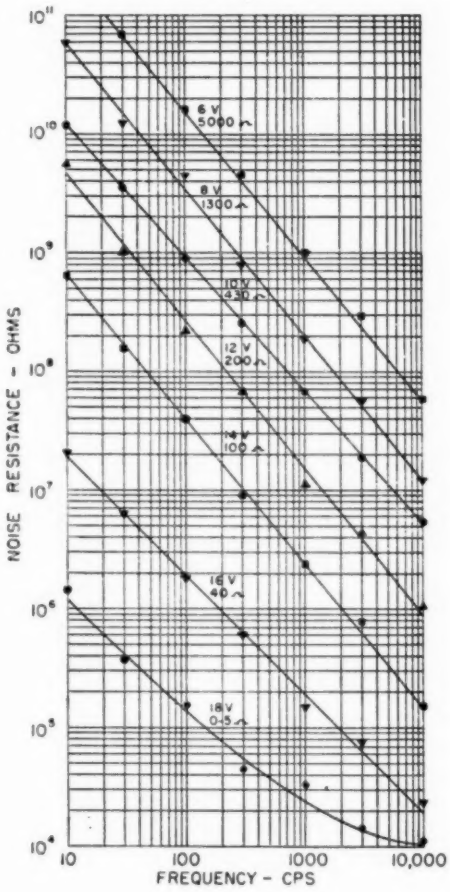

FIG. 4.

varies from 0 to 5000 ohms. If R_n is plotted *versus* R_i it is again found that R_n varies as R_i^2, though deviations occur at very low and at very high values of R_i. The deviation at the high interface resistance end is at present unexplained. Tube No. 341A was the only tube measured over so wide a range of R_n.

Figure 5 shows R_n plotted *versus* R_i for the tubes 12SN7 No. 309B, 12SN7 No. 347B, 12SN7 No. 341A, and 6SJ7 No. 5 at 30 cycles and 1 ma plate current. The figure shows the quadratic relationship for R_n and R_i and the deviations for tube 12SN7 No. 341A. We may thus sum up our experimental results by the ap-

proximate formula:

$$R_n = K\frac{I_p^2 R_i^2}{f^\alpha}, \qquad (1)$$

where the constant K may depend somewhat upon the way the interface layer has been treated.

That such a dependence of K upon treatment exists may be seen from Fig. 6 showing R_n for tube 12SN7 No. 355A as a function of frequency for 1 ma plate current after various treatments. First R_i was 260 ohms (curve A), then the interface layer was current activated and R_i dropped to a very low value (curve B); finally, the interface layer was deactivated again such that R_i became 150 ohms. Despite the difference in R_i between curves A and C, the noise resistance R_n is almost the same in both cases.

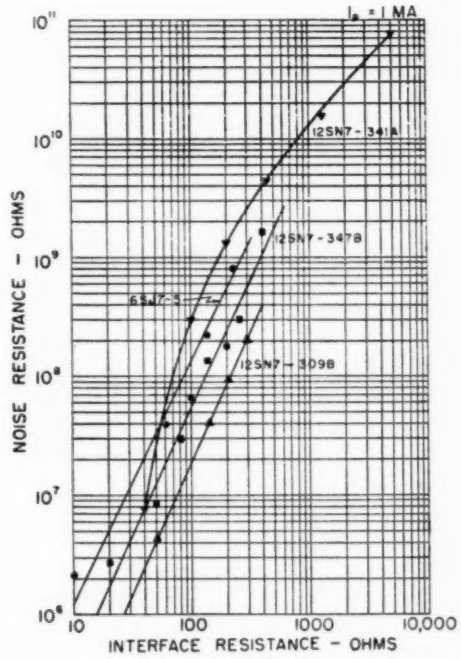

FIG. 5.

The fact that R_n depends so strongly upon R_i indicates that the above type of flicker noise is actually generated in the interface layer. This was verified directly by an experiment.

To understand the experiment we observed that a noise emf $(\langle e^2\rangle_{Av})^{\frac{1}{2}}$ (in a frequency interval df) in the coating of a diode with internal resistance R_p is equivalent to a noise current generator $(\langle i^2\rangle_{Av})^{\frac{1}{2}}$ in parallel to the output such that

$$\langle i^2\rangle_{Av} = \langle e^2\rangle_{Av}/R_p^2 = 2eI_s df \qquad (2)$$

where I_s is the equivalent saturated diode current of the diode. The influence of the noise emf in the coating should thus disappear if the diode is measured under the saturated condition, because R_p is then very large,

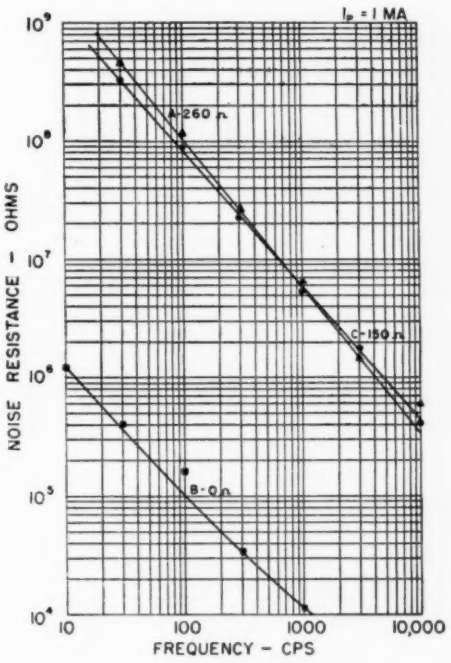

FIG. 6.

whereas its full effect will be felt under space-charge limited condition. No such effect would be observed if the noise was due to just a fluctuation in the emission.

Tube 12SN7 No. 354B was therefore connected as a diode and I_s was measured (Fig. 7, curve a) at a low filament temperature ($V_f = 3.6$ volts) and 120 μa plate current under saturated condition ($R_p = 0.8\times10^6$ ohms). Next the filament voltage was raised to $V_f = 4.0$ volts

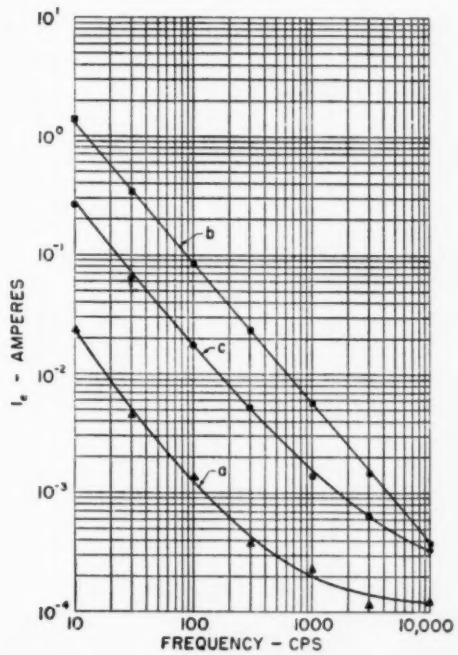

FIG. 7.

and I_s was measured at the same plate current (curve *b*). The tube was now under space-charge limited condition ($Rp=0.04\times10^6$ ohms) and as a consequence I_s was much larger.

Finally, at the same filament voltage $V_f=4.0$ volts, I_s was measured (curve *c*) at an increased anode current of 240 μa so that the tube was closer to saturation (Rp rose to 2.1×10^5 ohms). It was found that I_s decreased by roughly a factor 6 as would be expected from (2). For we know that $\langle e^2\rangle_{Av}$ is proportional to I_p^2, hence $\langle e^2\rangle_{Av}$ should increase by a factor 4 if the plate current is changed from 120 μa to 240 μa. The internal resistance R_p of the tube increased by a factor 5 and hence I_s should decrease by a factor 4/25 in agreement with experiment.

3. DISCUSSION OF THE RESULTS

Most of the results summarized in Eq. (1) can be explained by fluctuations ΔR_i in the interface resistance R_i. A current I_p flowing through a fluctuating resistance ΔR_i produces a fluctuating emf $\Delta V=\Delta R_i I_p$ in series with the interface resistance. At audio-frequencies this emf may be replaced by an equivalent fluctuating emf $\Delta V(1+1/\mu)$ in the grid lead, where μ is the amplification factor of the tube. Usually the factor $(1+1/\mu)$ may be neglected because it is so close to unity. The noise resistance R_n measures average noise power per unit bandwidth, hence R_n should be proportional to $I_p^2\langle\Delta R_i^2\rangle_{Av}$. This explains the current dependence in formula (1); the dependence of R_n upon R_i seems to indicate that $\langle\Delta R_i^2\rangle_{Av}/R_i^2$ is almost independent of R_i.

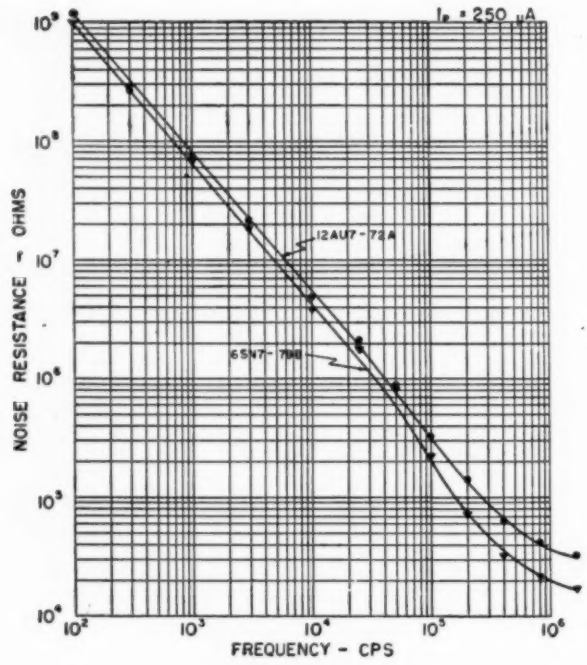

FIG. 8.

No adequate explanation for the frequency dependence of R_n is available at present.

The pulse response of tubes showing interface effects indicates that the interface layer has a time constant of the order of 1 μsec. The simplest equivalent circuit of the interface layer consists of a fixed resistance R_i and a fixed capacitance C_i in parallel, but this equivalent circuit is oversimplified. In fact, measurements as a function of frequency suggest that R_i and C_i are frequency dependent. We shall now show that this also follows from noise considerations.

According to the above explanations of formula (1), the noise emf generated in the interface layer is in series with the resistance R_i; this noise emf $(\langle e^2\rangle_{Av})^{\frac{1}{2}}$ has a noise power per unit bandwidth varying as $1/f^\alpha$. At high frequencies the capacitance C_i shunts this noise emf; one would thus expect the noise voltage $(\langle v^2\rangle_{Av})^{\frac{1}{2}}$ across the interface layer to be given by:

$$(\langle v^2\rangle_{Av})^{\frac{1}{2}}=\frac{(\langle e^2\rangle_{Av})^{\frac{1}{2}}}{(1+\omega^2C^2R^2)^{\frac{1}{2}}}, \tag{3}$$

Since $\langle v^2\rangle_{Av}$ is the quantity that is actually measured, one would thus expect $R_n=\text{const}/f^\alpha$ for $\omega CR\ll1$ and $R_n=\text{const}/f^{\alpha+2}$ for $\omega CR\gg1$.

Figure 8 shows noise measurements on two tubes with a high interface resistance at $I_p=250$ μa for frequencies up to 1.6 mc. At frequencies above 1 mc the value of R_n approaches the value required from shot effect. If this is subtracted, the measurements indicate that the frequency dependence changes from $1/f^{1.1}$ to $1/f^{1.6}$ around 100 kc. This change is thus much smaller than required by the simple equivalent circuit consisting of a fixed resistance R_i and a fixed capacitance C_i in parallel.

It is interesting to compare the flicker noise resistance of the interface layer and the noise resistance of a *p-n* junction. According to Anderson and van der Ziel, the noise resistance of a junction consists of a shot noise part and a flicker noise part, the latter part being negligible in comparison with the former part at high frequencies.[5]

The shot noise part is constant at low frequencies and varies as $f^{-1/2}$ at higher frequencies. The flicker noise part varies as f^{-1} at low frequencies and, in analogy with the behavior of the shot noise part, should vary as $f^{-1.5}$ at high frequencies. The flicker noise of a *p-n* junction should thus show a change from a f^{-1} spectrum at low frequencies to a $f^{-1.5}$ spectrum at high frequencies. This is almost identical with our results for the interface layer; it may be a mere coincidence, but it might also be an indication that the interface layer acts as a rectifying barrier (compare also Eisenstein[2]).

[5] R. L. Anderson and A. van der Ziel, Trans. Inst. Radio Engrs. PG ED-1, 20, November 1952.

Letters to the Editor

Scalloped Beam Amplification

T. G. MIHRAN
Research Laboratory, General Electric Company, Schenectady, New York
(Received May 17, 1954)

SCALLOPED beam amplification is a form of space-charge-wave amplification in which an rf signal traveling along an electron beam of periodically varying diameter is amplified.[1] No accompanying circuits or drift tubes of special construction are required to obtain gain. Test data have been obtained which establish the existence of scalloped beam amplification. The equipment used to obtain the data is shown diagrammatically in Fig. 1. A dc electron beam is produced in a magnetically shielded region by using a planar cathode, control grid, and accelerating grid. This beam is injected into a unidirectional magnetic field by means of an aperture in the magnetic shield. The beam travels down a drift tube free from external electric fields. The outer diameter of the beam is found to vary periodically even though approximately the Brillouin magnetic field is used. A 1000-Mc rf signal is introduced onto the beam by means of the control grid. A movable resonant cavity is used to measure the rf current at any point in the beam between the accelerating grid and collector. A fine wire probe, likewise movable, is used to obtain information about beam diameter.

Typical test data are shown in Fig. 2. Rf power gain and beam diameter are plotted as a function of drift distance. It is evident that upon leaving the accelerating grid the current bunches set up

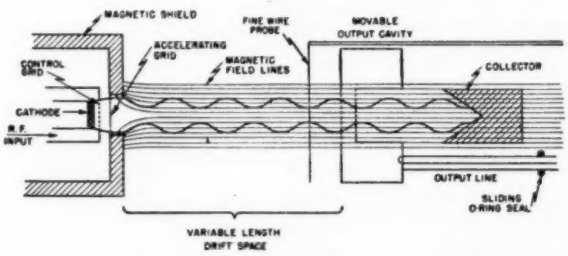

FIG. 1. Movable cavity setup for the study of scalloped beam amplification.

by space-charge-control action in the cathode control-grid region immediately begin to debunch. The magnetic field compresses the beam at this point, thus setting up the proper condition for scalloped beam amplification (rather than deamplification). For amplification, debunching should occur in the constricted portion of the dc beam and rebunching should take place when the beam is in an expanded state. By proper adjustment of the magnetic field strength these conditions can be maintained throughout beam travel. It is interesting to note the dissymmetry in the shape of the standing wave. This characteristic verifies the fact that the effective plasma wavelength is longer in the expanded portion of the beam than in the constricted region.

As a result of the interaction between the rf signal and the scalloped beam, the standing wave maxima increase exponentially. An over-all gain of 24 db was measured with this setup, of which 10.6 db was the result of scalloped beam amplification. A theoretical estimate of gain can be obtained by assuming the beam diameter changes abruptly rather than gradually every quarter plasma wavelength. In this case, current gain per scallop is given by

$$\text{Current gain}=\frac{F_A}{F_B}\frac{d_B}{d_A}, \qquad (1)$$

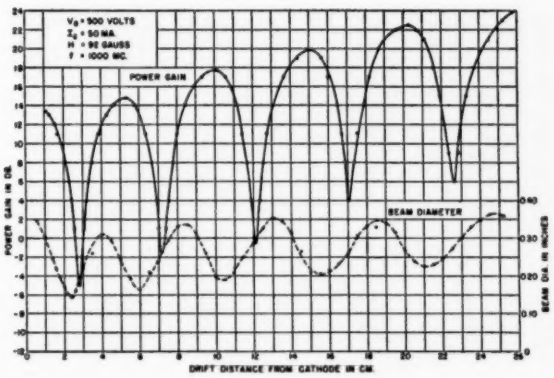

FIG. 2. Power output and beam diameter as a function of drift distance.

where d_B is the larger beam diameter and d_A is the smaller diameter. The factors F_A and F_B are the plasma frequency reduction factors in the two regions of the beam. Taking maximum and minimum diameters from the mid-region of Fig. 2, namely $d_A=0.200$ in. and $d_B=0.355$ in., it is found that $F_A=0.62$ and $F_B=0.78$. In the test setup, the drift tube diameter is ten times the beam diameter, hence it does not affect the plasma frequency reduction factors appreciably. Using these figures, (1) predicts an upper bound for power gain of 3.0 db/scallop. The average gain in the midregion of Fig. 2 is approximately 2.5 db/scallop. This agreement is very good in view of the approximate nature of the calculation.

[1] Peter, Bloom, and Ruetz, RCA Rev. 15, 113–120 (1954).

Equation of State of Argon

R. H. CHRISTIAN* AND R. G. SHREFFLER
Los Alamos Scientific Laboratory, Los Alamos, New Mexico
(Received June 3, 1954)

IN a recently published paper[1] it was necessary to present a Hugoniot of argon based on preliminary experimental data. Improved techniques[2] have led to the more precise data shown in Fig. 1.

The experimental measurements were made on gas shocks generated by a metal plate moving into an argon filled chamber. The plates were, within the limits of measurement, instantaneously

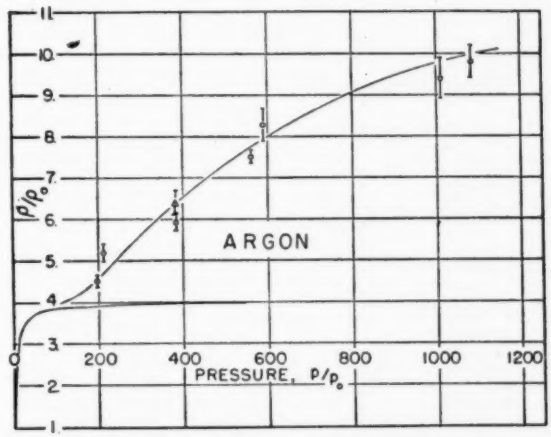

FIG. 1. Hugoniot of Argon (initial conditions, $T_0=27°C$, $P_0=.80\times10^6$ dynes/cm²). The point shown by the triangle is for a mixture of 93 percent argon, 7 percent oxygen.

accelerated to a constant velocity which was maintained throughout the interval of investigation. The experimental data consists of measurements of shock and particle velocity. Figure 1 shows the data, transformed through the equations conserving mass and momentum, in the pressure-compression plane.

The data is seen to agree rather well with the upper curve which was calculated by Dr. W. W. Wood[3] using standard methods of quantum statistical mechanics. This calculation assumed no energy to be radiated from the shocked into the unshocked gas. The lower curve in the figure is that calculated for an ideal gas defined by a $\gamma=5/3$.

The use of this Hugoniot would require changes of minor character only in the cited paper.[1]

It is anticipated that this work will be expounded in a later publication along with similar Hugoniots for other gases.

* R. H. Christian currently employed at the University of California, Radiation Laboratory, Livermore, California.
[1] R. G. Shreffler and R. H. Christian, J. Appl. Phys. 25, 324 (1954).
[2] Presented at the January, 1954 Meeting of American Physical Society in New York.
[3] Private communication.

Additional Comments on "Diffraction of Electromagnetic Waves by an Aperture in a Plane Screen"

RALPH D. KODIS
Cruft Laboratory, Harvard University, Cambridge, Massachusetts
(Received June 3, 1954)

IT is the purpose of this letter to discuss the paper by G. Bekefi[1] and the subsequent comments of J. H. Crysdale.[2] Two points will be made:

(1) By taking advantage of the apparatus of the dyadic Green's function as formulated by Levine and Schwinger[3] the expressions for the field components, given both by Bekefi and more directly by Crysdale, can be written down immediately. It is neither necessary nor desirable to proceed by the devious route of the Hertz vector.

(2) Crysdale criticizes Bekefi's formula (19) on the ground that it implies the angular independence of the current distribution function on the screen. It is easy to show, however, that this formula follows from Crysdale's assumption of a one-component current. Actually the two results, (19) and (21), given by Bekefi are identical, as will be shown below.

The discussion will be limited to the diffraction of the *E*-vector of an electromagnetic field by a perforated, perfectly conducting plane screen. Its extension to the magnetic vector is straightforward. If the screen is considered to be an obstacle in free space, an exact integral formula for the electric vector at a point $\mathbf{r}(x,y,z)$ is (time dependence, $e^{-i\omega t}$; rationalized MKS units)

$$\mathbf{E}(\mathbf{r})=\mathbf{E}^{inc}(\mathbf{r})-i\omega\mu\int_{S_m}\boldsymbol{\Gamma}(\mathbf{r},\boldsymbol{\rho}')\cdot\mathbf{K}(\boldsymbol{\rho}')dS'_m, \tag{1}$$

where dS_m' is an element of area on the screen which is located in the plane $z=0$, and where $\boldsymbol{\rho}(x,y)=\mathbf{r}(x,y,0)$ is a position vector in this plane. The free-space dyadic Green's function $\boldsymbol{\Gamma}$ is

$$\boldsymbol{\Gamma}(\mathbf{r},\mathbf{r}')=\left(\boldsymbol{\varepsilon}+\frac{1}{k^2}\nabla\nabla\right)G(\mathbf{r},\mathbf{r}'), \tag{2}$$

where $\boldsymbol{\varepsilon}$ is the unit dyad, $k^2=\omega^2\epsilon\mu$, and $G(\mathbf{r},\mathbf{r}')$ is the scalar Green's function

$$G(\mathbf{r},\mathbf{r}')=\frac{\exp ik|\mathbf{r}-\mathbf{r}'|}{4\pi|\mathbf{r}-\mathbf{r}'|}=\frac{\exp ik[(x-x')^2+(y-y')^2+(z-z')^2]^{\frac{1}{2}}}{[4\pi(x-x')^2+(y-y')^2+(z-z')^2]^{\frac{1}{2}}}. \tag{3}$$

The current distribution is given by the discontinuity in tangential H across the conductor,

$$\mathbf{K}(\boldsymbol{\rho})=\mathbf{a}_z x[\mathbf{H}(x,y,0^-)-\mathbf{H}(x,y,0^+)].$$

With an x-polarized incident field and the uniform "optical" current, $\mathbf{K}=\mathbf{a}_xK_0$, used by Crysdale the scattered field can be reduced to

$$\mathbf{E}^{sc}(\mathbf{r})=-i\omega\mu K_0\int_{S_m}\left(\mathbf{a}_x+\frac{1}{k^2}\nabla\frac{\partial}{\partial x}\right)G(\mathbf{r},\boldsymbol{\rho}')dS_m'. \tag{4}$$

Expanding the gradient in rectangular coordinates, one finds immediately that

$$\mathbf{E}_x^{sc}(\mathbf{r})=-i\omega\mu K_0\int_{S_m}G(\mathbf{r},\boldsymbol{\rho}')dS_m'-\frac{i}{\omega\epsilon}K_0\frac{\partial^2}{\partial x^2}\int_{S_m}G(\mathbf{r},\boldsymbol{\rho}')dS_m' \tag{5a}$$

$$\mathbf{E}_y^{sc}(\mathbf{r})=-\frac{i}{\omega\epsilon}K_0\frac{\partial^2}{\partial x\partial y}\int_{S_m}G(\mathbf{r},\boldsymbol{\rho}')dS_m' \tag{5b}$$

$$\mathbf{E}_z^{sc}(\mathbf{r})=-\frac{i}{\omega\epsilon}K_0\frac{\partial^2}{\partial x\partial y}\int_{S_m}G(\mathbf{r},\boldsymbol{\rho}')dS_m'. \tag{5c}$$

The integral arising in these formulas is identical with Crysdale's (21), and the field components obviously correspond to Bekefi's formulas (6). It is evident from (5c) that even with a current distribution having both x- and y-components, $\mathbf{E}_z^{sc}(\boldsymbol{\rho})=0$ since $\partial_z G(\boldsymbol{\rho},\boldsymbol{\rho}')=0$.

It can now be shown that all of Bekefi's results are contained in (5). The integral is first reduced by means of the Fourier integral representation of the Green's function (3),

$$\frac{\exp ik|\mathbf{r}-\mathbf{r}'|}{4\pi|\mathbf{r}-\mathbf{r}'|}=\frac{1}{(2\pi)^3}\int_{-\infty}^{\infty}\int\int d\xi d\eta d\zeta \times\frac{\exp[i\xi(x-x')+i\eta(y-y')+i\zeta(z-z')]}{k^2-\xi-\eta^2-\zeta^2}. \tag{6}$$

The ζ integral can be carried out by the calculus of residues. In $z>z'$ the integral converges for $Im\zeta>0$, so the contour can be closed in the upper-half plane, capturing the pole at $\zeta=(k^2-\xi^2-\eta^2)^{\frac{1}{2}}$. Since $z'=0$ in the geometry under consideration, we find that

$$G(\mathbf{r},\boldsymbol{\rho}')=\frac{i}{8\pi^2}\int_{-\infty}^{\infty}\int d\xi d\eta \times\frac{\exp[i\xi(x-x')+i\eta(y-y')+i(k^2-\xi^2-\eta^2)^{\frac{1}{2}}z]}{(k^2-\xi^2-\eta^2)^{\frac{1}{2}}} \tag{7}$$

with

$$\arg(k^2-\xi^2-\eta^2)^{\frac{1}{2}}=\frac{\pi}{2}\quad\text{for}\quad k^2<\xi^2+\eta^2.$$

Now in (5)

$$\int_{S_m}G(\mathbf{r},\boldsymbol{\rho}')dS_m'=\int_{-\infty}^{\infty}\int G(\mathbf{r},\boldsymbol{\rho}')dx'dy'-\int_{S_0}G(\mathbf{r},\boldsymbol{\rho}')dS_0',$$

where S_0 is the aperture area. Substituting (7) in the infinite integral, we find that the x', y' integrations are elementary, yielding

$$\int_{-\infty}^{\infty}\int G(\mathbf{r},\boldsymbol{\rho}')dx'dy'=\frac{i}{8\pi^2}\int_{-\infty}^{\infty}\int d\xi d\eta \times\frac{\exp i[\xi x+\eta y+(k^2-\xi^2-\eta^2)^{\frac{1}{2}}z]}{(k^2-\xi^2-\eta^2)^{\frac{1}{2}}}(2\pi)^2\delta(\xi)\delta(\eta),$$

so that with the properties of the δ function we have

$$\int_{S_m}G(\mathbf{r},\boldsymbol{\rho}')dS_m'=\frac{i}{2k}e^{ikz}-\int_{S_0}G(\mathbf{r},\boldsymbol{\rho}')dS_0'. \tag{8}$$

If the incident field is taken to be $\mathbf{E}^{inc}(\mathbf{r})=\mathbf{a}_xe^{ikz}$, the assumed current turns out to be

$$\mathbf{a}_x=K_0=-\mathbf{a}_x\frac{2k}{\omega\mu}, \tag{9}$$

and the combination of (8) and (9) with (4) gives

$$\mathbf{E}^{sc}(\mathbf{r}) = -\mathbf{a}_z e^{ikz} + 2ik\mathbf{a}_z \int_{S_0} G(\mathbf{r},\varrho')dS_0' - \frac{2i}{k}\nabla\frac{\partial}{\partial x}\int_{S_0} G(\mathbf{r},\varrho')dS_0'. \quad (10)$$

The integrated term is seen to cancel the incident field so that the electric vector in the region $z>0$ is represented by the last two terms of (10) which involve an integral over the aperture identical with Bekefi's (21).

The final consequence of this discussion is obtained by considering the integral

$$I = \int_{S_0} G(\mathbf{r},\varrho')dS_0'. \quad (11)$$

If we specialize to the circular aperture, irntoduce polar coordinates ρ, ϕ, and make use of (7), we obtain

$$I = \frac{i}{8\pi^2}\int_{-\infty}^{\infty}\int \frac{d\xi d\eta}{(k^2-\xi^2-\eta^2)^{\frac{1}{2}}} \exp i[\xi\rho\cos\phi + \eta\rho\sin\phi + (k^2-\xi^2-\eta^2)^{\frac{1}{2}}z] \times \int_0^a \rho' d\rho' \int_0^{2\pi} \exp -i[\xi\rho'\cos\phi' + \eta\rho'\sin\phi']d\phi'.$$

The integral can now be reduced by making use of the formulas

$$\int_0^{2\pi} \exp -i[\xi\rho'\cos\sigma' + \eta\rho'\sin\phi']d\phi' = 2\pi J_0[\rho'(\xi^2+\eta^2)^{\frac{1}{2}}],$$

$$\int_0^a \rho' J_0[\rho'(\xi^2+\eta^2)^{\frac{1}{2}}]d\rho' = \frac{a}{(\xi^2+\eta^2)^{\frac{1}{2}}} J_1[a(\xi^2+\eta^2)^{\frac{1}{2}}],$$

and by transforming the Cartesian coordinates ξ, η to an equivalent polar set defined by

$$\xi = k\nu\cos\theta, \quad \eta = k\nu\sin\theta.$$

Then

$$I = \frac{ia}{4\pi}\int_0^\infty \frac{d\nu}{(1-\nu^2)^{\frac{1}{2}}} \exp[ik(1-\nu^2)^{\frac{1}{2}}z] J_1(ka\nu)\int_0^{2\pi} \exp[ik\rho\nu\cos(\theta-\phi)]d\theta.$$

The last integral is evidently $2\pi J_0(k\rho\nu)$, so that the final results is

$$I = \frac{ia}{2}\int_0^\infty J_0(k\rho\nu)J_1(ka\nu)\exp[ik(1-\nu^2)^{\frac{1}{2}}z]\frac{d\nu}{(1-\nu^2)^{\frac{1}{2}}}. \quad (12)$$

Formula (12) corresponds exactly to Bekefi's (19) after the substitution $\lambda = k\nu$. It has been derived from the integral (11) obtained by both Bekefi and Crysdale. This integral, in turn, has been shown to be an immediate consequence of the dyadic Green's function formulation when one makes the approximation that the current distribution on the screen with aperture is the same as it would be for a complete screen. The analysis outlined above avoids the necessity of finding an approximate solution to an integral equation, and the result is directly related to the field through (10).

[1] G. Bekefi, J. Appl. Phys. **24**, 1123 (1953).
[2] J. H. Crysdale, J. Appl. Phys. **25**, 269 (1954).
[3] H. Levine and J. Schwinger, Communs. on Pure and Appl. Math. **3** (4), (1950).

Electron Beam Effects on Thin Evaporated Bismuth Films

P. J. Bryant, H. U. Rhoads, and A. H. Weber
Saint Louis University, St. Louis 3, Missouri
(Received June 18, 1954)

In a letter to this journal,[1] titled "Sudden Change in the Arrangement of Crystallites in Thin Evaporated Bismuth Films," the effect of the electron beam on the arrangement of crystallites in thin evaporated Bi films is discussed. Instability of the evaporated metal film from the moment of irradiation by the electron beam is reported; the observed changes in the crystallites being attributed to the tilting of these particles from their original position caused either directly or indirectly by the electron beam. The effect of the indirect action of the electron beam was assumed to be temperature change of the substrate (collodion) supporting the Bi films.

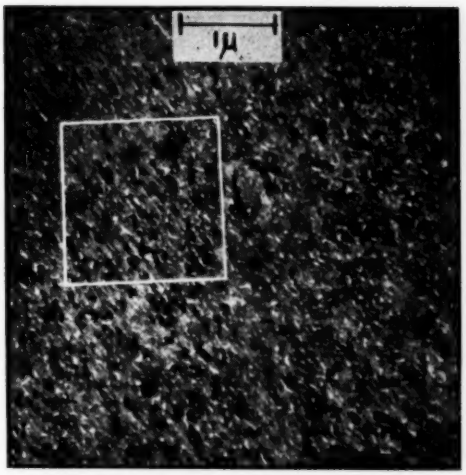

FIG. 1. Electron micrograph positive of 203 A-thick Bi film evaporated on glass and stripped off with collodion observed with low intensity electron illumination—*before* strong electron illumination.

Evaporated Bi films have been extensively investigated in our laboratories; structure and related properties of evaporated Bi films have been studied as a function of thickness, conductivity, orientation, and temperature. It is the purpose of this note to contribute some additional information on the effect of the electron beam on Bi films during electron microscopic investigations.

The Bi films prepared for our investigations may differ from those of Howard's since ours were evaporated upon glass rather than upon a collodion substrate and then were stripped off the glass substrate with collodion. Thus, in our films the Bi may be more strongly bonded to the collodion than were Howard's. However, we have noted no restriction in the mobility and activity of our Bi deposits due to this possible stronger bonding.

The evaporation rate for our Bi films is slow, 1–10 A/minute. The evaporation distance is 6–7 cm and the vacuum is usually 10^{-6} mm or better. Within a definite range of thickness, the re-

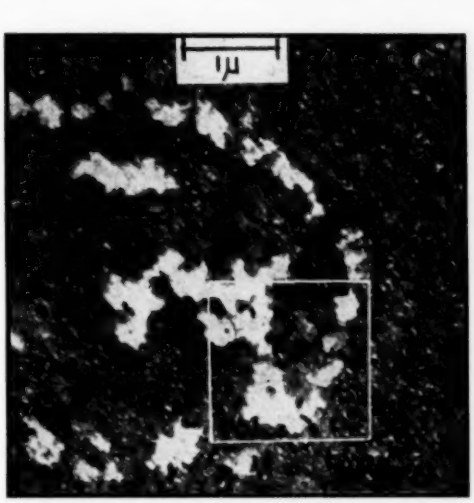

FIG. 2. Same area as Fig. 1 *after* complete (i.e., Bi film attains stability) electron beam bombardment damage.

sistivity[3] of the evaporated film is a simple function of thickness. An RCA EMU-2B electron microscope at a magnification of 7000 approximately and with a compensated objective pole piece was used for the microscopy of the films.

The movement or change ("drifting") of the crystallites as the sample is irradiated by the beam was noticed frequently. It has been observed to proceed, stop, and then start again as the beam intensity continuously increases. The specimen is quite stable under initial low intensity of the beam. After the drift activity has proceeded to a maximum, additional radiation does not produce reactivity of this drifting. This last observation is in agreement with Howard.

In our work specimen drifting caused by indirect action of the beam (motion caused by thermal effect of the beam on the unaged substrate) is always observed unless the samples are aged for 2–4 days in vacuum. Observations made on samples aged for this period exhibit no drifting whereas for longer or shorter aging periods drifting is always found.

Electron micrographs illustrating rearrangement of crystallites under the action of the beam appear in Howard's letter.[1] Films of the appearance of his Fig. 1 are characteristic in our work of a thickness of at least 500 A (average thickness) or more. Our film thickness measurements are based upon a radioactive tracer method,[3] having an over-all probable error of less than 4 percent.

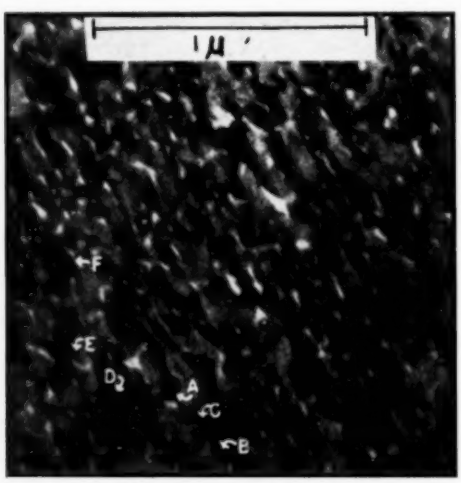

FIG. 3. The outlined area of Fig. 1 (*before* electron bombardment damage) enlarged to show individual crystallites more clearly. Compare *A–F* marked particles in Figs. 3 and 4.

Our typical results are shown by Figs. 1–4. In these photographs little if any tilting is observed. Close examination of individual particles of the micrographs *before* and *after* electron beam bombardment (Figs. 1–4) reveals no observable gross structural changes due to the electron beam. The same shapes and orientation of crystallites appear at corresponding points as is shown by Figs. 3 and 4. Hence the shape and location of Bi particles is unchanged but the electron optical density is changed by the action of the incident electron beam. Particles which appear dense (dark) in the *after* film were originally less dense (whiter) in the *before* film. Also, particles originally dense (dark) in the *before* film are usually whiter in the *after* film.

It is suggested that the effect of the direct beam is to cause a momentary melting and evaporation of individual Bi particles the magnitude of this effect depending upon the extent of contact between individual particles and their elevation above the average height of the surrounding Bi. On melting, during which time some aggregation takes place, better contact is established which conducts away the heat probably resulting in recrystallization.

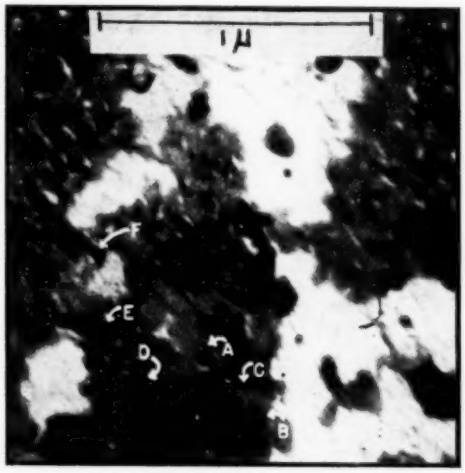

FIG. 4. The outlined area of Fig. 3 (*after* electron beam bombardment damage) enlarged to show individual crystallites more clearly. Compare *A–F* marked particles in Figs. 3 and 4.

It is suggested that the action of the electron beam on the Bi films is to enhance aggregation of Bi through the mechanism of extremely localized (over microscopic areas) melting, evaporation, and recrystallization. Thus certain areas, due to poor thermal contact, would lose Bi by evaporation and other areas of good thermal contact would act as condensation centers for the evaporated material. Such a mechanism would explain the observed variations in electron optical density in *before vs after* films. Close examination within the clear (white) areas of Figs. 2 and 4 shows small crystallites which may indicate recrystallization upon the substrate after evaporation of larger crystallites.

[1] L. L. Howard, J. Appl. Phys. **25**, 125 (1954); also **25**, 543 (1954).
[2] Bryant, Rhoads, and Weber, Phys. Rev. **92**, 1083 (1953).
[3] J. Antal and A. H. Weber, Rev. Sci. Instr. **23**, 424–426 (1952).

Re-examination of Low-Temperature Properties of Crystalline Quartz

A. PAVLOVIC AND R. PEPINSKY
X-Ray and Crystal Analysis Laboratory, The Pennsylvania State University, State College, Pennsylvania
(Received June 21, 1954)

ELECTRICAL resonance measurements of x and y plates of α quartz from room temperature to 89°K by Osterberg[1] indicated that these plates ceased to resonate at about 91°K. This phenomenon was attributed to an $\alpha \rightarrow \delta$ transition. Osterberg's result is in contradiction with reported data on the electrical resonance,[2] dielectric constant,[3] and the temperature volume expansion coefficient[4] of α quartz in this temperature range, however. It has appeared worthwhile to reexamine some of the properties of α quartz in the neighborhood of 91°K.

α-Quartz plates, cut parallel to the optic axis, were resonated in a Giebe-Schiebe apparatus from 293°K to 88°K. It was found that the plates resonated throughout that entire temperature range. In addition, four commercial plates—two shear mode and two thickness mode plates—were driven at their resonant frequencies by means of an rf generator, from room temperature down to 4.2°K, and were found to resonate throughout the temperature range.

The plates used in the Giebe-Schiebe experiments, plus other plates of fused and crystalline quartz cut perpendicular to the optic axis, were silver electroded by evaporation. The dielectric constant *versus* temperature curves were obtained for these plates from room temperature to 4.2°K. Typical curves are shown in

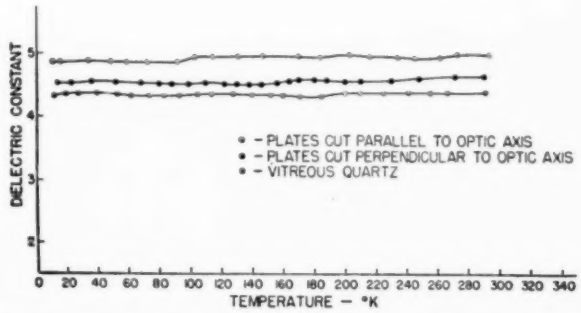
DIELECTRIC CONSTANT
5
4
3
2
• - PLATES CUT PARALLEL TO OPTIC AXIS
• - PLATES CUT PERPENDICULAR TO OPTIC AXIS
• - VITREOUS QUARTZ
0 20 40 60 80 100 120 140 160 180 200 220 240 260 280 300 320 340
TEMPERATURE — °K

FIG. 1. Dielectric constant *vs* temperature of crystalline and fused quartz.

Fig. 1. In all cases the largest dielectric constant was observed at room temperature, and decreased slightly as the temperature was lowered.

Finally, oscillation and Weissenberg x-ray diffraction photographs were taken with a single crystal of quartz both at room temperature and at ~80°K. Comparison of the photographs for the two temperatures showed no detectable alteration of the scattering patterns had occurred.

These results indicate no transition in α quartz from 846° to 4.2°K.

The examination was supported by a Fellowship Grant from the Owens-Illinois Glass Company of Toledo, Ohio, for which the authors express their gratitude.

[1] H. Osterberg, Phys. Rev. **49**, 552 (1936).
[2] H. K. Onues and A. Beckman, Kon. Akad. Amsterdam **15**, 1380 (1913).
[3] B. Doborzynski, Bull. intern. acad. polon. sci., Classe sci. math. nat. **1938A**, 153.
[4] R. B. Sosman, *The Properties of Silica* (Chemical Catalogue Company, Inc., New York, 1927), ACS Monograph No. 37.

An Additional Observation on Thermal Effects in Point Contact Rectifiers

H. L. ARMSTRONG
Clevite-Brush Development Company, Cleveland, Ohio
(Received June 23, 1954)

RECENTLY the author discussed the phenomenon of "turnover" in the reverse characteristic of point contact rectifiers, on the hypothesis that it is due to thermal effects.[1] The condition for the point of turnover was calculated to be [Eq. (10) of reference 1]

$$\exp(iv/2\pi gr_0)=iv(c-bv^{\frac{1}{2}})/2\pi gr_0kT, \quad (1)$$

where i=reverse current, v=reverse voltage (both taken as positive quantities), k=Boltzmann's constant, T=ambient absolute temperature, r_0=radius of point contact, g/T=thermal conductivity of germanium* at temperature T, and b and c are constants. Ordinarily $bv^{\frac{1}{2}}\ll c$ and $c/kT\gg 1$.

If, as suggested by the above inequalities, $bv^{\frac{1}{2}}$ is neglected, this is an equation of the form $\exp x=mx$, m being a constant. For m sufficiently large, this has two real roots, which may be approximated by $x=1/m$ and $x=\ln m$. In the original discussion, the root $x=1/m$ was used. This made the turnover power iv increase with temperature. It has since been shown that the turnover power, in fact, decreases with temperature, at least over the ordinary working range.[2] (This has also been pointed out in private communications.)

It is now felt that the root corresponding to $x=\ln m$ is actually the correct one, the other corresponding to a region in which the equations from which it was derived are not valid. This would give, at turnover,

$$iv=2\pi gr_0\ln(c/kT)\approx 2\pi gr_0\{\ln(c/kT_0)+1\}-(2\pi gr_0/T_0)T, \quad (2)$$

T_0 being some temperature in or near the operating range (say 300°K), and the approximation corresponding to the first two terms of a Taylor's series. This makes the turnover power decrease linearly, with a slope $2\pi gr_0/T_0\sim 3\times 10^{-3}$ at $T_0=300$°K.[1] This is in fair agreement with published results for similar rectifiers,[2] at least up to 100°C or so; the theory used here is not intended to be applicable to higher temperatures.

* Since this concerns germanium rectifiers.

[1] H. L. Armstrong, J. Appl. Phys. **24**, 1332 (1953).
[2] A. Lempicki and C. Wood, Proc. Phys. Soc. (London) **B67**, 328 (1954).

Erratum: Low Loss Ferrites

L. G. VAN UITERT, J. P. SCHAFER, AND C. L. HOGAN
Bell Telephone Laboratories, Murray Hill, New Jersey
[J. Appl. Phys. **25**, 925 (1954)]

IN Vol. 25, Number 7, page 925, the title of the Letter to the Editor which reads "Low Loss Ferrites for Applications at 4000 Millicyles per Second" should have read "Low Loss Ferrites for Applications at 4000 *Megacycles*."

Erratum: A Note on "Effect of Filament Voltage on the Plate Current of a Diode"

HENRY S. C. CHEN
Drexel Institute of Technology, Philadelphia, Pennsylvania
[J. Appl. Phys. **25**, 929 (1954)]

ON line 2, page 930, K should be replaced by k. In Eq. (3), k should be replaced by K and I^2, I^3, etc., by $2!$, $3!$, etc.

Cover Photograph

The photograph shows an interesting and typical pattern of ferroelectric domains of a $BaTiO_3$ single crystal. Similar to the ferromagnetic domains of iron,

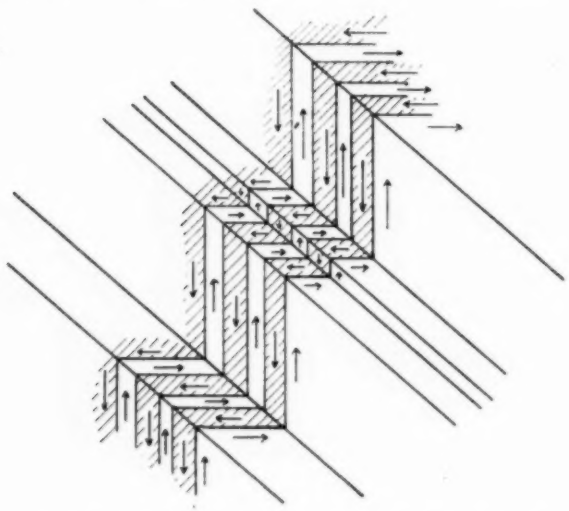

the electric polarization of the ferroelectric domains of $BaTiO_3$ can be along any one of the 6 (100) directions. The sharp 45° lines on the photograph are 90° walls (boundaries between domains polarized at 90° to each other). The 180° walls (boundaries between antiparallel polarized domains) cannot be seen very easily. However, by applying an external electric field or stress to the crystal, one can change the optical extinction position for parallel and antiparallel domains in opposite directions and thus make the two types of domains distinguishable in polarized light. The dark and bright horizontal and vertical bands on the photograph are the antiparallel domains and the 180° walls themselves cannot be seen. The crystals prevent the formation of surface charges on the 90° walls by joining the head of the polarization of one domain with the tail of the polarization of the neighboring domain, forming a zigzag head to tail arrangement. It is typical for $BaTiO_3$ that every regular domain consists of very many small antiparallel domains (width $\sim 10^{-4}$ cm) which can be aligned very easily by an applied electric field. On the other hand, the movement of 90° walls requires much higher field strengths.

The cover photograph and this explanation were supplied by Dr. Walter J. Merz, Bell Telephone Laboratories.